

SEASONAL POLAR CARBON DIOXIDE FROST ON MARS:  
SPATIOTEMPORAL QUANTIFICATION OF CO<sub>2</sub> UTILIZING  
2001 MARS ODYSSEY GAMMA RAY SPECTROMETER DATA

by

Eleanor Jane Kelly

---

A Dissertation Submitted to the Faculty of the

DEPARTMENT OF PHYSICS

In Partial Fulfillment of the Requirements  
For the Degree of

DOCTOR OF PHILOSOPHY

In the Graduate College

THE UNIVERSITY OF ARIZONA

2 0 0 6

THE UNIVERSITY OF ARIZONA  
GRADUATE COLLEGE

As members of the Final Examination Committee, we certify that we have read the dissertation prepared by Eleanor Jane Kelly entitled Seasonal Polar Carbon Dioxide Frost on Mars: Spatiotemporal Quantification of CO<sub>2</sub> Utilizing 2001 Mars Odyssey Gamma Ray Spectrometer Data and recommend that it be accepted as fulfilling the dissertation requirement for the Degree of Doctor of Philosophy.

\_\_\_\_\_  
William V. Boynton

Date: 28 March 2006

\_\_\_\_\_  
John P. Rutherford

Date: 28 March 2006

\_\_\_\_\_  
Ke Chiang Hsieh

Date: 28 March 2006

\_\_\_\_\_  
Michael A. Shupe

Date: 28 March 2006

\_\_\_\_\_  
Ann L. Sprague

Date: 28 March 2006

Final approval and acceptance of this dissertation is contingent upon the candidate's submission of the final copies of the dissertation to the Graduate College.

I hereby certify that I have read this dissertation prepared under my direction and recommend that it be accepted as fulfilling the dissertation requirement.

\_\_\_\_\_  
Dissertation Director: John P. Rutherford

Date: 28 March 2006

\_\_\_\_\_  
Dissertation Director: William V. Boynton

Date: 28 March 2006

## STATEMENT BY AUTHOR

This dissertation has been submitted in partial fulfillment of requirements for an advanced degree at The University of Arizona and is deposited in the University Library to be made available to borrowers under rules of the Library.

Brief quotations from this dissertation are allowable without special permission, provided that accurate acknowledgment of source is made. Requests for permission for extended quotation from or reproduction of this manuscript in whole or in part may be granted by the head of the major department or the Dean of the Graduate College when in his or her judgment the proposed use of the material is in the interests of scholarship. In all other instances, however, permission must be obtained from the author.

SIGNED: \_\_\_\_\_  
Eleanor Jane Kelly

## ACKNOWLEDGEMENTS

It would never be possible to sufficiently thank everyone who has helped, guided, and supported me to reach this point. I attempt here to recognize some of the individuals who have influenced my experience the most.

First and foremost, I would like to thank my parents for their unconditional love and constant support for all my dreams and ambitions throughout my life. From star-gazing with an old telescope on the roof of our house as a kid in Boulder, CO, to tackling a Ph.D. in physics as an adult in Tucson, AZ, and everything in between, your wise guidance and unshakable belief in me has created a solid foundation from which I can take on the world. For this, I could never repay you, and I only wish to offer a most sincere, heart-felt thank you. I love you.

Second, I would like to thank my fiancé, Nick Alonge, for making my years as a graduate student much richer and more wonderful than they could ever have been on my own. Your love, encouragement, and confidence in me have kept me strong during hard times. Your positive energy and celebration of even the small milestones in my career mean so much. And your simple, happy optimism and penchant for fun have allowed me to have a complete, well-rounded life while escaping the stresses of research and academia. To the best hugger in the world, I say thank you! I love you.

I would also like to thank those who have contributed to my growth as a student and scientist. My 6<sup>th</sup> grade teacher, Mr. Keeney, unknowingly instilled in me a good work ethic and taught me how exciting it is to explore the world and the universe. As my high-school volleyball coach, Dave Blessing gave me the strength and drive to keep pushing forward when I feel tired, am under pressure, or encounter obstacles.

In graduate school, Dr. John Rutherford was the first to teach and guide me in upper-level research. I truly appreciate his openness to my interests, responsiveness to my questions, and thorough and experienced advice to help me achieve my degree. To Bill (Dr. William Boynton), I would like to offer a considerable thank you for the amazing opportunity to achieve my lifelong goal of working in space exploration. Your wisdom, insight, advice, trust, and generosity with travel and conference experience have opened many doors while favorably shaping my graduate school experience. Also, deep thanks go to Dr. Ann Sprague, who has been a positive female role model in the field, and to the rest of the GRS Team for their extensive assistance, knowledge, and ability to create a friendly, teamwork environment. Along with the rest of my talented and kind committee (Drs. Ke Chiang Hsieh and Michael Shupe), you are all brilliant, and I am fortunate to have been able to work alongside you!

Finally, I thank my extraordinary friends for their unquestioning love and support, and Sparky, Cosmo, and Hank for reminding me what is truly important in life.

The GRS and its scientists are supported through NASA contract no. 1228726.

## DEDICATION

*To my amazing parents, Joe and Betty Kelly, for their endless love, support, trust, guidance, and encouragement throughout my life. I could not have been more fortunate; you are the best! And to my fiancé, Nick Alonge, for the same while giving me strength, confidence, balance, perspective, and silly stress-relieving fun during the crazy ups and downs of the graduate school process.*

*You guys mean the world to me. I am so lucky to have you, and I appreciate everything you've done.*

*Thank you so much!*

*\* I love you! \**

## TABLE OF CONTENTS

LIST OF FIGURES . . . . .	9
LIST OF TABLES . . . . .	11
ABSTRACT . . . . .	12
CHAPTER 1 Introduction . . . . .	14
1.1 Mars Exploration: History and Background . . . . .	14
1.2 Timeline: Previous Beliefs and Current Knowledge . . . . .	15
1.2.1 Ground-Based Observations . . . . .	15
1.2.2 Spacecraft Mission Observations . . . . .	19
CHAPTER 2 Science and Physics Overview . . . . .	26
2.1 Martian Environment . . . . .	26
2.1.1 Atmospheric Processes and Volatile Reservoirs . . . . .	30
2.1.2 Condensation/Sublimation Cycle of CO <sub>2</sub> . . . . .	31
2.2 Other Factors Influencing the CO <sub>2</sub> Cycle . . . . .	37
2.2.1 Water Vapor and Ice . . . . .	38
2.2.2 Dust . . . . .	43
2.2.3 Clouds . . . . .	51
2.2.4 Residual Polar Caps . . . . .	54
2.3 CO <sub>2</sub> Ground Frost Predictions . . . . .	58
2.3.1 Introduction . . . . .	58
2.3.2 Energy Balance Models . . . . .	59
2.4 Gamma Ray Sources and Nuclear Physics . . . . .	65
2.4.1 Inelastic Scattering . . . . .	68
2.4.2 Neutron-Capture . . . . .	68
2.4.3 Natural Radioactive Decay . . . . .	69
2.4.4 Transport and Interference of Gamma Rays . . . . .	70
2.4.5 Attenuation of Gamma Rays . . . . .	71
CHAPTER 3 2001 Mars Odyssey Satellite . . . . .	78
3.1 Satellite Description and Instrument Details . . . . .	78
3.1.1 Mission Overview . . . . .	78
3.1.2 Objectives and Significance . . . . .	80
3.1.3 GRS Instrumentation: Gamma Subsystem (GS) . . . . .	82

TABLE OF CONTENTS – *Continued*

3.1.4	GRS Instrumentation: Neutron Spectrometer (NS)	85
3.1.5	GRS Instrumentation: High Energy Neutron Detector (HEND)	86
3.1.6	Central Electronics Box	87
3.2	Mission Operations and Reduction of GRS Data	87
3.2.1	Overview	87
3.2.2	Spectral Analysis	88
3.2.3	Forward Processing	97
3.2.4	Satellite Background and Other Interferences	102
3.2.5	Corrections Based on Analysis of Mars' Mid-Latitude Regions	111
CHAPTER 4	Carbon Dioxide Quantification Calculations	114
4.1	Gamma Ray Attenuation	114
4.1.1	Beer-Lambert Theory	114
4.1.2	Application to the Gamma Ray Spectrometer Data	116
4.2	Model Dependence	119
4.2.1	Regolith Models	122
4.2.2	Atmosphere Models	124
4.2.3	Atmospheric Enrichment of Non-Condensables	126
CHAPTER 5	Results and Conclusions: Detailed Spatial and Temporal Dependence of Seasonal CO <sub>2</sub> Polar Frost	129
5.1	Introduction	129
5.2	CO <sub>2</sub> as a Function of Solar Areocentric Longitude ( $L_s$ )	129
5.2.1	GRS Results	129
5.2.2	Previous Model Predictions: NASA Ames Research Center Mars General Circulation Model (ARC GCM)	141
5.2.3	GRS Results Compared to Model Predictions and Other Independent Observations	144
5.3	CO <sub>2</sub> as a Function of Latitude	159
5.4	CO <sub>2</sub> Mass Calculations, Results, and Comparisons	166
5.4.1	Mass of Seasonal CO <sub>2</sub> Frost Caps: North and South Poles	168
5.4.2	Mass of Total Planet Seasonal CO <sub>2</sub> Frost	168
5.5	Suggested Future Work	172
5.5.1	CO <sub>2</sub> Longitudinal Variation Studies	172
5.5.2	Polar Maps	173
5.5.3	Seasonal Polar Cap Edge Studies	173
5.5.4	Density Estimates for the Seasonal Polar Frost	176

TABLE OF CONTENTS – *Continued*

CHAPTER 6 Conclusion . . . . .	180
6.1 Project Summary and Research Conclusions . . . . .	180
6.2 Final Words . . . . .	182
APPENDIX A Forward Model Spectrum Calculations . . . . .	184
REFERENCES . . . . .	207

## LIST OF FIGURES

1.1	Viking 1 Image: First Picture Taken from the Surface of Mars . . . . .	22
1.2	MPF Image: View of Twin Peaks . . . . .	23
1.3	MGS MOC Image: Mars in Early Northern Spring . . . . .	24
2.1	MGS MOLA Topographic Map of Mars . . . . .	29
2.2	Martian Seasonal Water Cycle Schematic . . . . .	42
2.3	HST Image: A Global Dust Storm . . . . .	45
2.4	MGS MOC Image: Dust Storm along the North Polar Cap Edge . . . . .	48
2.5	Bombardment of Mars by GCR and Related Nuclear Interactions . . . . .	67
2.6	Photoelectric Absorption . . . . .	72
2.7	Compton Scattering . . . . .	73
2.8	Pair Production . . . . .	74
2.9	Gamma Ray Interaction/Attenuation Processes . . . . .	75
2.10	CO <sub>2</sub> Attenuation/Absorption Coefficient as a Function of Energy . . . . .	76
3.1	Mars Odyssey Satellite Diagram . . . . .	79
3.2	Gamma Sensor Head Diagram . . . . .	83
3.3	Gamma Ray Signal Intensity as a Function of Distance from Nadir . . . . .	84
3.4	Entire Mars Spectrum . . . . .	91
3.5	Entire Mars Spectrum Details . . . . .	92
3.6	Spectral Peak Fitting in the Hydrogen Region . . . . .	95
3.7	Attenuation Effects in Spectral Peaks . . . . .	96
3.8	Radiogenic Gamma Ray Production: One Layer Model . . . . .	99
3.9	Radiogenic Gamma Ray Production: Two Layer Model . . . . .	100
3.10	Dependence of CO <sub>2</sub> Measurements on the H Background Signal . . . . .	105
3.11	Interference at 1461 keV: Ge in the Detector . . . . .	107
3.12	Interference at 1461 keV: Spacecraft vs. Atmospheric Origins . . . . .	109
3.13	Interference at 1461 keV: Atmospheric Ar . . . . .	110
4.1	Seasonal CO <sub>2</sub> Frost Photograph: Winter vs. Summer . . . . .	115
4.2	H Gamma Ray Signal: Winter vs. Summer . . . . .	115
4.3	Relative Atmosphere-Corrected H Gamma Ray Flux vs. Latitude . . . . .	117
4.4	CO <sub>2</sub> Thickness Model Dependency: Regolith Composition . . . . .	123
4.5	CO <sub>2</sub> Thickness Model Dependency: Atmospheric Column Density . . . . .	125
4.6	Neutron and Gamma Ray Flux Perturbation by Ar Enrichment . . . . .	128
5.1	CO <sub>2</sub> Columnar Thickness from H Gamma Rays: 60°N to 90°N . . . . .	131

LIST OF FIGURES – *Continued*

5.2	CO <sub>2</sub> Columnar Thickness from H Gamma Rays: 60°S to 90°S . . . . .	132
5.3	Comparing CO <sub>2</sub> Results from H and <sup>40</sup> K Gamma Rays: 60°N . . . . .	134
5.4	Comparing CO <sub>2</sub> Results from H and <sup>40</sup> K Gamma Rays: 67.5°N . . . . .	135
5.5	Comparing CO <sub>2</sub> Results from H and <sup>40</sup> K Gamma Rays: 75°N . . . . .	136
5.6	Comparing CO <sub>2</sub> Results from H and <sup>40</sup> K Gamma Rays: 60°S . . . . .	137
5.7	Comparing CO <sub>2</sub> Results from H and <sup>40</sup> K Gamma Rays: 67.5°S . . . . .	138
5.8	Comparing CO <sub>2</sub> Results from H and <sup>40</sup> K Gamma Rays: 75°S . . . . .	139
5.9	Comparing CO <sub>2</sub> Results from H and <sup>40</sup> K Gamma Rays: 82.5°S, 90°S . . . . .	140
5.10	NASA ARC GCM CO <sub>2</sub> Columnar Thickness Predictions: North . . . . .	142
5.11	NASA ARC GCM CO <sub>2</sub> Columnar Thickness Predictions: South . . . . .	143
5.12	GRS CO <sub>2</sub> Thickness Compared to Model Predictions: 60°N . . . . .	147
5.13	GRS CO <sub>2</sub> Thickness Compared to Model Predictions: 67.5°N . . . . .	148
5.14	GRS CO <sub>2</sub> Thickness Compared to Model Predictions: 75°N . . . . .	149
5.15	GRS CO <sub>2</sub> Thickness Compared to Model Predictions: 82.5°N . . . . .	150
5.16	GRS CO <sub>2</sub> Thickness Compared to Model Predictions: 90°N . . . . .	151
5.17	GRS CO <sub>2</sub> Thickness Compared to Model Predictions: 60°S . . . . .	154
5.18	GRS CO <sub>2</sub> Thickness Compared to Model Predictions: 67.5°S . . . . .	155
5.19	GRS CO <sub>2</sub> Thickness Compared to Model Predictions: 75°S . . . . .	156
5.20	GRS CO <sub>2</sub> Thickness Compared to Model Predictions: 82.5°S . . . . .	157
5.21	GRS CO <sub>2</sub> Thickness Compared to Model Predictions: 90°S . . . . .	158
5.22	Northern CO <sub>2</sub> Thickness as a Function of Latitude: Sublimation . . . . .	161
5.23	Northern CO <sub>2</sub> Thickness as a Function of Latitude: Condensation . . . . .	162
5.24	Southern CO <sub>2</sub> Thickness as a Function of Latitude: Condensation . . . . .	164
5.25	Southern CO <sub>2</sub> Thickness as a Function of Latitude: Sublimation . . . . .	165
5.26	Mass of Seasonal CO <sub>2</sub> Frost Caps: North and South Poles . . . . .	167
5.27	Mass of Total Planet Seasonal CO <sub>2</sub> Frost . . . . .	170
5.28	Mass of CO <sub>2</sub> in Seasonal Frost, Atmosphere, and Total Reservoir . . . . .	171
5.29	Example of Mapping H Gamma Ray Flux Ratios . . . . .	174
5.30	Example of Mapping CO <sub>2</sub> Seasonal Frost . . . . .	175
5.31	MGS TES Seasonal Polar Cap Edge Map . . . . .	177
5.32	Example of Mapping Seasonal Polar Cap Edge using GRS Data . . . . .	178
A.1	Diagram 1 . . . . .	198
A.2	Diagram 2 . . . . .	199
A.3	Diagram 3 . . . . .	201
A.4	Diagram 4 . . . . .	203

## LIST OF TABLES

2.1	General Characteristics of Mars as Compared to Earth . . . . .	27
2.2	Change in Detector Spatial Resolution with Increasing Frost Depth .	71
3.1	2001 Mars Odyssey Mapping Orbit Details and Parameters . . . . .	80

## ABSTRACT

The exchange of carbon dioxide between the atmosphere and the polar caps on Mars creates a seasonal cycle of growth and retreat of the polar caps. As the major component of the Martian atmosphere, CO<sub>2</sub> condenses in the polar regions of the planet during the winter seasons and precipitates as CO<sub>2</sub> frost. It then sublimates during the spring and summer seasons in response to solar radiation. Through natural radioactivity or when exposed to cosmic rays, elements in the Martian near-subsurface (uppermost meter) emit gamma rays with distinct, characteristic energies. The Gamma Ray Spectrometer (GRS) onboard the 2001 Mars Odyssey satellite is used to measure the gamma rays coming from the Martian regolith to calculate elemental distributions, abundances, and temporal variations in the gamma ray flux. Changes in the CO<sub>2</sub> frost over time can be quantified by observing attenuation effects of H (2223 keV hydrogen) and <sup>40</sup>K (1461 keV potassium) gamma ray signals transmitted through various depths of polar CO<sub>2</sub> overburden throughout the Martian seasons.

Conclusions are drawn about the spatial extent, column density, and mass of Mars' seasonal polar caps as a function of time utilizing GRS data. Columnar thickness and mass results are discussed and plotted for latitudes including  $\pm 60^\circ$  and poleward. GRS observations are compared to predictions from the NASA Ames Research Center Mars General Circulation Model (ARC GCM) and to similar experimental results from the Mars Odyssey High Energy Neutron Detector (HEND) and the Neutron Spectrometer (NS). Models for north and south polar atmosphere and regolith distributions are incorporated, and the results indicate that the assumption of a 100% H<sub>2</sub>O-ice residual cap underlying the seasonal frost in the north is accurate. The GRS CO<sub>2</sub> frost observations are in good agreement with the other studies mentioned, in particular for the timing of the beginning of frost deposition to the

complete sublimation of surface CO<sub>2</sub> back into the atmosphere. The total amount of condensed CO<sub>2</sub> mass derived from GRS data is on the order of  $6.0 \times 10^{15}$  kg and verifies previous reports that  $\sim 25\%$  of the total Martian exchangeable-CO<sub>2</sub> reservoir participates in the ground-atmosphere cycle.

## CHAPTER 1

### Introduction

#### 1.1 Mars Exploration: History and Background

Since ancient times, people have been fascinated by the Red Planet. Mars was named after the Roman god of war, agriculture, and the state, and it became the symbol for fire. In Greek mythology, Mars also symbolized the god of war, Ares. Its two satellites, Phobos and Deimos, which translate from Greek to English as fear and panic, respectively, were similarly named from Greek mythology for attributes personified as Ares' sons (Vasavada et al., 1998).

Initial telescopic observations of the planet began in 1610 by Galileo Galilei. During the close opposition of 1877, American astronomer Asaph Hall discovered and named Mars' two moons, and Giovanni Virginio Schiaparelli, among others, helped to usher in an age of more advanced observations. Astronomers continued to create detailed drawings and maps of Mars, while debates ensued about the existence of specific features, natural or artificially made canals, and intelligent life. Carbon dioxide was discovered in the atmosphere by spectroscopic analysis; however, until the mid-1960s, this CO<sub>2</sub> was believed to be only a minor component. Slightly later, the estimated value for the surface pressure was considerably reduced to a number reasonably close to the known measured value of today. A continual debate about the composition of the polar caps was aided by the surprising discovery during the Viking mission that the primary material in each of the perennial polar caps is different (Kieffer et al., 1992). The continued exploration of Mars by modern spacecraft is creating a vast accumulation of knowledge about the elaborate history of the Red Planet, as well as prompting new questions and fuelling scientists' desire to explore even more.

## 1.2 Timeline: Previous Beliefs and Current Knowledge

Since 1666, the polar caps of Mars have been observed and studied (Kieffer et al., 1992). The advance and retreat cycle of the frost at the poles was one of the first indications that Mars had seasons. It is now known that the polar caps are a large part of the driving force of the Martian climate. Approximately 25% of the atmosphere is cycled through these polar caps annually during periods of condensation and sublimation. (Tillman et al., 1993). To understand the Martian climate and the current state of Mars, it is essential to understand the nature of this seasonal polar carbon dioxide frost.

### 1.2.1 Ground-Based Observations

The polar CO<sub>2</sub> ice caps on Mars were first observed by Giovanni Domenico Cassini in 1666 while he was a Professor of Astronomy in Bologna, Italy. Christiaan Huygens also created elementary sketches of Mars which showed the southern polar cap in 1672. In 1719, Earth and Mars came closer to each other than they would for another 284 years, and Giacomo Maraldi was able to make relatively advanced and detailed observations. He noticed the polar “taches blanches” (white spots) and reported that the southern cap was not centered on Mars’ rotational axis (Plaxco, 1999a). Maraldi was one of the first to record the temporal changes in the white polar regions when he detected the seasonal advance and retreat of the (then mysterious) CO<sub>2</sub> frost, and he believed he saw melt-water as an observable dark ring around the border of the northern cap. Frederick William Herschel, a British astronomer, also studied the seasonal changes occurring at the poles of Mars and was the first to claim that the white areas were actually thin layers of snow or ice. Johann Hieronymus Schröter of Bremen regularly corresponded with Herschel during this time period and was able to add to and systematically improve upon Herschel’s polar cap observations (Kieffer et al., 1992).

In 1892, Camille Flammarion published the first of two summaries he would write in *La Planète Mars et ses Conditions d’Habitabilité* (Gauthier-Villars et Fils,

Paris) of all the knowledge about Mars for what he termed the “First Period” of observations lasting until 1830. At this point, Mars was known to have white spots at its poles, which were considered to be snow or ice and which varied in response to the level of insolation. Because the inclination of the axis of Mars is similar to that of the Earth, it was understood that Mars had comparable seasons. The waxing and waning of the white spots during the winter and summer time periods allowed for the observation that when at their minimum size, the roughly circular white areas are removed a small distance from the geographic poles. It was also accepted that Mars had an atmosphere containing white and possibly dark clouds that aided in the formation of snow (Karol and Catling, 2003).

What followed was a period of debate regarding Giovanni Virginio Schiaparelli’s assumption that numerous *canali* (Italian for channels) traversed Mars. Mars’ two moons were also discovered and named, the average temperature on Mars was calculated, and elaborate observatories like the Lowell Observatory in Flagstaff, Arizona were built. In 1953, the International Mars Committee was organized to enable continual observations to take place during the Mars’ opposition of 1954 (Plaxco, 1999b).

At this time, polarimetry began to be used to study the nature of the polar deposits (Dollfus, 1957, 1965). Ice, hoarfrost, and snow deposits usually exhibit a strong polarization due to internal refraction of light. However, the seasonal cap, when viewed at an angle so that it was near the edge of the planet, produced only weak polarization. A laboratory simulation involving comparable radiation flux and Martian environment illustrated that the ice deposits began to sublime and the surface became more porous. This process created polarization results similar to those actually observed at Mars and accounted for the unexpected initial discrepancy (Martin et al., 1992).

Seasonal changes in the polar frost have been recorded by many pre-spacecraft observers. In 1930, Eugène Michael Antoniadi published his visual observations, and in 1962, Earl C. Slipher did the same in *The Photographic Story of Mars*. Fischbacher et al. (1969) used photographic material from the Lowell Observatory

archive of all oppositions from 1905 through 1965 to compile mean frost regression curves. A review of the relevant literature shows that the north polar cap sublimation phase has been documented in detail from telescopic observations. The oppositions between 1946 and 1952 are described by Dollfus (1973). Miyamoto (1963) documented regression trends from the 1962-63 opposition, and C. Capen and V. Capen (1970) produced information from observations during the time period beginning in 1962 to 1968. During the 1970s and early 1980s, further details regarding the north polar cap seasonal sublimation process were published (Iwasaki et al., 1979, 1982, 1984; James et al., 1987). Dollfus (1965) also studied the south polar cap in the mid-1950s, and in 1971 and 1973, the International Planetary Patrol provided comprehensive coverage of the southern polar region which James and Lumme (1982) thoroughly analyzed. Iwasaki et al. (1986) then published independent observations of the 1973 recession after adding data from earlier in the associated opposition. More recently, the Mars oppositions in 1986 and 1988 were analyzed by Iwasaki et al. (1988, 1989, 1990) and also by James et al. (1990).

In preparation for the beginnings of spacecraft-based planetary exploration by the Mars Mariner and Viking missions, the United States government encouraged expansion of telescopic planetary observing programs in the late 1950s. At Lowell Observatory in 1965, the IAU Planetary Research Center was established and funded by NASA. Other important observing programs were financed at New Mexico State University; the Catalina Observatory and the Lunar and Planetary Laboratory, University of Arizona; the McDonald Observatory, University of Texas; and the Table Mountain Observatory, Jet Propulsion Lab (Martin et al., 1992). Various research studies were contracted including the one on Martian polar cap boundaries done by Fischbacher et al. (1969) mentioned above.

The International Planetary Patrol Program began in 1969 in time for the Mars apparition that year. This program involved coordinating seven observatories located at various longitudes around the Earth to photograph planets on an hourly basis. This allowed for nearly continuous monitoring of Mars as it went through daily and seasonal changes (Baum et al., 1970). Although participation in this pro-

gram was gradually reduced after 1973, observing stations were still operating in conjunction at Mauna Kea, Perth, and Lowell Observatory as late as 1982.

Throughout the 1980s, photography continued to be the primary mode for the study of Mars; however, some charge-coupled device (CCD) work became successful. (CCDs are used particularly in photometry, optical and UV spectroscopy, and high speed techniques which remove blurring effects caused by atmospheric turbulence.) Very promising results have been obtained from CCD cameras used for Mars observation. In France, this technology has been utilized at Pic-du-Midi and Meudon Observatory, and images of Mars from the one-meter telescopes were considered revolutionary because of the resolution, which exceeded that of previous Earth-based photographs (de Vaucouleurs, 1989). Other outstanding CCD images have been obtained at Steward Observatory in Tucson, Arizona (O'Meara, 1988) and at Lowell Observatory in Flagstaff, Arizona. Spectroscopic observations from Earth create an additional way to gain insight into Mars. Telescopic spectroscopy and high-resolution mineralogy studies have taken place at Mauna Kea Observatory in Hawaii (Bell et al., 1989; Clark et al., 1989), and at the University of Arizona's Catalina Station (Singer et al., 1989), among others.

Amateur observations also add to the library of Mars knowledge. The Mars Section of the British Astronomical Association currently receives over 1,000 observations from observers all over the world during each Mars apparition. By compiling the information in the submissions, the *Journal of the BAA* is able to detail the changes in surface features, polar hoods and caps, and variations in atmospheric activity (Martin et al., 1992). As one example of the abundance of Mars studies being undertaken worldwide, observers from Société Astronomique de France (SAF) have used the large 83 cm refractor at Meudon to document the recession of the south polar cap, cloud and dust storm activity, surface-marking variations, and atmospheric phenomena. In 1988, the International Mars Patrol (IMP) included over 250 observers from 38 countries and U.S. territories, and during the 1987-1989 apparition, over 5,300 high-quality observations in the form of photographs, CCD images and videos, and 200 micrometer south polar cap measurements were contributed (Martin

et al., 1992).

The extended database of Earth-based observations of Mars continues to be relevant to these polar caps studies. A large amount of interannual variability during the spring recession of seasonal CO<sub>2</sub> frost has been seen through micrometer observations of the north polar cap (Parker et al., 1983). The regression curves indicate that a plateau may occur during mid-spring, and analysis of Japanese photographs of Mars show that the seasonal location of this plateau appears to vary from year-to-year (Iwasaki et al., 1979, 1982, 1984). In addition, the recessions of the south polar cap in 1986 and 1988 seemed to have occurred slower than in previous years (Iwasaki et al., 1988, 1989, 1990; James et al., 1990).

The spring and summer seasons on Mars necessarily take place as the associated pole is tilted toward the sun, and therefore during opposition, toward the Earth. Conversely, the fall and winter seasons for each pole occur as the polar cap is aimed away from the Earth. In general for ground-based observations, this situation allows for better documentation of the carbon dioxide sublimation process than of its deposition. In addition, perihelion for Mars takes place close to the southern summer solstice, so the resolution of Earth-bound observations for the south pole is greater than that for the north pole.

Regardless of the limitations, Earth-based observations continue to be beneficial to planetary science and to contribute to the historical record of Mars studies. The research is important to supplement spacecraft data and to provide a wide angle of coverage over long periods of time. However, the overall understanding and knowledge regarding Martian polar processes increased dramatically with the advent of the space age and planetary exploration from space.

### 1.2.2 Spacecraft Mission Observations

Until the first space probes visited the planet and correctly identified the contribution and interaction of carbon dioxide, most Mars observers had the opinion that the seasonal caps were composed of water-ice. This belief stemmed mainly from the comparison to and similarity of Earth's polar caps. Although some researchers in

the early 1900s proclaimed that the polar cap composition must be mainly carbon dioxide due to the planet's low temperatures and apparent absence of water, Gerard Kuiper, Vasily Moroz, and Audouin Dollfus claimed as late as the 1950-60's that their observations proved that the ice caps were composed of frozen water. The possibility that the seasonal polar caps skipped the melting phase and sublimated directly to the atmosphere was not proposed until 1947 by Gerard de Vaucouleurs (Kieffer et al., 1992). In 1966, Robert Leighton and Bruce Murray were able to use CO<sub>2</sub> and pressure measurements made by the Mariner 4 spacecraft to create an atmospheric model that implied that the Martian poles got cold enough to condense CO<sub>2</sub> and that major atmospheric pressure variations occurred on a seasonal basis, as a result (discussed in more detail in Section 2.3.2). Kieffer (1970a,b) observed in infrared spectra laboratory experiments that the characteristics of carbon dioxide frost could be masked by small quantities of water and could thus explain previous misconceptions. Although the following information chronicles specifics of past and current spacecraft-based exploration of Mars, it should be noted that the details and peculiarities of the polar processes are still under investigation and debate today.

Exploration of Mars by spacecraft has been an important part of space programs worldwide. The United States, Russia/Soviet Union, Europe, and Japan have all contributed to the investigation of the planet through fly-by satellites, orbiters, landers, and rovers. Though there have been numerous unsuccessful attempts wherein the spacecraft were lost at launch, in transit, or upon arrival at the planet, only the details of the successful data-gathering missions will be mentioned here.

NASA's Jet Propulsion Lab (JPL) began significant exploration of the inner solar system with ten spacecraft built between 1962 and 1973 for the Mariner program. Launched off of an Atlas rocket, the small robotic explorers Mariner 3, 4, 6, 7, 8, and 9 were destined for Mars. Because Mariner 3's rocket-top shroud failed to open, Mariner 4 became the first successful space probe to fly by and study Mars on July 14, 1965 (Karol and Catling, 2003). Along with the first close-up photographs of another planet, Mariner 4 returned data that indicated the Martian atmosphere was composed mostly of carbon dioxide. In the late summer of 1969, Mariner 6

and 7 accomplished the first dual mission to Mars when they analyzed the Martian atmosphere and surface with remote sensors as they flew over the equator and south polar regions. They returned hundreds of pictures, but happened to miss Valles Marineris (huge equatorial canyon), and Olympus Mons and the Tharsis Montes (giant northern volcanoes). However, they did show that the dark surface features observed from Earth since the 1800s were, in fact, not canals as previously believed. Mariner 8 and 9 were the final pair of spacecraft sent from the Mariner program to study Mars. Although Mariner 8 failed during launch, Mariner 9 successfully arrived at Mars on November 13, 1971 and became the first artificial Mars-orbiting satellite. Mariner 9 observed a great global dust storm upon arrival, but after waiting for the dust to settle, it went on to provide high-quality photographs of 100% of the planet's surface, discovering giant volcanoes, canyons, and dry and dusty ancient riverbeds that had previously not been seen (Viotti et al., 2005b).

The first safe landing of a spacecraft on another planet was accomplished in 1976 by two identical orbiter-lander pairs: Viking 1 and 2. Upon entering Mars orbit, each pair split so that the lander sections could touch down on the surface to investigate.

The two landers took ground-level photographs, collected science data, and undertook three experiments searching for biological signs of life. Although there was no clear evidence of living microorganisms, the unusual chemical composition of Martian soil was examined. Pressure and temperature data from the Viking landers led scientists to believe that the northern permanent ice cap was indeed water-ice, while the southern residual cap was composed mainly of carbon dioxide, or dry ice (Snyder, 1979). These findings agreed with the Leighton-Murray model describing the condensation and sublimation of atmospheric  $\text{CO}_2$  and were mainly accepted as fact until shortly after the recent turn of the century when evidence began to suggest that the south pole may actually have water-ice under a surface layer of  $\text{CO}_2$ -ice (to be discussed). In any case, all studies agree that it is solely  $\text{CO}_2$  frost that accumulates and disappears at the poles on a *seasonal* basis (over the residual ice caps). In addition, the Viking pressure data is still used today as a key reference



Figure 1.1: The first picture taken from the surface of Mars. This photograph was taken by the Viking 1 lander on July 20, 1976. It revealed that the Martian regolith is composed of finely granulated material and rocks that are flat, angular, and pitted in places. The large central rock is about 10 cm wide. The lander's footpad can be seen on the right. Photo credit: NASA Headquarters Public Affairs Office, History Division.

for General Circulation Models (GCMs) when attempting to reproduce the Martian atmospheric and snowfall dynamics. The Viking landers outlasted their intended 90-day mission, and the last data transmission received from the surface was late in 1982.

Since contact was lost with the Mars Observer orbiter shortly before it entered Mars orbit to study the climate, geology, and geophysics of the planet in 1993, Mars Pathfinder became the next mission to return meaningful information from the Red Planet. Landing on the 4th of July, 1997, Pathfinder was the first lander to be accompanied by an independent robotic rover. The mission used a parachute and airbags to slow and protect itself during entry, descent, and landing (EDL) onto an ancient rocky flood-plain in Mars' northern hemisphere (Figure 1.2). The lander and rover (named Sojourner) outlived their primary design life by three and twelve times, respectively, and returned more than 17,000 images combined. Although extensive data analyses were done on the wind, weather, atmospheric pressure and temperature, and the chemical make-up of surrounding rocks and soil (Goodall, 1997), this important mission did not add significantly to the understanding or



Figure 1.2: Mars Pathfinder view of Twin Peaks, taken from Ares Vallis, ancient northern flood-plain. Photo credit: NASA/JPL/MPF Images Archive: Sept. 1998.

knowledge of Mars' polar areas.

Mars Global Surveyor (MGS) was the next spacecraft to enter Martian orbit on September 12, 1997. After shifting to a circular, low-altitude, nearly polar orbit, its primary mapping mission began in March of 1999 and ended on January 31, 2001. MGS is currently still fully operating in an extended mission phase. The spacecraft has analyzed the entire Martian surface, the atmosphere, and the interior of the planet using its numerous instruments: Mars Orbiter Camera (MOC), Mars Orbiter Laser Altimeter (MOLA), Thermal Emission Spectrometer (TES), Magnetometer/Electron Reflectometer, Radio Science, and Mars Relay antenna (Goodall and The MGS Team, 2005). The MOC polar images (James and Cantor, 2001; James et al., 2001), the MOLA topography and seasonal polar cap height measurements (Smith et al., 2001b; Fishbaugh and Head, 2001; Zuber et al., 1998), and the TES polar frost boundary studies (Titus, 2005; Kieffer et al., 2000) have all greatly contributed to Mars polar science and the investigation of the seasonal  $\text{CO}_2$  cycle. Details of these results, as well as comparisons to Mars Odyssey gamma ray observations are presented in the *Results and Conclusions* chapter.

In general, MGS has also returned important pictures of canyons, gullies, and debris flow features that suggest liquid water has acted at or near Mars' surface



Figure 1.3: Composite of MGS MOC daily global images of Mars during the beginning of northern spring. Acquired in early May 2002, this image shows the retreating north polar seasonal carbon dioxide frost cap. Photo credit: NASA/MSSS.

at some point. The magnetic studies indicate that the planet's magnetic field is localized in certain areas of the Martian crust, as opposed to being globally generated in the planet's core. Mars' moon, Phobos, has also been analyzed. And along with Mars Odyssey, MGS has acted as a data relay satellite for the Mars Exploration Rovers currently trekking around the surface of the Red Planet.

Following the success of MGS, the Mars Program underwent a couple of misfortunes at the end of 1999. An interplanetary weather satellite and communications

relay called Mars Climate Orbiter (MCO), and the Mars Polar Lander (MPL), which was meant to land near the edge of Mars' south polar cap to dig for water-ice, were lost upon arrival at Mars. On April 7, 2001, however, NASA launched its next highly successful mission: 2001 Mars Odyssey. The detailed description of this satellite and its instruments, a mission overview, and the objectives and significance of this mission are outlined in Chapter 3.

After Mars Odyssey, the European Space Agency (ESA) sent the Mars Express satellite to explore the surface and atmosphere of Mars in a polar orbit. Unfortunately, ESA then lost communication with Beagle 2, the small lander which accompanied this mission. The NASA Mars Exploration Rovers (MER A and B) landed successfully shortly afterward in January of 2004 and presently continue to return data while exploring Mars' mid-latitudes. Many future Mars exploration missions are also in progress or planned to continue to promote and sustain this exciting Mars research. Mars Reconnaissance Orbiter (2005), Phoenix (2007), Mars Science Laboratory (2009), Mars Telecommunications Orbiter (2009), and other various scout missions, deep drilling missions, and Mars sample return missions should all add significantly to Martian polar science and the study of the whole planet in general.

## CHAPTER 2

## Science and Physics Overview

## 2.1 Martian Environment

Mars is the fourth planet from the sun and is the outermost terrestrial planet. Its iron oxide red surface area is about one quarter that of Earth's because Mars' mean equatorial radius is only slightly more than half of the Earth's. Though the Martian year is about 687 Earth days, the Martian day is only 39 minutes longer than a day on Earth. (For these numbers and other general characteristics of Mars as compared to Earth, see Table 2.1.) Mars has seasons because its rotational axis is inclined to the orbital plane. Because of Mars' eccentricity, the seasons vary in length with northern spring and summer significantly longer than northern fall and winter. The situation is reversed in the southern hemisphere. At present, the south pole experiences warmer summers because it is tilted toward the sun during perihelion. The precession of the rotational axis causes the seasonal temperature differences between the northern and southern hemispheres to swap poles approximately every 51,000 years. The current obliquity of Mars is similar to Earth's; however, the obliquity of Mars can range between  $15^\circ$  and  $35^\circ$  and may occasionally reach  $\sim 60^\circ$  (Carr, 1998). During periods of high obliquity, the temperature profile of the planet changes dramatically.

Mars is known to have a north-south dichotomy in terms of its topography and physical geography. The southern hemisphere consists mostly of heavily cratered highlands (typical altitudes of 1 - 4 km above the zero-elevation reference line), while the northern terrain is lower in altitude (1 - 2 km below zero-altitude). (Note that the topographic zero-elevation line on Mars has been defined by Mars' gravity field described in terms of spherical harmonics with a 6.105 mbar atmospheric pressure surface at 273.15 K (the triple point of water) (Smith and Zuber, 1998). Analysis of

Table 2.1: General Characteristics of Mars as Compared to Earth.

	Mars	Earth
Mean equatorial radius (km)	3396	6378
Mean polar radius (km)	3376	6357
Oblateness	0.0074	0.0034
Mass ( $\times 10^{24}$ kg)	0.642	5.98
Mean density ( $\text{kg/m}^3$ )	3,934	5,515
Mean distance to Sun ( $\times 10^6$ km)	228	150
Perihelion ( $\times 10^6$ km)	207	147
Aphelion ( $\times 10^6$ km)	249	152
Orbit Eccentricity	0.093	0.017
Obliquity	$25.2^\circ$	$23.5^\circ$
Length of day	24 h 39 m 35 s	24 h
Length of year (Earth days)	686.9	365.3
Average orbital speed (km/s)	24.08	29.78
Seasons (Earth days)		
Northern spring	199	92.9
Northern summer	183	93.6
Northern fall	147	89.7
Northern winter	158	89.1
Atmosphere	95% $\text{CO}_2$ , 3% $\text{N}_2$ , 2% Ar	79% $\text{N}_2$ , 21% $\text{O}_2$
Mean surface pressure (mbar)	7	1000
Mean surface temperature (K)	215	288
Albedo	0.15	0.367
Surface gravity ( $\text{m/s}^2$ )	3.71	9.81
Number of moons	2	1

the number of ancient impact craters in the south suggest that the terrain formed over 3.8 billion years ago and is older than the smoother plains in the north. The smooth northern terrain is believed to perhaps have been flattened by lava flows and is now covered with dust and reddish sand. Superimposed on the described large scale topography are smaller, more extreme surface features. The volcanic Tharsis Montes and Olympus Mons, the highest mountain in the solar system rising 24 km, are found near the equator around 100°W longitude. Valles Marineris, the solar system's largest canyon system, is 2 - 9 km deep and 4000 km long. In the southern hemisphere, the huge Hellas impact basin extends to 8 km below the zero-altitude (6.1 mbar isobaric surface) level (Smith et al., 2001a). The poles of Mars also exhibit distinctive physiography. Poleward of about  $\pm 80^\circ$ , finely layered deposits can be found. These polar layered deposits are estimated to be a few kilometers thick and are presumably caused by periodic changes in thermal properties and wind profiles induced by Mars' orbital and rotational variations over time. Specifically, eccentricity changes, precession, and variations of Mars' obliquity most likely play critical roles (Carr, 1998).

Though the surface of Mars has been extensively studied, not much is known about Mars' interior. It is under debate whether this historically volcanically active planet has plate tectonics. Evidence in support of crustal movement comes from observations of Mars' magnetic fields made by the Mars Global Surveyor spacecraft. Apparently, the planet's crust has been magnetized in thin, alternating bands about 1000 km long (Connerney et al., 1999). Drawing a parallel to crustal formations seen on Earth, this would suggest that similar tectonic events and movements have occurred on both planets. However, if Mars indeed lacks plate tectonics as is also commonly believed, the crustal materials are not cycled through the upper mantle as is observed on Earth (Carr, 1998). In this scenario, the diverse land features are purely a result of the numerous surficial geologic processes such as erosion by wind, water, and ice.

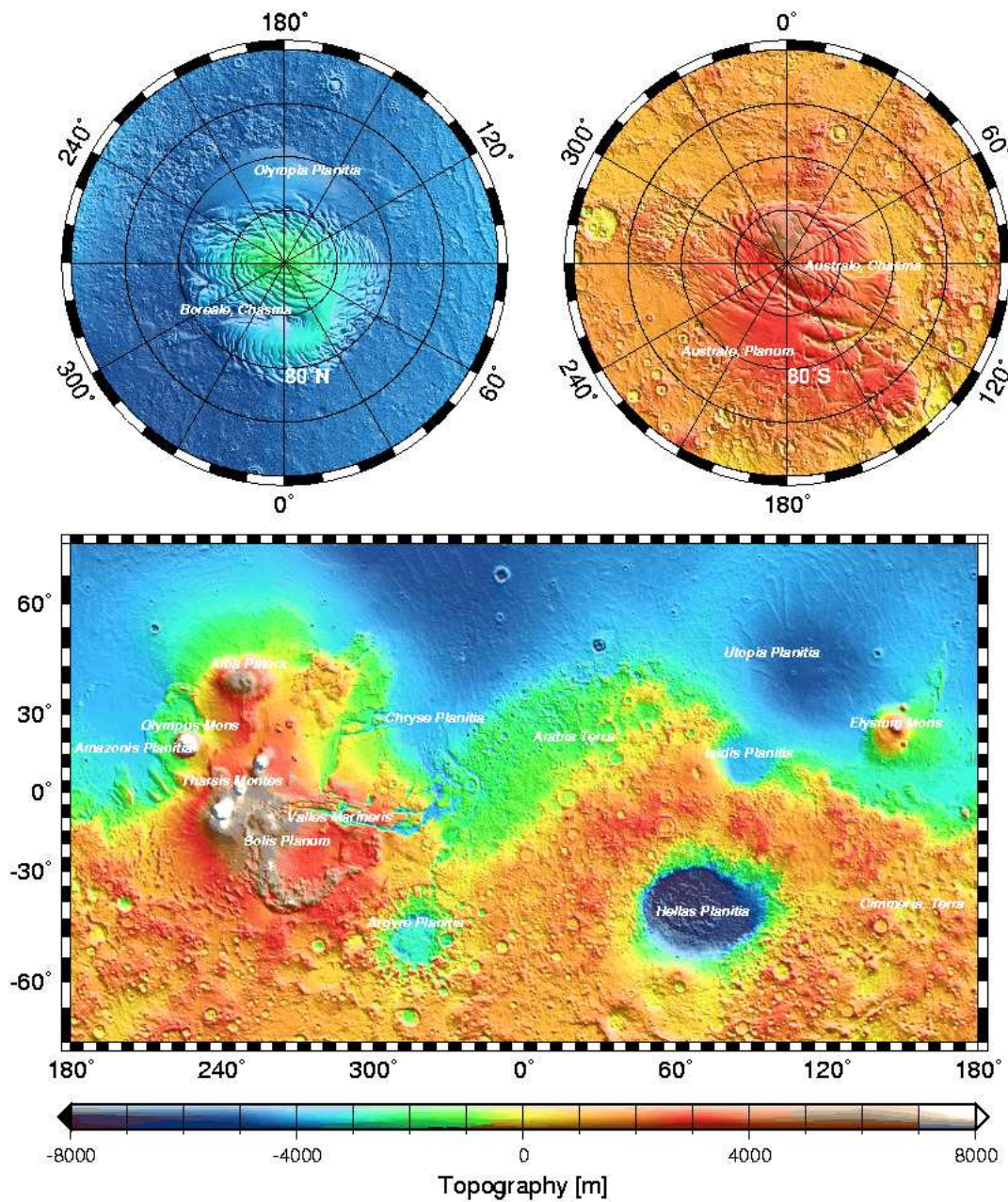


Figure 2.1: Topography of Mars in the absence of seasonal  $\text{CO}_2$  frost as measured by Mars Orbiter Laser Altimeter. The north and south polar projections are shown at upper left and right, respectively. The names of some of the major surface features are displayed. Figure credit: NASA/GSFC.

### 2.1.1 Atmospheric Processes and Volatile Reservoirs

The Martian atmosphere and climate are dynamic in nature. Though the atmosphere-surface systems of Mars and Earth are similar enough in thermal driving and seasonality to allow the use of theories and methodology developed for study of Earth's dynamic, radiative, geologic, and photochemical processes, Mars also exhibits unique aspects and phenomena (Zurek, 1992). Both planets are dynamically similar in that they are rotating rapidly with relatively clear and shallow atmospheres. For each planet, the thermal properties of the atmosphere depend on seasonally varying insolation, and H<sub>2</sub>O vapor amounts fluctuate significantly by date and location on the planet. However, Mars differs from Earth in that its thin atmosphere is primarily CO<sub>2</sub>, and mean global temperatures are much lower than on Earth.

As indicated, the Martian atmosphere is mostly carbon dioxide. Specifically, by volume the chemical composition is 95.32% CO<sub>2</sub>, 2.7% N<sub>2</sub>, 1.6% <sup>40</sup>Ar, and less than 1% O<sub>2</sub>, CO, H<sub>2</sub>O, and other trace elements (Owen, 1992). The atmospheric pressure at the surface of Mars averages about 7 mbar but has a wide range due to topography and the polar seasonal frost cycle. From the top of the highest volcanoes to the bottom of the deepest canyons, the pressure varies from 0.3 - 14 mbar. Almost no thermal blanketing is provided by the thin Martian atmosphere, so the surface temperatures also have a wide diurnal range. The reflectivity and thermal properties of the surface control the Martian temperatures, which can vary from a minimum of about 133 K, to a maximum of around 293 K. The mean surface temperature is ~215 K (Carr, 1998). When the temperature at the poles drops during the winter to the condensation temperature of CO<sub>2</sub> (147 K), CO<sub>2</sub> condenses out of the atmosphere to create a seasonal cap. See Section 2.1.2 for details of this process.

Understanding the water cycle on Mars (Section 2.2.1), and the stability of H<sub>2</sub>O in all forms, is crucial to deduce the history and geological details of the planet. Under current conditions, it is believed that a permafrost zone extends up to a few kilometers under the surface, being thickest in polar regions. Water-ice is stable at

the poles and has been identified as the primary constituent of the permanent north polar cap. The residual cap at the south pole has been identified as frozen carbon dioxide, perhaps overlying water-ice (Bryne and Ingersoll, 2003).

As mentioned above, during the fall and winter seasons at each pole, CO<sub>2</sub> condenses out of the atmosphere to form seasonal frost caps. Extending at times to nearly  $\pm 40^\circ$  latitude, this dry ice then sublimates back into the atmosphere during the warmer spring and summer months. During this process in the north, the amount of water vapor in the polar atmosphere increases dramatically as polar temperatures rise from the CO<sub>2</sub> frost point to the H<sub>2</sub>O frost point ( $\sim 200$  K). Because the southern permanent cap is CO<sub>2</sub>, the temperatures at the south pole remain near the CO<sub>2</sub> condensation temperature of 147 K. A cold trap occurs at the poles, and any water vapor added to the atmosphere from geologic processes will be frozen out at high-latitudes. Similarly, the polar layered deposits are believed to be mixtures of ice and dust because CO<sub>2</sub> freezing out of the atmosphere can also trap dust (Carr, 1998). On a broad scale, changes in the planet's eccentricity, precession, and obliquity affect Martian atmospheric dynamics and create variations in the interactions and stability of the CO<sub>2</sub> and H<sub>2</sub>O cycles at the poles (and elsewhere).

### 2.1.2 Condensation/Sublimation Cycle of CO<sub>2</sub>

The polar caps on Mars have been observed since the 17<sup>th</sup> century; however, they were thought to be composed of frozen water. Not until 1948 when Gerard Kuiper spectroscopically identified carbon dioxide as the major ingredient of the Martian atmosphere ( $\sim 95\%$ ) was it an accepted possibility that the seasonal polar frost on Mars was related to CO<sub>2</sub> (Kuiper, 1952). Now it is known that atmospheric CO<sub>2</sub> condenses as frost or ice onto the poles of the planet during each pole's respective polar night. The temperature drops during these periods until it reaches the CO<sub>2</sub> condensation temperature of about 147 K (at typical surface pressure). Latent heat is released as the CO<sub>2</sub> condenses at a rate that balances the energy lost due to thermal radiation at the top of the atmosphere (James et al., 1992). The ground CO<sub>2</sub> then sublimates back into the atmosphere in response to increased insolation

during the respective spring and summer seasons. During this stage, the surface temperature remains at the CO<sub>2</sub> condensation temperature as the absorbed solar radiation is converted back into latent heat of sublimation. (All phenomena related to the CO<sub>2</sub> caps are isothermal, and in fact, the condensation process effectively regulates the lower limit for surface temperatures on the planet (James et al., 1992).) For a more in-depth discussion of the atmospheric physics and associated energy balance models, refer to Section 2.3.2.

The physical properties and spectral details of carbon dioxide are important to this study. The following is a short compilation of introductory information about carbon dioxide. CO<sub>2</sub> is a linear, symmetric molecule with two double bonds and no electric dipole. The solid form is cubic (James et al., 1992). The spectral reflectance of CO<sub>2</sub> is dependent on frost grain size and has been measured in laboratory experiments; see Kieffer (1970b) for specifics of the major spectral bands. In any case, thermal emission from CO<sub>2</sub> ice is largely blocked by Mars' mostly CO<sub>2</sub> atmosphere because the spectral lines of the solid and gas are shifted little from each other. This is because strong intermolecular bonding does not occur in the solid, so the vibrational frequencies are nearly identical between the two phases (Osberg and Hornig, 1952). The basic thermodynamic properties of CO<sub>2</sub> are as follows: the specific heat of solid CO<sub>2</sub> over 73 to 198 K is the function of temperature  $(349 + 4.8T)$  J kg<sup>-1</sup> K<sup>-1</sup> (Washburn, 1948); the triple point for CO<sub>2</sub> is 216.6 K,  $5.18 \times 10^6$  Pa; the critical point is 304.1 K,  $7.4 \times 10^6$  Pa (Lide, 1991).

The wavelength dependent emissivity<sup>1</sup> and albedo<sup>2</sup> of CO<sub>2</sub> determines the rates of growth and retreat of the surface frost (James et al., 2005). Measurements of the index of refraction of CO<sub>2</sub> and modelling of the albedo and emissivity of the polar deposits as a function of grain size has been done by Hansen (1997, 1999). The results imply that visible albedo is only weakly dependent on grain size, but contamination by even a little dust can alter it. James et al. (2001) and James

---

<sup>1</sup>The emissivity is the ratio of the radiation emitted by a surface to the radiation emitted by a blackbody at the same temperature.

<sup>2</sup>The albedo is the fraction of incident electromagnetic radiation reflected by a surface.

and Cantor (2001) have also confirmed that the albedo of the CO<sub>2</sub> ice increases as the solar incidence angle increases, and Kieffer et al. (2000) report that CO<sub>2</sub> grain size appears to decrease during this time, as does the amount of dust in the frost. Overall, pure CO<sub>2</sub> is bright with little wavelength variation in the visible part of the spectrum (James et al., 2005).

The amount of condensed CO<sub>2</sub> is controlled by the vapor pressure curve, which dictates the sublimation temperature of CO<sub>2</sub> on Mars (James et al., 1992). In thermodynamics, the Clausius-Clapeyron relation is a way of characterizing the phase transition between two states of matter. On a pressure-temperature (P-T) diagram, the line separating the two phases is known as the coexistence curve, and the Clausius-Clapeyron relation gives the slope of this curve. The CO<sub>2</sub> sublimation curve for Mars closely follows this relation over the temperature range applicable for Mars (James et al., 1992). It is useful here in the form:

$$\ln p = a - \frac{b}{T} \quad (2.1)$$

where  $\ln p$  is the natural log of the vapor pressure,  $T$  is the temperature in degrees Kelvin,  $a$  is an appropriate value for  $\ln p$  with  $p$  measured in mbar, and  $b$  is proportional to the molar heat of vaporization. Meyers and Van Dusen (1933) have made measurements and analyzed data to determine the vapor pressure of solid CO<sub>2</sub> over the temperature range: 90 to 216.5 K; however, various CO<sub>2</sub> vapor pressure relations have actually been used in planetary literature (James et al., 1992). The International Critical Tables list  $a = 23.102$  and  $b = 3148.0$  (Washburn, 1948). James et al. (1992) have done calculations to determine that the Clausius-Clapeyron form with  $a = 23.3494$  and  $b = 3182.48$  has a maximum deviation in  $\ln p$  of 0.011 from 120 to 160 K (0.04 to 31.4 mbar), which they say falls well within the scatter of measurements.

It is apparent from the discussion above that pressure variations and the CO<sub>2</sub> cycle on Mars are intimately intertwined. In fact, the total atmospheric pressure on the planet undergoes a seasonal variation due to the seasonal mass flux of CO<sub>2</sub> between the two poles. When the CO<sub>2</sub> freezes out of the atmosphere onto the ground,

the atmospheric pressure drops. Conversely, the atmospheric pressure increases when the seasonal ground frost sublimates back into the atmosphere. Tillman (1988) has shown that the seasonally varying pressure observed at the Viking Lander sites (after adjustment for elevation differences) conclusively illustrates these effects and the connection to the condensation and sublimation of CO<sub>2</sub> at the poles.

The interdependence of pressure and carbon dioxide on Mars is further complicated by the fact that the CO<sub>2</sub> on the southern polar cap sublimates after the condensation at the north pole has already begun. In data analysis, this complexity can be handled by observing seasons in which there is only one active cap, as is true during the southern condensation period (James et al., 1992). An overall minimum of atmospheric pressure occurs at this point. An additional complication that arises while studying the Martian pressure cycle is that the total mass of CO<sub>2</sub> that condenses on each pole is different. The southern winter is longer than the northern winter because of the large eccentricity of Mars' orbit. To first order, the quantity of CO<sub>2</sub> condensed on each pole is proportional to the amount of time without insolation (James et al., 1992). In actuality, water, dust, and cloud cycles, for example, also affect the amount of condensed seasonal frost by altering the polar radiative properties. See Sections 2.2.1 (water), 2.2.2 (dust), and 2.2.3 (clouds) for details. It is interesting to note, however, that although large variations in global dust storm activity were seen during the Viking Lander years, only slight deviations in the pressure curves were observed (James et al., 1992). This indicates that the overall pressure cycle on the large scale is fairly invariant on an interannual basis.

There are multiple CO<sub>2</sub> reservoirs on Mars, such as: the atmosphere, the seasonal polar caps, the residual polar caps, the clouds, and the regolith. Only a general description of the seasonal polar caps will be presented here, as the other CO<sub>2</sub> reservoirs are discussed elsewhere in this document. What follows is an introductory discussion of previous polar observations, while the current more detailed analysis of seasonal CO<sub>2</sub> frost resulting from the GRS data can be found in the *Results and Conclusions* chapter (Chapter 5). In terms of quantities measured by the GRS, the northern and southern CO<sub>2</sub> deposits vary in range, density, thickness, mass,

and condensation/sublimation rate. There are also variations in albedo, emissivity, temperature, and topography as measured by other spacecraft.

The seasonal behavior of carbon dioxide is qualitatively different between the north and south poles. At its maximum extent during late winter, the seasonal frost in the north has been observed to extend to roughly  $55^\circ\text{N}$  with the  $\text{CO}_2$  covering between  $55^\circ\text{N}$  and  $65^\circ\text{N}$  appearing somewhat thin and patchy in nature (James et al., 1992). This time period of maximum frost often coincides with the occurrence of relatively optically thick clouds and remains visually obscured until around  $L_s = 20^\circ$ . (Degrees of  $L_s$ , the areocentric longitude of the sun, is a measure of time in degrees of the progression of Mars in its orbit around the sun.  $L_s = 0^\circ$  marks Mars' northern vernal equinox, and  $360^\circ$  of  $L_s$  is one full Martian year or one revolution around the sun. See the first paragraph in Section 5.2.1 for a more detailed description.) The  $\text{CO}_2$  directly over the pole begins to recede at this point, and the visible recession of the frost edge is fairly symmetric in relation to the geographic pole (James et al., 2005). Though the exact dates vary from year to year, previous observations have recorded a “plateau”, or pause, in the recession around  $66^\circ\text{N}$  latitude between  $L_s = 20^\circ$  and  $45^\circ$ . This has been confirmed by the Viking Orbiter Infrared Thermal Mapper (IRTM) data set (James et al., 1992). The north polar cap has also been found to contain areas of high water frost concentrations. This is often observed in large craters such as Korolev (James et al., 2005), which is found at roughly  $72^\circ\text{N}$  latitude,  $165^\circ\text{E}$  longitude.

The southern surface frost has an irregular boundary that has previously been observed to expand to  $40^\circ\text{S}$  latitude at its largest scope. The seasonal frost also extends to cover the lower elevation basins such as Hellas and Argyre (Briggs et al., 1977). The cap edge tends to remain fairly symmetric about Mars' rotation axis until the middle of southern spring when patchy frost located between approximately  $155^\circ\text{E}$  and  $300^\circ\text{E}$  longitude begins to rapidly sublime leading to a very asymmetric seasonal cap (James et al., 2005). The observed asymmetry continues to increase until the center of the  $\text{CO}_2$  deposit is displaced by  $6.5^\circ$  of latitude from the geographic pole around the time of the southern summer solstice (James et al., 1992).

At this point, the seasonal CO<sub>2</sub> ice continues its sublimation to leave the underlying residual cap. Though similar events take place from year to year, the exact timing of these events varies somewhat. Observations of the cap's regression as a function of time for multiple years (see Chapter 5) is a good method to test for interannual variations in the behavior of the seasonal CO<sub>2</sub> frost. Veverka and Goguen (1973) have reported that numerous high- and low-albedo areas can be found within and near the edge of the seasonal ice, and James et al. (2001) note that the albedo of the southern polar frost exhibits a tremendous amount of geographical variability. It is thus accepted that the southern cap recession appears more symmetric when the surface temperature is used to identify the location of CO<sub>2</sub> frost rather than the albedo (James et al., 2005).

The southern ice cap has been perceived to have an annular structure with a darker interior surrounded by a brighter perimeter (James et al., 1992). The very core of this annulus, however, which is based on the residual cap, actually remains brighter than the adjacent terrain as can be seen by albedo measurements from the Viking IRTM instrument mentioned earlier (Kieffer, 1979). It is believed that irregularities in the frost deposit are largely a consequence of the surface properties. As an example, bright albedo frost streaks that are assumed to be associated with craters are often observed in the south polar area during the spring (James et al., 2005). Thomas et al. (1979) give a detailed discussion of the occurrence of these streaks, their seasonal behavior, thickness, inferred wind patterns, and the favored locations of formation. Found to extend from the rims of many craters, these albedo markings are apparently created by CO<sub>2</sub> frost that preferentially accumulates in the wind-sheltered areas of the craters (Thomas et al., 1979). Another example of surface-feature-controlled CO<sub>2</sub> phenomena is that the darker sand dune regions seen at the bottom of craters in the southern summer are predisposed for new CO<sub>2</sub> deposition as temperatures turn cooler (James et al., 1992).

For both seasonal polar caps, Titus et al. (2001) suggest that fine grain snow can be deposited from clouds. A dry ice (CO<sub>2</sub>) blizzard has actually been observed. However, both Kieffer et al. (2000) and Titus et al. (2001) imply that slab ice

is also very common in the polar regions, therefore, it has been suggested that the fine-grained snowfall-deposited  $\text{CO}_2$  may transform into larger grain material as  $\text{CO}_2$  continues to condense directly onto the cold surface (Eluszkiewicz, 1993; Eluszkiewicz and Titus, 2002).

In summary, the spatial extent and timing of the solid  $\text{CO}_2$  deposits are a consequence of their equilibrium balance with the atmosphere. The albedo and emissivity of the caps in part determine the surface/atmosphere interactions; however, the  $\text{H}_2\text{O}$ , dust, and cloud cycles also play an important role. These seasonal cycles are all complexly intertwined, and they are directly related to the global pressure variations seen on Mars. It is necessary to consider all of these details to advance our understanding of the present climate regime on Mars and to fully appreciate the significance of the  $\text{CO}_2$  cycle. Further details about the coupling and feedback of the other cycles relevant to  $\text{CO}_2$  processes can be found in following sections.

## 2.2 Other Factors Influencing the $\text{CO}_2$ Cycle

There are many details to take into account when analyzing the carbon dioxide cycle on Mars. The rate, amount, and location of seasonal  $\text{CO}_2$  condensation and sublimation on both poles depend upon factors such as: surface deposition of dust, dust clouds and atmospheric condensates, advection and atmospheric dynamics, and properties of the underlying regolith and residual polar caps. There is much coupling and interplay between the  $\text{CO}_2$ ,  $\text{H}_2\text{O}$ , dust, and cloud/atmospheric seasonal cycles. Before describing the details of these cycles individually in the following sections, an explanation of how these processes are interconnected is given here.

The radiation balance in the polar regions of Mars can be influenced by the presence of ice clouds or by dust which is deposited on or in the seasonal polar  $\text{CO}_2$  frost. The exchange rates of both  $\text{CO}_2$  and water vapor between the atmosphere and the ground are affected. For example, dust in the atmosphere can act as condensation nuclei and alter the atmospheric condensation of these volatile substances. The atmospheric water vapor is cold trapped by the  $\text{CO}_2$  surface ice. In addition,

variations in CO<sub>2</sub> deposition will create changes in the total surface pressure, and therefore the capability to lift dust from the surface, which can influence the number and intensity of dust storms. Condensation (sublimation) of CO<sub>2</sub> in the polar regions creates winds and atmospheric circulation by causing pressure gradients that initiate movement of the atmosphere from the mid-latitudes into (out of) the polar latitudes. (For further information on these atmospheric movements and the tracer or non-condensable elements used to study such effects with Mars Odyssey GRS data, see Sprague et al. (2004).) These winds affect the transport of water (in vapor and condensate form) and also the amount and location of airborne dust. The specifics of the associated atmospheric movements and the type of circulation depend on the constituents in the atmosphere, as well as the vertical mixing of the dust and H<sub>2</sub>O vapor. Overall, it can be seen that the investigation of any one of these seasonal cycles individually is a difficult task that must take into account the intricate coupling of all of these volatile processes (James et al., 1992; Jakosky and Haberle, 1992; Kahn et al., 1992; Zurek, 1992).

### 2.2.1 Water Vapor and Ice

In addition to the seasonal CO<sub>2</sub> and dust cycles, the Martian climate is greatly affected by the behavior and annual exchange of water between the planet's atmosphere, regolith, and polar caps. The influence of H<sub>2</sub>O condensates on the absorption of solar radiation, the overall solar energy distribution, and the removal of CO<sub>2</sub> and dust from the atmosphere via condensation influences the Martian climate system on a grand scale. Observations of water variations can also act as a tracer of current atmospheric motions and as an indicator of global climate change over time (Jakosky and Haberle, 1992). Whether on a long time scale or over a seasonal period, the water cycle behavior in the *polar regions* is especially important in governing the global climate. The polar sources and sinks for water at various times and seasons during the Martian year are discussed below and illustrate the dynamic equilibrium that occurs and regulates the quantity of atmospheric water vapor and ground ice at any given time. Seeking to understand these processes and their feedback and

influence on the major planet-governing CO<sub>2</sub> cycle and associated mass transport can lead to an understanding of the current Martian climate and its behavior during past epochs. Outside the immediate context of this CO<sub>2</sub> study, knowledge of the state, location, and interaction of Martian water is crucial to the search for past or present life, which as we know it, is dependent on water. For further reading and a more detailed analysis than is given here of the seasonal water cycle and the physical mechanisms for water exchange on Mars, see Jakosky (1985). In addition, results from the Viking Orbiter Mars Atmospheric Water Detectors (MAWD) are considered a primary and definitive data set for actual observations of the Martian water cycle (Jakosky and Farmer, 1982; Fedorova et al., 2004; Arvidson and Slavney, 2005), and the MGS Thermal Emission Spectrometer (TES) is currently investigating, among other things, the latitude and longitude dependence and vertical distribution of Martian water vapor as a function of time (Smith, 2002, 2004; Hamilton and Ruff, 2005).

Although Mars exhibits evidence of erosion by liquid water during a wetter and warmer period in the past, at the present time, the Martian atmosphere is so thin and the temperatures are so low that liquid water is unstable on the planet's surface. Under current conditions, there exists a substantial zone of permanently frozen subsoil (permafrost) that extends perhaps a few kilometers deep at the poles and over a kilometer in depth at the equator (Carr, 1998). At low latitudes, even ice is unstable near the surface, and if liquid water exists at Mars it would be below the permafrost zone.

The stability of frozen water and CO<sub>2</sub> varies during different epochs due to changes in Mars' obliquity cycle and precession. Currently, water-ice is stable at the poles, as is evidenced by the 100% water-ice north polar residual cap. Moving equatorward, from  $\sim 80^\circ\text{N}$  down to  $\sim 40^\circ\text{N}$ , any ice frozen on the surface during the winter will sublime during the summer; however, a few meters below the surface, ice may remain permanently stable (Carr, 1998). Any ice buried in the Martian regolith will be lost to the atmosphere at a rate governed by the capability of the sublimed water to diffuse up through the soil. Only if the soil overlying the ice is

impermeable and prevents the water from subliming into the atmosphere, or if there is another water source supplying the area (such as active volcanic activity), would it be possible to find low latitude water-ice presently (Carr, 1998).

Even when saturated, Mars' cold, thin atmosphere holds 6,500 - 13,000 times less water vapor (equivalent to 1 - 2 km<sup>3</sup> of ice) than Earth's atmosphere (Zurek, 1992). The globally averaged column abundance is on the order of just  $\sim 10$  precipitable micrometers (10 pr- $\mu\text{m}$ , or  $10^{-3}$  g/cm<sup>2</sup>) (Jakosky and Haberle, 1992). However, Mars' atmospheric mass undergoes considerable seasonal changes due to the large amount of CO<sub>2</sub> that freezes out of and then sublimates back into the atmosphere at different times of the year. In addition to producing extensive meridional heat and momentum transports, atmospheric trace constituents like water are also greatly affected (Zurek, 1992). Relatively significant seasonal, spatial, and diurnal variations in the atmospheric column abundance of water vapor result. Recent epithermal-neutron studies over the southern hemisphere indicate that the column abundance of atmospheric water could actually range from 5 - 30 pr- $\mu\text{m}$  (Mellon et al., 2004). Besides transport of vapor within the atmosphere, there is the additional effect of water exchange with non-atmospheric reservoirs, such as the seasonal and residual polar caps, other surface or near-surface ground ice, and water adsorbed into the regolith (Jakosky and Haberle, 1992).

When the seasonal CO<sub>2</sub> caps at the poles sublime in the late spring and early summer, temperatures rise from the frost point of CO<sub>2</sub> ( $\sim 147$  K) to the frost point of H<sub>2</sub>O ( $\sim 200$  K). At the latter higher temperature, water sublimates from the northern cap and is lost to the atmosphere at a rate of about 10  $\mu\text{m}/\text{day}$  (Toon et al., 1980). Because it is free from seasonal CO<sub>2</sub> during this period, the residual (100% water-ice) north polar cap is a source for the water cycle on Mars (Zurek, 1992), and the amount of water vapor over the cap increases dramatically (Carr, 1998). The southern residual polar cap, which has CO<sub>2</sub> as its outermost layer<sup>3</sup>, is an annual sink

---

<sup>3</sup>There is evidence that the "residual" CO<sub>2</sub> ice covering the south polar cap may disappear in some years to expose the underlying water-ice cap. This would allow water to sublime into the atmosphere. Modelling of the south polar cap seasonal behavior has demonstrated that it is

for water vapor as any water supplied to the atmosphere by active geologic processes will ultimately be frozen out onto the cold pole. In this sense, the poles can act as cold traps for water. In the years during the Viking mission when observations implied that the overlying south polar CO<sub>2</sub> cap did not completely sublime and temperatures remained at 147 K, no increase in southern atmospheric water vapor was detected (Carr, 1998).

The CO<sub>2</sub> frost-free regolith outside the permanent polar caps can act as either a source or a sink for Martian water vapor depending on the time of year. During spring, when the ground warms, the water vapor is released into the atmosphere, and conversely, it is then adsorbed during the late summer and fall when the ground temperatures drop. The efficiency of this cycle and the amount of overall atmospheric transport of water vapor depends on the surface concentration and the vertical and horizontal distribution of the water vapor in the lower atmosphere (Zurek, 1992). Zurek (1992) further explains that winds near the surface can also influence the rate of water-ice sublimation, while the condensation phase is more affected by temperatures and relative humidity. Water vapor supplied to the atmosphere in the northern hemisphere is often transported across the equator to the south by Hadley Cell circulation and may condense onto the southern polar cap. Transport in the reverse direction from south to north may occur; however, the magnitude of such events is less well-known (Jakosky and Haberle, 1992). It currently appears that during the Martian year, there is a net loss of H<sub>2</sub>O from the northern polar area, while there is a net gain onto the south pole residual cap. The circulation necessary for these atmospheric movements is created by latitudinal variations in insolation, and Mars' seasonal fluctuations drive the exchange of H<sub>2</sub>O with the *non*-atmospheric reservoirs (Jakosky and Haberle, 1992).

All of this information supports the conclusion that the Martian water cycle possible for the pole to have a CO<sub>2</sub> covering throughout an entire year and then have a complete disappearance of the CO<sub>2</sub> the following year, or vice versa. Though most recent observations indicate that a layer of condensed CO<sub>2</sub> remains on the southern cap all year, the cap is apparently stable in both cases (Jakosky and Haberle, 1990).

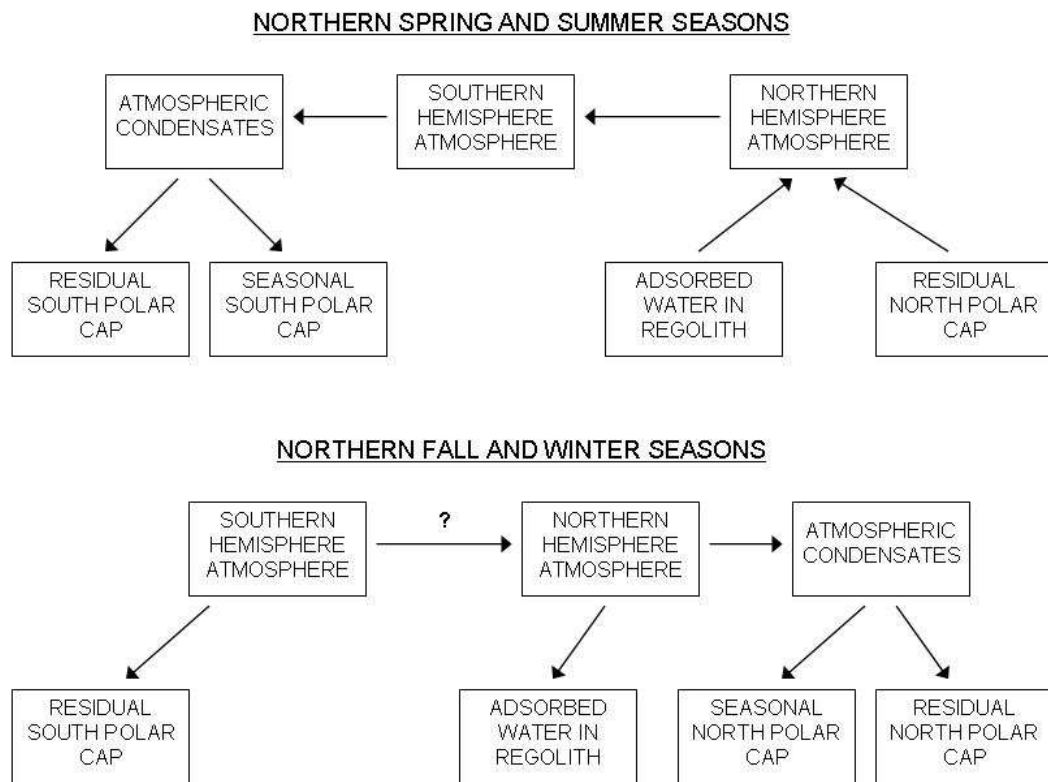


Figure 2.2: Schematic of the seasonal water cycle on Mars. Arrows represent the direction of water exchange between the given atmospheric and non-atmospheric reservoirs during the indicated seasons. Constructed from Jakosky and Haberle (1992).

plays an important role in the planet's global climate and atmospheric dynamics, in general, and interacts with the seasonal CO<sub>2</sub> cycle, in particular. The water cycle is more significantly governed by the behavior of the polar caps than by exchange with the regolith or other reservoirs. Because the behavior of the polar caps is primarily determined by the planetary energy balance dictated by the CO<sub>2</sub> cycle, subtle changes in this balance can greatly affect the seasonal trends of atmospheric water (Jakosky and Haberle, 1990). Observations corroborate this belief and suggest that there is dramatic variability in the atmospheric water vapor cycle from year to year (Jakosky and Haberle, 1992). Although, in the reverse manner, the effect of the water cycle on the CO<sub>2</sub> cycle is not as pronounced, it is still crucial to investigate, understand, and incorporate the interplay between these two major systems to achieve an accurate overall view of the seasonal CO<sub>2</sub> cycle on Mars.

### 2.2.2 Dust

Dust suspended in the Martian atmosphere affects the atmosphere's circulation and thermal structure. For this reason, it is important to understand the dust cycle on Mars to study the past and current climate and geology of the planet. Dust storms and wind play a role in current processes and interactions, such as the CO<sub>2</sub> deposition cycle, and have also been significant factors in the evolution of surface features. This section will give a basic description of the dust cycle and associated mechanisms on Mars followed by an explanation of how dust affects the CO<sub>2</sub> deposition and sublimation cycle directly.

The seasonal cycle of dust, as it is understood in the present era, is comprised of dust-raising events that vary on a seasonal basis, redistribution on a local scale, and regional exchange. Large dust storms that encircle the planet create an observed transfer of dust between major regions of the planet; however, the quantity of particles involved is equivalent to a dust layer only a few  $\mu\text{m}$  thick. Most recent observations suggest that dust is moving mostly from the southern to the northern hemisphere (Kahn et al., 1992). Redistribution of dust creates observed changes in surface albedo, wind streak patterns, and other surficial features.

Dust storms are generally classified as local, regional, or planet-encircling, and even the large storms are believed to begin as one or more local storms (Kahn et al., 1992). As opposed to white or bluish water-ice clouds, atmospheric dust has been classically observed as “yellow” clouds. These clouds, which appear every Martian year and most likely during every season, can be quite opaque and can cover areas on the order of a few  $10^6$  km<sup>2</sup>. The sediment carried and deposited during the largest, planet-enveloping storms can cause variations in surface albedo that may last from weeks up to years. It is believed that the dust distributed into the polar regions will likely be incorporated into the polar ice or layered terrains; however, the exact quantity of this dust is unfortunately uncertain.

Some dust storms on Mars have been observed to be extensive, opaque, and long-lived. When compared to Earth, observations of infrared radiances indicate that Mars’ atmospheric circulation and thermal structure are affected to a much higher degree by solar heating of airborne dust. Besides absorbing incoming solar radiation, airborne dust also absorbs thermal emission from the Martian surface. The region most significantly heated by the atmospheric dust is the *lower atmosphere*, defined as the region from the ground to  $\sim 45$  km above the reference geoid. Heat exchange with the ground and radiative transfer occurs most strongly in the lower parts of this region (sometime called the *troposphere*). The amount of dust present is known to vary with season and area on the planet, and the column abundance and distribution in the atmosphere can change unexpectedly and significantly (Zurek, 1992).

Other varying unknown quantities are the associated opacity of the atmosphere, and the size, shape, and composition of dust particles that are suspended and re-deposited on the Martian surface. The perpetual background dust opacity ranges from a few tenths to greater than 1.0 at visible wavelengths (Colburn et al., 1989), and the greatest opacities, as expected, are in regions at times where dust is being raised directly. Variations in atmospheric opacity influence the thermal inertia of the atmosphere and observations of higher than normal morning temperatures and decreased afternoon temperatures can be an indirect indication of increased opacity. Similarly, interannual differences of observed temperatures may result largely from



Figure 2.3: Hubble Space Telescope images of Mars before (left image) and during (right image) a global dust storm. The change in colors and contrast of the surface markings is a result of dust in the atmosphere. Image credit: NASA, James Bell (Cornell Univ.), Michael Wolff (Space Science Inst.), and the Hubble Heritage Team (STScI/AURA).

changes in atmospheric opacity (due to dust and H<sub>2</sub>O or CO<sub>2</sub> clouds) (Wilson and Smith, 2005).

The processes which raise and move the dust are not well understood because there are many factors determining the location, frequency, and intensity of such activities (Kahn et al., 1992). For example, the atmosphere over the polar regions frequently appears to be relatively clear of airborne particles, perhaps due to the removal of dust by the condensation of CO<sub>2</sub> or water during the polar night. In support of this theory and relative to the CO<sub>2</sub> study described in this document, numerical simulations of the Martian atmosphere carried out with the NASA Ames General Circulation Model imply that as the dust content over the winter poles increased, the rate of atmospheric CO<sub>2</sub> condensation also increased sharply (Pollack et al., 1990).

Solar heating of airborne dust particles plays an essential role in the generation of dust storms. Similar to conditions seen during the summer in deserts on Earth, low-latitude local Martian storms can be initiated by free convection, where direct heating of the surface can cause dust-devil type whirlwinds (Gierasch and Goody, 1973). Another theory is that regional winds superimposed onto the large-scale atmospheric circulation will produce the initial shear stress that mobilizes surface dust (Leovy et al., 1973). Arvidson et al. (1983) suggest that winds greater than 30 m/s at a 1.6 m height are sufficient to generate this dust-lifting shear stress, and information from Carr (1998) indicates that this would be possible because typical maximum daily winds on Mars are on the order of several meters per second with dust storms causing gusts up to 40 m/s. The associated winds develop for numerous reasons, including from topographical slopes and significant horizontal surface temperature variations as are found at the polar cap edges and in regions of substantial thermal inertia or albedo contrast, for example (Kahn et al., 1992). Global winds (associated with the seasonal atmospheric mass flow driven by the condensation and sublimation of CO<sub>2</sub> in the winter polar regions) may also initiate dust motion; however, Kahn et al. (1992) report that these planetary winds may instead play a larger role in the expansion of local storms to larger scales.

Although dust movement occurs all over the planet, in general, there appear to be the most local dust storms near the edges of both seasonal polar caps during the spring, and the largest dust devil activities occur in the southern low latitudes during the summer. Dust can spread over a large part of the planet in just a few weeks during planet-encircling storms following the planet's general circulation patterns, but it is also interesting to note from studies of albedo pattern variations that dust transport still takes place during those years that do not have such large storms (Kahn et al., 1992).

It is unknown whether there is a net accumulation of dust anywhere specifically on Mars. However, net deposition of such airborne sediments is likely to have occurred under earlier Martian conditions or over long time scales, as is evidenced by polar and low-latitude layered terrains and other debris deposits. Two theoretical long-term sinks for dust have been proposed for the current epoch: the north polar residual cap, and the bright, low-thermal-inertia regions in the northern low latitudes. Observations of planet-wide dust storms over the last few decades are consistent with a net transfer of dust from the southern to the northern hemisphere, as mentioned previously. It is unclear whether a less dramatic mechanism is actively reversing the presumed one-way dust transport. The south polar region currently appears to be a less probable place for a significant dust sink because major dust storms are not observed to occur during the southern winter while frost is condensing. In addition, observations seem to suggest instead that overall net erosion of the southern surface is taking place (Kahn et al., 1992).

Dust storm activity has often been compared to the interannual variability of the growth and retreat of the seasonal polar caps to determine how the dust cycle and the seasonal CO<sub>2</sub> cycle are related. However, it is uncertain how strong this relationship actually is, and at present, these cycles seem to be only weakly coupled (James et al., 2005). Contrary to expectations, as the database of Mars observations increases, the seasonal dependence of dust storms and clouds seems to become less clear, although, there do appear to be some general trends (Martin et al., 1992).

For the most part, comparisons of the polar caps of Mars during dusty and non-

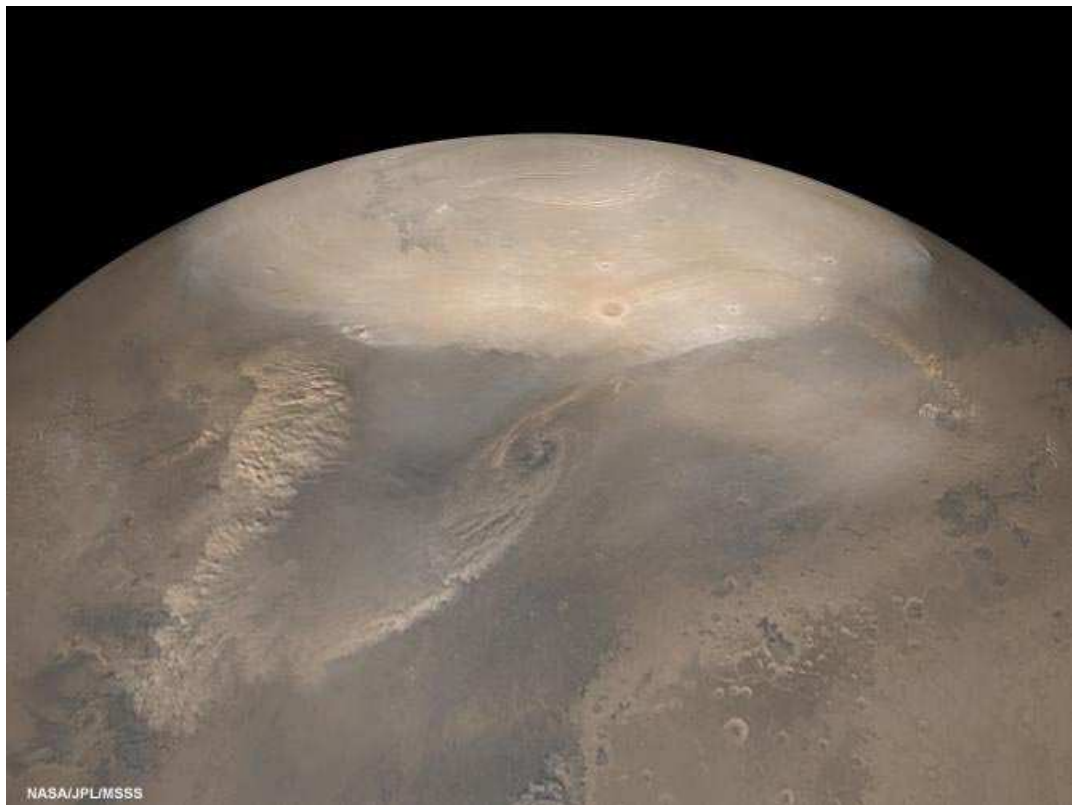


Figure 2.4: Dust is swept up and funnelled into swirling dust storms along the north polar cap edge as the flow of cool polar air evaporating off the cap encounters the temperature contrasts between the cold CO<sub>2</sub> seasonal frost and the adjacent warm ground. These dust storms were captured by the Mars Global Surveyor (MGS) Mars Orbiter Camera (MOC) in May 2002 during Mars' recent northern spring. Photo credit: NASA/JPL/MSSS.

dusty times reveal a couple things. There appears to be no substantial difference in seasonal frost condensation and sublimation at a large scale for years with versus without major dust storms. The Mars Global Surveyor (MGS) Mars Orbiter Camera (MOC) observed the south polar cap for two consecutive Martian winters in the years: 1999-2000 and 2001-2002. The first winter was free of dust storms, while the second winter included a large, global dust storm. Even though the edges of the polar cap were obscured by significant dust activity during the second winter and spring as can be seen in Figure 2.4, there were only minor differences detected in the overall behavior of the CO<sub>2</sub> ice. On the other hand, temporal differences in CO<sub>2</sub> activity *can* be observed in localized patches or around specific formations. For example, the south polar Mountains of Mitchel formation appeared to lose its CO<sub>2</sub> frost cover about 4 - 5° of L<sub>s</sub> sooner during the dusty year (Bonev et al., 2002b). The MGS Thermal Emission Spectrometer (TES) results support the same conclusion. TES data also imply that the dust activity had an opposite effect for the Cryptic region where the seasonal CO<sub>2</sub> frost recession rate was slowed due to dust interactions. (Roughly located between latitudes 85°S and 75°S and longitudes 150°W and 310°W, the Cryptic region is an area of anomalously low albedo. Although it is unusually dark, it also remains cold (Titus et al., 2003b).)

As mentioned above, variations in atmospheric dust and, therefore, opacity can alter the temperature and thermal inertia of Mars' atmosphere around the planet and at the poles. Utilizing spectra for CO<sub>2</sub> deposits of varying grain size and dust content can possibly explain the minor localized changes in the behavior of the seasonal caps during differing dust histories, as well as account for the lack of major large-scale polar cap variations from year to year (James et al., 2005). When the sun shines on dust in the atmosphere, the dust absorbs visible insolation. The absorbed solar radiation is then emitted back into Mars' atmosphere as infrared radiation. The way CO<sub>2</sub> deposits are affected by this visible-to-infrared radiation shift depends on the frost's observed albedo. Although the grain size of the CO<sub>2</sub> frost is important, the amount of intermixed dust is the major factor controlling the frost's visible albedo and accordingly the sublimation rate (Bonev et al., 2002b). Hansen (1999)

explains that the visible albedo will be lowered by dust deposited on top of, or mixed into, the frozen CO<sub>2</sub>. The infrared albedo of CO<sub>2</sub> is also affected by dust, but to a lesser extent. Bright areas of CO<sub>2</sub> frost, such as over the Mountains of Mitchel mentioned earlier, do not absorb much visible radiation, so the shift of radiation to infrared creates a type of energy input that accelerates the usual recession rate of the seasonal CO<sub>2</sub> cap in this area. Regarding the reverse effect of the dust on the CO<sub>2</sub> seen in the Cryptic region, modelling by Portyankina et al. (2005) shows that dusty times decrease surface albedo in the area as expected; however, surface temperatures also appear to be lowered. There are the opposing effects of the higher atmospheric opacity reducing the solar radiation available at the surface, and the increased fraction of solar radiation absorbed by the frost due to the dust reducing the frost's albedo. The model results suggest that the net effect seems to be later than usual seasonal sublimation of both CO<sub>2</sub> and water ices in the Cryptic region.

As in the scenario above, dust that has fallen onto the polar caps or has been trapped during seasonal CO<sub>2</sub> condensation is exposed to insolation. Due to their low albedo, the dust grains absorb energy and increase in temperature relative to the surrounding CO<sub>2</sub>. The CO<sub>2</sub> surrounding a heated dust grain may sublime and create a gaseous pocket encapsulating the grain. Smaller grained dust near the surface of the cap could possibly be advected off of the cap in the vertical wind of the sublimating CO<sub>2</sub>. This upward gas velocity is estimated to be about 0.002 m/s for frost with a typical cap albedo and summer insolation, so it is therefore sufficient to support dust grains <5 μm in radius (James et al., 1992). Studies by Kieffer et al. (2000) estimate that the majority of dust grains are small enough to be removed from the polar cap in such a manner. According to James et al. (1999), small dust particles suspended in the wind currents might be a source for the dust activity seen during the spring seasons around the edge of the receding seasonal polar caps. For the larger dust particles that become heated on or in the polar frost, Kieffer et al. (2000) predict that the grains might sink down into the CO<sub>2</sub> frost and effectively “burrow” to a level where they no longer affect the albedo and absorption.

The detailed interactions between the dust and CO<sub>2</sub> cycles are complicated;

however, calculations for the south polar cap incorporating the visible and infrared properties of condensed CO<sub>2</sub> (Bonev et al., 2002a) reveal that the net effect of dust activity on a CO<sub>2</sub> cap of typical size and intermediate dust content and visual albedo is small overall. Therefore, despite significant variations in atmospheric dust content on an interannual basis, which may cause slight localized fluctuations of the frost sublimation rate, the seasonal frost recession from year to year at the large scale can be highly repeatable (James et al., 2005).

### 2.2.3 Clouds

Another CO<sub>2</sub> reservoir (besides the seasonal or residual polar caps, the regolith, or the general atmosphere) is the Martian cloud system. Clouds can store CO<sub>2</sub> at various times during the seasonal CO<sub>2</sub> cycle, and observations suggest that clouds may be involved in the CO<sub>2</sub> condensation process during each pole's respective winter (James et al., 1992). Currently, there is a lack of evidence supporting any substantial amount of CO<sub>2</sub> storage by clouds outside the polar region at any time of year.

It is important to understand the distribution of clouds to adequately model the Martian atmosphere. As discussed, cloud formation and activity are closely related to the Martian CO<sub>2</sub> cycle, water cycle, and dust cycle (Wang and Ingersoll, 2002). In addition, studies have indicated that the magnitude of an earlier Mars CO<sub>2</sub> and/or H<sub>2</sub>O greenhouse effect may have been limited by CO<sub>2</sub> cloud condensation trends (Kasting, 1991). This means that the validity of the popular theory of a warmer, wetter climate in the Martian past, which has evolved to the current Mars, is highly dependent on the results of current and ongoing Mars' cloud research (Bell et al., 1996).

Gierasch and Goody (1968) depicted various key aspects of CO<sub>2</sub> cloud behavior on Mars in an early theoretical study. Their results implied that when atmospheric temperatures drop to the local CO<sub>2</sub> frost condensation temperature, carbon dioxide could condense into clouds in the atmosphere that would remain at a constant temperature fixed by the CO<sub>2</sub> partial pressure. This means that surface CO<sub>2</sub> frost

and any zero-elevation clouds would be at the same temperature. Above that, the model implies that temperatures decrease by about 1 K per kilometer of altitude.

In their thermal model of the Martian surface discussed in Section 2.3.2, Leighton and Murray (1966) considered the effects of blanketing of the planet (or polar regions) by clouds of condensed  $\text{CO}_2$  or  $\text{H}_2\text{O}$ . Atmospheric models of Mars conducted around that time implied that solid particles of  $\text{CO}_2$  could be present in the Martian atmosphere at all latitudes (Fjeldbo et al., 1966). In addition, polar haze had been regularly observed in the respective autumn seasons at each pole (Slipher, 1962). These large clouded regions are now generally referred to as polar hoods. Leighton and Murray theorized that the accumulation of  $\text{CO}_2$  on the ground could be reduced due to  $\text{CO}_2$  or  $\text{H}_2\text{O}$  clouds because thermal emission from the surface would be retarded. Conversely, they also made the point that the amount of  $\text{CO}_2$  on the surface may be increased due to snowfall from such  $\text{CO}_2$  or  $\text{H}_2\text{O}$  ice crystals in the atmosphere (Leighton and Murray, 1966). Thus, the overall influence of Martian clouds is not straight forward. Paige and Ingersoll (1985) utilized a one-dimensional polar radiative model to show that the likelihood that atmospheric temperatures will fall to the  $\text{CO}_2$  frost point is greatly increased by the presence of water-ice or dust clouds. The atmospheric temperature decrease is due to the increase of infrared emissivity, which is the net radiative effect of adding either dust or ice crystals into the system. However, the situation is further complicated because this cooling via thermal emission is counteracted by the competing effect of heating from dynamical motions of the atmosphere (James et al., 1992).

Pollack et al. (1990) then developed a three-dimensional Mars GCM, which included orbital conditions, dust, and topography effects when simulating the Martian polar atmosphere. They determined that regardless of the dust opacity,  $\text{CO}_2$  clouds will form in the polar regions during the winter seasons. However, it appears that as the concentration of dust increases, so does the rate of  $\text{CO}_2$  cloud formation. The results even reveal that if the dust optical depth is greater than 1, a considerable fraction of the total  $\text{CO}_2$  condensation will occur in the atmosphere. The overall implications of the investigation were that  $\text{CO}_2$  ice may comprise a large fraction of

the polar hood and other Martian clouds. This cloud activity, which can obscure the polar caps (particularly in the north), can also affect observations of the seasonal CO<sub>2</sub> cap growth. During the fall and winter seasons, some telescopic studies have actually confused the atmospheric and surface condensates (Martin et al., 1992).

Historically, it has long been observed that clouds on Mars tend to form in particular regions and during specific seasons. Also, there does seem to be a qualitative difference in the cloud cover and atmospheric activity of the northern versus the southern hemisphere (James et al., 1992). In the north, there usually appears to be an extensive condensate hood present during most of the fall and winter seasons (Martin et al., 1992) that often persists until early spring (James et al., 1992). The northern polar hood has been more thoroughly studied than its southern counterpart due to its appearance during favorable oppositions, and its activity appears remarkably variable from year to year (Martin and McKinney, 1974) especially in the presence of large dust storms. In general, the cloud cover can be observed from approximately  $L_s = 180^\circ - 360^\circ$  (Martin et al., 1992). Clouds that follow the retreat of the northern seasonal polar frost cap edge have also been recorded and identified as water-ice clouds associated with the water vapor released by the receding frost (Zurek, 1992). In fact, Briggs and Leovy (1974) declared that all portions of the polar hoods that are equatorward of Martian arctic and antarctic circles are composed primarily of water-ice. At least in the north, the Pollack et al. (1990) model has determined that water clouds near the pole most likely assist in the transport and removal of atmospheric dust and water.

The southern cloud activity has been more elusive and is less understood. Clouds tend to form around mid-winter at  $L_s \sim 135^\circ$  (Briggs et al., 1977) and are mostly dispersed by the southern vernal equinox (James et al., 1992). Recently, the MGS MOLA has detected sharply defined, thick clouds of uncertain origin that appear in the southern regions only (James et al., 2005). Otherwise, the south pole often looks clear with the exception of cloud streaks near the terminator (James et al., 1992).

The qualitative behavioral differences between the northern and southern clouds

can perhaps be attributed to hemispherical asymmetries in polar seasonal CO<sub>2</sub> cycle (James et al., 1992). Pollack et al. (1990) would add that seasonal differences in aerosol concentrations may also play a role. Wang and Ingersoll (2002) point out one commonality between the two poles: both experience stormy periods before circumpolar clouds form in the early fall. Also, similar thin and diffuse clouds have been discerned by the MGS MOLA in both polar regions during the winter (Ivanov and Muhleman, 2001). Colaprete and Toon (2002) have reported that the adiabatic cooling associated with such cloud formations is adequate to condense and precipitate substantial amounts of CO<sub>2</sub> as dry ice snow deposits in specific geographic locations dictated by topography. This reinforces observations of preferential deposition of CO<sub>2</sub> as was discussed in previous sections. In general, the prevalence of polar hoods and the cloud activity at both poles are important factors that cannot be ignored due to their connection to and influence on the seasonal CO<sub>2</sub> cycle and other volatile processes on Mars.

#### 2.2.4 Residual Polar Caps

Though they do not experience the same magnitude of seasonal change as the water, dust, and cloud cycles mentioned above, the influence of the permanent polar caps underlying the seasonal CO<sub>2</sub> frost is important to discuss. The annual heat balance of the Martian residual polar caps strongly influences the placement of available CO<sub>2</sub> among all known CO<sub>2</sub> reservoirs. Interestingly, the partitioning and behavior of CO<sub>2</sub> at both poles is not identical. Investigating this asymmetry and determining the responsible physical processes is crucial to understanding the current Martian climate and its seasonal trends.

Permanent polar caps remain on both hemispheres of Mars during the summer season when the *seasonal* carbon dioxide polar frost sublimates. The Viking spacecraft were the first to make concrete observations of these residual caps. The diameter of the north cap is around 1000 km, while the southern deposit is noticeably smaller and measures about 350 km in diameter (James et al., 1992). Although neither polar cap is exactly circular or centered on the planet's axis, the northern deposit

is the most symmetric about Mars' geographic pole. It is also associated with several outlying patches that remain throughout the year. The southern residual cap, though smaller, is a bright albedo feature that is displaced by  $\sim 3.5^\circ$  from the pole approximately along  $30^\circ\text{W}$  longitude. This feature has classically been called Hypernotius Mons, and is known to have a large influence on the Martian climate (Dobbins et al., 1988). Howard et al. (1982) document that both caps are terraced, layered, and exhibit swirl-like formations. The northern residual cap consists of 100%  $\text{H}_2\text{O}$ -ice, while the southern deposit is composed of  $\text{CO}_2$  as its top layer. There is recent evidence, however, that underlying this permanent carbon dioxide is a reservoir of water-ice. Model results by Bryne and Ingersoll (2003), which are consistent with thermal infrared data from the Mars Odyssey mission, imply that the  $\text{CO}_2$  layer is roughly 8 m thick and is slowly dissipating in specific ways to create observable features such as the so-called Swiss cheese formations and fingerprint terrain. In addition, current thermal models also establish that the overlying veneer of remnant  $\text{CO}_2$  could possibly dissipate completely in some years. See the footnote in Section 2.2.1 for details.

In the past during the Viking mission, a popular idea was that Mars' atmospheric pressure was regulated in response to orbital parameters by permanent  $\text{CO}_2$  polar caps (James et al., 1992). A useful relationship for this investigation is that the average annual insolation at the poles is proportional to the sine of the planet's obliquity (which is currently  $25.2^\circ$  and varies from  $10.8^\circ$  to  $38.0^\circ$  on a cycle on the order of  $10^5$  years) (Ward, 1979). Through energy balance considerations of a residual  $\text{CO}_2$  polar cap, it can be determined that the sine of the obliquity is roughly proportional to the 4th-power of the temperature of the deposits:

$$\frac{(1 - A)Q_o(\sin \alpha)}{\pi\sqrt{1 - \varepsilon^2}} = \langle e\sigma T^4 \rangle \quad (2.2)$$

where  $A$  and  $e$  are the radiometric albedo and emissivity of the ice deposits.  $Q_o$  is the appropriate solar constant,  $\sigma$  is the Stefan-Boltzmann constant ( $5.670 \times 10^{-8} \text{ W m}^{-2} \text{ K}^{-4}$ ),  $\alpha$  and  $\varepsilon$  are the obliquity and eccentricity of the orbit, and  $T$  is the temperature of the ice (James et al., 1992). Furthermore, the

average pressure is also a function of the obliquity because the Clausius-Clapeyron equation (2.1) relates the ice deposit's sublimation temperature to the CO<sub>2</sub> pressure. Assuming that the permanent CO<sub>2</sub> caps contain a greater amount of CO<sub>2</sub> than the atmospheric reservoir, Leighton and Murray (1966) argued that the caps' vapor pressure would determine the average atmospheric pressure at the surface on Mars. Following the relationships above, the Martian pressure would vary due to changes in insolation at the poles depending on whether Mars was in a period of high or low obliquity. The theory that the polar CO<sub>2</sub> reservoir could function as a long-term buffer to the atmosphere is plausible as long as there is enough CO<sub>2</sub> in the permanent polar deposits to produce the observed current average pressure (allowing for variations in the albedo of the buffering deposits). This concept is important to mention because it sustained support and popularity for an extended period of time. However, despite evidence that the current CO<sub>2</sub> pressure is consistent with buffering, present-day models and observations imply that the amount of CO<sub>2</sub> in the residual polar caps is inadequate to effectively regulate the atmospheric pressure in such a manner (Bryne and Ingersoll, 2003; James et al., 2005).

Heat balance studies are a common way to analyze what is occurring on the Martian poles. The underlying principle is that the rate at which energy is stored in a given region must equal the total net flux of energy into that region (James et al., 1992). Conveniently, variations of the heat-balance parameters at the poles are just a function of the season because there are no diurnal variations in insolation. For the most part, the energy storage at the poles of Mars is in the form of latent heat during the condensation and sublimation of the seasonal carbon dioxide frost. A lesser factor is the storage of potential energy within the atmospheric column above the pole. The corresponding energy flux into the polar regions can come from incident solar radiation, reflected solar radiation, and emitted infrared radiation at the top of the atmosphere. Conductive heating at the base of the seasonal frost deposits can also play a role. This is due to the seasonal storage and release of heat within the underlying residual polar caps. At a less significant level, atmospheric motions can cause horizontal heat transport (James et al., 1992).

The instantaneous polar heat balance can primarily be described as an equilibrium between the seasonal CO<sub>2</sub> frost latent heat storage and the net radiative flux at the top of the atmosphere. When the temporary, condensed CO<sub>2</sub> completely sublimates, the subsurface heat conduction of the permanent caps becomes important. The large heat capacity of the north polar water-ice cap is especially influential during this CO<sub>2</sub> frost-free time period.

Paige and Ingersoll (1985) modelled the polar heat and annual radiation budgets to deduce information about the behavior of the seasonal CO<sub>2</sub> frost. The fall and winter CO<sub>2</sub> condensation rates in the north and south were roughly comparable despite the fact that the residual water-ice cap in the north reduced CO<sub>2</sub> accumulation by about 10% - 15% from what would otherwise be expected. Over the southern permanent cap, CO<sub>2</sub> frost was shown to condense and sublime at a fairly constant rate during the fall/winter and spring/summer seasons, respectively. Interestingly, the total annual amounts of CO<sub>2</sub> that condensed versus sublimed on a seasonal basis were approximately equal, thus confirming that the underlying residual CO<sub>2</sub> cap was not contributing or removing mass during the process and was therefore stable (Paige and Ingersoll, 1985).

Although the model results mentioned above predicted similar behavior for seasonal CO<sub>2</sub> in the north and in the south, spacecraft data for the two poles reported something different. Early models of the CO<sub>2</sub> sublimation rate over the northern permanent cap conflicted with actual observations in that the rates observed were significantly higher than predicted. Over the southern remnant cap, sublimation rates were lower than the model predictions. This implies that the springtime radiative properties of the two poles differ. Surface frost albedo variations and/or radiative effects of atmospheric dust are proposed as possible causes for the discrepancies (James et al., 1992). The present asymmetric behavior of the seasonal CO<sub>2</sub> frost is definitely related to differences between the two residual caps and the corresponding polar environments. Physical differences of each pole during the summer season, such as the dust optical-depth trends or perhaps the intrinsic disparities in the volatiles that accumulate permanently, affect the energy balance over the

perennial caps (James et al., 1992). Other mysteries about the observed nature of the residual caps include: the north cap is more reflective than one would expect for contaminated water-ice (Kieffer, 1990), and the unusually high albedo of the southern deposit is nearly unaffected by dust contamination. The offset of the southern permanent cap is in itself also puzzling. Perhaps it is related to topography, as the unique surface profiles around the pole suggest topographical influence on the atmospheric dynamics during the colder condensation seasons (James et al., 1992). Finally, the south pole is elevated in relation to the north pole due to the northern-lowlands/southern-highlands dichotomy on Mars. Thermodynamics would tend to favor the retention of permanent solid CO<sub>2</sub> in the north more than in the south because the lower elevation allows CO<sub>2</sub> to equilibrate with the atmosphere at a higher temperature and pressure than is possible in the south (James et al., 2005). However, it is now well-known that this is not what actually occurs.

The ongoing study of the Martian residual polar caps and the present asymmetry between the northern and southern CO<sub>2</sub> budgets has long been an intriguing investigation. The determination of the properties and processes that cause the observed differences is an important step in solidifying current knowledge about the principles that govern the Martian CO<sub>2</sub> cycle on a seasonal basis and at extended time scales.

## 2.3 CO<sub>2</sub> Ground Frost Predictions

### 2.3.1 Introduction

Since the beginning of Mars exploration, scientists have speculated greatly over the composition and behavior of the planet's polar caps. Various theories have proclaimed that these white, polar regions are comprised of frozen water, carbon dioxide, or oxides of nitrogen. It has thus always been important to develop scientific models to address and investigate the poles, and to determine which possibilities lead to behavior that matches actual observations. What follows is a brief history of Martian polar models over time with an emphasis on the landmark Leighton and

Murray paper in 1966 and the model most utilized and relevant to this current study, the NASA Ames Research Center Mars General Circulation Model (ARC GCM).

### 2.3.2 Energy Balance Models

As mentioned in previous sections, the behavior of the seasonal CO<sub>2</sub> cycle at the poles of Mars is a result of an ongoing energy balance. The total net flux of energy into (or out of) a given region must equal the rate at which energy is stored in (or released from) that region. The latent heat of carbon dioxide is a primary component of such an energy balance, but other factors in the net energy flux include: incident and reflected insolation at that top of the atmosphere, infrared thermal radiation exiting the atmosphere, horizontal advection, heat transport by clouds, conduction within subsurface layers, and heat dissipation by winds near the surface (James et al., 1992). Although every attempt is made to correctly model the polar environment, there are also numerous poorly quantified or variable parameters, such as, the relevant albedos, emissivities, optical depths, and cloud behavior.

There are two main varieties of Martian thermal models that predict activity at the poles over time. The first are called *zonally symmetric models*, where values are averaged into latitudinal bands, and the longitudinal degree of freedom is suppressed. The second group divides the planet into smaller cells defined by latitude and longitude and are classified as *three-dimensional models*. The full three-dimensional models have the advantage in that they can most accurately portray the physics of the situation on a finer grid (James et al., 1992). There are also various methods for accounting for (or neglecting) the atmosphere by incorporating vertical degrees of freedom above the surface of Mars.

A major step and turning point in Martian polar science came in 1966 when Robert Leighton and Bruce Murray produced an atmospheric model that forever changed beliefs about the Martian polar caps. At the time of the publication of their paper, *Behavior of Carbon Dioxide and Other Volatiles on Mars*, the current understanding was that water-ice was the dominant constituent of the polar caps. Leighton and Murray decided to reexamine this belief and were able to shift the par-

adigns of then-current Martian polar ideology. By posing the study as a problem of heat balance of the planet, they managed to achieve multiple important realizations. First, their calculations indicated that the temperatures at the poles of Mars become cold enough to condense carbon dioxide in solid form. Second, their model predicted major seasonal variations in pressure that result from this polar frost condensation (Leighton and Murray, 1966). In addition to happening on a seasonal basis, the substantial surface pressure fluctuations were also forecasted to occur on a time scale long enough to incorporate orbital variations that affect the distribution of solar radiation on the planet (Zurek, 1992). These thermal model based predictions were the first to assert and show through calculations that the  $\text{CO}_2$  in the atmosphere and the  $\text{CO}_2$  condensed on the surface of Mars are part of a major cycle of  $\text{CO}_2$  exchange that is integrally linked to daily, seasonal, and long term climatic trends.

Leighton and Murray (1966) created a one-dimensional surface energy balance equation to compute the surface temperatures for Mars as a function of latitude and season. Ignoring atmospheric energy advection, their model showed that with no condensible gases, the planet's surface temperature at the poles would fall below  $\sim 147$  K, the condensation temperature of  $\text{CO}_2$ . When  $\text{CO}_2$  changes from gas to solid at the  $\text{CO}_2$  partial pressure of approximately 4 mbar (which was observed by Mariner 4), the temperature will be stabilized at the sublimation point by releasing  $6.0 \times 10^5$  J  $\text{kg}^{-1}$  of latent heat (James et al., 1992). Leighton and Murray concluded from their results that both permanent polar caps would, therefore, consist of  $\text{CO}_2$ . It is now known that this assumption was not completely true (see Section 2.2.4 regarding the Residual Caps), but instead was a result of their simplified view of Mars and the resulting inaccuracy of the annual insolation at each pole.

From their model work Leighton and Murray came to the conclusion that  $\text{CO}_2$  must condense in large amounts relative to  $\text{H}_2\text{O}$ . The main conclusions of the study are quoted directly below (Leighton and Murray, 1966):

1. The atmosphere and frost caps of Mars represent a single system with  $\text{CO}_2$  as the only active phase.

2. The appearance and disappearance of the polar caps are adequately explained on the presumption that they are composed almost entirely of solid CO<sub>2</sub> with perhaps an occasional thin coating of water ice.
3. If the currently reported water-vapor observations are correct, water-ice permafrost probably exists under large regions of the planet at polar and temperate latitudes.
4. The geochemically anomalous enrichment of CO<sub>2</sub> relative to N<sub>2</sub> in the present Martian atmosphere may be a result of selective trapping of CO<sub>2</sub> in the solid phase at and under the surface.
5. If the basic evaporation and condensation mechanisms for CO<sub>2</sub> and H<sub>2</sub>O [discussed in their article] are correct, the possible migration of volatile organic compounds away from the warm temperate regions of the planet and their possible accumulation in the polar regions need to be carefully considered.

Work on similar heat balance models of the Martian polar caps has continued throughout the years. Leovy and Mintz (1969) were first to adapt a terrestrial atmospheric circulation model produced at UCLA to Martian conditions. Cross (1971) repeated a Leighton and Murray type calculation and found that in terms of the seasonal CO<sub>2</sub> cycle, the heat conduction with the surface does not significantly affect the model results. Jakosky and Haberle (1990) determined, however, that when dealing with the residual caps, the heat storage and conduction terms are very important in regards to interannual variations. New data from Mariner 9 and the Viking mission enabled Briggs (1974) to match observations of the seasonal frost cap edge movement by including heat exchange between the surface and the atmosphere of Mars. He deduced that effects from polar hood clouds played a more substantial role in the polar cycles than previously believed. Further refinement of these thermal models occurred when north polar water-vapor measurements and IRTM (Viking Infrared Thermal Mapper) polar temperature data were incorporated by Davies et al. (1977) and Kieffer et al. (1977). In 1979, Hess et al. were able to

use Viking lander pressure measurements for an entire seasonal cycle to compare to the current model predictions. Davies (1979) added the radiative effects of dust storms by utilizing a Monte Carlo photon propagation simulation. And eventually, a model including CO<sub>2</sub> condensation and sublimation, and the effects of atmospheric circulation and dust dispersal, was created by Haberle et al. (1982). This model incorporated a more precise vertical atmospheric structure, could distinguish between surface and atmospheric CO<sub>2</sub> condensation, revealed that CO<sub>2</sub> frost is reduced during periods of high optical depth, and assessed the influence of dust on the CO<sub>2</sub> cycle. Pollack et al. (1990) applied to the CO<sub>2</sub> cycle a three-dimensional model with improved horizontal and vertical resolution and more realistic dust and CO<sub>2</sub> radiative properties. It was the first thermal simulation to include CO<sub>2</sub> cloud occurrence and atmospheric CO<sub>2</sub> condensation in detail.

Paige and Ingersoll (1985) also wrote about their comprehensive study using Viking observations to investigate the annual thermal balance occurring at the poles of Mars. Choosing the boundaries of the regions of study to correspond to the general location of the residual polar caps, they were able to determine associated annual radiation and heat budgets. Paige and Ingersoll used the same basic polar heat balance principles involving the total net flux of energy into the system compared to the energy stored within the system. The procedure and equations outlined in their paper give a good introduction to the relevant background physics. They modelled the instantaneous heat balance equation for the atmosphere and seasonal CO<sub>2</sub> frost deposits as:

$$F_{Rad} + F_{Horiz} + F_{Cond} = S_{Atm} + S_{CO_2} \tag{2.3}$$

where  $F_{Rad}$  is the net flux of incoming solar and infrared radiation at the top of the atmosphere;  $F_{Horiz}$  is the net flux of sensible and latent heat coming into the region horizontally; and  $F_{Cond}$  is the upward subsurface conductive heat flux coming into the region from the top surface of the underlying residual polar caps.  $S_{Atm}$  is the rate of total potential energy storage in the overlying atmospheric column, and  $S_{CO_2}$  is the rate of latent heat storage in the CO<sub>2</sub> as it condenses and sublimates. Because of

their relatively smaller magnitudes, the terms for kinetic energy generation, latent heat storage by H<sub>2</sub>O condensates, and heat flow from Martian interior were not included (Paige and Ingersoll, 1985).

Regarding the seasonal polar CO<sub>2</sub> frost behavior, the most relevant term of the heat balance equation is the CO<sub>2</sub> latent heat storage rate. Represented here again as  $S_{CO_2}$ ,

$$S_{CO_2} = -L_{CO_2} \frac{dM_{CO_2}}{dt} \quad (2.4)$$

relates this rate to the net rate of solid CO<sub>2</sub> accumulation within the region's boundaries,  $dM_{CO_2}/dt$ .  $L_{CO_2}$  is the latent heat of sublimation for CO<sub>2</sub> (Paige and Ingersoll, 1985). Utilizing these equations along with planetary albedo values and radiation budget measurements from the Viking IRTM, the authors simulated Martian polar processes and modelled, rather successfully, the influence of the CO<sub>2</sub> cycle on Mars' overall environment and climate.

There have been a few recent updates to the beliefs and theories presented in popular models of the past. As mentioned in Section 2.2.4, one idea from Leighton and Murray (1966) that maintained widespread support until recently was that the Martian atmosphere is controlled by vapor equilibrium with the solid CO<sub>2</sub> deposits. However, newer thermal models and observations imply that the permanent polar caps do not contain enough CO<sub>2</sub> for such a buffering effect. In fact, it is now believed that the permanent CO<sub>2</sub> southern polar cap is, in actuality, a thinner layer of CO<sub>2</sub> covering a water-ice layer<sup>4</sup> (Bryne and Ingersoll, 2003; Titus et al., 2003a). This idea is also supported by observations of the south polar summer of 1969, in which an unusually large amount of H<sub>2</sub>O vapor appeared over the pole suggesting that

---

<sup>4</sup>This brings up the question: If it is not in the southern residual polar cap, then where is all the CO<sub>2</sub> really? Researchers agree that it must be somewhere on Mars, and one theory is that the CO<sub>2</sub> is perhaps mostly underground. However, there are theoretical arguments that imply that CO<sub>2</sub> would not be stable buried in the regolith because underground heat would cause the CO<sub>2</sub> to diffuse up through porous areas of the surface. Another possibility is that CO<sub>2</sub> exists locked in carbonate minerals in Martian rocks. So far though, investigations of the spectral signatures of the rocks on the planet do not support such a hypothesis (Rayl, 2003).

the CO<sub>2</sub> veneer had dissipated to reveal underlying H<sub>2</sub>O-ice (Barker et al., 1970). A final objection to the original Leighton and Murray theory is that some believe the outlined rate of seasonal CO<sub>2</sub> retreat in the spring is too high for long-term survival of CO<sub>2</sub>-ice (Ingersoll, 1974). Regardless of these criticisms, it is important to point out that the central tenets of the Leighton-Murray model are still legitimate, and the ideas apply to the surface-atmosphere interaction of CO<sub>2</sub> sublimation and condensation, as is central to this seasonal polar frost research.

The NASA Ames Research Center Mars General Circulation Model (ARC GCM) has modelled the condensation and sublimation cycle of seasonal carbon dioxide as a function of space and time on Mars for many years now. The CO<sub>2</sub> model predictions from this GCM will be compared to the actual observations from the GRS in the Results Chapter (Chapter 5), and specifics about the model and the data output are described in Section 5.2.2. A general introduction and information about the current model work can be found in the next paragraph. In addition to the ARC GCM, there are also numerous other research groups working on similar projects at the Laboratoire de Météorologie Dynamique in France (LMD), the Oxford University Atmospheric, Oceanic, and Planetary Physics (AOPP) department, and the Geophysical Fluid Dynamic Laboratory (GFDL), for example.

The ARC GCM predicts accumulation and dissipation of CO<sub>2</sub> by reproducing the atmospheric pressure variations observed by the Viking landers, while incorporating other atmospheric and ground properties (Haberle et al., 1993, 1999; Pollack et al., 1990; Murphy et al., 1995). Although various versions of this GCM have played a primary and steadfast role in replicating and predicting the behavior of volatiles on Mars, there have been some concerns that the values selected for the ice emissivity and albedo were unrealistic. The fact that the model results best matched observations while the chosen emissivities were too low implied that the simulation was missing a heat source, was missing thermal emission from the polar hood, or was underestimating subsurface heat conduction (Haberle, 2005, pers. comm.). The third possibility is the most likely because it corresponds to the lack of including subsurface ice in the model at the polar regions. It is now well-known that such

subsurface ice does exist (Boynton et al., 2002a; Feldman et al., 2002a; Mitrofanov et al., 2002b). The GRS CO<sub>2</sub> calculations presented in this dissertation play a large role in a joint study comparing the latest Mars Odyssey data to the GCM results, which is currently in progress as part of the Mars Data Analysis Program (MDAP). For this project, Haberle et al. have recently updated the GCM's surface properties utilizing Viking and MGS TES data. They have also included subsurface heat conduction from ground ice and have fixed the emissivity at the more reasonable value of 1. Current model runs incorporate a subsurface ice latitude distribution extending from the poles to 45°N in the northern hemisphere and 52.5°S in the southern hemisphere (Haberle, 2005, pers. comm.). These changes represent a more realistic representation of the situation at Mars, and the results still do a fairly good job of fitting the established Viking data (and the GRS data as is presented here in later chapters).

Energy balance calculations and model simulations have often attempted to reproduce the behavior of carbon dioxide at the poles of Mars. Although the formation and regression of the seasonal caps have yet to be exactly matched by these methods, the model results do closely mimic the observed general behavior. This suggests that the basic physical principles have probably been incorporated, and that energy balance considerations are fundamental for predictions and comparisons to actual data in Martian polar science.

## 2.4 Gamma Ray Sources and Nuclear Physics

Galactic cosmic rays (GCR) continually permeate interplanetary space and bombard the atmosphere and surface of Mars. Protons (nuclei of <sup>1</sup>H) account for about 87% of the GCR, and alpha particles (nuclei of <sup>4</sup>He with an electrostatic charge of 2<sup>+</sup>) and heavier nuclei (with typical energies around 0.1 - 10 GeV/nucleon) make up the other 12% and 1%, respectively (Boynton et al., 2004a). The 2001 Mars Odyssey GRS is able to map the elemental composition of the surface of Mars by archiving the spectra of gamma rays radiated from the planet. The various elements are identified

by the corresponding energies of the observed gamma rays, while the concentration of each element can be determined from the associated intensity of the gamma ray line (Boynton et al., 2004a). The gamma rays observed by the satellite arise from nuclear interactions initiated by the charged cosmic-ray particles with materials in the Martian regolith and also from the natural decay of long-lived radioactive species (Reedy et al., 1973; Reedy, 1978; Evans et al., 1993; Masarik and Reedy, 1996). Figure 2.5 illustrates the possible processes.

In addition to discussing gamma ray production by natural radioactivity, this section will give an overview of inelastic scattering and neutron-capture-produced gamma rays. The creation, transport, and moderation of neutrons is therefore important to mention here. As a result of the wide range of reactions induced by GCR particles, cascades of secondary particles are created. Many neutrons are produced with energies of approximately 0.1 - 20 MeV, which travel until they escape to space or undergo an interaction with a nucleus in Mars' surface. In such interactions, fast neutrons (MeV energies) are moderated down to epithermal ( $\sim 0.1 - 1000$  eV) or thermal ( $\leq 0.1$  eV) energies. The overall production and transport of neutrons depends on the composition of the surface of the planet. For free neutrons at the lower end of the energy range (from below 0.1 eV up to  $\sim 0.5$  MeV), elastic scattering and the resulting recoil of the target nucleus is the dominant energy-loss (moderation) mechanism. For neutrons with energies above the first excited levels of the nuclei in their path ( $\geq 0.5$  MeV for light nuclei), both elastic and nonelastic scattering can occur. The following sections discuss the sources that generate the majority of the more intense gamma rays: nonelastic scattering reactions with fast neutrons and neutron-capture reactions with thermalized neutrons. The photons emitted in these interactions (by the excited nuclei) in the range of 0.2 - 10 MeV are the gamma rays of most interest for mapping elemental abundances (Boynton et al., 2004a).

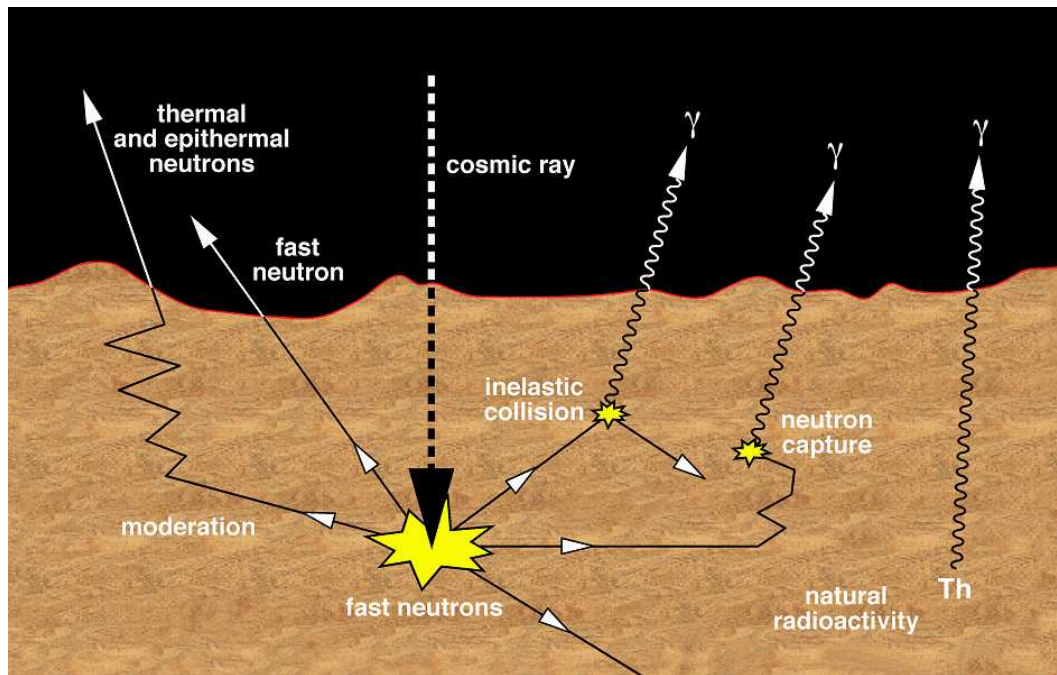


Figure 2.5: Energetic charged particles in the galactic cosmic rays continually bombard Mars and interact with nuclei near the surface of the planet, producing nuclear emission, especially of neutrons. The gamma rays observed by Mars Odyssey arise from inelastic or neutron-capture reactions involving these energetic neutrons or from the decay of naturally radioactive species.

### 2.4.1 Inelastic Scattering

In particle physics, inelastic scattering is a fundamental scattering process in which the momentum of an incident particle is not conserved. At the nuclear level, the collision causes the target nucleus to become excited or to break up, and the recoil of this nucleus adds to the energy loss from the incident particle (in this case, a GCR-produced neutron). When a target nucleus is excited in such a manner, it decays back to the ground state with a life-time on the order of a picosecond. In the process, it emits a characteristic gamma ray.

Besides the very lightest elements that do not have gamma-ray-emitting excited levels, such as H and He, almost all elements can generate gamma rays from inelastic scattering interactions. The gamma ray lines that are usually strong and useful in planetary science are 6129 keV (oxygen), 1369 keV (magnesium), 1014 keV (aluminum), 1779 keV (silicon), 3737 keV (calcium), and 847 keV and 1238 keV (iron) (Boynton et al., 2004a).

Doppler broadening can occur in these inelastic scattering reactions when the gamma ray is emitted from the excited nucleus while it is still recoiling from the associated collision. In fact, because of the longer time required for a recoiling nucleus in the Martian atmosphere to slow down, most gamma rays produced by inelastic reactions in the planet's atmosphere are Doppler broadened. However, as observed by the GRS and demonstrated through experimental simulations by Brückner et al. (1992), gamma rays resulting from nuclei in the Martian surface containing excited energy levels with life-times  $\geq 0.5$  picoseconds will not be broadened.

### 2.4.2 Neutron-Capture

Gamma rays produced by neutron-capture reactions are another major source utilized for mapping elemental concentrations on Mars. Recall that many high energy neutrons are produced during bombardment of the planet by GCR particles. These neutrons are then moderated, or slowed down, by inelastic and elastic collisions with nuclei until they are *thermalized*, meaning that they have an energy on the

order of the thermal energy of the surrounding regolith. Because many elements on Mars have high neutron capture cross sections, the thermal neutrons are readily captured by nuclei, changing the nucleus from  $(Z,A)$  into  $(Z,A+1)$  and leaving it in an excited state (where  $Z$  is the atomic number or number of protons, and  $A$  is the mass number or total number of nucleons). When the nucleus is excited in such a way by absorbing a low-energy neutron, the emission of a gamma ray or a cascade of gamma rays results.

The neutron-capture hydrogen gamma ray is the primary gamma ray used to investigate the seasonal polar carbon dioxide frost in this study. Hydrogen is also a good thermalizer of neutrons, therefore, it actually acts both as a moderator and a capture target. Its capture cross section is large enough that thermal neutrons are readily absorbed. When thermal neutrons are captured by hydrogen nuclei, they produce deuterium ( ${}^2\text{H}$  represented as D) by the reaction:  $n + p \rightarrow D + \gamma$ . The binding energy of the deuteron is released in the form of a 2223 keV gamma ray (Krane, 1988). Seasonal frost measurements are complicated by the fact that  $\text{CO}_2$  is also a good moderator of neutrons, but not an effective absorber. This effect and its inclusion in the  $\text{CO}_2$  frost measurement calculations are discussed in Section 4.2.

### 2.4.3 Natural Radioactive Decay

Another gamma ray production process that is important to mention involves naturally radioactive materials whose nuclei spontaneously emit radiation and thereby change the state of the nucleus. These substances follow the exponential law of radioactive decay,  $N(t) = N_o e^{-\lambda t}$ , where  $N_o$  is the constant of integration and gives the original number of nuclei present at  $t = 0$ .  $\lambda$  is the disintegration or decay constant (Krane, 1988).

There are several elements on Mars today that have natural radioactive isotopes with long half-lives ( $t_{1/2}$ , the time necessary for half of the nuclei to decay). In fact, many of the radioactive nuclei have not yet decayed since they were created by nucleosynthetic processes before the formation of the planets over  $4.6 \times 10^9$  years ago. The radioactive isotope  ${}^{40}\text{K}$  makes up 0.012% of the abundance of normal

potassium on Mars (Boynton et al., 2004a), and it has a half-life of  $1.28 \times 10^9$  years (Krane, 1988). Besides the hydrogen gamma ray mentioned in the neutron-capture section, this naturally radioactive potassium-40 gamma ray can also be used to investigate polar CO<sub>2</sub> columnar thickness up to a depth of about 40 g/cm<sup>2</sup>. It is created when the decay of <sup>40</sup>K produces the first excited level of <sup>40</sup>Ar, which happens 10.6% of the time. This excited argon level is at an energy of 1461 keV, and it decays almost immediately to the <sup>40</sup>Ar ground state by emitting a characteristic 1461 keV gamma ray (Boynton et al., 2004a). Fluctuations in the flux of this gamma ray signal as observed at the spacecraft over time indicate changes in the CO<sub>2</sub> at the poles of Mars on a seasonal basis. Other naturally radioactive isotopes on Mars that the GRS uses to characterize and map the planet are <sup>232</sup>Th (Thorium) and <sup>238</sup>U (Uranium).

#### 2.4.4 Transport and Interference of Gamma Rays

En route from the surface or atmosphere of Mars to the GRS detector, gamma rays may be absorbed or lose energy through certain interactions. The overall reduction in gamma ray energies through scattering and interference mechanisms contributes to the low-energy gamma ray continuum observed at the spacecraft<sup>5</sup>. Mars' atmosphere also plays a role by collimating the gamma rays (especially those with low energy) travelling from the surface to the detector (Masarik and Reedy, 1996). This has the effect of improving the spatial resolution of the GRS because gamma rays from directions near the horizon are attenuated more than those from locations more directly beneath Mars Odyssey. The result is increased for thicker atmosphere and for lower orbits (Metzger and Arnold, 1970). The CO<sub>2</sub> frost also adds to the collimation effect. As shown in Table 2.2, the area on the planet from which the GRS receives 50% of its signal during frost-free conditions versus when there is a layer of 100 g/cm<sup>2</sup>-thick seasonal CO<sub>2</sub> frost differs by a factor of  $\sim 2.5$ . This implies that at

---

<sup>5</sup>The gamma ray continuum can be used to analyze compositional variations between measured spectra, but the detailed, quantitative investigation of Mars is done using only the more defined, narrow spectral peaks (Thakur, 1997).

Table 2.2: Change in Detector Spatial Resolution with Increasing Frost Depth.

CO <sub>2</sub> Frost Column Density (g/cm <sup>2</sup> )	50% Signal by Radius (km)	50% Signal by Radius (deg)
0	187	3.2
20	146	2.5
40	121	2.0
60	103	1.7
80	90	1.5
100	78	1.3

greater frost thickness there is better spatial resolution of martian surface features; however, this improved resolution is not actually achieved because the spectra are summed over a larger region for better statistics.

Another issue that needs to be recognized and accounted for when analyzing Mars through the observation of gamma rays is the possible interference of signals by gamma rays of the same energy emitted from sources other than those under investigation. Along the same lines, gamma rays with energies similar to the commonly observed peaks can cause interference by making the classification and separation of spectral peaks difficult. Boynton et al. (2004a) give some good examples of specific interferences that occur in the GRS data. Also, the *Satellite Background* section (Section 3.2.4) discusses interferences from atmospheric argon and germanium in the detector itself that affect the measurement of the 1461 keV potassium gamma ray. The relative contributions from these spurious sources need to be identified in order to accurately measure the desired element.

#### 2.4.5 Attenuation of Gamma Rays

The attenuation of gamma rays by the atmosphere and the seasonal CO<sub>2</sub> frost complicates calculations to determine actual elemental concentrations at the surface of Mars. However, it is the gamma ray attenuation by the seasonal frost that creates the foundation for these CO<sub>2</sub> measurements and makes this CO<sub>2</sub> quantification study

possible overall. Attenuation can be defined as “the decrease in intensity of a signal, beam, or wave as a result of absorption of energy and of scattering out of the path to the detector” (Telecommunications Definitions, 1994). This does not include the reduction in signal due to geometric spreading. Gamma rays can interact with other matter and attenuate in three ways: photoelectric absorption, Compton scattering, and pair production.

In photoelectric absorption (Figure 2.6), the gamma photon loses its entire energy when it is absorbed by an atom. An electron from the atom is released in the process (a photoelectron) with kinetic energy equal to the original gamma photon energy minus the binding energy of the electron:  $T_e = E_\gamma - B_e$  (Krane, 1988). The probability for photoelectric absorption is most significant for low energy photons ( $\sim 100$  keV) and has discontinuous jumps at energies associated with the electron shells’ binding energies. The absorption probability increases with the absorber atom’s atomic number as roughly  $Z^4$ , but becomes less probable as the photon energy increases roughly as  $E_\gamma^{-3}$ .

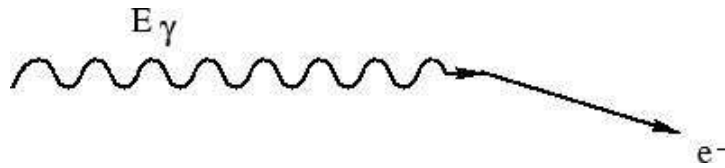


Figure 2.6: The process of photoelectric absorption.

During Compton scattering (Figure 2.7), the gamma photon loses energy by scattering off of a nearly free electron. This results in a less energetic gamma ray and a scattered electron that now carries the photon’s lost energy (Krane, 1988). Using relativistic dynamics, conservation of linear momentum (Equations 2.5 and 2.6) and conservation of total energy (Equation 2.7) can be written as:

$$\frac{E_\gamma}{c} = \frac{E'_\gamma}{c} \cos \theta + \frac{mc\beta \cos \phi}{\sqrt{1 - \beta^2}} \quad (2.5)$$

$$0 = \frac{E'_\gamma}{c} \sin \theta - \frac{mc\beta \sin \phi}{\sqrt{1 - \beta^2}} \quad (2.6)$$

$$E_\gamma + mc^2 = E'_\gamma + \frac{mc^2}{\sqrt{1 - \beta^2}} \quad (2.7)$$

where  $E_\gamma$  is the incident gamma photon energy,  $E'_\gamma$  is the scattered gamma photon energy,  $m$  is the rest mass of the electron ( $9.11 \times 10^{-31}$  kg) (or  $mc^2 = 0.511$  MeV is the electron's rest energy),  $c$  is the speed of light ( $3.0 \times 10^8$  m/s),  $\beta$  is the resulting velocity of the electron divided by the speed of light ( $v/c$ ), and the scattering angles  $\theta$  and  $\phi$  are as shown in Figure 2.7 (Krane, 1988). The Compton-scattering formula can be obtained by considering the scattered photon to eliminate the unobserved variables  $\phi$  and  $\beta$ :

$$E'_\gamma = \frac{E_\gamma}{1 + (E_\gamma/mc^2)(1 - \cos \theta)} \quad (2.8)$$

It is clear from this equation that the resulting attenuated gamma ray energy,  $E'_\gamma$ , can range from a maximum of  $E_\gamma$  after forward scattering where  $\theta = 0^\circ$  (no interaction) to a minimum of approximately  $mc^2/2$  ( $\approx 0.25$  MeV) when  $\theta = 180^\circ$  (assuming  $E_\gamma \gg mc^2$ ).

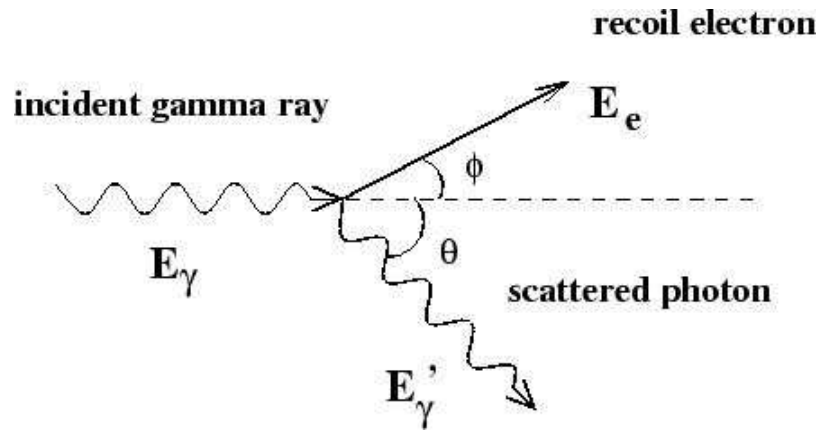


Figure 2.7: The geometry of Compton scattering.

The final way gamma rays can be attenuated is through pair production (Figure 2.8). This is the process in which a gamma photon interacts with the electric

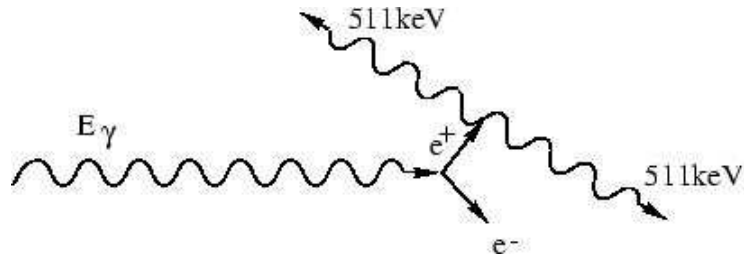


Figure 2.8: The process of pair production or annihilation.

field of a nucleus and annihilates to create an electron-positron pair, which share the available energy. The gamma ray energy must be at least twice the electron rest mass ( $E_\gamma \geq 2mc^2$ ), and in general, pair production is important only for gamma rays with energies above  $\sim 5$  MeV (Krane, 1988).

The three ways that ionizing photons interact with matter (or the ways gamma rays attenuate) are shown as a function of energy and the atomic number of the absorbing material in Figure 2.9.

The total probability per unit length for the attenuation of a gamma ray (photon) is called the *total linear attenuation coefficient*,  $\mu$ . Logically, the value of  $\mu$  is the sum of the probabilities of the three interactions for gamma ray attenuation discussed above: photoelectric absorption ( $\tau$ ), Compton scattering ( $\sigma$ ), and pair production ( $\kappa$ ) (Krane, 1988).

$$\mu = \tau + \sigma + \kappa \quad (2.9)$$

It provides an indication of how effective a given material is, per unit thickness, in promoting these photon interactions. The actual magnitude of  $\mu$  varies depending on the gamma ray energy and the attenuating material. A larger (smaller) value of the attenuation coefficient implies that it is more likely (less likely) that photons of a given energy will interact with the material and lose energy. Boynton et al. (2004a) report that actual attenuation coefficient values range from around  $0.125 \text{ cm}^2/\text{g}$  at  $0.2 \text{ MeV}$  to  $0.024 \text{ cm}^2/\text{g}$  at  $10 \text{ MeV}$ . The  $\mu$  values for various gamma ray energies through carbon dioxide and the associated contributions from each of the individual

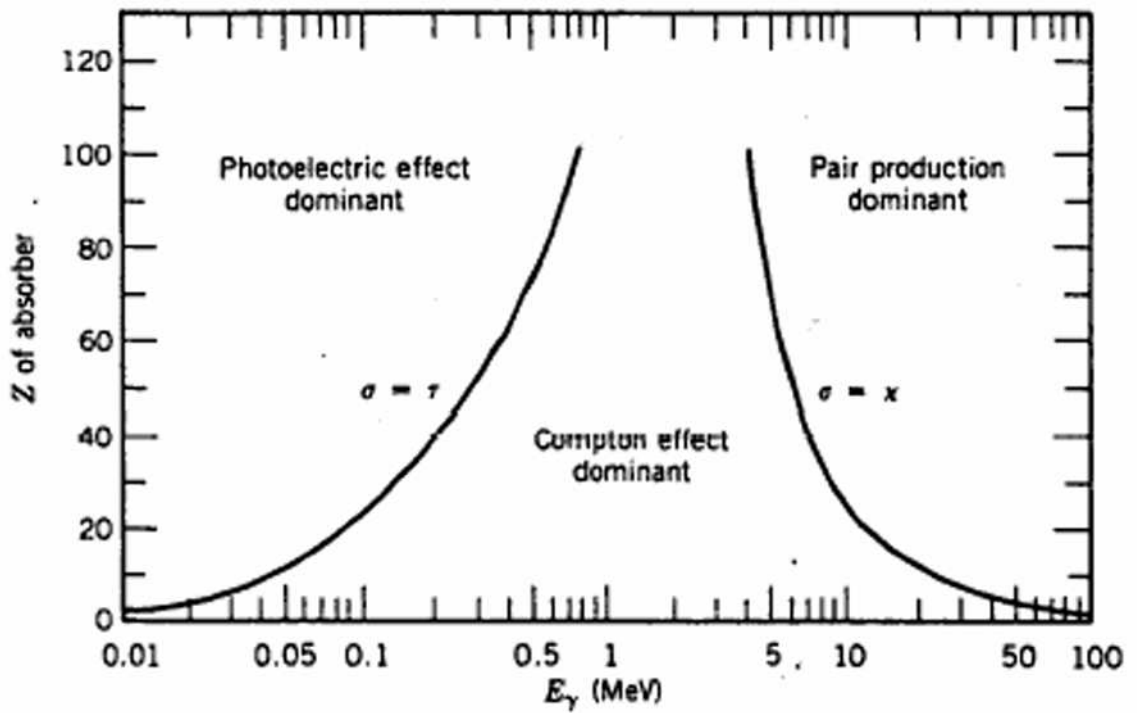


Figure 2.9: Interaction/Attenuation processes of gamma rays with matter. Energy regions of dominance by the photoelectric effect (absorption), the Compton effect, and pair production as a function of the absorber's atomic number. Figure 7.8 of Krane (1988).

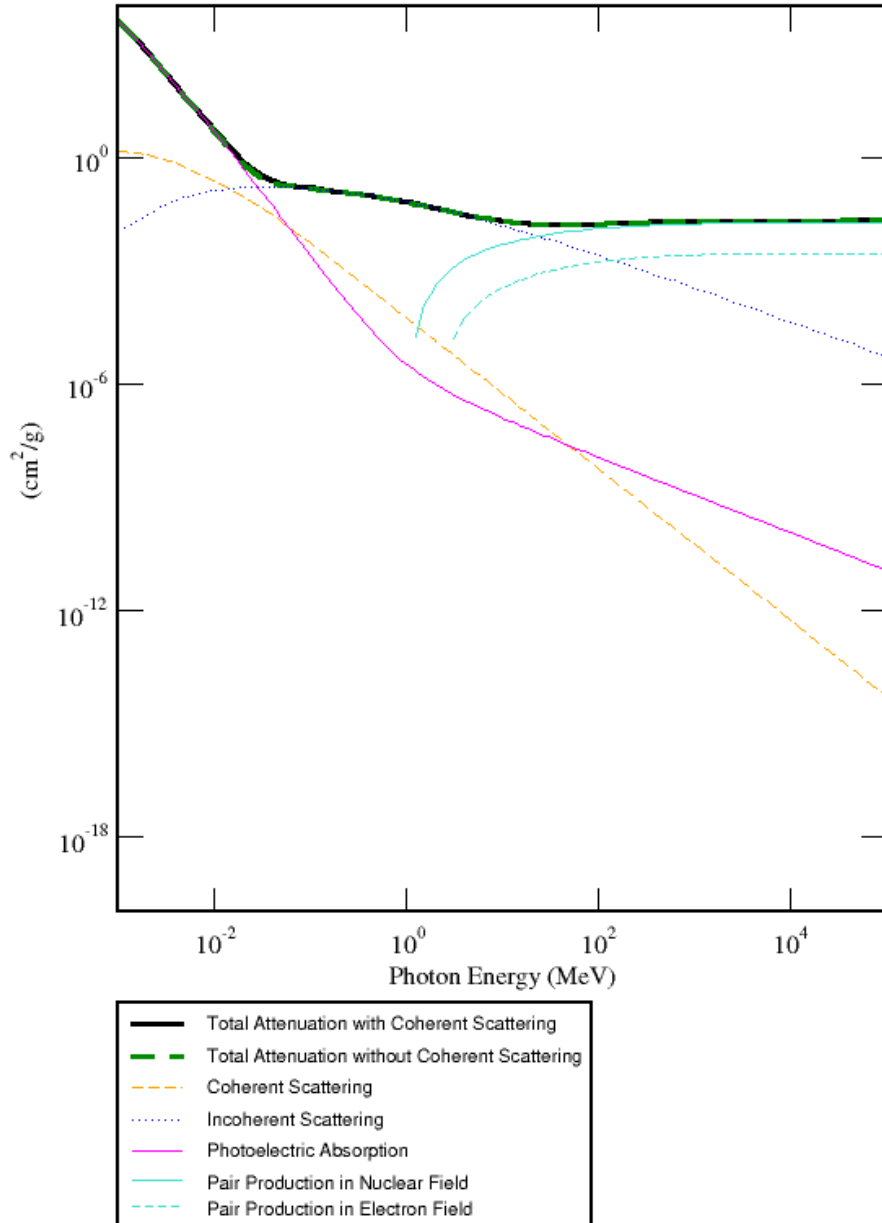


Figure 2.10: Gamma ray linear attenuation/absorption coefficient values as a function of energy through  $\text{CO}_2$ . The contributions from each of the various interaction processes described in this chapter are shown. Figure generated from: National Institute of Standards and Technology (NIST) Physics Laboratory, XCOM: Photon Cross Sections Database (Berger et al., 1998).

interaction processes can be seen in Figure 2.10. For the 2223 keV (2.223 MeV) hydrogen and 1461 keV (1.461 MeV) potassium gamma rays utilized in this seasonal polar CO<sub>2</sub> study, the attenuation coefficients are 0.0420 cm<sup>2</sup>/g and 0.0526 cm<sup>2</sup>/g, respectively (Berger et al., 1998).

Gamma ray attenuation (or photon absorption) can be quantified through the application of Beer-Lambert Theory, which is discussed in Chapter 4, *Carbon Dioxide Quantification Calculations*. Commonly referred to as Beer's Law, equation 4.2 can be used to calculate the fractional loss in intensity of gamma rays crossing a material in terms of the absorption coefficient and thickness of the material. The chapter contains further details and the implementation of this theory to measure the seasonal polar carbon dioxide frost on Mars.

## CHAPTER 3

### 2001 Mars Odyssey Satellite

#### 3.1 Satellite Description and Instrument Details

##### 3.1.1 Mission Overview

The remarkable 2001 Mars Odyssey mission began when the satellite was launched during its very first launch opportunity from Cape Canaveral Air Station, Florida. It lifted off from Space Launch Complex 17 on April 7, 2001 at 11:02 a.m. EDT (Saunders et al., 2004). Mars Odyssey arrived at Mars on October 24, 2001 carrying three primary instruments: THEMIS, MARIE, and GRS. The Thermal Emission Imaging System (THEMIS) seeks to determine the distribution of minerals on the surface of Mars by imaging the planet in the visible and infrared. The Mars Radiation Environment Experiment (MARIE) studied the radiation environment of Mars until October 28, 2003 when a large solar particle event damaged a computer chip on the MARIE computer board rendering the instrument unable to collect further significant data (Viotti et al., 2005a). The third instrument suite, the Gamma Ray Spectrometer (GRS), contains within it the Gamma Subsystem (GS), the Neutron Spectrometer (NS), and the High Energy Neutron Detector (HEND). As the name implies, the GS uses gamma ray spectrometry to determine the abundance and location of up to 20 chemical elements at/near the surface of Mars. Besides using changes in the observed intensity of hydrogen gamma ray flux to monitor the carbon dioxide seasonal frost activity, the verification of hydrogen in the shallow subsurface has been critical to the investigation of the amount and distribution of water-ice (Viotti et al., 2005a). The NS and HEND work in parallel with the GS by measuring variations in the flux of neutrons of multiple energy ranges. Using neutrons, it is also possible to calculate the abundance of hydrogen on Mars to infer the presence of frozen water. The neutron detectors are sensitive to concentrations of hydrogen in

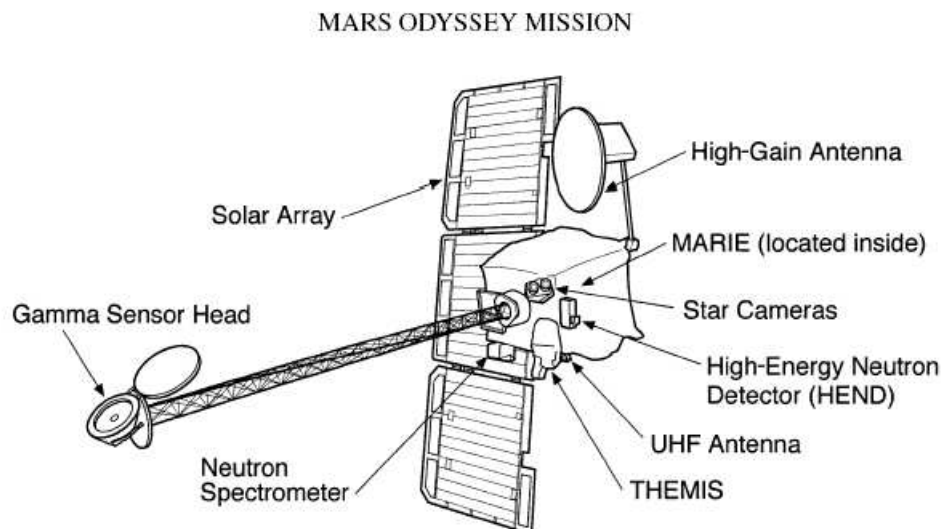


Figure 3.1: 2001 Mars Odyssey spacecraft in mapping configuration. The spacecraft consists of a central spacecraft bus with the gamma sensor head extended on a 6-meter boom. The solar arrays provide electrical power, and the high-gain antenna is pointed toward Earth. The GRS instrument suite includes the GS, the NS, and the HEND. The MARIE and nadir-pointing THEMIS instruments are also depicted (Saunders et al., 2004).

the upper meter of the surface (Boynton et al., 2004a). More specific details about the operation of the GRS instruments can be found in following sections.

A diagram of the 2001 Mars Odyssey satellite (Figure 3.1) shows articulated solar arrays, the high-gain and UHF antennae, and the gamma sensor head, which is displaced from the spacecraft body by a 6-meter boom to minimize the interception of interfering gamma rays coming from the satellite itself. All other science instruments are located on the spacecraft bus. The low-, medium-, and high-gain antennae provide communications with Earth, and the solar arrays provide the necessary electrical power (Saunders et al., 2004).

Odyssey's primary science mission took place from February 2002 through August 2004. The first extended mission for the satellite began on August 24, 2004 (Viotti et al., 2005a), and the orbiter is expected to participate in at least a second extended mission time period of one Martian year (approximately two Earth years)

Table 3.1: 2001 Mars Odyssey Mapping Orbit Details and Parameters.

Launch	April 7, 2001
Mars Arrival	October 24, 2001
Aerobraking	Nov. 2001 - Jan. 2002
Start of Mapping	February 18, 2002
1 <sup>st</sup> Detector Annealing	March 9 - 12, 2002 (50°C)
2 <sup>nd</sup> Detector Annealing	May 7 - 18, 2002 (72°C)
GRS Boom Erected	June 4, 2002
Index Altitude	392 km
Semi-Major Axis	3785 km
Inclination	93.2°
Eccentricity	0.0115
Orbit Period	1.964 hr
Longitude of Ascending Node	173.7°
Argument of Periapsis	268°
Solar Beta Angle	-54.5° to -80°

after completion of the first.

Table 3.1 gives details about Mars Odyssey’s voyage to Mars and about specific orbital parameters and science mapping configurations. For further information and an in-depth description and discussion of these topics, see the *2001 Mars Odyssey Mission Summary* by Saunders et al. (2004).

### 3.1.2 Objectives and Significance

“The name *2001 Mars Odyssey* was selected as a tribute to the vision and spirit of space exploration as embodied in the works of renowned science fiction author Arthur C. Clarke. Evocative of one of his most celebrated works, the name speaks to our hopes for the future and of the fundamental human desire to explore the unknown despite great dangers, the risk of failure and the daunting, enormous depths of space” (Viotti et al., 2005a).

As a whole, Mars Odyssey has been extremely successful in furthering NASA’s

Mars Exploration Program and its overall science goals. Under the theme “Follow the Water”, the strategy revolves around discovering if there has ever been life on Mars, characterizing the climate and geology of Mars, and undertaking investigations that will prepare for human exploration of the planet. Specific scientific objectives of the mission are to use the GRS to map the elemental composition of the surface on a global scale, and as previously mentioned, to determine the extent of hydrogen in the shallow subsurface. The THEMIS instrument goals are to investigate the surface mineralogy by acquiring high spatial and spectral resolution images, as well as to observe details about the morphology of the Martian surface. Finally, the MARIE component helped to characterize the Martian near-space radiation environment, which will be useful in the determination of risk to possible future human explorers (Viotti et al., 2005a).

The gamma subsystem has made a significant contribution to the overall understanding of Mars. For the first time ever, the instrument has quantified and mapped the distribution of chemical elements and minerals in the martian regolith. The astounding confirmation of an abundance of polar water-ice in the upper few tens of centimeters of the surface, as determined from the H gamma ray signal, occurred very soon after the spacecraft’s arrival at Mars. The *New York Times* was one of the first to announce, “Scientists see signs of water, a crucial ingredient of life” (March 2, 2002), and *Discover* magazine named the finding 6<sup>th</sup> out of the 100 top science stories in 2002 (Special Issue: The Year in Science, 2003). For the actual results as published in *Science*, see Boynton et al. (2002b), Feldman et al. (2002b), and Mitrofanov et al. (2002a). The spacecraft globally mapped many elements, but it is mainly this strong hydrogen signal that allows this current work on quantifying the seasonal polar CO<sub>2</sub> through attenuation effects.

Besides being the first chemical mapper at the planet, the satellite has aided in astrophysical investigations about gamma ray bursts (GRBs), the extra-galactic gamma ray background, solar processes, and the space radiation environment in low Mars orbit. It has also played (and continues to play) a crucial role in other exploration missions by providing a communications relay for Spirit and Opportunity,

the Mars Exploration Rovers, currently roaming the surface of the planet. Up to this point, Mars Odyssey has actually transmitted over 85% of the rovers' data to Earth. It will also support telecommunications of future lander missions, as well as assist in providing data to determine the landing sites for these upcoming endeavors (Viotti et al., 2005a).

In its extended mission(s), Mars Odyssey is advancing many important projects. It will allow scientists to continue to map and study chemical elements and minerals in the Martian regolith and to further investigate and quantify the vast amounts of water-ice buried in the polar regions. This will also make it possible to better constrain and understand interannual variations in the seasonal CO<sub>2</sub> cycle over multiple Martian years.

### 3.1.3 GRS Instrumentation: Gamma Subsystem (GS)

Most instruments used for detecting nuclear radiation operate in similar ways. Usually, the radiation enters the detector, where it interacts with the atoms of the detector material and loses part or all of its energy. In this process, a large number of relatively low-energy electrons are released from their atomic orbits. By collecting these released electrons, a voltage or current pulse can be created and analyzed by electronic circuitry. The type of radiation that is being detected, as well as what information about the radiation is desired, determines the material used in the detector (Krane, 1988). To be able to measure the energy of the radiation (as is done on Mars Odyssey), it is necessary to use a detector in which the amplitude of the output pulse is proportional to the energy of the radiation. There are many other factors to consider during detector selection and design, such as: if unusually high counting rates are expected, the detector needs to be able to recover quickly from one radiation strike before counting the next. Conversely, for low counting rate situations, the detector should ideally be able to count every event, while the influence of any background radiation must be reduced.

For the above purposes, the GRS system contains the Gamma Subsystem developed in the Lunar and Planetary Laboratory (LPL) of the University of Arizona.

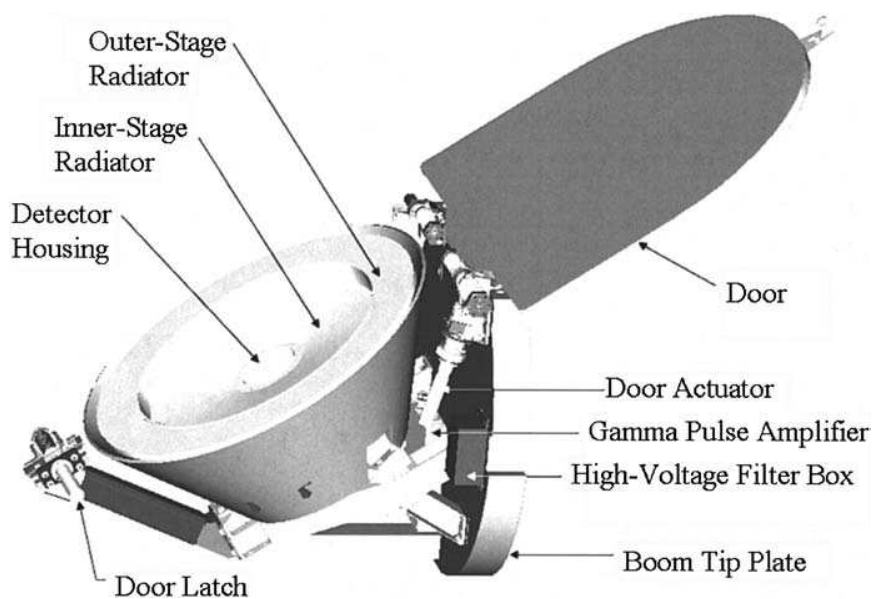


Figure 3.2: Drawing of the GRS gamma sensor head (Boynton et al., 2004a).

This Gamma Ray Spectrometer consists of a 1.2 kg (67 mm x 67 mm), passively cooled high-purity n-type germanium (Ge) crystal mounted 6 m from the orbiter on the end of a boom. For science data collection, a cooler door is opened to expose a radiator allowing the sensor to passively cool to below 90 K. Spectrometry of gamma rays emitted from Mars in the energy range of 130 - 10,000 keV occurs when an electric charge from a high-energy particle strike is measured, amplified, and digitally converted into one of  $2^{14}$  (16,384) channels, from which a histogram (gamma spectrum) is eventually created. The Mars Odyssey spacecraft is in a nearly polar orbit with an inclination of  $86.9^\circ$ . Because the GRS observes a relatively large area due to the instrument's gamma ray energy-dependent spatial resolution of approximately 360 - 450 km in diameter (from which 50% of the signal is received), the instrument accumulates about six hours of data per each region near the equator and on the order of five times more near the poles (Boynton et al., 2004a).

The spatial resolution of the GRS is important for mapping the elements and the  $\text{CO}_2$  on Mars. Since different types of reactions produce gamma rays with different depth distributions, the detector spatial resolution for a planet with no atmosphere

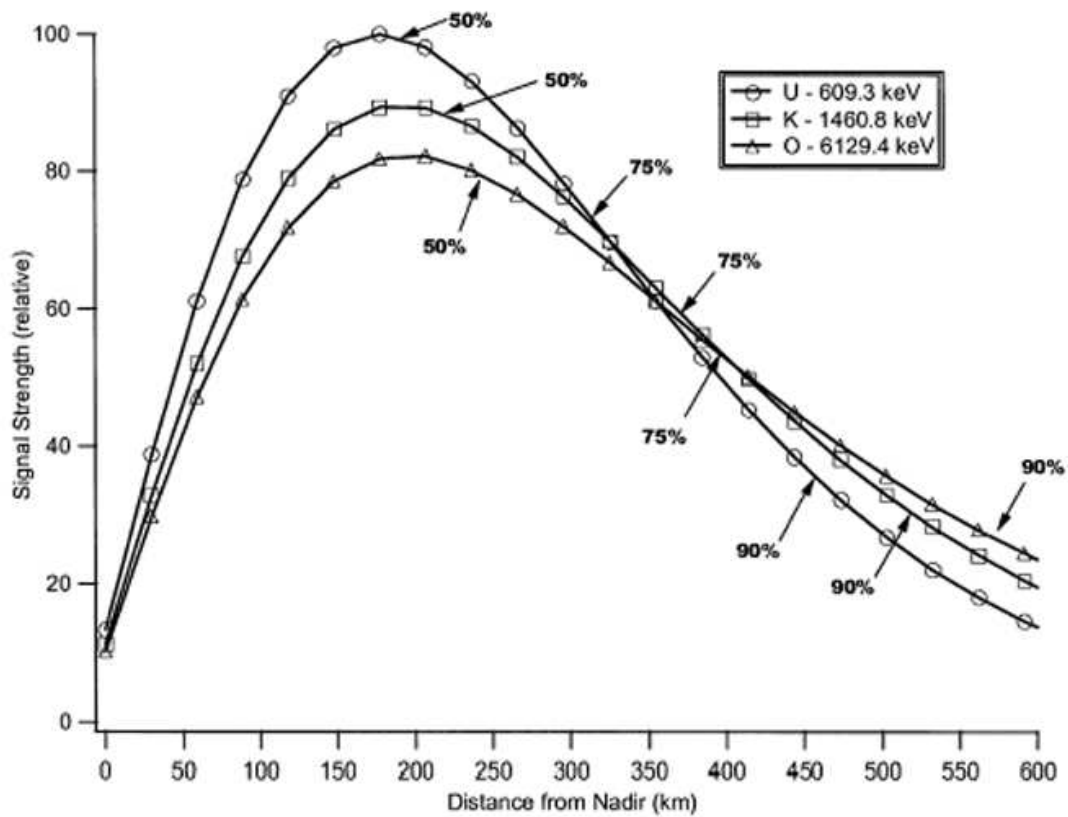


Figure 3.3: Gamma ray signal intensity as a function of distance from nadir for three different gamma ray energies. The K gamma ray signal at 1461 keV is most relevant to this seasonal CO<sub>2</sub> research. The distances from inside of which are collected 50%, 75%, and 90% of the signal are as indicated. This diagram was generated by Boynton et al. (2004a) for a nominal Mars atmospheric thickness of 15 g/cm<sup>2</sup> and a spacecraft altitude of 400 km.

varies slightly with the type of reaction producing the gamma ray (Reedy et al., 1973). The gamma rays from Mars are, in general, detected from the range of horizon to horizon, and the GRS is roughly equally sensitive to gamma rays incident from all directions (Boynton et al., 2004a). The signal intensity varies as a function of distance from nadir (the sub-spacecraft point) for differing gamma ray energies. For a planet with atmosphere, the signal increases as the distance from nadir and the area in the corresponding annulus of observation increases, until attenuations effects (as the gamma rays travel through greater regolith and atmospheric path lengths) dominate and decrease the signal intensity. These trends can be seen for three gamma ray energies including the 1461 keV,  $^{40}\text{K}$  signal in Figure 3.3. Boynton et al. (2004a) approximate the radius of the spatial-resolution circle below the detector as about one-half of the satellite's altitude above Mars' surface. Collimation effects due to Mars' atmosphere as discussed in Section 2.4.4 also occur. Spatial resolution increases with thicker atmosphere as the area from which the detector receives most of the gamma rays decreases.

### 3.1.4 GRS Instrumentation: Neutron Spectrometer (NS)

The Neutron Spectrometer (NS), which was built by Los Alamos National Laboratory (LANL), is another instrument in the suite onboard Mars Odyssey. The neutron results are used as a comparison and to enhance gamma ray observations. The Mars Odyssey NS detector consists of a cubical block of boron-loaded plastic scintillator which is segmented into four optically isolated, prism shaped quadrants. Each quadrant is viewed by a 3.8 cm (diameter) photomultiplier tube (PMT), and to block thermal neutrons coming from the ends of the prisms, cadmium sheets are employed as shields. The downward-looking prism utilizes an identical cadmium shield so that it responds to epithermal and fast neutron ranges (energies larger than approximately 0.4 eV) (Boynton et al., 2004a).

Through elastic scattering collisions, neutrons entering the detector lose energy to the carbon and hydrogen nuclei that comprise the scintillator. The similar mass of protons and neutrons (and the fact that the scattering cross-section for (n,p) is

about four times greater than that for  $(n,^{12}\text{C})$  at low energies) allows for most of the neutron energy to be lost to proton recoils, which produce multiple ion-electron pairs as the protons slow down in the scintillator. The ion-electron pairs eventually recombine to create photons that produce pulses of charge when collected by the PMTs. A histogram is generated when the neutron detector analog electronics amplify and digitize these photon pulses (Boynton et al., 2004a). The signatures of thermal, epithermal, and fast neutrons in the scintillator can be analyzed, and the counting rates from each of the quadrants are used to determine observed neutron fluxes. Thermal and epithermal components are separated using a Doppler-filter technique along with the relative counting rates of the forward- and backward-facing prisms (Feldman and Drake, 1986).

### 3.1.5 GRS Instrumentation: High Energy Neutron Detector (HEND)

The High Energy Neutron Detector (HEND), constructed by Russia's Space Research Institute (IKI), is an additional instrument that works in parallel with the other detectors on the Mars Odyssey spacecraft. Developed in Moscow, Russia, the HEND contains a set of five electronics boards and sensors: three detectors with  $^3\text{He}$  proportional counters and two scintillators in a scintillation block. Three separate signals are produced by the proportional counter detectors. The detectors are: the Small Detector (SD), which is most sensitive for neutrons in the energy range 0.4 eV - 1 keV, the Medium Detector (MD), which observes neutrons with energies from 0.4 eV - 100 keV, and the Large Detector (LD), which is most sensitive for neutrons in the range 10 eV - 1 MeV. The scintillation block includes an internal and external scintillator. The internal component utilizes a PMT and a stylybene crystal in which high energy neutrons produce recoil protons. These proton-based counts fall in the energy range from 800 keV to 15 MeV. Although the stylybene is also sensitive to gamma ray photons from 60 keV - 2 MeV, the HEND analog electronics separates proton-based counts (resulting from neutron flux) from electron-based counts (arising from gamma ray photons). For detection of gamma rays and charged particles above 30 keV, the external scintillator contains a PMT and a CsI crystal.

The three detector signals along with the two internal signals and one external signal from the scintillators are digitized into 16 energy channels. The time intervals over which these energy spectra can be accumulated vary from 12 seconds to one hour; however, the accumulation times are usually synchronized to be the same as for the rest of the GRS (Boynton et al., 2004a).

### 3.1.6 Central Electronics Box

The Central Electronics Box (CEB) is a fourth component within the GRS instrument suite. Mounted on the bottom of the instrument deck inside the spacecraft, it contains the power supplies, the main amplifiers, the analog-to-digital converters (ADCs), the GS and NS pulse-height analyzers (PHAs), and the central processing units and memory (Boynton et al., 2004a). The PHAs count each photon that the detector sees and generate spectra by creating histograms of the number of events in each energy channel. The count rates within the GS are monitored by several counters, such as the lower-level discriminator (LLD) and the upper-level discriminator (ULD). These components act to determine the minimum and maximum energies that the ADC will convert. In this way, off-scale noise is removed because the ADC will only digitize events that fall within a select range of appropriate values. The CEB also collects temperature, voltage, current, and other engineering data from the GS and NS. The information is then used for diagnostic purposes like correcting for temperature drift within the GRS, as described in Boynton et al. (2004a).

## 3.2 Mission Operations and Reduction of GRS Data

### 3.2.1 Overview

The process by which we go from counts in the GRS instrument (Boynton et al., 2004a) to elemental concentrations on the surface of Mars (Boynton et al., 2006b) and then from concentration variations to seasonal carbon dioxide frost columnar thickness is complicated. The flux of gamma rays (as well as neutrons) depends

on the subsurface composition of the regolith, and in general the signal is detected from a median depth of approximately 20 g/cm<sup>2</sup>. Most relevant to this study, the emission depth for H gamma rays at 2223 keV is 19 g/cm<sup>2</sup>, which is 13 cm assuming a regolith bulk density of around 1.5 g/cm<sup>3</sup>. For further details on gamma ray emission intensities, see Kim et al. (2006). Every 19.2 seconds, the GRS returns a gamma ray spectrum (along with several neutron spectra) collected along 59 km of orbital arc, or one degree of motion, over the surface of Mars. Statistics are improved by binning the data over regions of interest. Since converting from gamma ray counts directly to surface concentrations is not possible, a series of forward calculations are performed that predict expected gamma ray counts based on a priori assumed planetary abundances and atmospheric thicknesses as a function of time and location. These model results, which take into account many production, transmission, attenuation, and conversion factors, are compared to observed results to derive a measure of elemental concentrations on Mars. Further details can be found in Section 3.2.3 and Appendix A.

### 3.2.2 Spectral Analysis

The GRS observes around 290 spectral peaks and features while detecting gamma ray spectra from Mars and from the material around the detector itself. As discussed in Chapter 2, the associated gamma rays arise from nuclear interactions between Mars' surface materials and cosmic ray particles, and from the decay of naturally radioactive species (Reedy et al., 1973; Reedy, 1978; Evans et al., 1993; Masarik and Reedy, 1996). For scientific investigations, the energy resolution ( $\Delta E/E$ ) is an important factor and is standardly quantified by the full-width at half maximum (FWHM) and/or the full-width at tenth maximum (FWTM) of the <sup>60</sup>Co peak at 1332 keV (Evans et al., 2006). These parameters tend to degrade over time because of the interactions between the detector crystal and high-energy solar and galactic particles (Brückner et al., 1991). Radiation damage from charge trapping in the Ge crystal can cause low-energy tailing in the observed spectral peak. In these cases, the FWTM is the best indication of the amount of degradation. The GRS detector

goes through an annealing process, when necessary, to improve its energy resolution and bring it back to a level close to the launch value. The reference FWHM was 4.1 keV and the FWTM was 9.9 keV at the start of mapping in June 2002 after Mars Odyssey reached the planet, the spacecraft's boom was extended, and the detector was annealed (Evans et al., 2006).

For accurate geochemical analysis, it is crucial to identify and remove gamma ray interferences and background signals. Details about this complex process as relevant to the H and  $^{40}\text{K}$  gamma rays used for this seasonal  $\text{CO}_2$  study can be found in Section 3.2.4. There are also other issues that arise when using gamma ray spectrometry to measure elemental abundances. Orbiting instruments such as the GRS are photon limited and require numerous hours of data to increase spectra counting statistics to a level sufficient for peak analysis. The GRS count rates are  $\sim 190 \text{ s}^{-1}$ , but because more than 96% of these counts are in the continuum rather than in discrete line peaks, spectral summing is necessary (Evans et al., 2006).

When summing spectra, the gain and offset of each spectrum, which are affected by the temperatures of the electronic components within the GRS, must be corrected to a common energy scale. A family of temperature curves were independently generated for various GRS components to characterize their temperature dependence in order to make these corrections. In addition, bad or questionable data collected during solar particle events, active solar flares, and the satellite's non-nadir-pointing periods must be flagged and excluded from all sums. Unstable high voltage, gain shifts, and large temperature shifts in the instrument are also conditions for the removal of certain data. Finally, the GRS's field-of-view (FOV) and the spacecraft's latitude and longitude in relation to the planet (provided by the navigation team at NASA's Jet Propulsion Lab) must be taken into account during spectral summing in order to map the elemental abundances accurately (Evans et al., 2006). The GRS's limb-to-limb FOV at an altitude of 400 km is  $26.5^\circ$  of arc on the Mars surface; however, overall processing time is reduced by a factor of 2 by summing only within a  $17^\circ$  angle from which comes 99% of the gamma ray signal.

The resulting gamma ray spectra are available through the GRS data processing

system via a query tool, which sums calibrated data in numerous ways such as: over selected latitude and longitude grids, for selected time intervals, for regions defined by compositional variations, or over predefined standard regions as small as the Hellas basin or Tharsis Montes to as large as the entire planet. The entire Mars spectrum has the best statistics because it has the largest accumulation time, which began immediately after boom-deployment. This allows the analysis of small and weak peaks and includes time variations like the seasonal changes at the Martian poles. Figure 3.4 shows this entire Mars spectrum. Since the spectrum intensity range varies over a factor of 1000, more detail concerning the naturally radioactive  $^{40}\text{K}$  and neutron-capture H peaks can be seen in Figure 3.5.

A relatively-smoothly varying continuum accounting for around 96% of the gamma ray counts can be seen below the distinct peaks in the figures. To analyze the peaks, it is critical that this background continuum is correctly identified and not calculated into the peak areas. The scattering of gamma rays escaping Mars, bremsstrahlung of charged particles in matter, weak gamma rays, and cosmic gamma rays all contribute to the observed continuum.

The spectral peaks are usually narrow with a finite width inherent to the detector, although other features and shapes can be identified. A standard peak has a Gaussian shape with approximately exponential-shaped low-energy tailing caused by electron-hole pairs trapped in the detector after radiation damage (Brückner et al., 1991). In general, the peak widths tend to increase slowly and systematically as a function of energy. The FWHM values range from about 3 - 16 keV, and the possibility of overlapping peaks increases as the widths (and energy) increase (Evans et al., 2006).

Doppler broadening occurs when gamma rays are emitted while the associated nucleus is still in motion during de-excitation. This happens for excited levels with lifetimes less than  $\sim 0.5$  ps and for gamma rays created during nonelastic-scattering reactions in Mars' low density atmosphere because the nuclei stop slowly relative to the gamma ray emission time. The average energy of Doppler broadened peaks is usually shifted to a slightly higher energy since most neutrons involved in the



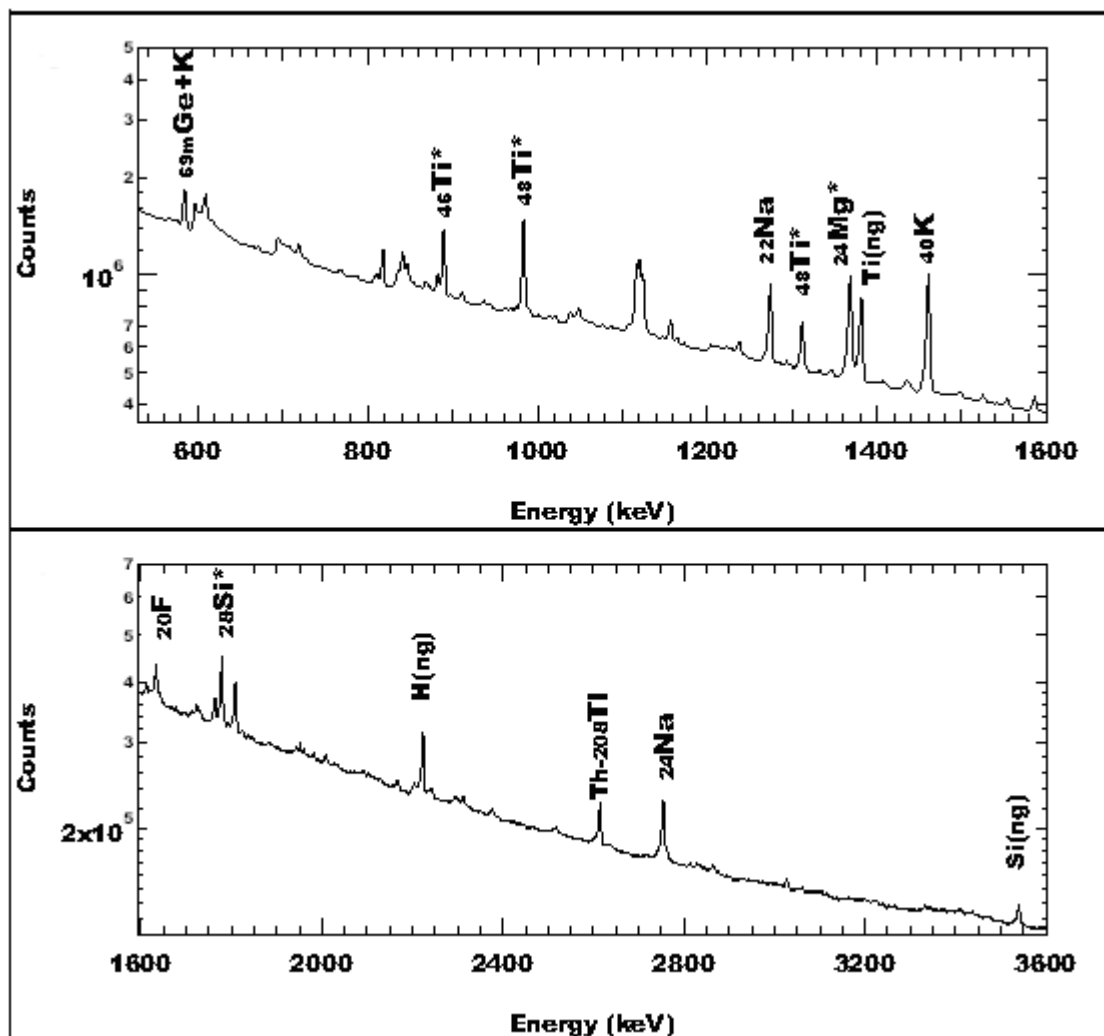


Figure 3.5: Details of the entire Mars spectrum shown in Figure 3.4. The top spectrum from 530 keV to 1600 keV shows the naturally radioactive, 1461 keV  $^{40}\text{K}$  peak. The bottom spectrum from 1600 keV to 3600 keV includes the neutron-capture H peak at 2223 keV. Some of the other prominent gamma ray peaks not used to quantify the polar  $\text{CO}_2$  are also labelled. Spectral peaks from Ge, Ti, and Mg from materials in and surrounding the detector itself are also apparent (Evans et al., 2006).

process are travelling upwards away from Mars' surface (and toward the detector). There are even a few gamma rays broadened because of the uncertainty principle when the half-lives of levels from which they are emitted are exceedingly short. (For example, the  $^{12}\text{C}$  spectral peak at 4438 keV has a  $\sim 41$  fs half-life and is  $\sim 200$  keV wide (Evans et al., 2006).)

Although not often seen in GRS spectra, a Compton edge is the energy below which occurs a continuum of counts created by Compton scattering of gamma rays in the detector. Single- and double-escape peaks are observed when gamma rays with energies above 1022 keV undergo pair production. The electron and positron usually stop in the Ge detector, and the positron annihilates with an electron to produce two 511 keV gamma rays that can escape. Spectral peaks are created at energies of 511 or 1022 keV less than the primary gamma ray depending on whether one or both of the 511 keV gamma rays escape. Irregularly shaped peaks that appear roughly Gaussian in shape with a slowly decreasing tail at higher energies are called sawtooths. They occur when fast (MeV) neutrons interact with Ge nuclei in the detector and the de-excitation energy is summed with the recoil energy of the Ge nucleus (Brückner et al., 1987).

In order to get information about the abundances of various elements on Mars, the areas of the spectral peaks must be determined. The most straightforward method is to set a lower and upper bound at the edges of an observed peak and draw a line connecting these points to delimit the background continuum. The counts within the defined area inside the peak are then calculated. This technique is highly effective for stand-alone peaks, but becomes more troublesome when peak shapes are created by multiple overlapping spectral lines added together.

Software programs exist to fit peaks to a predetermined analytic shape, such as a Gaussian with a low energy tail (Phillips and Marlow, 1976). Some programs that analyze Ge gamma ray spectra both detect specific peaks and determine the associated peak areas. Others require a user to interactively fit a peak and determine how much above the background it must be to be considered significant. Because peak fitting software often assumes peak widths equal to precalculated values or that

all peaks in a region have the same width, special analysis routines were developed at the University of Arizona Lunar and Planetary Laboratory (UA/LPL) using WaveMetrics' Igor Pro software to evaluate spectral regions in which both narrow and broadened peaks occur (Hamara, 2003). This is useful for measuring the H peak at 2223 keV because it falls in an energy region that contains 3 narrow and 2 broadened peaks. Figure 3.6 shows this region and the 5 important peaks that sum to give the observed complex spectral signature.

Once the spectral peaks are fit, it is important to correctly identify their sources. Numerous approaches are used with the GRS spectra to minimize incorrect identifications. The team consults publications from accelerator experiments on Earth and from other spacecraft missions involving similar planetary or Earth-facing satellite detector systems. Nuclear data libraries and search engines such as Brookhaven National Laboratory's National Nuclear Data Center (NNDC) are helpful to research radionuclides and excited nuclear levels. The decay of naturally radioactive elements should also produce gamma rays peaks that change in such a way as to be consistent with their known half-lives. Gamma ray lines from material near the GRS or onboard the spacecraft can be compared to data gathered during the cruise period when the satellite travelled to Mars.

An additional identification aid is to check that certain gamma rays attenuate as expected in spectra collected over the Martian poles while seasonal CO<sub>2</sub> frost is present. This attenuation of <sup>40</sup>K can be seen in Figure 3.7 where non-frosty regions are compared to seasonal-frost-covered areas. It is interesting to note that as the condensed CO<sub>2</sub> creates a decrease in the observed naturally radioactive K signal, the neutron-capture Ti line at 1382 keV increases because the CO<sub>2</sub> at the poles is very effective at moderating fast neutrons to thermal levels (and therefore promoting capture reactions). The fact that the K peak does not disappear completely during the winter period when it should be completely attenuated suggests that there are interference lines near 1461 keV. These will be discussed in detail in Section 3.2.4.

Of the 290 discrete gamma ray spectral peaks observed during the GRS mission, all but 8 have a tentative identification listed in Evans et al. (2006), and ~55 of the

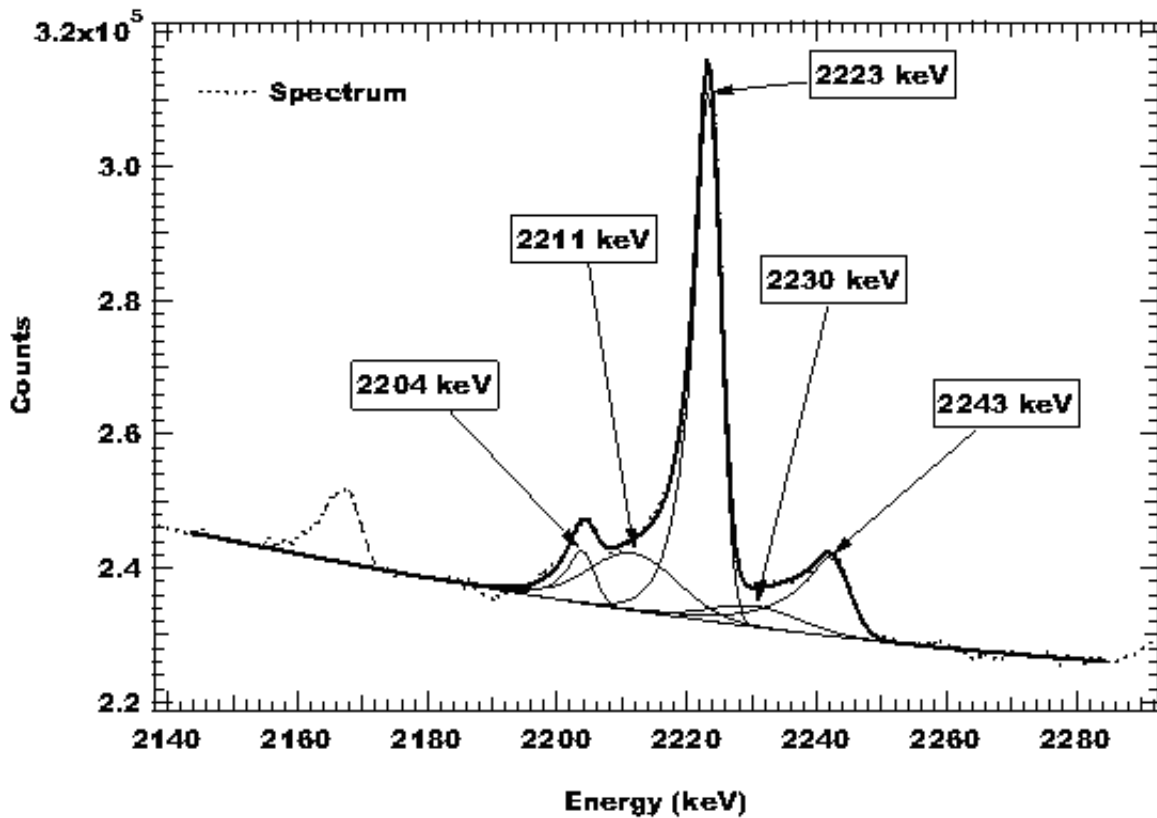


Figure 3.6: Spectral peak fitting of five peaks in the region of 2223 keV hydrogen (Evans et al., 2006). This complex energy region has 3 narrow peaks and 2 Doppler broadened peaks at 2211 keV and 2230 keV. The 2204 keV peak is from U- $^{214}\text{Bi}$ , the 2211 keV peak is from  $^{27}\text{Al}$ , the 2230 keV peak is from  $^{32}\text{S}$ , and the 2243 keV peak is from single-escape  $^{24}\text{Na}$  and  $^{24}\text{Mg}$ . The straight downward-slanted line at the base of the peaks delimits the underlying background continuum.

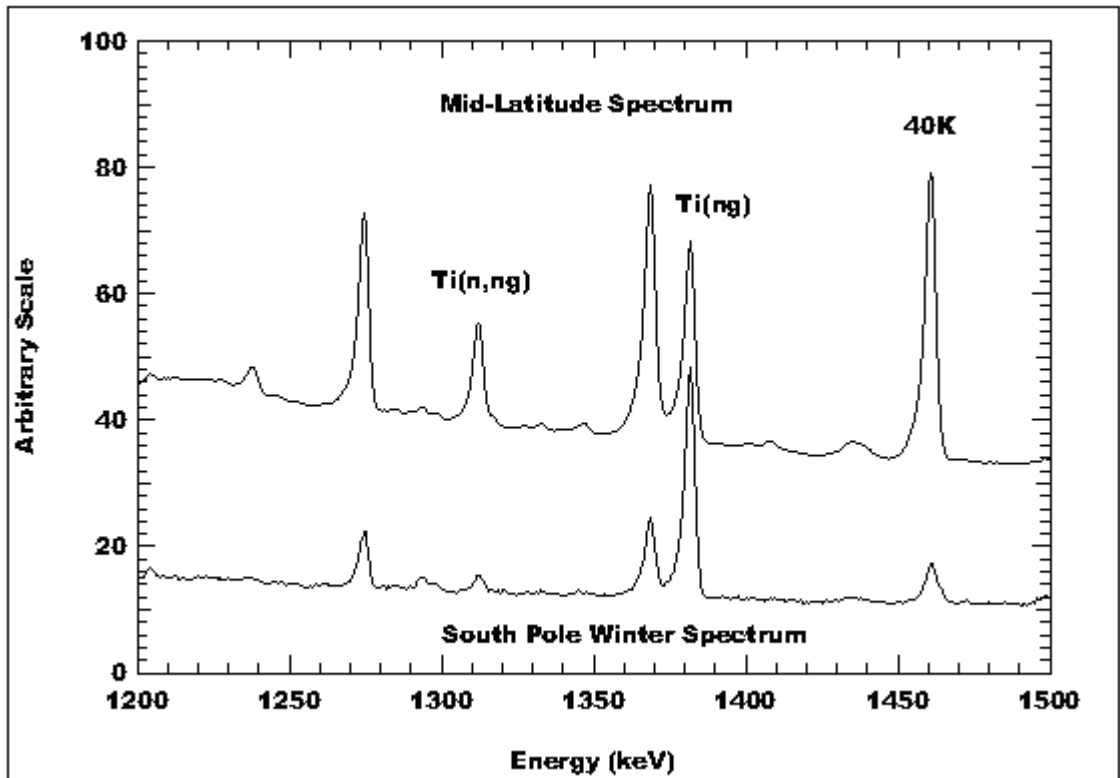


Figure 3.7: Comparison of the south polar (85°S to 90°S) winter spectrum with a frost-free mid-latitude spectrum. The vertical-axis intensity scale is adjusted to facilitate the comparison (Evans et al., 2006). Note the attenuation of the  $^{40}\text{K}$  peak at 1461 keV, but the increase in the 1382 keV neutron-capture Ti peak because of the effectiveness of the seasonal  $\text{CO}_2$  in thermalizing fast neutrons.

peaks are used to determine the elemental distribution and composition of Mars. Many secondary weak peaks are not necessary for chemical mapping. In some cases, the peaks are so weak that the associated high uncertainty requires more accumulation time to improve statistics, as may be possible during future extended missions. The current GRS spectrum has the best statistics of any spectrum taken around Mars up to this point, and all peak assignments are confirmed as best as possible through tests and checks as mentioned above.

### 3.2.3 Forward Processing

After analyzing the GRS spectra to determine the gamma ray counts at various energies, the next step is to use this information to determine the corresponding elemental abundances on Mars. Unfortunately, spectral counts do not directly convert to surface concentrations, so a series of forward calculations must be performed. The forward calculations in this case predict the amount of gamma ray counts that the GRS would observe when specific elemental surface compositions and distributions are assumed. The model results can then be compared to actual GRS observations to calculate the true concentrations of various elements at Mars. Through the use of production constants, attenuation factors, and conversion factors, this procedure takes into account the production of gamma rays within the regolith, their transmission through the soil and atmosphere, and their detection and conversion to counts within the GRS (Boynton et al., 2006b).

For non-radioactive elements in these simulations, we employ a Monte Carlo N-Particle eXtended code (MCNPX) (Waters, 1999) to calculate the neutron flux distribution at depth in the Martian soil. Then, cross-section data is used to calculate the production of gamma rays as a function of depth, and we compute the attenuation of these gamma rays as they travel to the surface through the overlying soil. (Similar methods are described in Prettyman et al. (2002).) These predictive models initially assume surface concentrations based on the composition of the soil as measured by the Mars Pathfinder Alpha Proton X-Ray Spectrometer (APXS) (Wänke et al., 2001).

For gamma rays that are produced naturally by radioactive decay in the Martian regolith (e.g. potassium, thorium, uranium), gamma ray production rates and attenuation effects along the path to the spacecraft must be calculated to determine the flux at the detector as a function of regolith composition and spacecraft position. The production rate,  $P$ , for a given radioactive element depends on its quantity in the soil and other factors:

$$P = \frac{C \cdot R \cdot \lambda \cdot I_\gamma \cdot mf}{4\pi} \quad (3.1)$$

Where  $C$  is the number of atoms per gram of the element (Avogadro's number divided by atomic weight),  $R$  is the percent of the element (by number) that is the radioactive isotope,  $\lambda$  is the decay constant of the isotope in  $\text{sec}^{-1}$  ( $\ln(2)$  divided by the half-life),  $I_\gamma$  is the fraction of decays that yield the relevant gamma ray (intensity), and  $mf$  is the mass fraction of the element in the Martian regolith.  $P$  is in units of (number of photons)/(sec)/(gram of regolith)/(steradian). Isotope fractions, half-lives, and intensities are as listed in Firestone (1996), and the mass fractions are taken from Laul et al. (1986); Wänke et al. (2001); Boynton et al. (1992).

Gamma rays produced in the soil at rate  $P$  are attenuated as they proceed toward the GRS along a path length,  $z$ . The attenuation coefficient,  $\mu$ , associated with the regolith is determined from Berger et al. (1998). Assuming a one-layer model (a single regolith composition) modelled as an infinite half-space (Figure 3.8), the integral of the production and attenuation from the surface to an infinite depth gives the flux of photons,  $F$ , leaving the Martian surface toward the spacecraft:

$$F = \int_0^\infty P e^{-\mu z} dz \quad (3.2)$$

Substituting  $u = \mu z$ , Equation 3.2 evaluates to:

$$F = \frac{P}{\mu} \quad (3.3)$$

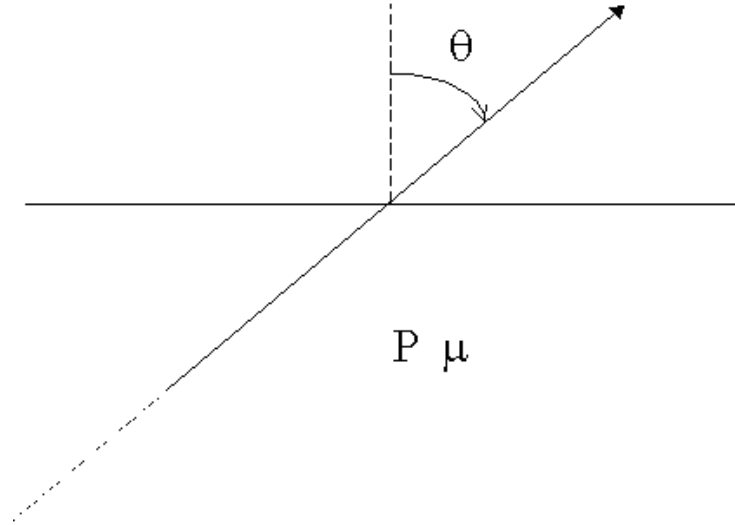


Figure 3.8: One layer regolith model geometry (Janes, 2002).

Since for a homogeneous, infinite half-space photons leave the surface at the same rate in all directions, there is so far no dependence on geometry. The gamma ray flux toward the detector can be corrected for projection effects by:

$$F = \frac{P}{\mu} \cos(\theta) \quad (3.4)$$

The Martian regolith is more realistically modelled by a two-layer composition that simulates a dry, dusty layer over a more water-ice rich lower layer. For an upper layer thickness of  $T_1$ , and  $P$  and  $\mu$  variables as seen in Figure 3.9, the total flux leaving the surface is the sum of the fluxes from each of the two layers. The flux at the boundary where the two layers meet is described by Equation 3.3; however the flux at the surface due to the bottom layer will be further attenuated as it travels through the top layer of soil:

$$F_o = \frac{P_o}{\mu_o} e^{-\mu_1 z_1} = \frac{P_o}{\mu_o} e^{-\mu_1 T_1 / \cos(\theta)} \quad (3.5)$$

As in Equation 3.2, the gamma ray flux from the upper regolith layer can be found from:

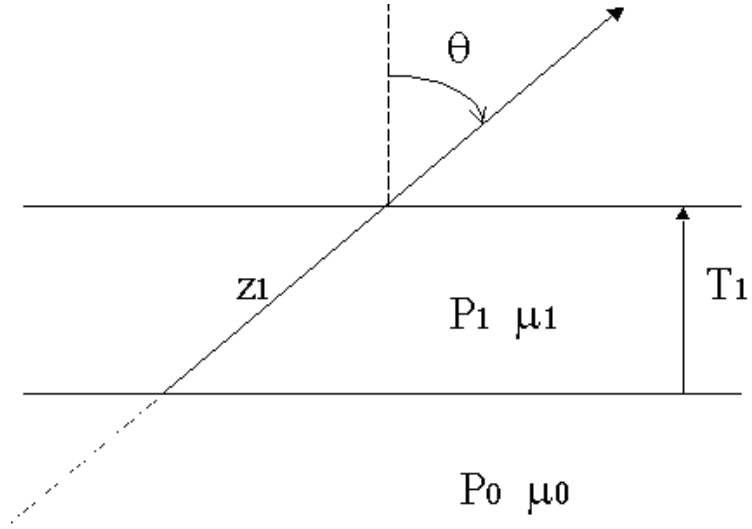


Figure 3.9: Two layer regolith model geometry (Janes, 2002).

$$F_1 = \int_0^{z_1} P_1 e^{-\mu_1 z} dz = \int_0^{T_1/\cos(\theta)} P_1 e^{-\mu_1 z} dz \quad (3.6)$$

Again substituting  $u = \mu z$ , Equation 3.6 becomes:

$$F_1 = \frac{P_1}{\mu_1} (1 - e^{-\mu_1 T_1/\cos(\theta)}) \quad (3.7)$$

Adding the contributions from both regolith layers (Equations 3.5 and 3.7) and correcting for projection effects, the total flux leaving the surface of Mars toward the satellite can be calculated from:

$$F_{tot} = \left[ \frac{P_o}{\mu_o} e^{-\mu_1 T_1/\cos(\theta)} + \frac{P_1}{\mu_1} (1 - e^{-\mu_1 T_1/\cos(\theta)}) \right] \cos(\theta) \quad (3.8)$$

For this GRS work, the resulting fluxes are calculated in increments of 0.05 units of  $\cos(\theta)$  and written to binary (.bin) files for use in the forward model.

For all gamma rays measured by the GRS (radiogenic or otherwise), the signal is assumed to come from a large footprint defined as the circular region on Mars

from which  $\geq 98\%$  of the signal (depending on gamma ray energy) would come when approximating the planet as a sphere with uniform atmosphere and no topography. Within each footprint, a grid of  $0.5^\circ$  cells is defined over the surface to allow the specification of various compositions, altitudes, and atmospheric thicknesses. We employ a model of the change in atmospheric thickness with time based on the NASA Ames Research Center Mars General Circulation Model (ARC GCM) version 1.7.1 to correct all gamma ray flux values for the predicted variations in the atmosphere. For further information on this model, see Haberle et al. (1999). The atmospheric column density in  $\text{g}/\text{cm}^2$  at 259,200 points on the  $0.5^\circ$  by  $0.5^\circ$  grid on the surface is calculated using altitudes from the latest Mars Orbiter Laser Altimeter (MOLA) topography. Temperature and pressure values are also calculated for each grid point for two times per Martian sol at 5 a.m. and 5 p.m. On the order of 10,000 cells are processed for each spectrum yielding *expected gamma ray counts*. We then compare measured counts to these predicted counts and determine relative concentrations for various elements as functions of latitude and longitude on the planet (Boynton et al., 2006b). For H and K, the equations to determine these relative elemental concentrations are as follows:

$$H_{conc} = \frac{\left[ (PA)_{Raw} - (PA)_{Bkg} \cdot \frac{(PA)_{Ti}}{1000} \right]}{Norm \ FpFs \ Counts} \cdot (mf) \cdot (cf) \quad (3.9)$$

$$K_{conc} = \frac{\left[ (PA)_{Raw} - (PA)_{Bkg} \cdot \frac{Time(sec)}{1000} \right]}{Norm \ FpFs \ Counts} \cdot (mf) \cdot (cf) \quad (3.10)$$

where the *conc* or *concentration* found here is actually relative gamma ray flux that has been corrected for atmospheric attenuation.  $(PA)_{Raw}$  stands for the raw peak area and is the number of gamma ray counts in the element's spectral peak for that time period.  $(PA)_{Bkg}$  is the satellite background radiation peak area, and it allows a subtraction for background radiation as discussed in Section 3.2.4. For H and other neutron-reaction-produced gamma rays, this background subtraction is based on the spectral peak area observed for titanium in the satellite,  $(PA)_{Ti}$ . For K and other naturally radioactive elements, the background subtraction is a

function of the time (in seconds) over which the data were summed to create the relevant spectral peak. The *Norm FpFs Counts* term represents the number of *expected gamma ray counts* in each peak, and these values are stored as an array of results calculated as explained above and in Appendix A. *mf* is the mass fraction (%) of the element in the Martian regolith taken from Laul et al. (1986); Wänke et al. (2001); Boynton et al. (1992) and is 3.001 for H (as H<sub>2</sub>O) and 0.5 for K in all calculations. Lastly, a correction factor, *cf*, is applied individually to every data group summed over 15° of L<sub>s</sub>. The origin and explanation of this varying correction factor are discussed in Section 3.2.5.

From these derived hydrogen and potassium concentration profiles, (more precisely, the relative atmosphere-corrected gamma ray flux), attenuation effects due to the seasonal CO<sub>2</sub> frost at the poles can be investigated, and the seasonal polar frost can be quantified in various ways.

### 3.2.4 Satellite Background and Other Interferences

The interactions that occur on the surface of Mars to create gamma ray emission also produce emission from the detector itself, the material surrounding the detector, and from the spacecraft, in general. These background emissions are produced from the same elements as are found on Mars and affect the calculation of both H and K flux used to quantify the CO<sub>2</sub> cycle. As discussed in Section 2.4.4, there can also be interference from Martian gamma ray signals of the same or similar energies, but from sources other than the element being studied. This complicates the process of classifying and separating spectral peaks for accurate geochemical analysis. This type of interference affects the K gamma ray measurements. It is crucial that the satellite-produced background gamma rays, the contributions from sources other than the element under investigation, and their intensities are identified and subtracted from the spectral peak measurements in order to obtain an accurate understanding of the composition of Mars.

The process of identifying and removing gamma ray interferences and background signals is complex. Unfortunately, these complications pertain to both the

H and  $^{40}\text{K}$  gamma rays used for this seasonal  $\text{CO}_2$  investigation. When hydrogen gamma rays are used to quantify the  $\text{CO}_2$  condensed on the ground, there is an uncertainty in the data reduction that results from the background signal of H gamma rays within the GRS instrument itself. If the H background is not well characterized, then the GRS data are only acceptable for determining relative  $\text{CO}_2$  thickness measurements throughout the year, but not for determining absolute  $\text{CO}_2$  columnar thickness values. This H background, like the H signal coming from Mars, depends both on the amount of H in the instrument and the local flux of thermal neutrons. The local flux of thermal neutrons varies from place to place above the planet, and also varies from time to time, especially in the polar regions because of the waxing and waning of the polar frost. The H content of the instrument obviously does not change with time, but the variation in thermal neutron flux at the instrument itself needs to be determined. This is done by measuring the number of counts in the 1382 keV spectral peak emission resulting from thermal-neutron capture of Ti in the GRS instrument. The contribution from Ti coming from Mars is very small but will be discussed below.

The hydrogen background is determined by assuming that during maximum  $\text{CO}_2$  frost depth over the south pole, the frost overburden is effectively infinitely thick relative to the H gamma ray signal, so gamma rays from the planet are completely attenuated. (The peak frost period at the south pole was chosen because a larger amount of condensed  $\text{CO}_2$  accumulates there than during the respective time in the north.) This assumption allows the determination of the H background signal from the spacecraft because any observed gamma ray flux during that time should necessarily come entirely from the satellite. This minimum in the H signal occurs in the south from approximately  $L_s = 165^\circ$  to  $210^\circ$  and can be seen best at the left side of Figure 4.3 (in Chapter 4) by the red line, which represents the last one-third of this period:  $L_s = 195^\circ$  to  $210^\circ$ . The background is then measured and calculated from this time period in units of H-counts/1000 Ti-counts. The background determined in this manner is really an upper limit to the true background, as a small percentage of the H flux still actually leaks through the frost and is transmitted from the planet.

This limiting value is  $39 \pm 3$  H-counts/1000 Ti-counts.

It is worth noting that a small fraction of the Ti signal (estimated at only a few percent of the frost-free signal) also comes from Mars. Over the winter poles when the signal-attenuating CO<sub>2</sub> is present, it is clear that the Ti signal from Mars is negligible so the limit to the H background discussed above does not need a correction. However, as is explained in Chapter 4, the frost columnar thickness is determined by comparing the ratio of Mars' signal with and without the seasonal frost. The signal without frost needs to be corrected for the background, and if there is a small amount of Ti gamma rays coming from the planet, it is possible to slightly over correct for the background since gamma ray counts are subtracted based on Ti from the instrument plus Ti from Mars. In the case that Ti from the planet is as high as 5% of the total Ti measured, the subtracted background signal would be too large by 5%. Luckily, in the polar regions, the frost-free H signal radiating from Mars is so large that the overall satellite background is not significant. In fact, when the frost is thinner than  $\sim 40$  g/cm<sup>2</sup>, reasonable variations in the background signal value become unimportant. Figure 3.10 illustrates this point using actual GRS CO<sub>2</sub> mass results at four times during the Martian year. These data are computed by applying a range of H background signal values to characterize the overall dependence of our measurements on this background signal. In the lower Martian latitudes where the flux of H gamma rays from the planet is very small, the precision of the H background measurement may need to be improved, but our current upper limit H background value discussed above is sufficient for the polar frost results determined and presented in this study.

Although this method gives a good upper limit to the H background signal, it is impossible to determine whether the background is any lower than this limit without having an independent determination of the frost depth. Using a lesser background value will lower the observed column density and mass of seasonal CO<sub>2</sub> frost on the ground, so the amount of frost calculated with the limiting background number above is an upper limit. However, it appears that this upper limit background number is probably close to the true value since the GCM (to which we compare

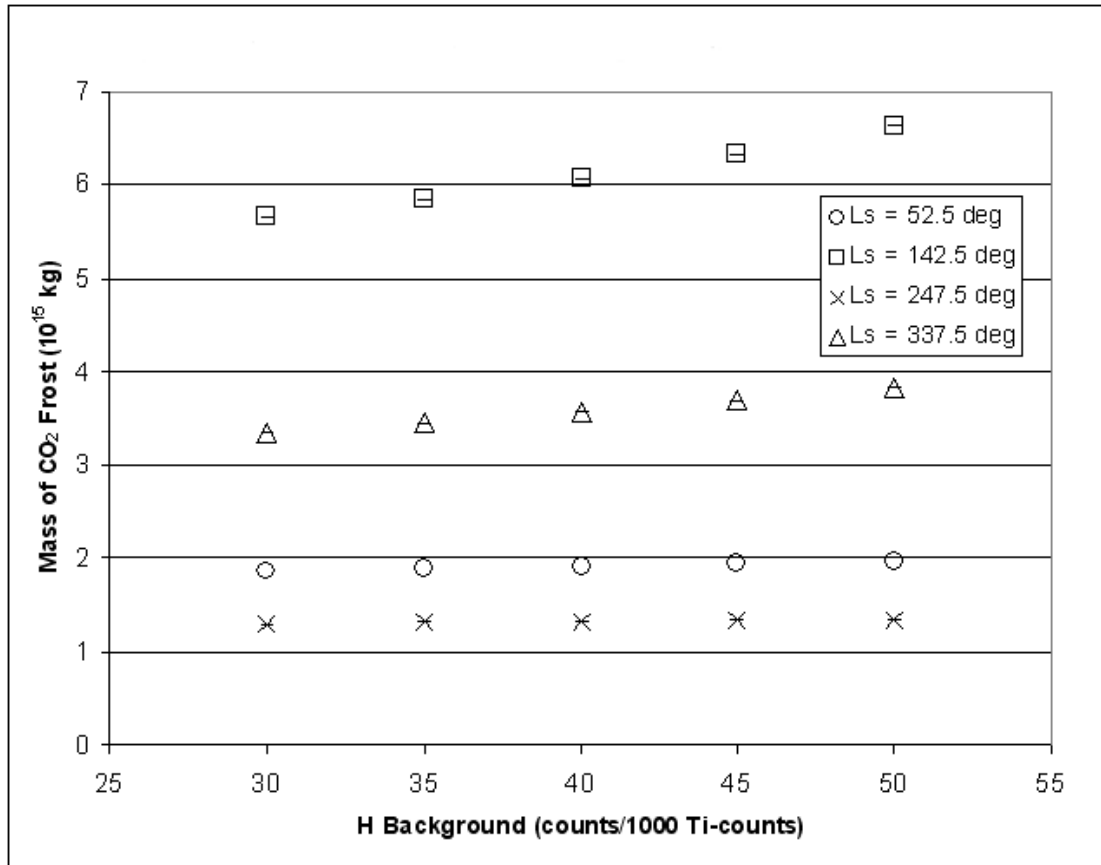


Figure 3.10: Mass of total CO<sub>2</sub> frost observed to condensed on the surface of Mars as a function of H background counts. Four times of the Martian year are shown (in degrees of L<sub>s</sub>). During times of less frost when the H gamma ray signal coming from the planet is larger, the CO<sub>2</sub> frost observations are nearly independent of the H background value. As the frost mass increases and the gamma rays from Mars are increasingly attenuated, the H background signal is relatively more significant and influences the frost measurements to a greater extent.

our results) actually predicts a greater mass than that calculated by the GRS when utilizing this upper limit to the satellite's H background.

In addition to the H gamma ray, I have also used the 1461 keV potassium-40 signal in this research. An understanding of all background contributions and other interfering gamma rays is necessary to get correct abundances of  $^{40}\text{K}$  and to infer the thickness and mass of the seasonal  $\text{CO}_2$  polar caps through attenuation observations. Currently, a  $^{40}\text{K}$  satellite background of  $40.10 \pm 0.55$  K-counts/1000 sec is subtracted based on the method described for the H background above. (Measure the contribution from the satellite using spectra taken over the winter poles when the thick seasonal  $\text{CO}_2$  cover should be opaque to gamma rays from Mars' surface.) However, Reedy (1978) cautions that studying  $^{40}\text{K}$  and  $^{40}\text{Ar}$  gamma rays is difficult because of interferences by other gamma rays of the same or nearly the same energy. The  $^{40}\text{K}$  gamma ray at 1461 keV is produced when  $^{40}\text{K}$  decays to the first excited level of  $^{40}\text{Ar}$ , which occurs for 10.6% of  $^{40}\text{K}$  decays. The same gamma ray can be produced by reactions with  $^{40}\text{Ar}$ , both by prompt inelastic-scattering reactions and by the decay of  $^{40}\text{Cl}$  made by (n,p) reactions with  $^{40}\text{Ar}$ .

A 1461 keV background interference was first noticed in the GRS data when spectral analysis showed a gamma ray signal at this energy during periods when the signal should have been completely attenuated by thick  $\text{CO}_2$  frost on the poles of Mars (similar to the small peak for the south pole winter spectrum seen in Figure 3.7). Investigation revealed that the unexpected gamma ray counts are produced by 1464 keV Ge thermal-neutron-capture reactions in the detector itself. There is also a contribution at certain times of the year from a line produced by inelastic scatter with argon in Mars' atmosphere. The  $^{40}\text{Ar}(n,ng)^{40}\text{Ar}$  reaction creates a Doppler-broadened peak at  $\sim 1466$  keV.

Since the Ge gamma ray signal coming from the detector is a neutron-capture line, data during times of high thermal neutron activity were summed to create a spectrum. This spectrum (Figure 3.11) shows the largest Ge peak that we would expect to observe. Peak 1 is the usual 1461 keV  $^{40}\text{K}$  peak, and peak 0 is the contributing Ge peak. Plotting the Ge peak area over time along with the Ti peak

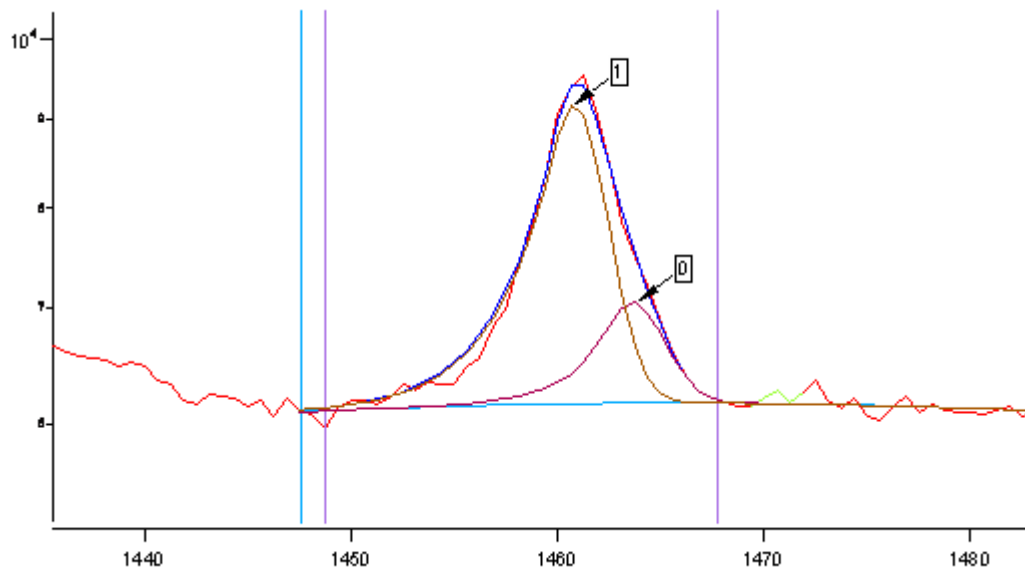


Figure 3.11: Interference at 1461 keV from Ge in the detector. This spectrum is created by summing data during periods of high thermal neutron activity to facilitate observation of the Ge peak at 1464 keV (peak 0). The fit to the  $^{40}\text{K}$  peak at 1461 keV (peak 1) is in blue and can be seen to include the satellite background counts from thermal-neutron-capture Ge. The vertical axis represents gamma ray counts, and energy in keV is depicted horizontally along the baseline.

area resulting from thermal-neutron capture by titanium in the GRS sensor head made it clear that both gamma ray lines follow similar temporal behavior. The Ti peak is well-understood because it is used to normalize neutron-capture signals from other elements on Mars. This confirmed that there is a time-varying Ge contribution at 1464 keV coming from the detector that adds counts into the peak area measured at 1461 keV expected to be from naturally radioactive  $^{40}\text{K}$  at the surface of Mars.

Argon in Mars' atmosphere is non-condensable and becomes enriched over the southern pole when the atmospheric  $\text{CO}_2$  condenses to form the southern seasonal frost cap. Sprague et al. (2004, 2006) has used GRS data to show that during the southern winter, atmospheric Ar is enhanced by up to a factor of 6. The unexpected excess 1461 keV  $^{40}\text{K}$  signal observed during this time is plotted in Figure 3.12 as a function of time (degrees of  $L_s$ ) along with the normalized Ar and scaled Ti count rates of the same time period. This shows that the excess K counts are actually more strongly related to atmospheric  $^{40}\text{Ar}$  than to the thermal-neutron reactions in the detector as represented by the Ti curve.

The  $^{40}\text{Ar}(n,\text{ng})^{40}\text{Ar}$  reaction that creates 1461 keV gamma rays should lead to a Doppler-broadened peak because it takes place in Mars' low-density atmosphere. As Section 3.2.2 explains, Doppler broadening occurs when the nuclei involved are still in motion from an inelastic scatter reaction as the gamma rays are emitted. The GRS observes Mars atmospheric oxygen as a 70 keV-wide Doppler-broadened peak at 6129 keV from the  $^{16}\text{O}(n,\text{ng})^{16}\text{O}$  reaction. There are a few differences between Ar and O to take into account: The  $^{40}\text{Ar}$  nucleus is  $\sim 2.5$  times heavier than  $^{16}\text{O}$  and is made by neutrons with about half the energy of those making the 6129 keV gamma ray, so we would expect the Ar peak to be much narrower; however, the lifetime of the excited state of  $^{40}\text{Ar}$  is about 16 times shorter than the 18 ps lifetime of  $^{16}\text{O}$ , which would tend to make the 1461 keV peak wider. Based on the  $^{16}\text{O}$  measurement and these theoretical considerations, we estimated that the  $^{40}\text{Ar}$  peak would have a width of about 14 keV or more. Also, like the atmospheric 6129 keV gamma ray, which peaks at 6139 keV, the  $^{40}\text{Ar}$  gamma ray was expected to be shifted several keV higher in energy because most neutrons making atmospheric gamma rays are

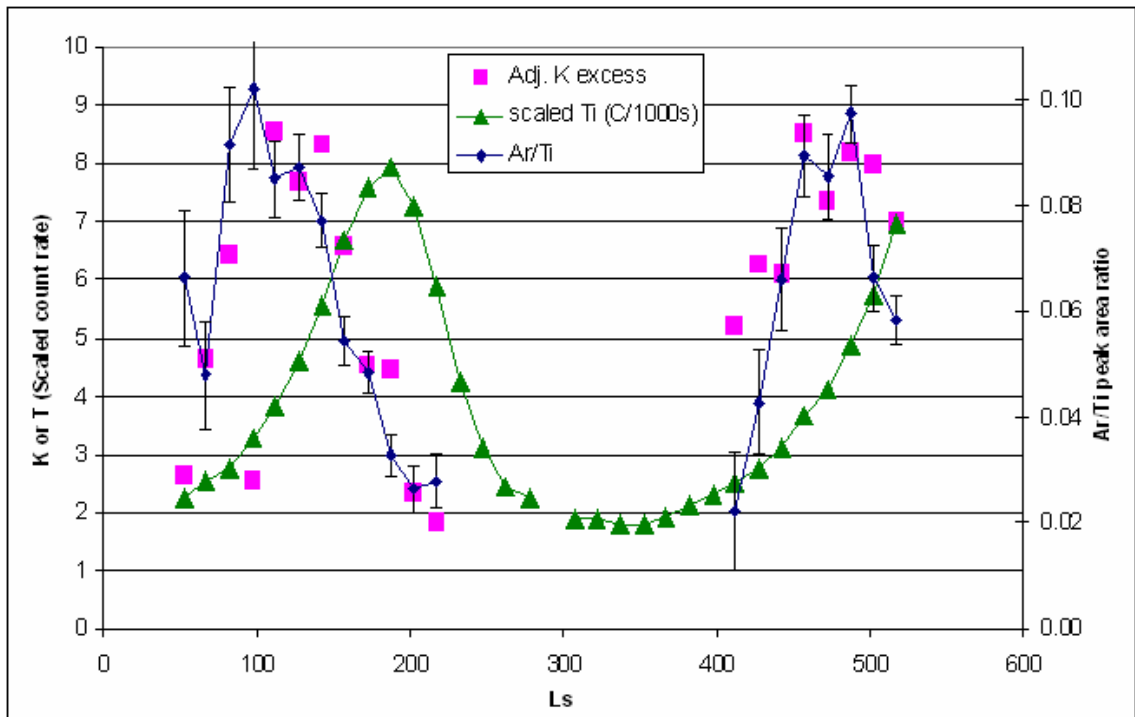


Figure 3.12: The observed excess of  $^{40}\text{K}$  at 1461 keV (square, pink data points) as compared to normalized Ar (dark blue diamonds curve) and scaled Ti count rates (green triangles curve) as a function of time (degrees of  $L_s$ ). The interference at 1461 keV appears to be more strongly related to atmospheric  $^{40}\text{Ar}$  than to thermal-neutron reactions in the detector (as represented by Ti).

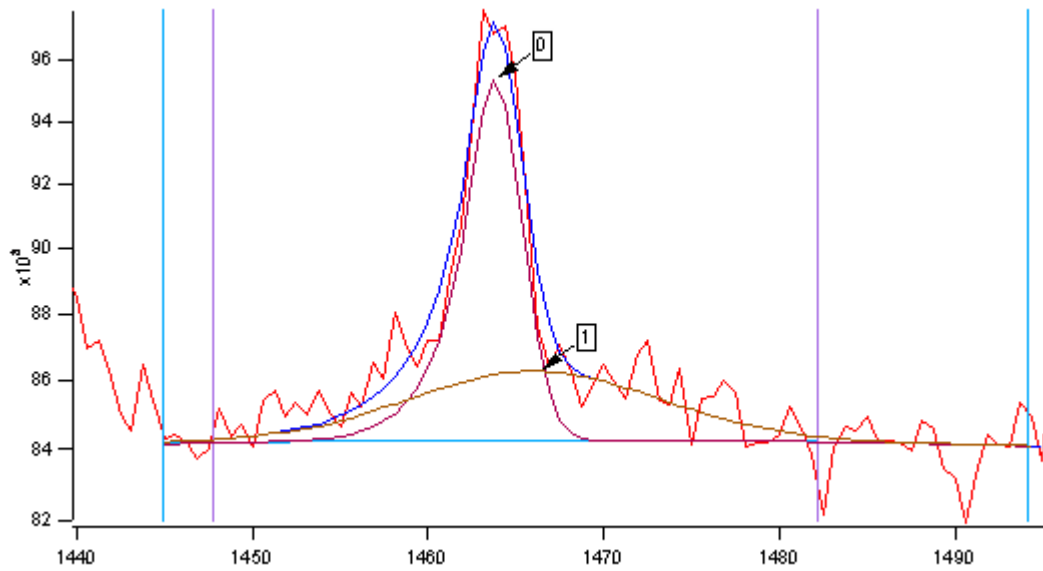


Figure 3.13: Interference at 1461 keV from  $^{40}\text{Ar}$  in Mars' atmosphere. This spectrum represents GRS data summed over a period when non-condensable atmospheric Ar becomes enriched over the southern pole while the atmospheric  $\text{CO}_2$  condenses to form the southern seasonal frost cap. Peak 0 at 1461 keV is the desired  $^{40}\text{K}$  signal from naturally radioactive K on Mars, and peak 1 is the Doppler-broadened atmospheric Ar interference. The smooth blue curve that fits the  $^{40}\text{K}$  peak can be seen to include gamma ray counts from  $^{40}\text{Ar}$ . The vertical axis represents gamma ray counts, and energy in keV is depicted horizontally along the baseline.

moving upwards toward the GRS.

A spectrum sum over the time period of highest atmospheric Ar content was created with the Ge interference removed. Figure 3.13, shows the resulting (somewhat noisy) 1461 keV peak as it is fit to calculate peak area by the blue, smooth peak. In addition to the standard  $^{40}\text{K}$  signal (peak 0), a low, broad peak (1) can definitely be fit to the data. This peak has a width of 16 keV and a centroid at 1466 keV, which corresponds well to what we estimated should be expected for the signature of the shifted, Doppler-broadened  $^{40}\text{Ar}$  signal. This implied that as it is currently fit, we are actually attributing some Ar gamma ray counts to the K signal.

For this research, it is important to identify and remove the spacecraft spectral signature and other interfering gamma rays to accurately measure the H and K spectral peak areas at various times. The H background as described above is currently accounted for in the seasonal  $\text{CO}_2$  frost results. The corrections for  $^{40}\text{K}$  interferences from neutron-capture Ge in the detector and inelastic scatter of Ar in the atmosphere are still in progress. The Ge line will be corrected by assuming the Ge/Ti ratio observed by the GRS is constant because both signals come from thermal-neutron capture reactions at the satellite. A determined amount of Ge will then be subtracted from the  $^{40}\text{K}$  peak based on the Ti counts in the same spectrum. The  $^{40}\text{Ar}$  line is small, broad, and cannot be fit using normal GRS peak fitting methods. Therefore, Ar counts will be estimated over the south pole during periods of Ar enrichment, and then a subtraction will be made for K spectra at other times based on the associated atmospheric thickness and assumptions of normal Ar mixing ratios. For these reasons (and the fact that the K gamma rays attenuate completely at a low  $\text{CO}_2$  depth of  $\sim 40 \text{ g/cm}^2$ ), the derived  $\text{CO}_2$  measurements based on K will not be used as extensively in the presented  $\text{CO}_2$  results.

### 3.2.5 Corrections Based on Analysis of Mars' Mid-Latitude Regions

This section provides an explanation of the correction factors, *cf*, applied in Equations 3.9 and 3.10. During the data processing for gamma ray flux and  $\text{CO}_2$  calculations, an unexpected pattern arose in data for the middle-latitude (non-polar)

regions on Mars. The corrected flux for all elements analyzed appeared to have a downward trend when plotted as a function of time in the standard  $15^\circ$  of  $L_s$  increments. This latitude region between  $45^\circ\text{N}$  and  $45^\circ\text{S}$ , which we commonly refer to as the ‘bellyband’, is always frost-free, so gamma ray attenuation effects do not play a role (besides the standard planet-wide atmospheric attenuation). Assuming that all corrections applied to the data are performed correctly, the spectral peak measurements are accurate, and there is no long term drift associated with an instrument component or its quality, one would expect that an analysis of the frost-free bellyband over time would yield statistically equal flux values for a given element at all times. The downward trend observed in the mid-latitude data contradicted these expectations, but was not to be believed because the elemental abundances at all locations on Mars can not change so significantly on the short timescale of our GRS observations.

It turns out that there are multiple causes for the observed trends. What was originally thought to be simply a change in the detector efficiency was also found to be related to increased Cosmic Ray Flux (CRF) over time. Though relevant only to non-radioactive elements, the CRF adjustment implemented in data processing apparently could use improvement. This adjustment needs to better correlate to the effects of CRF at the surface of Mars rather than determining it based on what is observed in orbit, as is the practice. In addition, there appears to be a small dead-time or recovery time in the detector after detection of a high-energy cosmic-ray event. The pattern of CRF over time is anti-correlated with the spectrometer’s internal pulser count rate, as well as elemental corrected flux. This issue requires a data correction based on the pulser count rate, and though it is not currently done for all elements, the effect should only be on the 2% level. Finally, it appears that the FWHM and tail parameters of the GRS spectral peaks are increasing as the peaks are gradually degrading and broadening over time. This necessitated a change in our peak fitting/measurement technique. Instead of using a ‘window’ fit where the lower and upper energy bounds for each peak are fixed, we have adopted a more interactive and dynamic ‘floating’ fit method where appropriate when calculating

spectral peak areas.

The correction factors in Equations 3.9 and 3.10 account for the issues above by adjusting the data to reduce or remove the undesired downward trend from the mid-latitude data. The decreasing data are fit with a trend line and then the data are normalized in such a way as to flatten out (make constant) the overall mid-latitude gamma ray flux trend for each element (while maintaining the observed scatter in the points). The associated/resulting correction factors are determined for each period of  $15^\circ$  of  $L_s$  individually, and then these factors are applied to data of the same time period at the poles.

## CHAPTER 4

## Carbon Dioxide Quantification Calculations

## 4.1 Gamma Ray Attenuation

The hydrogen and potassium concentration profiles (the relative atmosphere-corrected gamma ray flux derived in the previous chapter) allow investigation of gamma ray attenuation effects at the poles of Mars due to seasonal CO<sub>2</sub> frost coverage. In addition to increasing the number of thermal neutrons at the surface of Mars, the carbon dioxide acts to block gamma ray photons emitted at the planet. By analyzing the changes in gamma ray flux, I can measure the CO<sub>2</sub> frost caps as they grow during the winter months and shrink during the summer months at each pole. The H and K gamma ray signals used in this research are the only gamma ray signals statistically strong enough to allow the determination of CO<sub>2</sub> columnar thickness. Figures 4.1 and 4.2 give a simple illustration of this seasonal effect. Figure 4.1 shows pictures of the northern hemisphere of Mars taken during the winter and the summer. Sublimation of the winter CO<sub>2</sub> frost has created a summer pole free of condensed CO<sub>2</sub>. The H<sub>2</sub>O-ice residual northern polar cap remains throughout the summer in the right image of Figure 4.1. The corresponding hydrogen gamma ray signal emitted from the H-rich polar regolith (and the residual polar cap) during the summer is strong in the right image of Figure 4.2. Observe in the left image that a lower gamma ray signal is detected when the pole is covered in seasonal CO<sub>2</sub> frost and the H gamma rays are attenuated. Using observations such as these along with attenuation theory, the condensed CO<sub>2</sub> can be quantified in several ways.

## 4.1.1 Beer-Lambert Theory

The total linear attenuation coefficient and the associated interactions of ionizing radiation (gamma rays) with matter that contribute to it are discussed in detail in

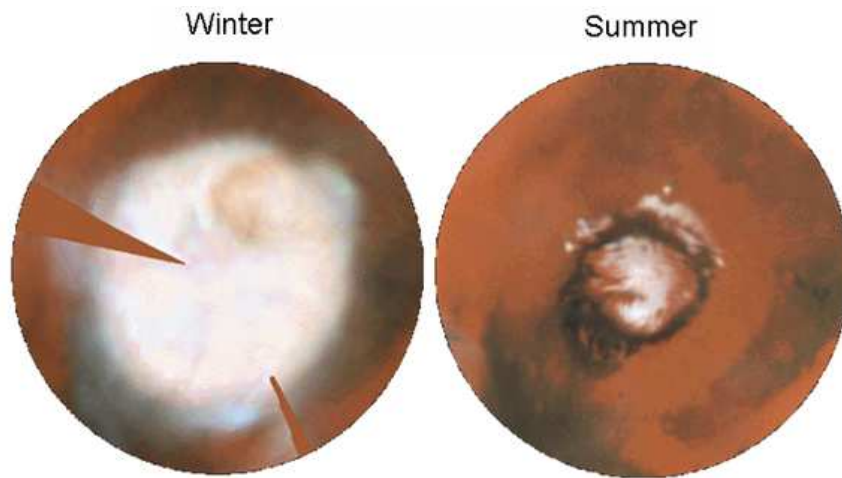


Figure 4.1: Pictures of Mars' north pole during the winter and summer. Changes in the seasonal  $\text{CO}_2$  frost can be seen. The residual  $\text{H}_2\text{O}$ -ice north polar cap remains in the summer. Photo credit: NASA/STScI HST/WFPC2.

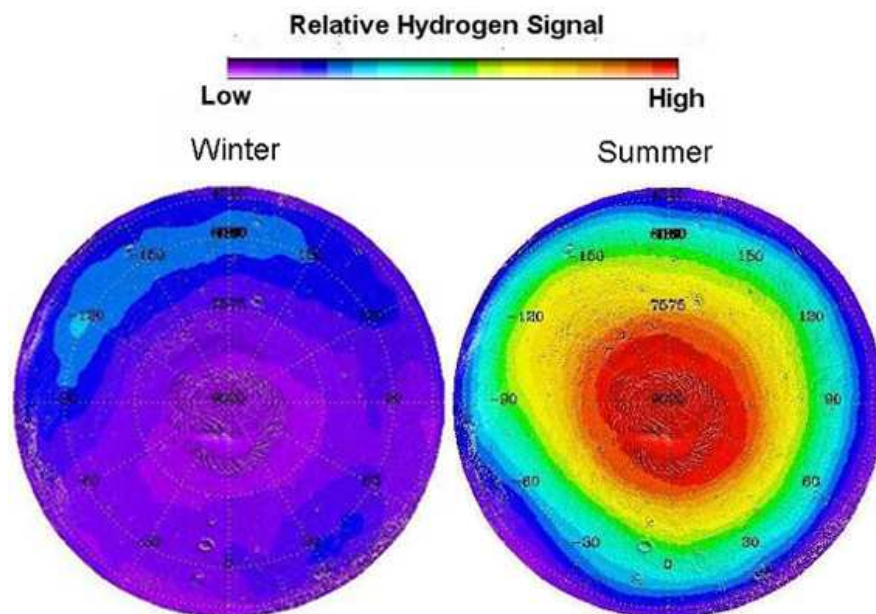


Figure 4.2: GRS H gamma ray data for Mars' north pole during the winter and summer. Sublimation of the seasonal  $\text{CO}_2$  frost allows more of the signal from H in the polar soil to reach the detector. Changes in the gamma ray signal intensity due to attenuation can be compared to visual pictures of the pole in Figure 4.1.

Section 2.4.5. Here I discuss Beer-Lambert Theory and its application to the poles of Mars in the process of quantifying the seasonal CO<sub>2</sub> frost deposits. The Beer-Lambert Law (also “Beer’s Law”) states that the radiation absorbed per unit length in a medium depends at any wavelength only on the incident radiation intensity:

$$\frac{dI(\lambda)}{dx} = -\mu I(\lambda) \quad (4.1)$$

It can also be represented in the integrated form as:

$$I_t = I_o e^{-\mu x} \quad (4.2)$$

where  $x$  is the columnar thickness of the attenuator (CO<sub>2</sub> polar frost), and  $\mu$  is the attenuation/absorption coefficient calculated from a photon cross-section database such as Berger et al. (1998). As described by Equation 2.9,  $\mu$  is the sum of the probabilities of gamma ray attenuation by photoelectric absorption, Compton scattering, and pair production. This coefficient is dependent on wavelength and, to a minor amount, on the composition of the attenuating medium.  $I_o$  and  $I_t$  are the initial (incident) and final (transmitted) radiation intensities.

#### 4.1.2 Application to the Gamma Ray Spectrometer Data

The relative atmosphere-corrected gamma ray flux profiles are used to determine changes in the polar carbon dioxide frost throughout the Martian seasons. Figure 4.3 shows a sampling of time periods for H flux data similar to what was seen in Figure 4.2, but in a more quantified format. Various measurements of the H gamma ray flux (concentration %) over multiple time periods and latitudes are plotted. Notice the fairly constant gamma ray signal coming from the middle latitudes where there is no seasonal frost coverage. Data for both poles (on the left and right sides of the plot) indicate a highly variable signal dependent on the amount of attenuation by the seasonal condensed CO<sub>2</sub>. High gamma ray counts during low frost periods at one pole correspond to low gamma ray counts during high frost periods at the other pole. Figure 4.3 is also representative of the <sup>40</sup>K signal, which follows the

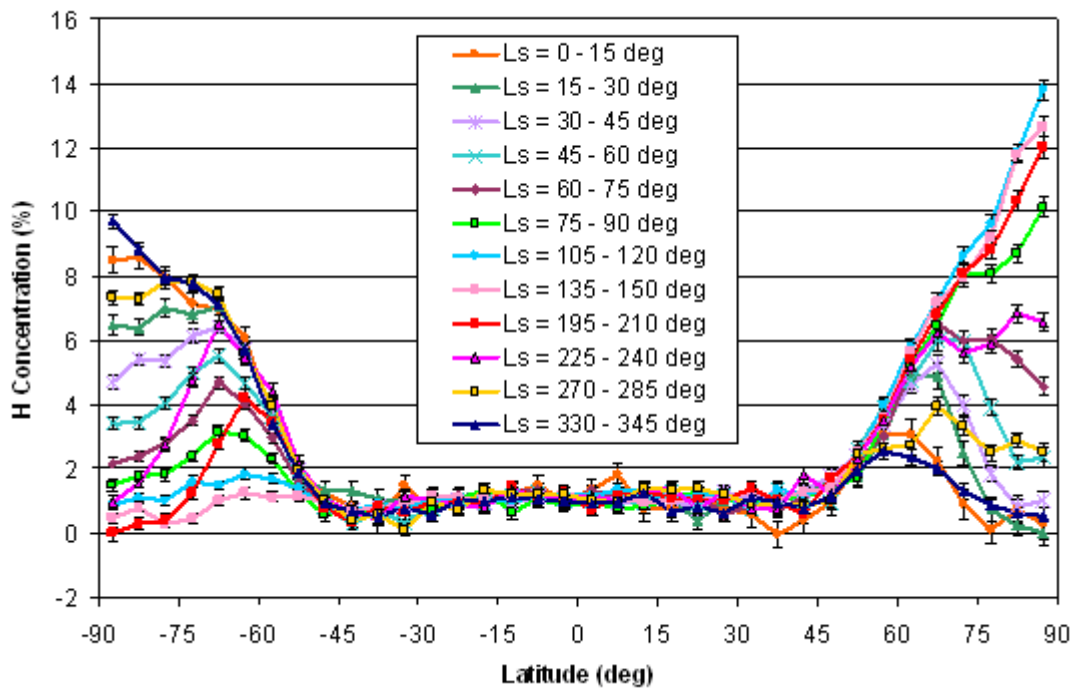


Figure 4.3: Relative atmosphere-corrected hydrogen gamma ray flux versus latitude. Attenuation of the H gamma ray line (2223 keV) due to seasonal carbon dioxide frost at the poles can be seen by observing the changes in the signal strength over various periods of  $L_s$ . Variations in the thickness of the frost over time can then be approximated from calculations incorporating the ratio of the signal at a given time to that of maximum H flux (and therefore minimum  $\text{CO}_2$  frost).

same spatial and temporal trends.

To determine the columnar thickness of the seasonal frost, first recall that the flux of gamma rays attributed to the natural decay of radioactive potassium is a model independent value because the signal strength does not depend on neutron flux. I can therefore employ the Beer-Lambert Law to obtain a fairly good estimation of the CO<sub>2</sub> column density at various times throughout the Martian year. Using Equation 4.2 and the actual, observed changes in gamma ray intensity at the poles during the condensation and sublimation of CO<sub>2</sub> frost, I can obtain numerical values for the columnar thickness,  $x$ . The attenuation coefficient ( $\mu$ ) for 1461 keV, <sup>40</sup>K gamma rays through carbon dioxide is 0.0526 cm<sup>2</sup>/g (Berger et al., 1998). Inserting this value and the relative gamma ray flux observed by the GRS for a seasonal-frost-free versus CO<sub>2</sub>-covered surface, the integrated form of the Beer-Lambert equation above gives frost thickness approximations in g/cm<sup>2</sup>. All results are shown in the CO<sub>2</sub> columnar thickness plots in Chapter 5. For both <sup>40</sup>K- and H-based calculations, depths are given in terms of the mass abundance per unit area of the column of CO<sub>2</sub> above the surface to avoid assumptions regarding the density of the column. The “thicknesses” determined here can be divided by an assumed frost density to derive CO<sub>2</sub> accumulated depth results in the more standard units of cm (or m, etc.). (Although the CO<sub>2</sub> density varies by location and time of year, an acceptable rough estimate is  $\sim 1$  g/cm<sup>3</sup>.)

Since the signal intensity is independent of neutron flux, determining frost depths using naturally radioactive <sup>40</sup>K gamma rays is beneficial because the calculation is independent of assumptions or models of Mars’ surface layers. There are also a few disadvantages of using the K signal. As described in Section 3.2.4, there are complicated interferences with the 1461 keV line from neutron-capture Ge in the detector itself and from atmospheric <sup>40</sup>Ar contributions during enrichment of non-condensable Ar over the southern winter pole. In addition, the K signal is only strong enough to measure thin seasonal caps up to  $\sim 40$  g/cm<sup>2</sup> at which point the signal becomes completely attenuated and measurement of thicker frost is not possible. Up to that limiting depth, however, the agreement with the H-based CO<sub>2</sub> results is

fairly good. This method of double-checking the derived CO<sub>2</sub> measurements using two independent gamma ray lines is advantageous, but outside of this application the <sup>40</sup>K results will not be shown as extensively in the plotted results.

For a first-order comparison, I can do the same Beer-Lambert Law calculation to estimate CO<sub>2</sub> columnar thickness using the hydrogen line at 2223 keV. A representative sample of the necessary H relative atmosphere-corrected gamma ray flux values for various latitudes and time periods are shown directly in Figure 4.3.

In the investigation of attenuation effects, a model of the change in atmospheric thickness with time based on the ARC GCM is employed in the forward calculation to correct all gamma ray flux values for the predicted variations in the atmosphere. As with the K data, I then compare the maximum H flux observed (which occurs when the relevant pole is free of seasonal CO<sub>2</sub> frost) to a weaker signal from hydrogen gamma rays that have been attenuated as they passed through a layer of seasonal CO<sub>2</sub> frost condensed on the surface. The seasonal-frost-free data are determined by a combination of spectra summed at different time periods at each latitude depending on when that particular area of the planet is free of condensed CO<sub>2</sub>. The magnitude of the change in signal intensity at any time from the frost-free reference value provides the estimate of the amount of the seasonal CO<sub>2</sub> overburden at that time. To first order, the model dependencies in this calculation are small because attenuation coefficients for gamma rays passing through CO<sub>2</sub> are well known. For the hydrogen energy line at 2223 keV, the standard attenuation coefficient,  $\mu$ , is 0.0420 cm<sup>2</sup>/g (Berger et al., 1998).

## 4.2 Model Dependence

Because the H gamma ray is not created by natural radioactivity, but is instead emitted from a neutron-capture event, the attenuation interaction is more complex than that for <sup>40</sup>K gamma rays. In actuality, there are second-order effects that need to be taken into account. The necessary calculations are not straight forward because we cannot assume that the flux of gamma rays under the frost is constant for all (and

independent of) frost thickness values. This is because CO<sub>2</sub> frost is a good moderator of neutrons, and the true effect of the CO<sub>2</sub> is to increase the flux of thermal neutrons (Feldman et al., 2003) creating a related increase of neutron-capture-produced H gamma rays. In fact, Monte Carlo particle simulations using MCNPX imply that over the range of frost depths reasonable for this study, the presence of CO<sub>2</sub> seasonal frost raises the thermal-neutron flux in the soil by approximately 20% (Boynton et al., 2006a). By incorporating these models for the flux of hydrogen gamma rays through various depths of CO<sub>2</sub> frost covering the regolith, we can plot the ratio of the flux through a range of thicknesses of CO<sub>2</sub> frost to that when no CO<sub>2</sub> frost is present (i.e. the *intensity ratio*) to derive the relevant attenuation equations. Equation 4.2 can be rearranged to solve for CO<sub>2</sub> thickness,  $x$ , as:

$$x = -\left(\frac{1}{\mu}\right) \times \ln\left(\frac{I_t}{I_o}\right) \quad (4.3)$$

The model-derived attenuation equations for H gamma rays, which are shown below as a function of latitude in the form of Equation 4.3, relate the CO<sub>2</sub> columnar thickness (represented here as  $CT$  instead of  $x$ ) to the observed change in signal intensity:

*Northern model:*

$$86^\circ N - 90^\circ N : CT (g/cm^2) = -24.675 \times \ln(\textit{intensity ratio}) \quad (4.4)$$

$$78.5^\circ N - 86^\circ N : CT (g/cm^2) = -23.559 \times \ln(\textit{intensity ratio}) \quad (4.5)$$

$$< 78.5^\circ N : CT (g/cm^2) = -22.0 \times \ln(\textit{intensity ratio}) \quad (4.6)$$

*Southern model:*

$$\textit{All latitudes} : CT (g/cm^2) = -21.3 \times \ln(\textit{intensity ratio}) \quad (4.7)$$

The equations above are used to obtain an approximation of the seasonal polar frost thickness in  $\text{g}/\text{cm}^2$ . Again, depths ( $CT$ ) are given in terms of the mass per unit area of the column of  $\text{CO}_2$  above the surface to avoid assumptions regarding the density of the condensed  $\text{CO}_2$ .

For all analyses and results presented in this work, the north polar environment was assumed to have seasonal  $\text{CO}_2$  frost deposition over a 100%  $\text{H}_2\text{O}$ -ice residual cap surrounded by a two-layered regolith modelled as a  $10 \text{ g}/\text{cm}^2$  dry layer (3%  $\text{H}_2\text{O}$  contained in soil with the composition observed by the Mars Pathfinder APXS) overlying a more water-rich soil of 75%  $\text{H}_2\text{O}$  (by weight). In the south,  $\text{CO}_2$  was modelled to condense and sublimate over the same two-layered regolith composition as modelled for the north, but without the inclusion of the 100%  $\text{H}_2\text{O}$ -ice residual cap. The atmospheric column density used for both poles was  $18 \text{ g}/\text{cm}^2$ . (Note that in reality, the atmospheric thickness is not the same at both poles, and it varies slightly with the seasons.) Independent of  $\text{CO}_2$  frost, the gamma ray flux varies as a function of latitude because of changes in the surface and underlying terrain, and therefore, the associated regolith layer compositions used in the models. Further details about the effects of the regolith composition (and atmospheric column densities) incorporated into the models are discussed in following subsections. Ideally, every latitude band observed would have its own derived attenuation equation; however, the variations that result in the case of H gamma rays occur gradually over a large enough area that the latitude regions designated above are sufficient. These models take into account both the efficiency of the detector as a function of angle and the effect of peaking of the emission in the upward direction with thicker  $\text{CO}_2$  frost. The determined relationships for hydrogen gamma rays (Equations 4.4 - 4.7) hold for all columnar thicknesses up to approximately  $75 \text{ g}/\text{cm}^2$  after which the gamma ray flux is nearly completely attenuated. At this point,  $\text{CO}_2$  thickness values are ambiguous because of greater associated uncertainties.

### 4.2.1 Regolith Models

The concentration of an element in the Martian regolith is of primary importance in determining the flux of the associated gamma ray line; however, to second order, the gamma ray flux is dependent on the overall composition of the soil and the overlying atmospheric thickness. These factors can affect the thermal-neutron flux beneath Mars' surface where the gamma rays are generated. This section and Section 4.2.2 give the results of an investigation into the magnitude of these effects. For this study, a large number of MCNPX models were run, in which both the modelled regolith composition and the atmospheric column density were varied to determine how the seasonal CO<sub>2</sub> frost measurements were affected as a function of the *natural log* of the gamma ray flux *intensity ratio*. (This ratio compares the gamma ray signal at frosty times to that during periods when the pole is seasonal-frost-free, as described above.)

Whether for a single, given composition or for multiple surface layers with varied compositions, Monte Carlo neutron-transport codes such as MCNPX are necessarily utilized to calculate the distribution of low-energy neutrons in Mars' regolith. These calculations are complex because numerous elements with high neutron-capture cross-sections affect the transport and thermalization of neutrons. This makes it otherwise very difficult to predict the associated flux of neutron-capture gamma rays (such as 2223 keV H). In the polar regions, it is especially necessary to take these effects into account when including known H<sub>2</sub>O ground-ice because the presence of only 0.1% hydrogen in the soil increases the flux of thermal neutrons considerably and moves the peak of the depth-versus-flux distribution significantly closer to the surface than when no hydrogen is present (Boynton et al., 2004a, and sources therein). Luckily, since all elements produced via neutron-capture are equally affected in such a case, the ratio of the flux of these elements (or the ratio of the flux of the same element at different times, as is relevant to these CO<sub>2</sub> attenuation studies) is much less sensitive to variations in regolith composition.

Figure 4.4 shows the resulting CO<sub>2</sub> thicknesses predicted as a function of

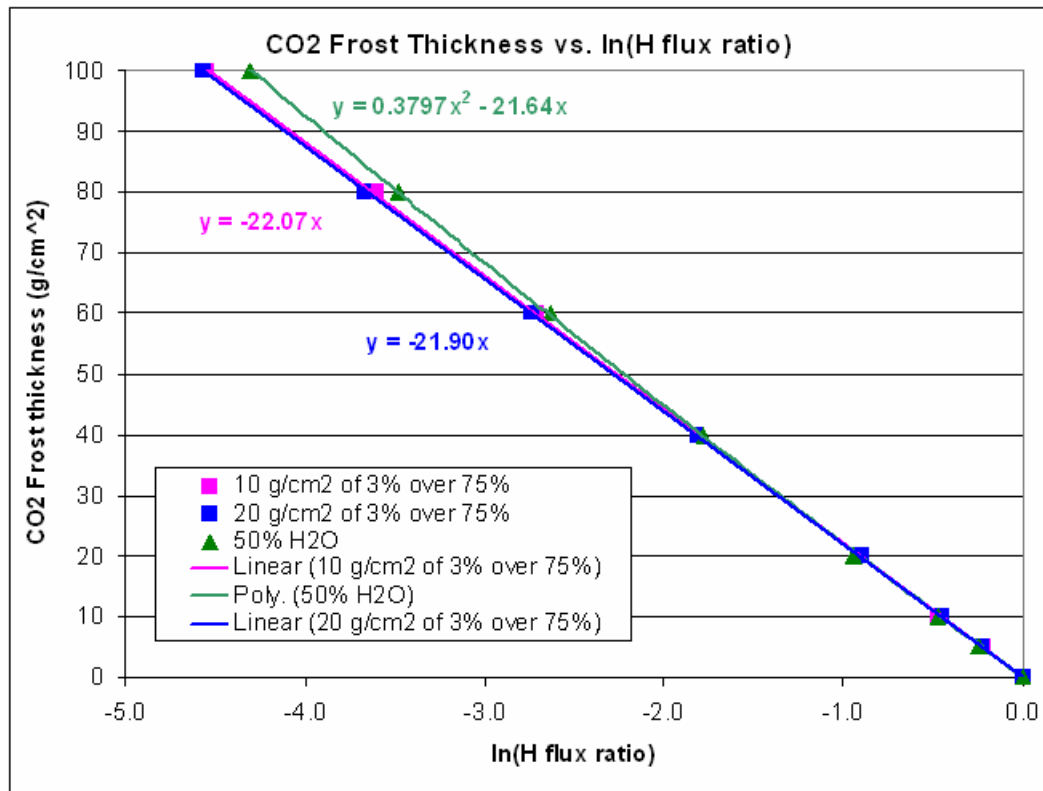


Figure 4.4: Model results for three possible regolith compositions are plotted to quantify the effects on the CO<sub>2</sub> thickness values. The north and south polar regolith is believed to consist of a dry soil layer (~3% H<sub>2</sub>O content) of some depth overlying a more water-ice-rich layer of about 75% H<sub>2</sub>O by weight (blue and pink data points). The model for 50% H<sub>2</sub>O-ice in the soil homogeneously distributed with depth is representative of earlier beliefs about Mars' south polar regolith composition (green data points). Further details about the comparison of these models and the implications for the seasonal frost results can be found in the main text.

$\ln(H \text{ flux ratio})$  for three regolith compositions. A single layer model with 50% H<sub>2</sub>O distributed homogeneously with depth is compared with two layered models of a dry layer of soil with 3% H<sub>2</sub>O by weight overlying a more ice-rich 75% H<sub>2</sub>O region. The upper dry layer for these models varies from 10 g/cm<sup>2</sup> to 20 g/cm<sup>2</sup> thick. The associated attenuation-type equations are determined by fitting the data points as is also shown.

Notice that these different regolith models do not actually have a large effect on the resulting CO<sub>2</sub> thickness values. The biggest difference occurs when modelling the ground as layered versus non-layered. The 50% homogeneously distributed H<sub>2</sub>O-ice data is representative of the regolith composition of the south pole. If the H<sub>2</sub>O-ice is mixed all the way to the surface in the north outside of the residual polar cap, which is not likely based on other observations, the error in my CO<sub>2</sub> results could be up to  $\sim 7$  g/cm<sup>2</sup> at the 100 g/cm<sup>2</sup> level. As it is now widely accepted that the northern regolith is truly composed of a layer of dryer soil of some depth overlying a more H<sub>2</sub>O-ice rich layer, either of the layered-model results could be accurate (blue and pink data points in Figure 4.4). Increasing the dry-layer depth from 10 g/cm<sup>2</sup> to 20 g/cm<sup>2</sup> here (a fairly substantial difference) only results in a variation of  $\sim 0.8$  g/cm<sup>2</sup> of CO<sub>2</sub> at the 100 g/cm<sup>2</sup>-level. At 70 g/cm<sup>2</sup> of CO<sub>2</sub>, which is approximately the maximum depth of seasonal frost that I observe, the difference between the layered models only creates a variation of  $\sim 0.5$  g/cm<sup>2</sup>. This implies that outside of the northern residual polar cap, which is correctly modelled as 100% H<sub>2</sub>O-ice, the exact details in the layered model are not very significant. The current regolith compositions incorporated into the models as detailed in Section 4.2 are best estimates based on studies such as Boynton et al. (2004b, 2005), and they are clearly sufficient. Any plausible changes to beliefs about the north or south polar regolith composition in the future will not notably affect any of these CO<sub>2</sub> results.

#### 4.2.2 Atmosphere Models

The columnar thickness of the atmosphere through which the gamma rays travel to reach the detector in the MCNPX model simulations also has a slight effect on the

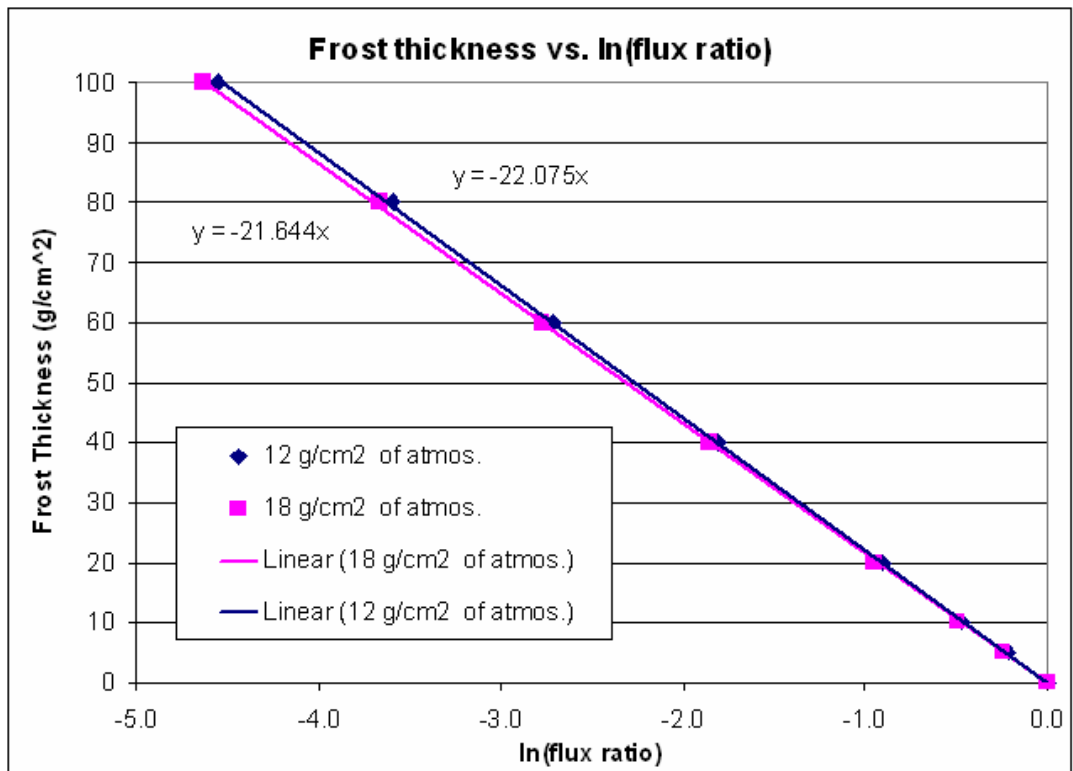


Figure 4.5: The dependence of seasonal CO<sub>2</sub> frost thickness results on the modelled atmospheric thickness. Pink data points corresponding to 18 g/cm<sup>2</sup> of atmosphere are representative of an average northern atmospheric thickness. The thinner atmosphere at the south pole over the Martian southern highlands is represented here as 12 g/cm<sup>2</sup> (blue data points). These results indicate that the CO<sub>2</sub> calculations are not highly dependent on the atmospheric thickness values used in the MCNPX models.

determination of seasonal frost thickness. A thicker Martian atmosphere will attenuate gamma rays to a greater extent. To test the dependence of the H-based CO<sub>2</sub> thickness results to variations in the atmospheric thickness, the plot in Figure 4.5 was created. The format is similar to that of Figure 4.4. The CO<sub>2</sub> frost thickness in g/cm<sup>2</sup> is plotted as a function of  $\ln(\text{flux ratio})$ . The pink data points corresponding to 18 g/cm<sup>2</sup> of atmosphere are representative of an average atmospheric thickness in the north. The increase in elevation of the Martian southern highlands correlates to thinner atmosphere at the south pole represented here as 12 g/cm<sup>2</sup> by the blue data points. These results indicate that the CO<sub>2</sub> calculations are not highly dependent on the atmospheric thickness values used in the models. The difference is only  $\sim 2$  g/cm<sup>2</sup> in the calculated frost depth at 100 g/cm<sup>2</sup>. Since 100 g/cm<sup>2</sup> is above (or an upper limit to) the seasonal frost depth actually observed, the 2 g/cm<sup>2</sup> is actually the maximum difference possible and is well within the error bars of the associated frost thickness plots. Therefore, any reasonable variation in the Martian atmosphere that is incompletely or even inaccurately modelled in the MCNPX runs will have a minimal effect on the final condensed CO<sub>2</sub> thickness values.

### 4.2.3 Atmospheric Enrichment of Non-Condensables

The GRS also measures the flux of 1294 keV gamma rays resulting from the decay of <sup>41</sup>Ar. Sprague et al. (2004, 2006) have shown that there are significant variations in atmospheric Ar with season and latitude. The atmosphere over both the northern and southern polar regions is enriched with non-condensable Ar (and N<sub>2</sub>) by a factor of 3 to 6 during the winter when CO<sub>2</sub> in the atmosphere condenses onto Mars' surface. The greatest enhancement is observed in the south because the column density of CO<sub>2</sub> condensed on the surface is greater and the atmosphere is thinner than in the north. The Ar concentration then drops back to normal levels in the late winter and spring as the seasonal CO<sub>2</sub> frost sublimates and is mixed back into the atmosphere.

It is important to determine the effect that this enrichment of atmospheric non-condensables over the polar regions may have on the sub-surface thermal neutron

distribution, and therefore, on the H gamma rays produced from thermal-neutron-capture reactions. The table in Figure 4.6 provides numerical results based on adjusting the atmospheric composition in the MCNPX model simulations. For various CO<sub>2</sub> frost thicknesses, the resulting H gamma ray flux is shown for a normal atmospheric content (the content measured by the Viking Landers) and for an Ar-enriched atmosphere. The non-condensable constituents are enhanced by a factor of 3 in the enriched versions compared to the normal-atmosphere runs. The ratio of the H gamma ray flux from these two scenarios is also computed. Although it may seem likely that the change in atmospheric composition would have a large effect because Ar has a significant cross-section, it can be seen from these numbers that the enrichment of Ar and N<sub>2</sub> in the polar regions due to CO<sub>2</sub> frost condensation has no effect on the neutron distribution or gamma ray flux. The maximum effect of 1% is within the MCNPX statistics.

Frost Thickness (g/cm <sup>2</sup> )	H gamma flux		
	Normal atmosphere	Ar-enriched atmosphere	Ratio
20	235.97	235.83	1.00
40	96.16	96.11	1.00
60	38.97	38.72	0.99
80	16.10	16.12	1.00

Figure 4.6: H gamma ray flux through various thicknesses of seasonal CO<sub>2</sub> frost for a normal (Viking Lander observed) atmosphere and an atmosphere enriched in non-condensables. The enhancement of atmospheric Ar by a factor of 3 to 6 over the poles during the winter when the CO<sub>2</sub> condenses onto the Martian surface could possibly produce a perturbation of the sub-surface thermal-neutron flux and associated neutron-capture-produced H gamma rays. The results of this investigation show a 1% effect that is actually within model statistics.

## CHAPTER 5

Results and Conclusions: Detailed Spatial and Temporal Dependence of Seasonal  
CO<sub>2</sub> Polar Frost

## 5.1 Introduction

The amount and location of seasonal CO<sub>2</sub> condensation and sublimation on the poles of Mars, and the rate at which these processes take place, depend upon many factors. Surface deposition of dust, dust clouds and atmospheric condensates, H<sub>2</sub>O-ice effects, and advection and atmospheric dynamics are just a few of the components that act in guiding the CO<sub>2</sub> surface-atmosphere exchange cycle. The research presented here is the first study to use gamma ray spectrometry to analyze and quantify the temporal and spatial behavior of the seasonal polar frost on Mars. Although the winter polar caps are not 100% predictable nor exactly repeatable on an interannual basis, the current 1.5 Martian years of GRS data provide a good glimpse into the overall Martian climate and the CO<sub>2</sub> cycle.

5.2 CO<sub>2</sub> as a Function of Solar Areocentric Longitude ( $L_s$ )

## 5.2.1 GRS Results

The growth and retreat of the Martian seasonal polar carbon dioxide frost can be plotted for specific latitudes as a function of  $L_s$  (time in degrees of the progression of Mars in its orbit around the sun) utilizing the relative, atmosphere-corrected flux data for hydrogen and potassium gamma rays (2223 keV and 1461 keV, respectively). Degrees of  $L_s$ , the areocentric longitude of the sun, represent the angle that Mars has reached in its orbit relative to the vernal (spring) equinox in the northern hemisphere. The northern vernal equinox establishes  $L_s = 0^\circ$ , and the completion of a full Martian year is represented by  $L_s = 360^\circ = 0^\circ$ . The northern summer

solstice, autumnal equinox, and winter solstice occur at  $L_s = 90^\circ$ ,  $180^\circ$ , and  $270^\circ$ , respectively. The seasons are reversed for the southern hemisphere. By binning GRS data into zonal bands of  $360^\circ$  of longitude by  $7.5^\circ$  of latitude, I can investigate the condensation and sublimation trends of the  $\text{CO}_2$  frost over time at various latitudes.

Figures 5.1 and 5.2 show the GRS results for the change in seasonal frost columnar thickness ( $\text{g}/\text{cm}^2$ ) for five latitude bands determined from the varying H gamma ray signal at each pole starting at the zonal band centered at  $\pm 60^\circ$  latitude. Note that the plots were constructed so that the time period shown begins and ends in the summer for each pole in order to capture the advance and retreat of the seasonal cap in its entirety. The data for each latitude band are plotted in a single color. The solid data points represent information from the first Mars year of observations, and the partial second Mars year data are shown as open data points. In the northern hemisphere, the data overlaps during the sublimation period. In the south, the GRS has observed two  $\text{CO}_2$  condensation periods. In general, there is not a significant amount of interannual variation between the two years of calculated  $\text{CO}_2$  frost patterns. Mars Odyssey went into a safe-mode configuration around  $L_s = 285^\circ$  due to a large solar particle event (SPE), and there were no data gathered during that time.

Each of the ten latitude bands presented in Figures 5.1 and 5.2 ( $\pm 60^\circ$ ,  $\pm 67.5^\circ$ ,  $\pm 75^\circ$ ,  $\pm 82.5^\circ$ , and  $\pm 90^\circ$ ) will be shown individually in Section 5.2.3 where I compare these GRS data points to predictions derived from Mars atmospheric circulation models. That section also contains a more thorough discussion of the GRS-derived  $\text{CO}_2$  behavior and comparison to other spacecraft observations.

Because  $^{40}\text{K}$  is a naturally radioactive element, it is useful in analyzing seasonal gamma ray attenuation because the calculation can be model-independent. The composition of the regolith and the presence and distribution of  $\text{H}_2\text{O}$  ground ice, for example, affect thermal neutron flux and the 2223 keV H gamma ray line, but K gamma rays are left unperturbed. For this reason, K data provide a useful, independent measurement of the polar frost accumulation by which to double-check the H-based results.

$\text{CO}_2$  quantification using the K gamma ray data is compared to the H-based

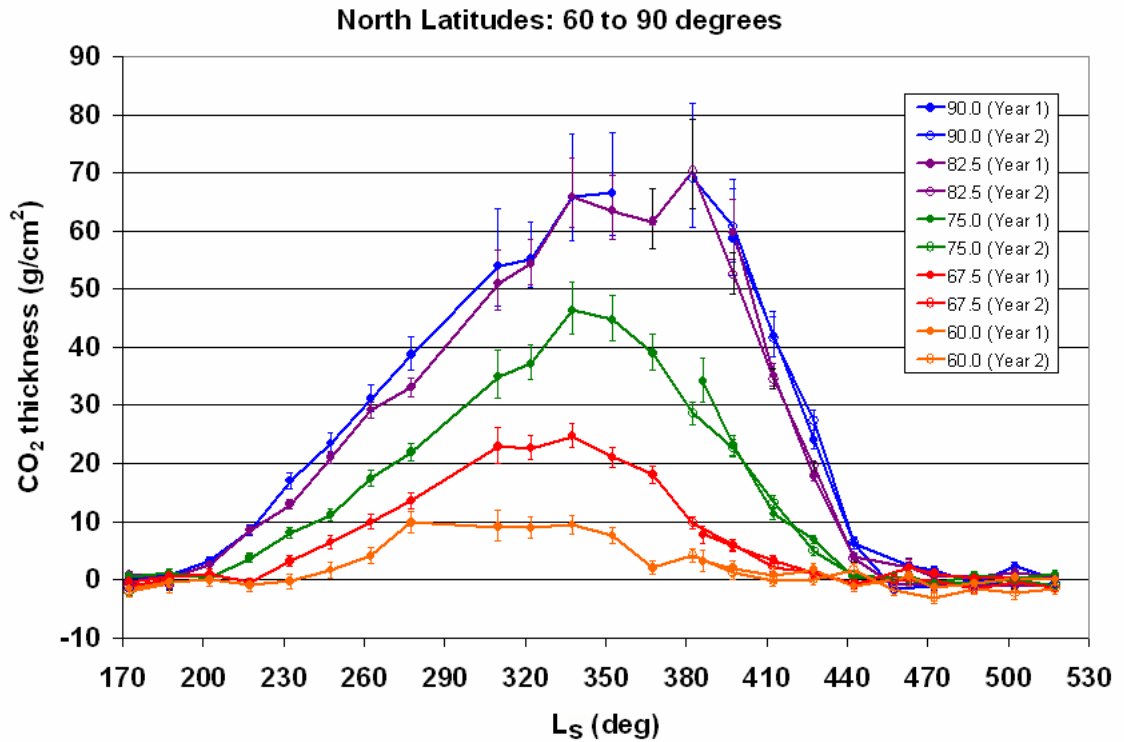


Figure 5.1: Columnar thickness ( $\text{g}/\text{cm}^2$ ) of seasonal  $\text{CO}_2$  condensed on Mars' north pole as determined by H gamma rays at 2223 keV. The results shown here as a function of time (degrees of  $L_s$ ) represent approximately 1.5 Martian years of observations. The GRS data are averaged over periods of  $15^\circ$  of  $L_s$  and into 5 zonal latitude bands beginning near the seasonal polar cap edge at  $\sim 60^\circ\text{N}$ .

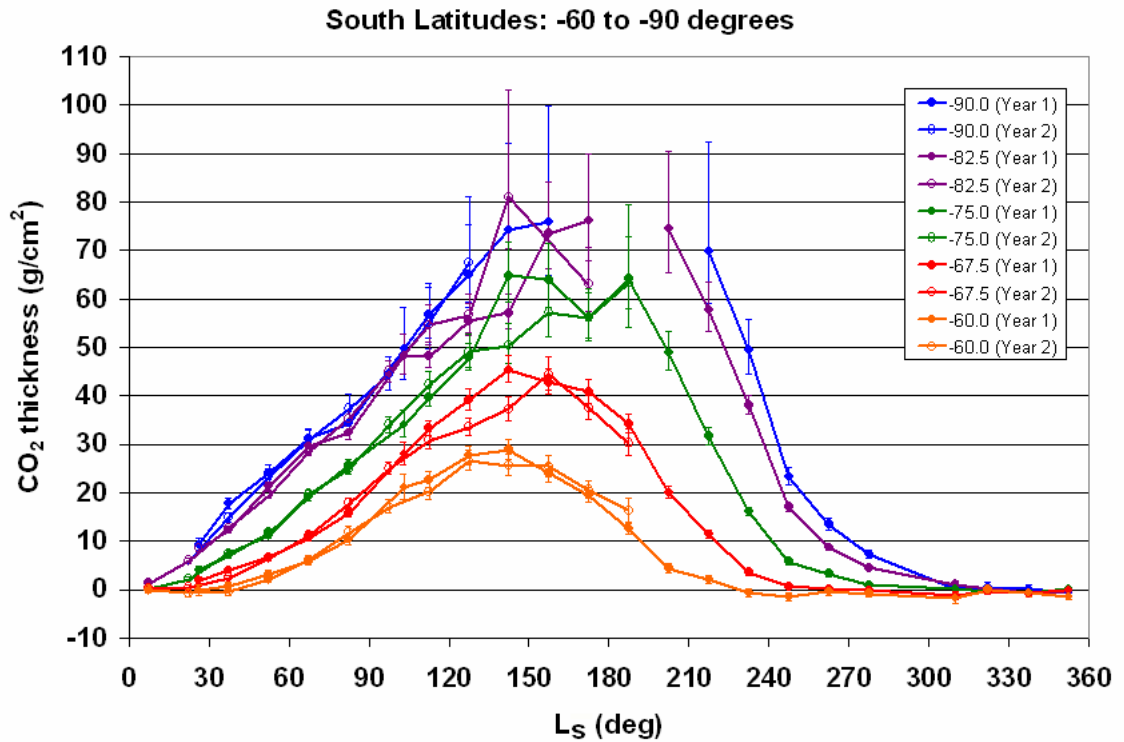


Figure 5.2: Columnar thickness ( $\text{g}/\text{cm}^2$ ) of seasonal  $\text{CO}_2$  condensed on Mars' south pole as determined by H gamma rays at 2223 keV. The results shown here as a function of time (degrees of  $L_s$ ) represent approximately 1.5 Martian years of observations. The GRS data are averaged over periods of  $15^\circ$  of  $L_s$  and into 5 zonal latitude bands beginning near the seasonal polar cap edge at  $\sim 60^\circ\text{S}$ .

values in Figures 5.3 through 5.9. Figures 5.3, 5.4, and 5.5 show three latitude bands in the northern hemisphere centered on  $60^\circ\text{N}$ ,  $67.5^\circ\text{N}$ , and  $75^\circ\text{N}$ , respectively. The region that is poleward of these bands accumulates so much  $\text{CO}_2$  frost that the seasonal cap is basically opaque to the  $^{40}\text{K}$  gamma rays. Unfortunately,  $\text{CO}_2$  columnar thickness can only be measured to  $\sim 40 \text{ g/cm}^2$  when using this lower-energy 1461 keV signal. In the figures for  $60^\circ\text{N}$  and  $67.5^\circ\text{N}$ , it is clear that the GRS-measured seasonal frost depth and condensation/sublimation temporal patterns are very similar when comparing H and K data. Within statistics, both independent methods agree, which lends confidence to the results. At  $75^\circ\text{N}$  where the  $\text{CO}_2$  reaches a maximum around  $40 \text{ g/cm}^2$ , the dashed line and open data points for the K results (green curve) indicate that the calculated error bars are unreasonably large or even infinite due to near total attenuation of the gamma ray.

The next figures (5.6 through 5.9) show the same comparisons for the south pole. All five latitude bands are shown to give an example of how the blocked K signal during maximum winter frost can still give confirmation, at the early and late stages of the seasonal cap evolution, that the stronger H gamma ray results are legitimate. In Figure 5.6 showing  $60^\circ\text{S}$ , notice that the K-derived  $\text{CO}_2$  columnar thickness is 5 - 10  $\text{g/cm}^2$  less than the H-based result during maximum frost. This discrepancy is consistent with the issues discussed in detail in Section 3.2.4 concerning interference with the 1461 keV,  $^{40}\text{K}$  gamma ray signal. If gamma rays from Ge in the detector at 1464 keV and from a Doppler-broadened, atmospheric Ar spectral peak at 1466 keV are incorrectly attributed to the 1461 keV gamma ray counts, the GRS appears to see a stronger K signal than is actually emitted from Mars' surface. A stronger gamma ray signal implies less attenuation, and therefore, less  $\text{CO}_2$  overburden. The lower K-based frost measurements in the south illustrate such an effect.

At  $67.5^\circ\text{S}$  and  $75^\circ\text{S}$  as the condensed  $\text{CO}_2$  frost approaches  $40 \text{ g/cm}^2$  and more, the plotted K-based values can be seen to become more sporadic with large and increasing error bars. We even begin to lose K data points between roughly  $L_s = 180^\circ$  and  $210^\circ$  in Figure 5.8 when no 1461 keV gamma ray signal can be observed. The most poleward southern latitude bands shown in Figure 5.9 clearly illustrate the

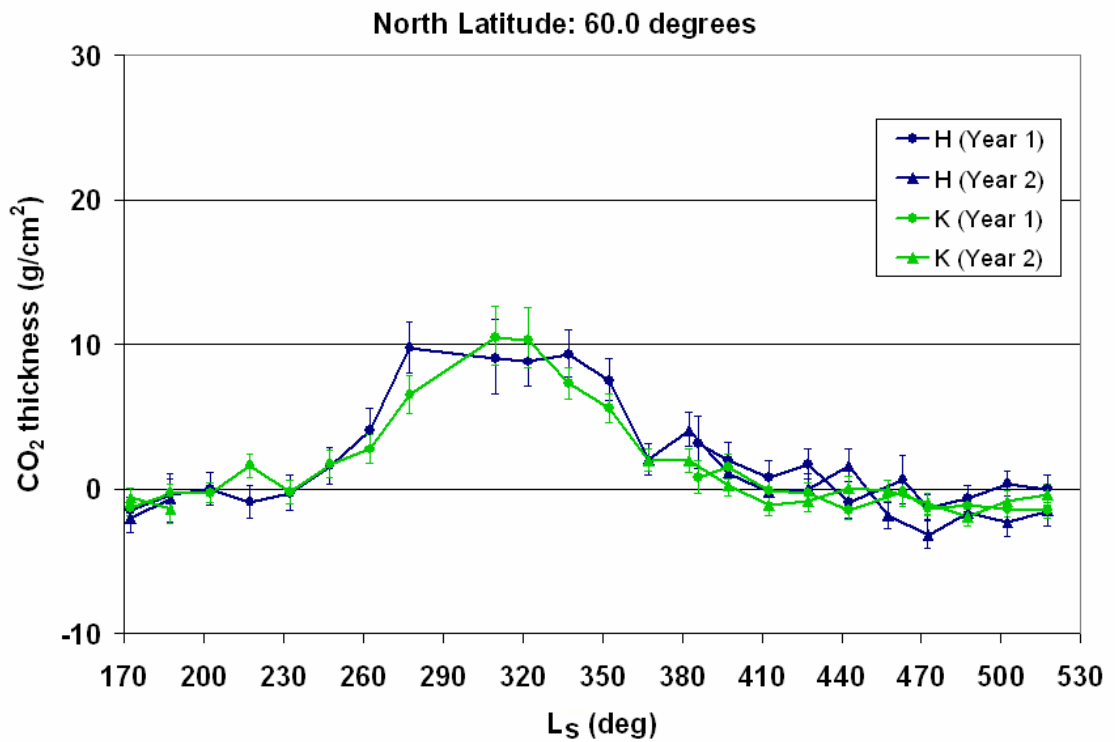


Figure 5.3: CO<sub>2</sub> columnar thickness (g/cm<sup>2</sup>) as determined by H gamma rays at 2223 keV (dark blue) and <sup>40</sup>K gamma rays at 1461 keV (green). The results shown here as a function of time (degrees of L<sub>s</sub>) represent ~1.5 Martian years of data.

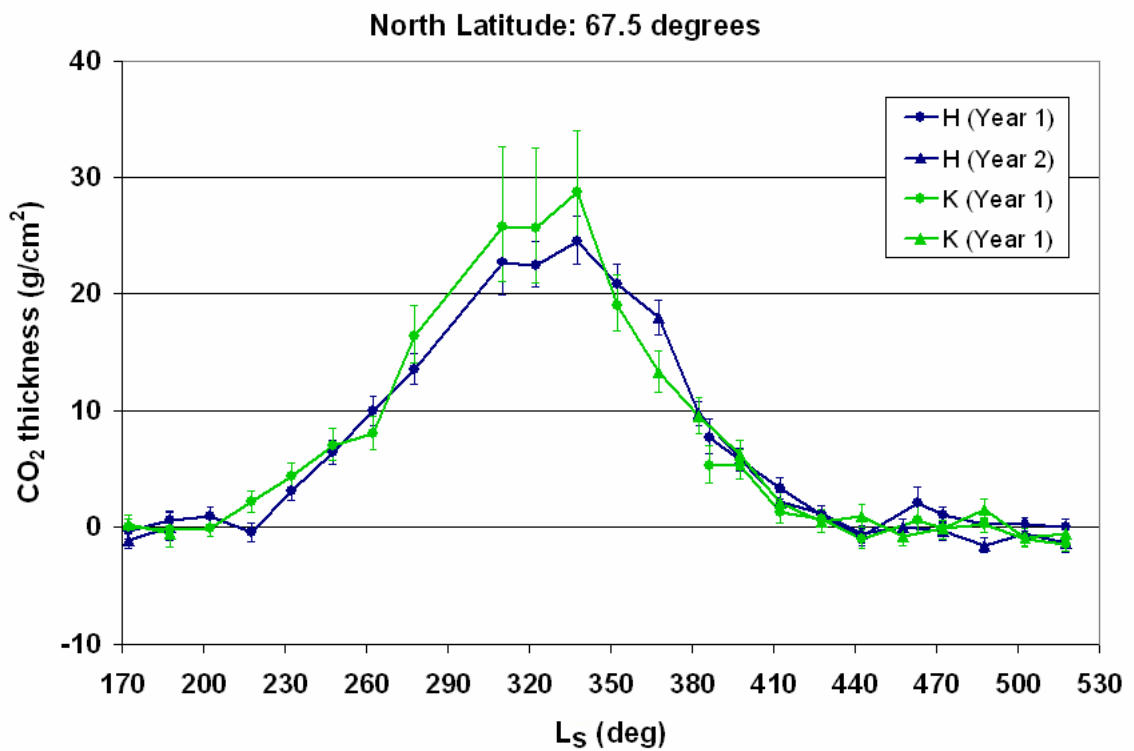


Figure 5.4: CO<sub>2</sub> columnar thickness (g/cm<sup>2</sup>) as determined by H gamma rays at 2223 keV (dark blue) and <sup>40</sup>K gamma rays at 1461 keV (green). The results shown here as a function of time (degrees of L<sub>s</sub>) represent ~1.5 Martian years of data.

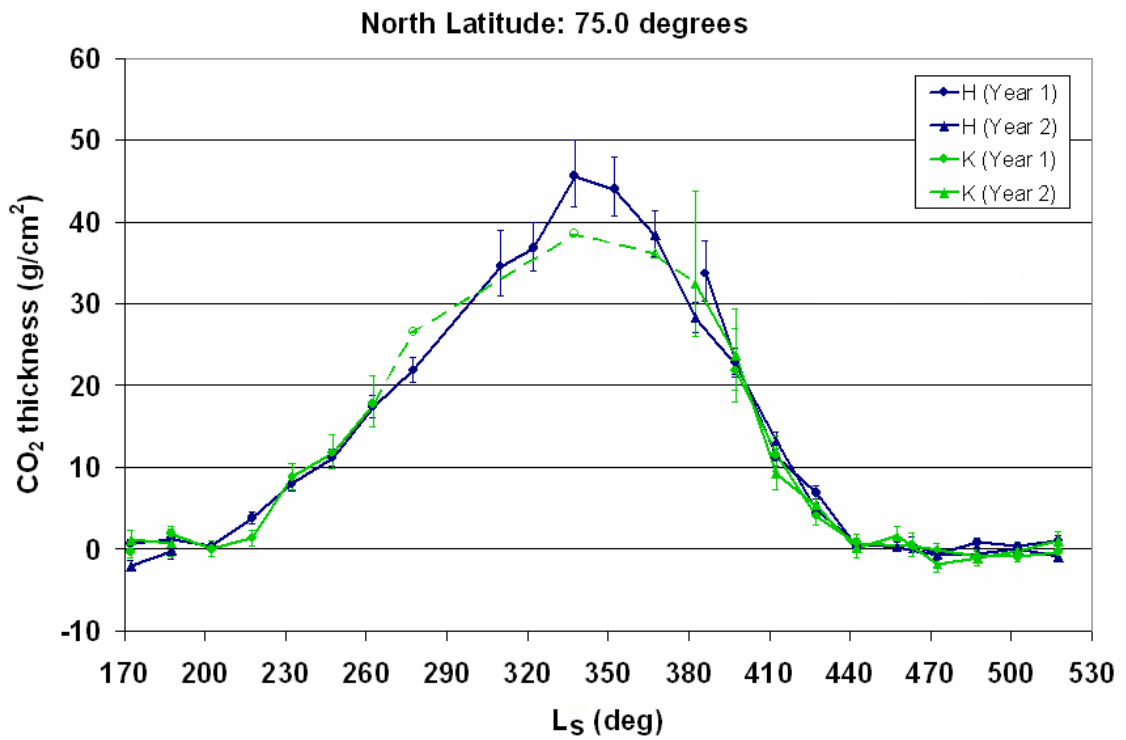


Figure 5.5: CO<sub>2</sub> columnar thickness (g/cm<sup>2</sup>) as determined by H gamma rays at 2223 keV (dark blue) and <sup>40</sup>K gamma rays at 1461 keV (green). The open data points and dashed lines signify infinite upper error bars, which occur when the gamma ray signal is almost completely attenuated. The results shown here as a function of time (degrees of L<sub>s</sub>) represent ~1.5 Martian years of data.

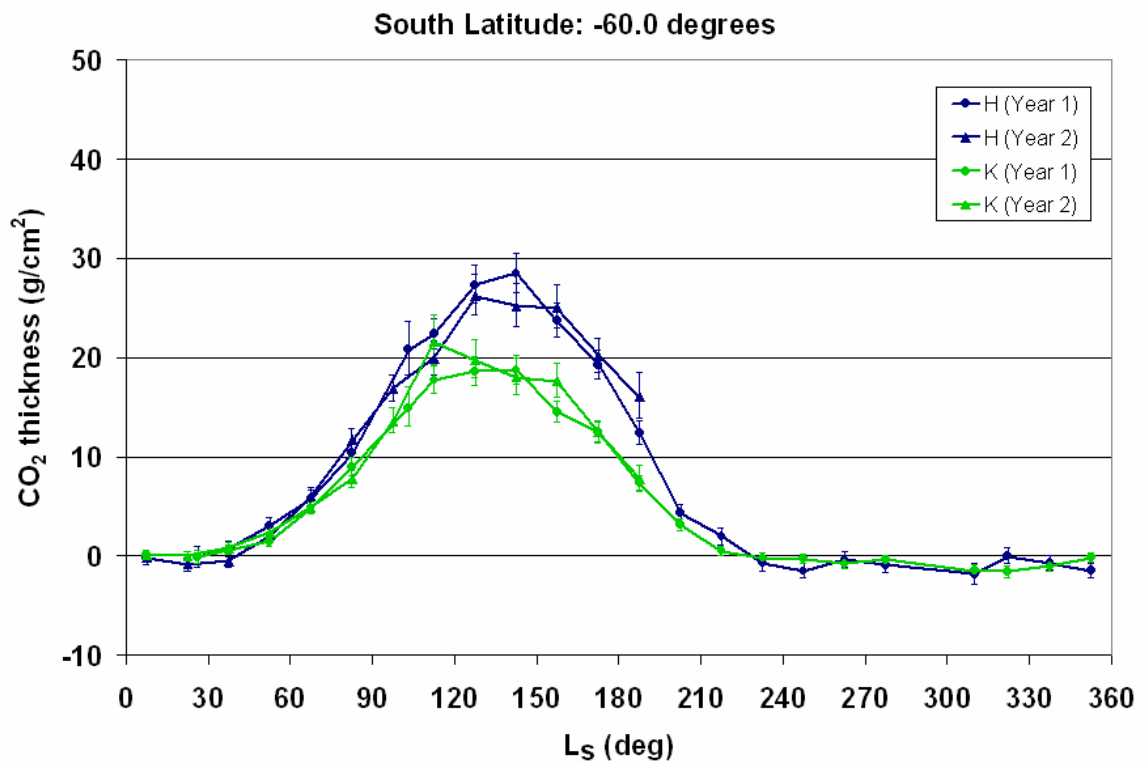


Figure 5.6: CO<sub>2</sub> columnar thickness (g/cm<sup>2</sup>) as determined by H gamma rays at 2223 keV (dark blue) and <sup>40</sup>K gamma rays at 1461 keV (green). The results shown here as a function of time (degrees of L<sub>s</sub>) represent ~1.5 Martian years of data.

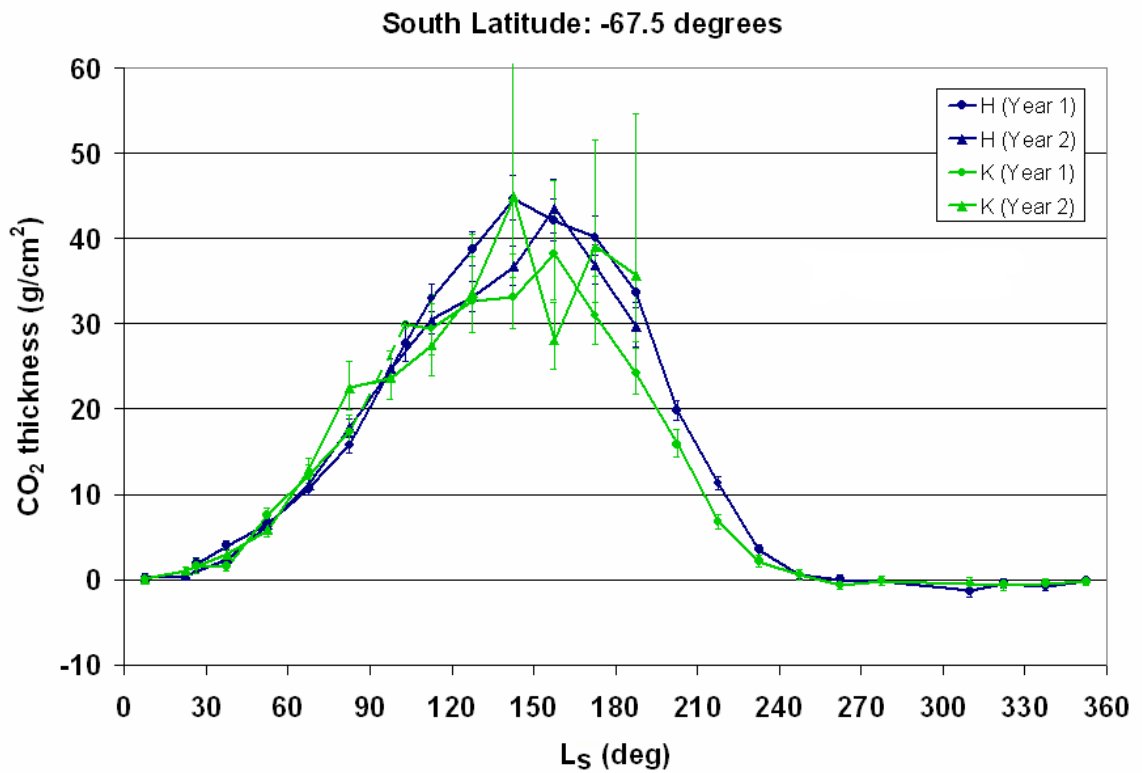


Figure 5.7: CO<sub>2</sub> columnar thickness (g/cm<sup>2</sup>) as determined by H gamma rays at 2223 keV (dark blue) and <sup>40</sup>K gamma rays at 1461 keV (green). The open data points and dashed lines signify infinite upper error bars, which occur when the gamma ray signal is almost completely attenuated. The results shown here as a function of time (degrees of L<sub>s</sub>) represent ~1.5 Martian years of data.

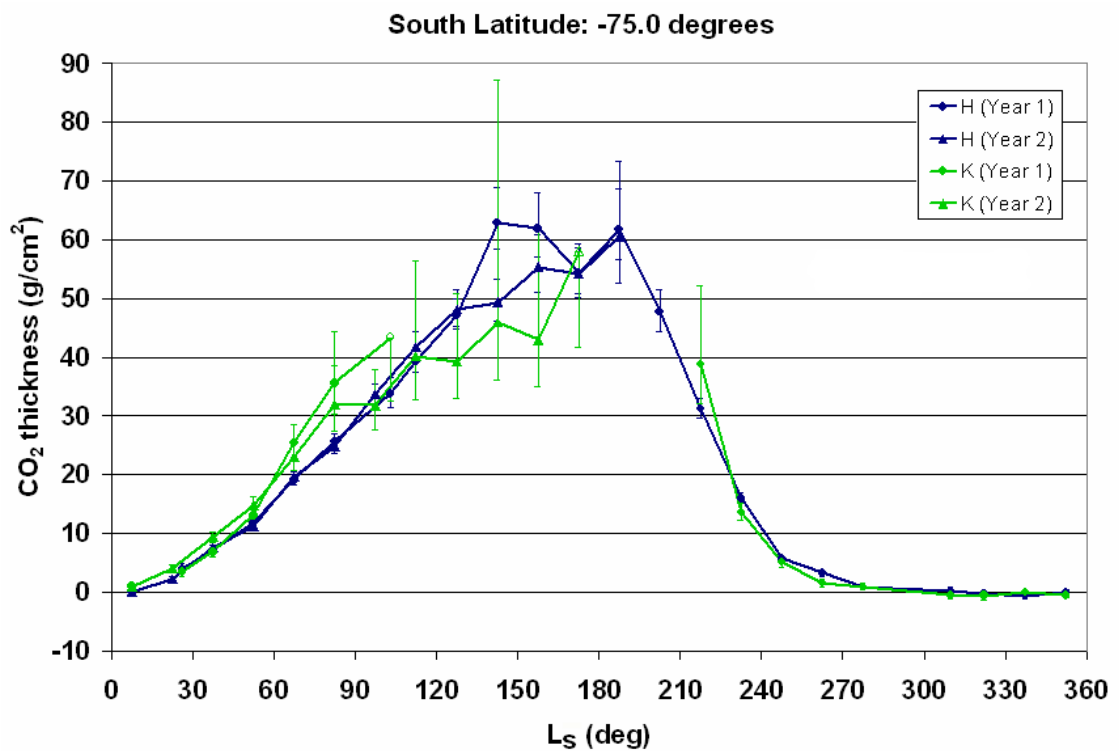


Figure 5.8: CO<sub>2</sub> columnar thickness (g/cm<sup>2</sup>) as determined by H gamma rays at 2223 keV (dark blue) and <sup>40</sup>K gamma rays at 1461 keV (green). The open data points signify infinite upper error bars, which occur when the gamma ray signal is almost completely attenuated. No data points are plotted during periods when the gamma ray signal is blocked entirely. The results shown here as a function of time (degrees of L<sub>s</sub>) represent ~1.5 Martian years of data.

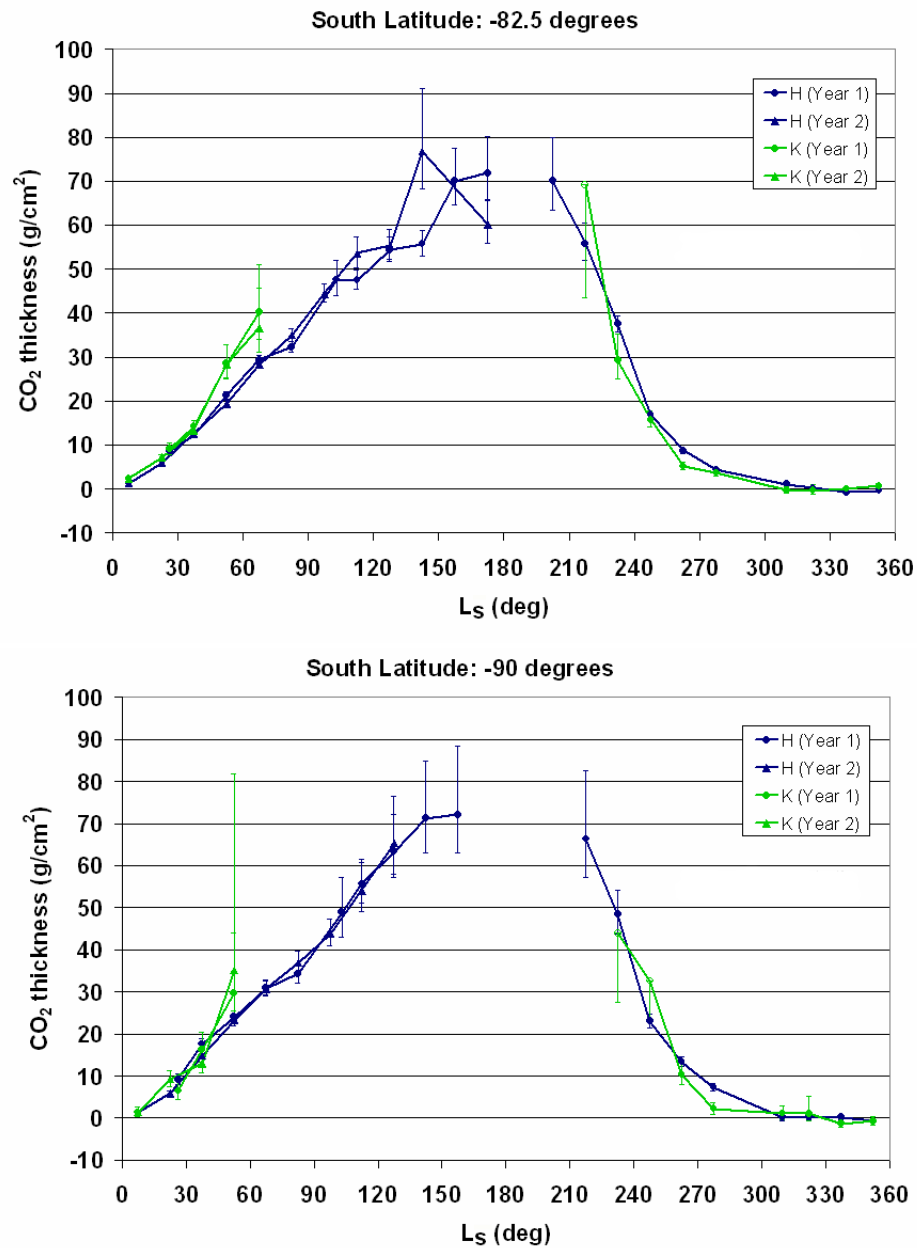


Figure 5.9: CO<sub>2</sub> columnar thickness (g/cm<sup>2</sup>) as determined by H gamma rays at 2223 keV (dark blue) and <sup>40</sup>K gamma rays at 1461 keV (green). The open data points signify infinite upper error bars, which occur when the gamma ray signal is almost completely attenuated. No data points are plotted during periods when the gamma ray signal is blocked entirely. It is clear that the <sup>40</sup>K signal is not sufficient to measure thick frost, but it provides a good check of the H-based results at lower frost depths. The results shown here as a function of time (degrees of L<sub>s</sub>) represent ~1.5 Martian years of data.

limits of using  $^{40}\text{K}$  gamma rays to derive Martian polar frost thickness. Again, at  $\sim 40 \text{ g/cm}^2$  and deeper, the K signal error bars are large or infinite, or the gamma ray signal vanishes completely (after subtraction of the satellite background radiation). These top south polar latitudes also show that the H gamma ray signal becomes completely attenuated around  $70 - 75 \text{ g/cm}^2$ . Up until the total attenuation point for K, however, the H and K results correspond very well for the timing and rate of the onset of seasonal frost condensation and then the sublimation period as the pole returns to its seasonal-frost-free state. Therefore, verification of the GRS  $\text{CO}_2$  measurements by comparing results derived from both independent gamma ray signals still remains advantageous and encouraging.

Unfortunately, because the weaker 1461 keV gamma rays are attenuated completely at such a low frost columnar thickness, not much information can be obtained during times of peak winter  $\text{CO}_2$  condensation. In addition, the corrections described at the end of Section 3.2.4 for interferences of the K gamma ray line require significant effort to implement at a fundamental GRS data processing level. This task has not yet been completed and has been delegated for future work. For both of these reasons, the remainder of the GRS-based seasonal frost results and conclusions detailed in this chapter are derived exclusively from the stronger 2223 keV gamma ray signal.

## 5.2.2 Previous Model Predictions: NASA Ames Research Center Mars General Circulation Model (ARC GCM)

The ARC GCM is a Martian atmospheric model that predicts the exchange of carbon dioxide between the atmosphere and the ground during the process of seasonal condensation and sublimation. It accounts for atmospheric dynamics, albedo, thermal inertia, and other surface thermal properties, and the influence of Martian dust on the  $\text{CO}_2$  deposition rate. The model, along with predicting atmospheric values that match the variations in pressure observed by the Viking landers, can be utilized to determine the expected  $\text{CO}_2$  at any given location on Mars for a specific time.

This GCM outputs data at increments of sixteen times per sol (Martian day)

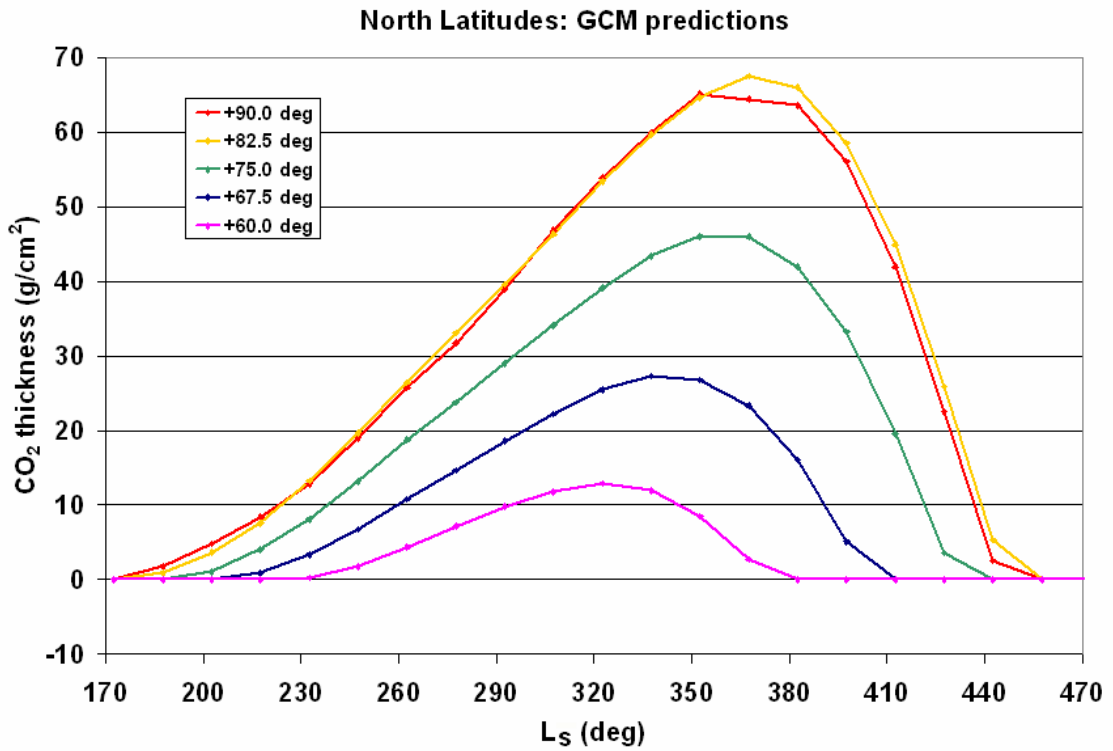


Figure 5.10: NASA ARC Mars GCM predictions for the condensation and sublimation of seasonal carbon dioxide frost over time for the north pole. The plot represents the model data averaged over periods of  $15^\circ$  of  $L_s$  and into  $7.5^\circ$  latitude by  $360^\circ$  longitude bands centered at  $60^\circ\text{N}$ ,  $67.5^\circ\text{N}$ ,  $75^\circ\text{N}$ , and  $82.5^\circ\text{N}$ . The topmost annuli indicated at  $90^\circ\text{N}$  is  $3.75^\circ$  wide.

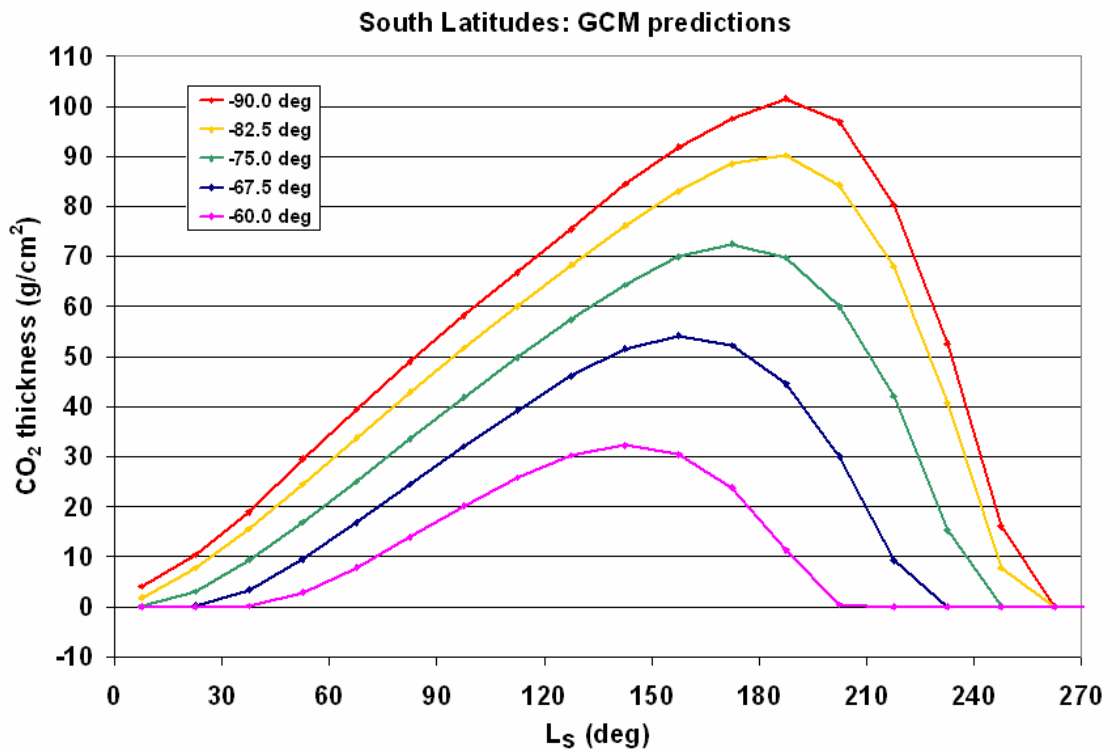


Figure 5.11: NASA ARC Mars GCM predictions for the condensation and sublimation of seasonal carbon dioxide frost over time for the south pole. The plot represents the model data averaged over periods of  $15^\circ$  of  $L_s$  and into  $7.5^\circ$  latitude by  $360^\circ$  longitude bands centered at  $60^\circ\text{S}$ ,  $67.5^\circ\text{S}$ ,  $75^\circ\text{S}$ , and  $82.5^\circ\text{S}$ . The polar annuli indicated at  $90^\circ\text{S}$  is  $3.75^\circ$  wide.

for one Mars year in  $7.5^\circ$  latitude by  $9.0^\circ$  longitude cells (Haberle et al., 1999). The horizontal grid structure employed does not center a full grid cell over the pole, but instead has a top latitude grid width of  $3.75^\circ$ . The model's vertical grid for these simulations extends from the surface to an altitude of approximately 80 km to the 0.0001 mbar level. The  $\text{CO}_2$  saturation temperature at any given location is based upon the local  $\text{CO}_2$  gas pressure at that location. The  $\text{CO}_2$  is modelled to condense at those places where the local temperature is less than the  $\text{CO}_2$  saturation temperature. The condensed  $\text{CO}_2$  is assumed to fall immediately to the surface as 'snow' in these simulations. The GCM accounts for solar and thermal infrared absorption and re-emission by  $\text{CO}_2$  and suspended dust when calculating radiative heating rates. It also includes the effects of varying diurnal and seasonal insolation, as well as latent heat changes due to the deposition/sublimation of  $\text{CO}_2$ . For further information and details about recent model updates and work currently in progress, see the last few paragraphs in Section 2.3.2 and Haberle et al. (1999).

I have utilized the well-known NASA ARC GCM version 1.7.1, run 2002.17 for the research presented here. For comparison to the GRS data, the output carbon dioxide values have been averaged into  $7.5^\circ$ -wide latitude bands and into intervals of  $15^\circ$  of  $L_s$  (corresponding to the time periods used in the GRS data processing and summation). The results of these GCM averages for the condensation and sublimation of seasonal  $\text{CO}_2$  in terms of columnar thickness ( $\text{g}/\text{cm}^2$ ) over time for latitude bands centered at  $\pm 60^\circ$  and poleward can be seen in Figures 5.10 and 5.11. Each of the latitude bands shown in these figures will be plotted individually along with the corresponding  $\text{CO}_2$  columnar thickness results from the GRS in Section 5.2.3. I have also included a detailed analysis and comparison discussion there.

### 5.2.3 GRS Results Compared to Model Predictions and Other Independent Observations

In this section, I compare the GRS  $\text{CO}_2$  columnar thickness results to the NASA ARC GCM predictions and other spacecraft observations. It is advantageous to sum and bin the GRS data into zonal spatial bands of  $7.5^\circ$  of latitude by  $360^\circ$  of

longitude as described above to correspond to the divisions used in the predictive models of the ARC GCM. (For calculations and comparisons of total condensed CO<sub>2</sub> *mass* presented in Section 5.4, 5°-wide latitude bands are used for better spatial resolution.) The CO<sub>2</sub> progression observed by Mars Odyssey's GRS can be compared to the GCM-calculated evolution for both north and south poles.

Figures 5.12 through 5.21 show the CO<sub>2</sub> thickness values predicted by the GCM in Section 5.2.2 as compared to those calculated using the H gamma ray attenuation results displayed in Section 5.2.1. These ten plots cover the five north and five south polar zonal latitude regions that accumulate seasonal frost. Represented by data points, the gamma ray results for the first Mars year (circles) and second Mars year (horizontal dashes) are shown. The GCM model results are displayed as a solid curve. Both latitude bands and time periods are represented by their midpoint value. Notice that, in accordance with the GCM partitions, the topmost latitude band for each pole (labelled  $\pm 90^\circ$ ), is only 3.75° of latitude in width, after which, all zonal bands are 7.5° wide. The error bars on all plots shown represent one standard deviation (one sigma) and correspond to a 68.27% confidence interval.

With the obvious exception of the summer time periods for each pole when the surface is completely seasonal-frost-free, the overall seasonal frost depth at any given date increases as we move toward the poles for both hemispheres, and the vertical CO<sub>2</sub> thickness scales on the plots change accordingly. As sublimation of the CO<sub>2</sub> frost to the atmosphere occurs on one pole, the growth of the CO<sub>2</sub> cap occurs on the opposite pole. Growth/retreat takes place at a fairly constant rate as the seasons advance. In the north, the CO<sub>2</sub> cap coverage near the pole as shown by both the GRS and the GCM results generally spans  $L_s = 170^\circ$  to  $460^\circ$  from the beginning of the condensation of carbon dioxide from the atmosphere to the point when all frost has once again sublimed. (Values of  $L_s$  greater than  $360^\circ$  listed here simply represent a different Martian year and can be converted to a number within the standard  $0^\circ$  -  $360^\circ$  convention by subtracting  $360^\circ$  from the given value.) For regions near the cap edge, however, the frosty season is approximately from  $230^\circ$  to  $390^\circ$  of  $L_s$ . (The GRS calculations show a lingering coverage of less than  $5 \text{ g/cm}^2$  of CO<sub>2</sub> for longer than

predicted by the GCM.) In either case, this indicates that the edge of the northern seasonal cap forms later than the frost at the tip of the pole, and it begins to recede while the snowfall at the pole is still in progress. The observation that the maximum CO<sub>2</sub> columnar thickness at the pole is reached at approximately  $L_s = 367.5^\circ$ , but at  $L_s = 322.5^\circ$  for the frost cap edge also supports this conclusion. Similarly, in the southern hemisphere, both gamma ray studies and the GCM predictions confirm that the interval of condensation at the CO<sub>2</sub> frost edge begins later and ends earlier than the frost accumulation period at the pole. The peak snow depth at the cap boundary occurs approximately  $45^\circ$  of  $L_s$  sooner than at the highest latitude bands. These trends were also noted for the south pole from NS observations (Prettyman et al., 2004).

Beginning with  $60^\circ\text{N}$ , the latitude closest to the equator that is plotted for the north pole, it is apparent that the columnar thickness of CO<sub>2</sub> displayed is in general agreement for both the GRS data and the GCM model. The gamma ray observations show a maximum amount of frost near the cap edge that is a few  $\text{g}/\text{cm}^2$  less than what the GCM predicts; however, if the plotted 1-sigma error bars are increased to 2-sigma, the CO<sub>2</sub> columnar thickness values basically agree in magnitude and timing. In fact, for all northern latitudes shown (Figures 5.12 - 5.16), the time periods from the beginning of frost appearance to when it sublimates back into the atmosphere, as determined from the GRS and the GCM for each zonal band, are in close agreement.

For the  $67.5^\circ\text{N}$  latitude, the crocus date (time of frost disappearance) appears to be approximately  $L_s = 415^\circ$  based on the averaged GCM data, while the gamma-determined CO<sub>2</sub> seems to linger with a few  $\text{g}/\text{cm}^2$  of frost coverage for a little longer. The crocus date determined from the HEND neutron data is  $L_s = 60^\circ = 420^\circ$ . This date is ascertained by observing when the decreasing neutron flux for the  $65^\circ\text{N}$  to  $69^\circ\text{N}$  latitude band stabilizes following sublimation (Mitrofanov et al., 2003). All three of these independent CO<sub>2</sub> frost investigations seem to be in close agreement here. For both the  $67.5^\circ\text{N}$  and  $75^\circ\text{N}$  zonal bands, Figures 5.13 and 5.14 show that the temporal and latitudinal dependence of the CO<sub>2</sub> deposition cycle as determined by H

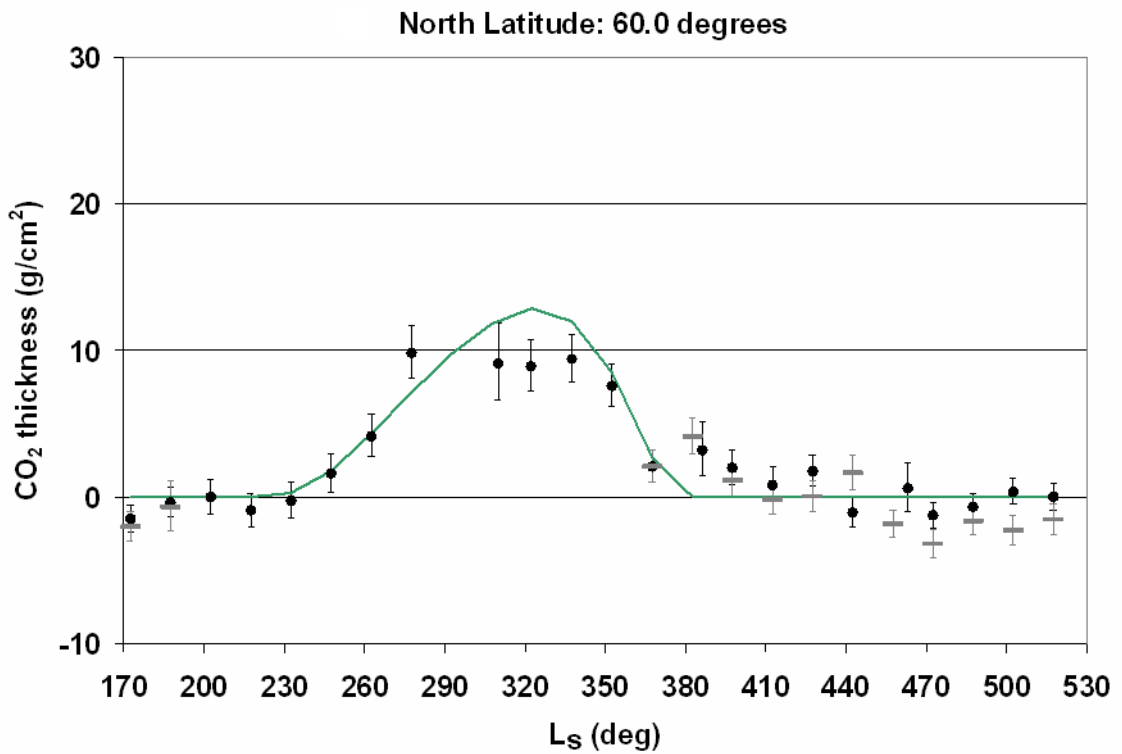


Figure 5.12: Thickness of seasonal CO<sub>2</sub> frost in g/cm<sup>2</sup> as a function of time (degrees of L<sub>s</sub>). North (Figures 5.12 through 5.16) and south (Figures 5.17 through 5.21) polar data is presented for zonal latitude bands of 7.5° by 360° longitude centered at ±60°, ±67.5°, ±75°, ±82.5° with the exception of the ±90° bands, which are 3.75° wide. GRS results from observations of the first and second (partial) Mars years are represented by circular and horizontal-dash data points, respectively. For comparison at each latitude, the corresponding CO<sub>2</sub> frost accumulation predicted by the ARC GCM version 2002.17 is shown as a solid curve.

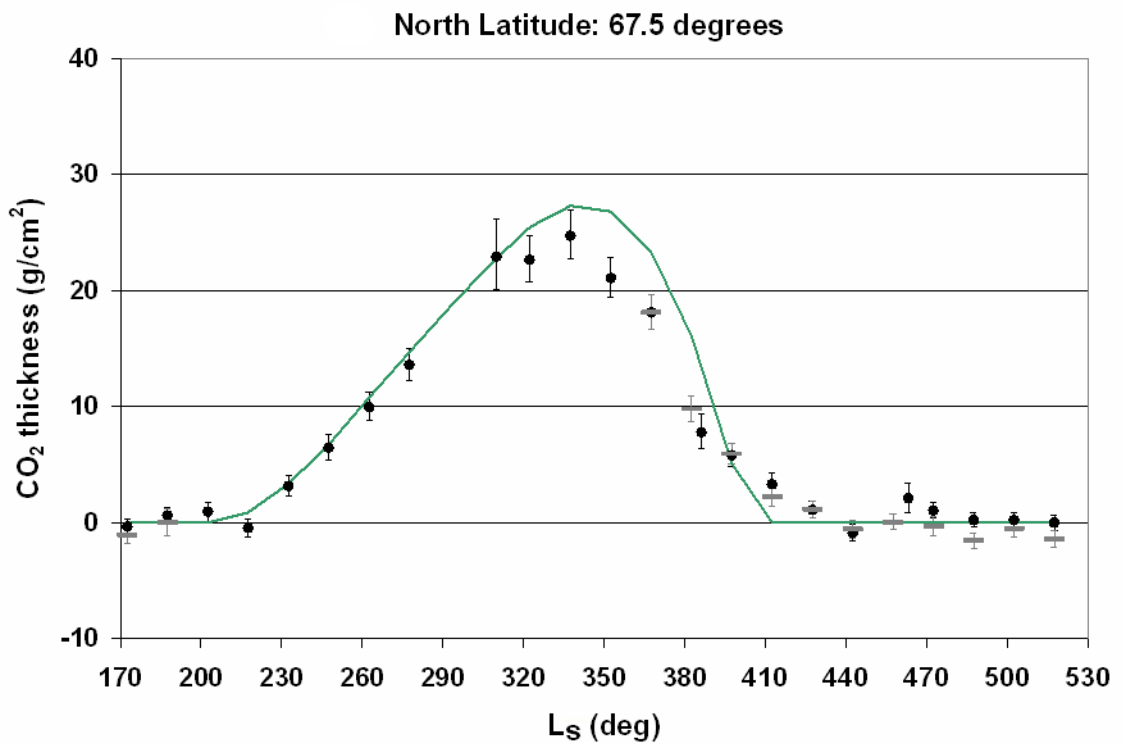


Figure 5.13: Thickness of seasonal CO<sub>2</sub> frost in g/cm<sup>2</sup> as a function of time (degrees of L<sub>s</sub>). North (Figures 5.12 through 5.16) and south (Figures 5.17 through 5.21) polar data is presented for zonal latitude bands of 7.5° by 360° longitude centered at ±60°, ±67.5°, ±75°, ±82.5° with the exception of the ±90° bands, which are 3.75° wide. GRS results from observations of the first and second (partial) Mars years are represented by circular and horizontal-dash data points, respectively. For comparison at each latitude, the corresponding CO<sub>2</sub> frost accumulation predicted by the ARC GCM version 2002.17 is shown as a solid curve.

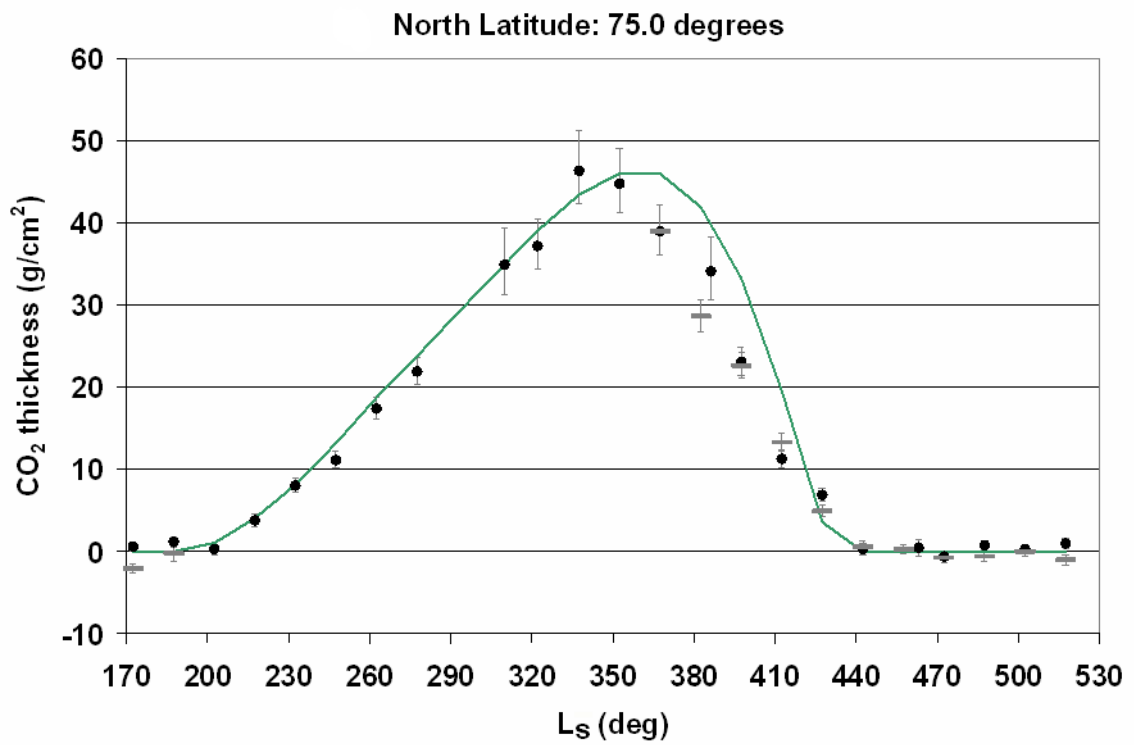


Figure 5.14: Thickness of seasonal CO<sub>2</sub> frost in g/cm<sup>2</sup> as a function of time (degrees of L<sub>s</sub>). North (Figures 5.12 through 5.16) and south (Figures 5.17 through 5.21) polar data is presented for zonal latitude bands of 7.5° by 360° longitude centered at ±60°, ±67.5°, ±75°, ±82.5° with the exception of the ±90° bands, which are 3.75° wide. GRS results from observations of the first and second (partial) Mars years are represented by circular and horizontal-dash data points, respectively. For comparison at each latitude, the corresponding CO<sub>2</sub> frost accumulation predicted by the ARC GCM version 2002.17 is shown as a solid curve.

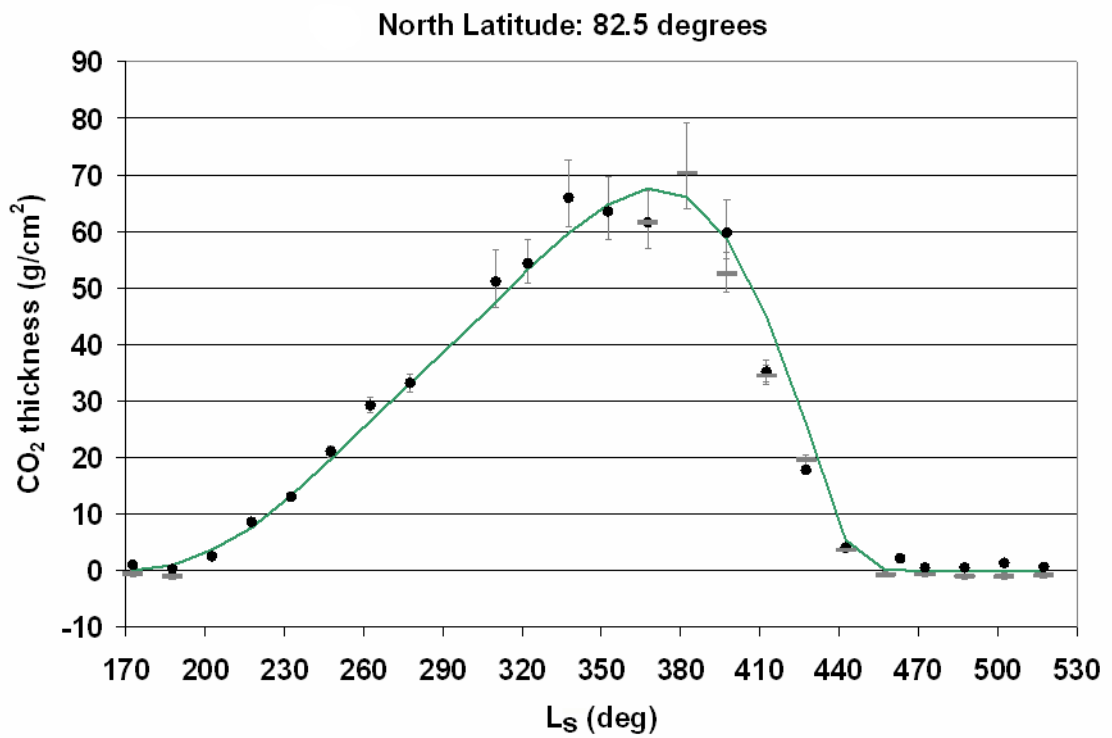


Figure 5.15: Thickness of seasonal CO<sub>2</sub> frost in g/cm<sup>2</sup> as a function of time (degrees of L<sub>s</sub>). North (Figures 5.12 through 5.16) and south (Figures 5.17 through 5.21) polar data is presented for zonal latitude bands of 7.5° by 360° longitude centered at ±60°, ±67.5°, ±75°, ±82.5° with the exception of the ±90° bands, which are 3.75° wide. GRS results from observations of the first and second (partial) Mars years are represented by circular and horizontal-dash data points, respectively. For comparison at each latitude, the corresponding CO<sub>2</sub> frost accumulation predicted by the ARC GCM version 2002.17 is shown as a solid curve.

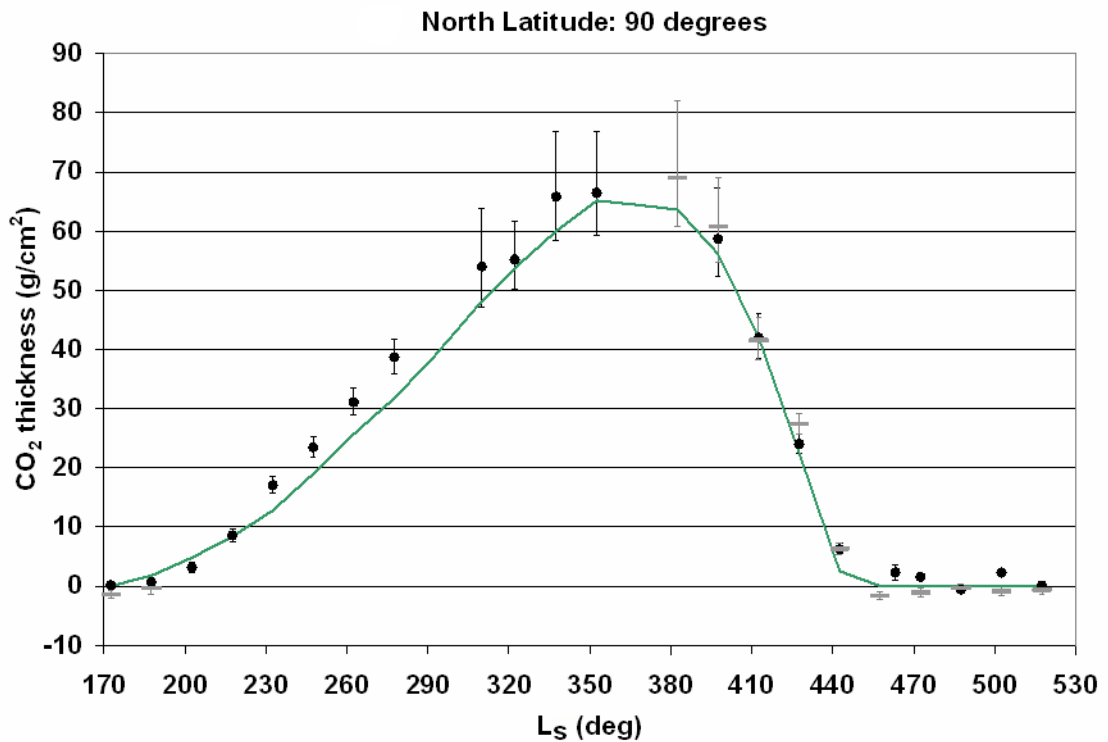


Figure 5.16: Thickness of seasonal CO<sub>2</sub> frost in g/cm<sup>2</sup> as a function of time (degrees of L<sub>s</sub>). North (Figures 5.12 through 5.16) and south (Figures 5.17 through 5.21) polar data is presented for zonal latitude bands of 7.5° by 360° longitude centered at ±60°, ±67.5°, ±75°, ±82.5° with the exception of the ±90° bands, which are 3.75° wide. GRS results from observations of the first and second (partial) Mars years are represented by circular and horizontal-dash data points, respectively. For comparison at each latitude, the corresponding CO<sub>2</sub> frost accumulation predicted by the ARC GCM version 2002.17 is shown as a solid curve.

gamma rays and as predicted by the GCM is very similar for the entire condensation period and for the late sublimation period. CO<sub>2</sub> columnar thickness as calculated from gamma rays appears to peak to a maximum slightly earlier than what the GCM reveals. After the maximum frost depth is reached (which approximately agrees within the errors with the magnitude of the GCM curves), the gamma ray results for this area, 63.75°N - 78.5°N, imply that the frost is dissipating earlier in time than in the model. However, the rate of sublimation allows the crocus date of the GRS and GCM to occur around the same L<sub>s</sub> in each band. The time of total frost sublimation at the upper latitude as observed using the HEND is 90° = 450° of L<sub>s</sub> (Mitrofanov et al., 2003), which is comparable to the GRS and the GCM results of L<sub>s</sub> = 442.5° plotted here.

At the highest north polar latitudes, the GRS and GCM data continue to correspond well and give a maximum CO<sub>2</sub> depth on the order of 70 g/cm<sup>2</sup>. Be aware that the GRS statistics of the ±90° latitude bands are not as good as at all other latitudes due to the decreased width of these bands (3.75°). In addition, the Mars Odyssey science orbit inclination is 86.9°, so the data representing these topmost annuli are actually received from polar latitude bands slightly less than 1° wide. However, because Mars Odyssey passes over the polar regions every orbit, the total time of data accumulation in these thin bands is actually 30% as much as for the next lower 7.5°-wide band. The associated error bars are on average about two times larger. Both methods for determining seasonal frost depth match very well for the frost sublimation period from L<sub>s</sub> = 360° to 460°, with the 82.5°N zonal band exhibiting the slightly earlier-than-model-predicted sublimation trend from the adjacent equatorward latitudes. In addition, HEND data also determine the completion of the sublimation period at L<sub>s</sub> = 100° = 460° for the region: 80°N to 85°N latitude (Mitrofanov et al., 2003). Altogether, these results indicate that the model used for this analysis of the GRS data (various amounts of CO<sub>2</sub> frost deposition over a 100% H<sub>2</sub>O residual ice cap near the north pole) is effectively correct.

This investigation of the north pole for 1.5 Martian years allows interannual comparisons (at least during the sublimation phase) of the CO<sub>2</sub> exchange cycle. In

general and within the error range shown here, there appears to be very little variation in frost columnar thickness or latitudinal distribution between these consecutive years. For both poles, in instances where a GRS data point appears to be missing, it is either because the satellite was in a non-operational, safe-mode configuration or because the full attenuation of the gamma rays by the seasonal frost (during periods of high frost) prevents us from obtaining meaningful results.

In the south,  $L_s = 0^\circ$  corresponds to the beginning of the fall season, and  $\text{CO}_2$  condensation can be readily observed after this date as the  $\text{CO}_2$  columnar thickness increases at all latitudes shown. Southern spring brings increasing temperatures slightly before and around  $L_s = 180^\circ$ , at which point, sublimation begins again to thin the seasonal carbon dioxide layer.

Starting with the most equatorward latitude band plotted ( $60^\circ\text{S}$ , Figure 5.17), the H gamma ray results from both Mars years show a slightly lower  $\text{CO}_2$  maximum depth than predicted by the GCM. Nevertheless, the temporal correspondence is good for the beginning of frost accumulation, its peak, and its dissipation near the cap edge. Moving closer to the pole to the  $67.5^\circ\text{S}$  band, the results correspond very well to the period forecasted by the GCM for the onset of  $\text{CO}_2$  condensation and the final dissipation of the frost back into the atmosphere. However, the overall maximum amount of seasonal frost condensed on the ground as observed by the GRS for both Martian years is on the order of  $\sim 10 \text{ g/cm}^2$  less than what is predicted by the GCM for this latitude band. A trend that can be seen for the data at this latitude and those poleward is that although the initial and final seasonal cap timing corresponds to the GCM results, the gamma ray observations imply the seasonal  $\text{CO}_2$  tends to accumulate slower, peak slightly lower, and then also dissipate at a slower rate compared to what is expected from the GCM model. In fact, the GRS data for these latitudes consistently show a minor amount of  $\text{CO}_2$  remaining in the seasonal cap for a few degrees of  $L_s$  after the GCM indicates the pole should be frost-free.

Comparisons can be made between the south polar condensation periods of the two Mars years observed. The data suggest that there is not a large difference in the

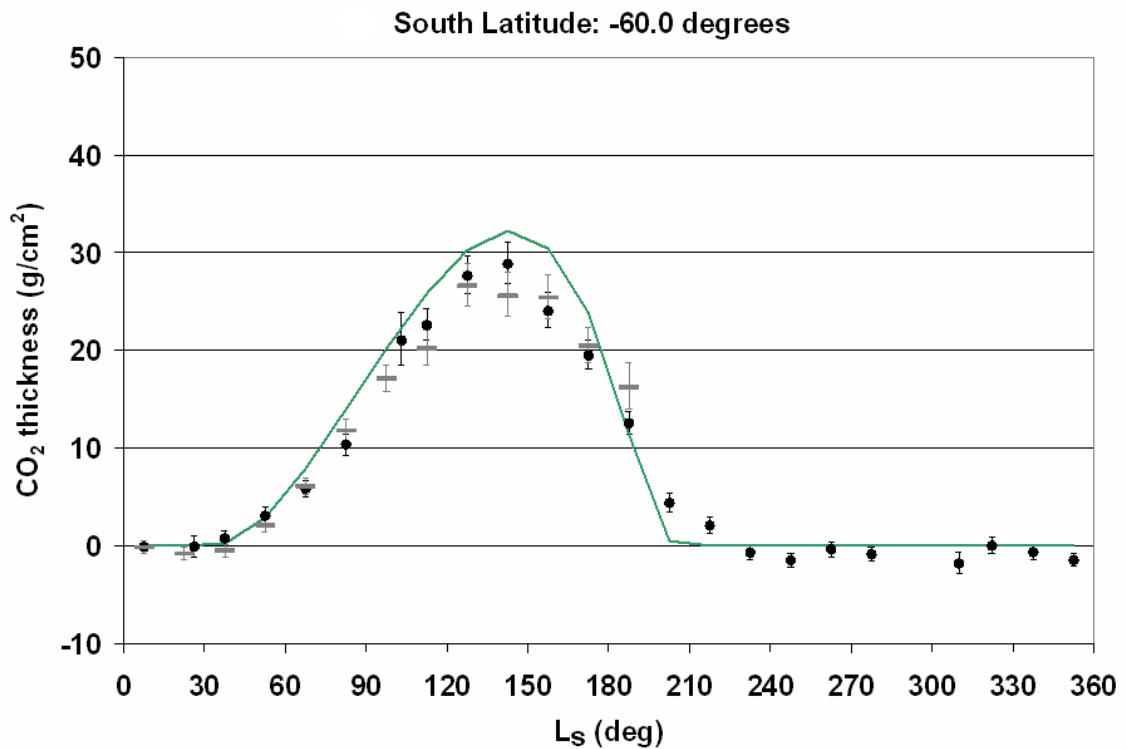


Figure 5.17: Thickness of seasonal CO<sub>2</sub> frost in g/cm<sup>2</sup> as a function of time (degrees of L<sub>s</sub>). North (Figures 5.12 through 5.16) and south (Figures 5.17 through 5.21) polar data is presented for zonal latitude bands of 7.5° by 360° longitude centered at ±60°, ±67.5°, ±75°, ±82.5° with the exception of the ±90° bands, which are 3.75° wide. GRS results from observations of the first and second (partial) Mars years are represented by circular and horizontal-dash data points, respectively. For comparison at each latitude, the corresponding CO<sub>2</sub> frost accumulation predicted by the ARC GCM version 2002.17 is shown as a solid curve.

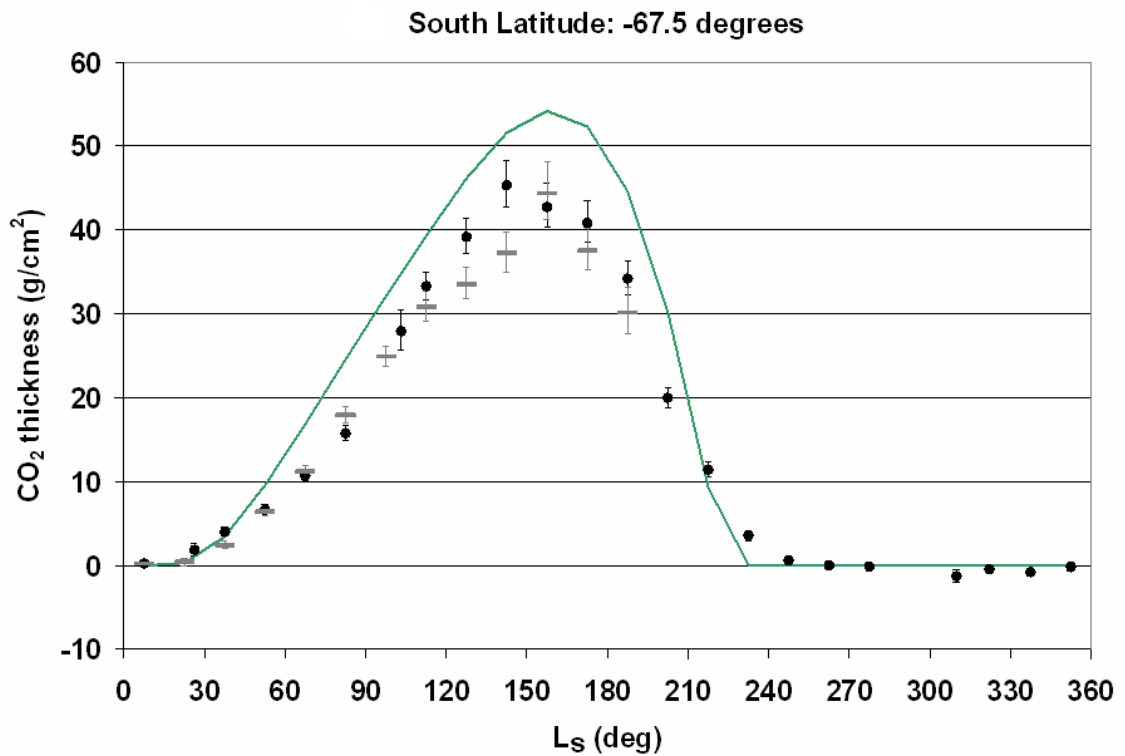


Figure 5.18: Thickness of seasonal CO<sub>2</sub> frost in g/cm<sup>2</sup> as a function of time (degrees of L<sub>s</sub>). North (Figures 5.12 through 5.16) and south (Figures 5.17 through 5.21) polar data is presented for zonal latitude bands of 7.5° by 360° longitude centered at ±60°, ±67.5°, ±75°, ±82.5° with the exception of the ±90° bands, which are 3.75° wide. GRS results from observations of the first and second (partial) Mars years are represented by circular and horizontal-dash data points, respectively. For comparison at each latitude, the corresponding CO<sub>2</sub> frost accumulation predicted by the ARC GCM version 2002.17 is shown as a solid curve.

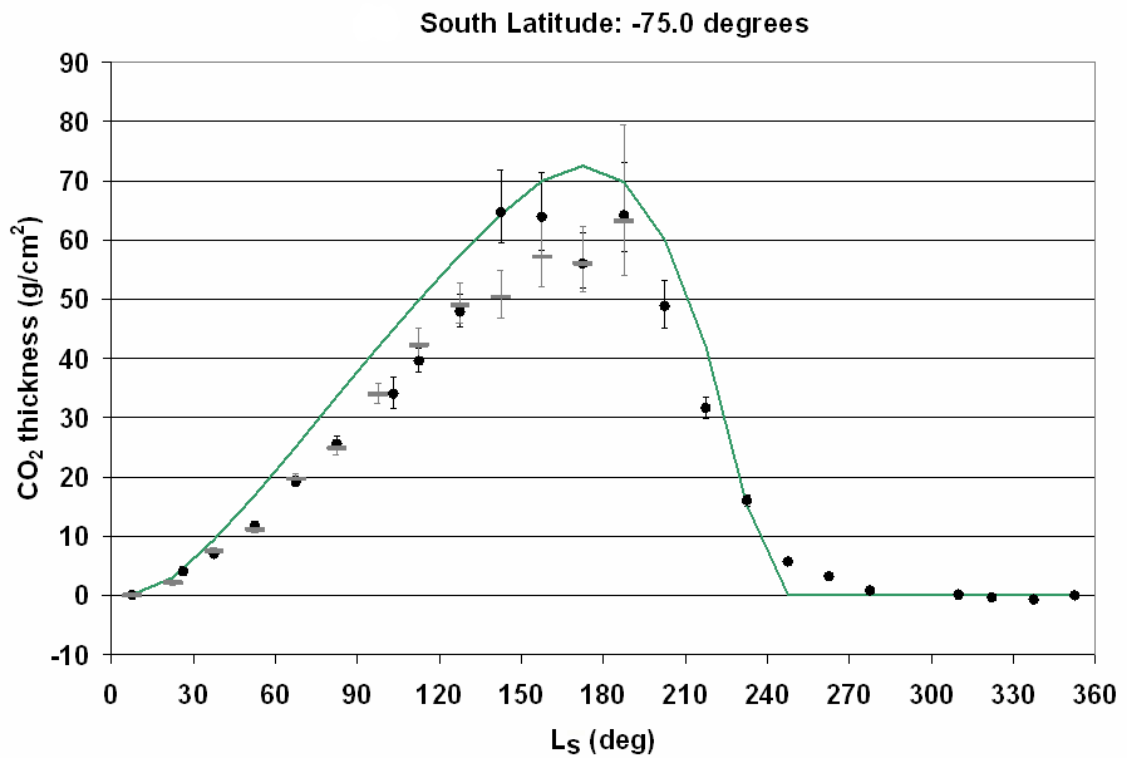


Figure 5.19: Thickness of seasonal CO<sub>2</sub> frost in g/cm<sup>2</sup> as a function of time (degrees of L<sub>s</sub>). North (Figures 5.12 through 5.16) and south (Figures 5.17 through 5.21) polar data is presented for zonal latitude bands of 7.5° by 360° longitude centered at ±60°, ±67.5°, ±75°, ±82.5° with the exception of the ±90° bands, which are 3.75° wide. GRS results from observations of the first and second (partial) Mars years are represented by circular and horizontal-dash data points, respectively. For comparison at each latitude, the corresponding CO<sub>2</sub> frost accumulation predicted by the ARC GCM version 2002.17 is shown as a solid curve.

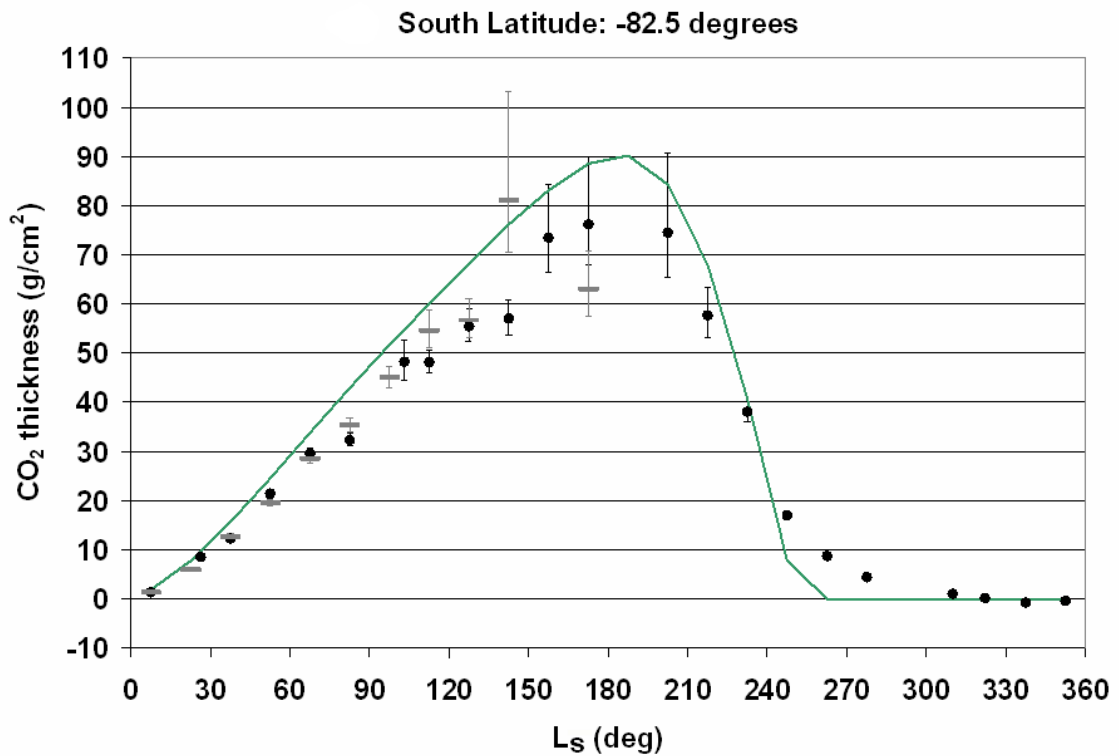


Figure 5.20: Thickness of seasonal CO<sub>2</sub> frost in g/cm<sup>2</sup> as a function of time (degrees of L<sub>s</sub>). North (Figures 5.12 through 5.16) and south (Figures 5.17 through 5.21) polar data is presented for zonal latitude bands of 7.5° by 360° longitude centered at ±60°, ±67.5°, ±75°, ±82.5° with the exception of the ±90° bands, which are 3.75° wide. GRS results from observations of the first and second (partial) Mars years are represented by circular and horizontal-dash data points, respectively. For comparison at each latitude, the corresponding CO<sub>2</sub> frost accumulation predicted by the ARC GCM version 2002.17 is shown as a solid curve.

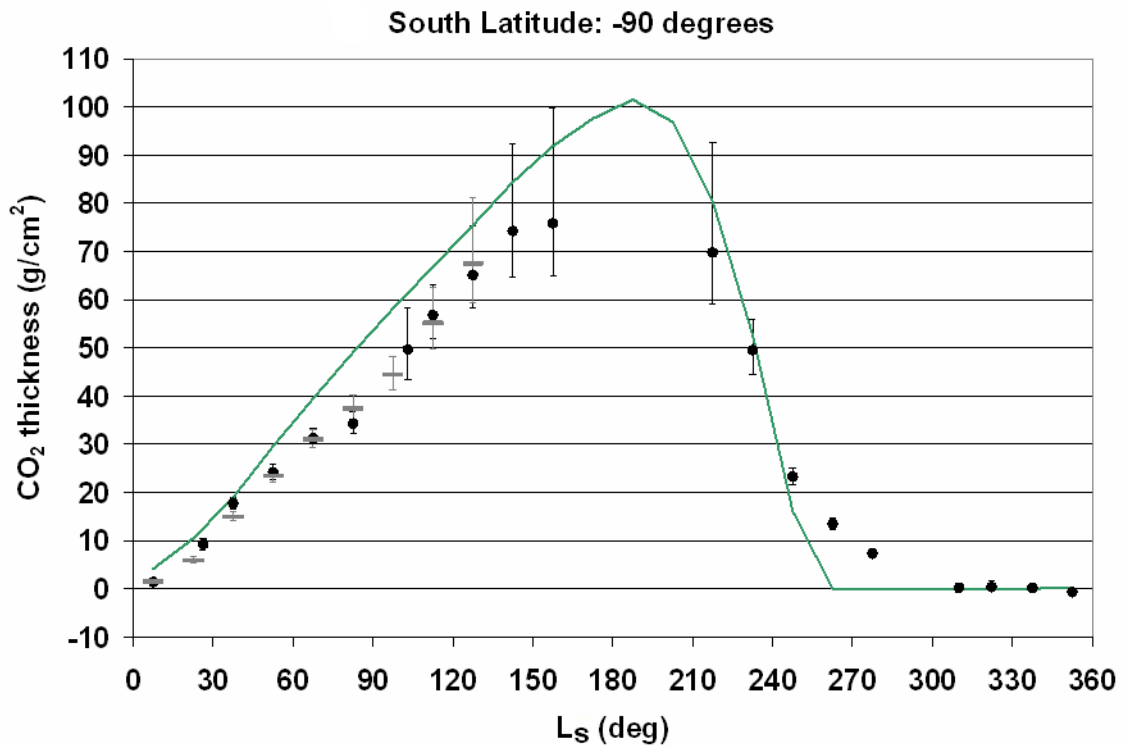


Figure 5.21: Thickness of seasonal CO<sub>2</sub> frost in g/cm<sup>2</sup> as a function of time (degrees of L<sub>s</sub>). North (Figures 5.12 through 5.16) and south (Figures 5.17 through 5.21) polar data is presented for zonal latitude bands of 7.5° by 360° longitude centered at ±60°, ±67.5°, ±75°, ±82.5° with the exception of the ±90° bands, which are 3.75° wide. GRS results from observations of the first and second (partial) Mars years are represented by circular and horizontal-dash data points, respectively. For comparison at each latitude, the corresponding CO<sub>2</sub> frost accumulation predicted by the ARC GCM version 2002.17 is shown as a solid curve.

magnitude or distribution of seasonal CO<sub>2</sub> condensation. The variations between the two years appear to increase as the frost becomes thicker. However, during these time periods, the scatter and error bars of the data points also increase because of worse statistics from a weak gamma ray signal due to the large CO<sub>2</sub> overburden. For the most part, the scatter of the points is not in a uniform direction, so it does not imply an obvious difference in frost level from year to year. The error bars shown are 1-sigma errors, so it can be expected that around one-third of the data points will not overlap. At the 2-sigma level, one would expect about 95% of the points to agree within error, which in fact, they do.

It is worth mentioning that for lower values, the most sensitive measurements of CO<sub>2</sub> column density are obtained from gamma ray spectrometry; however, it is evident that even hydrogen gamma ray studies (which is the only gamma ray that is effectively strong enough for this type of study) encounter limits in the determination of CO<sub>2</sub> depths greater than approximately 75 g/cm<sup>2</sup>. At high CO<sub>2</sub> columnar thickness where the gamma ray signal approaches full attenuation, neutrons provide the most effective frost measurements (see Feldman et al. (2003), and Prettyman et al. (2004) for detailed polar CO<sub>2</sub> analyses using neutron data: seasonal north and residual south polar caps, respectively). At the extreme southern latitudes, the gamma rays cannot penetrate the seasonal frost completely at its maximum, so we utilize complementary results inferred from the NS, the HEND, or from the Mars GCMs. At the tip of the south pole, the ARC GCM predicts a maximum zonally averaged frost thickness of  $\sim 100$  g/cm<sup>2</sup> at  $L_s = 188^\circ$ .

### 5.3 CO<sub>2</sub> as a Function of Latitude

The derived CO<sub>2</sub> columnar thickness results presented in Section 5.2.3 can also be plotted as a function of latitude. In Figures 5.22 through 5.25, the H-based CO<sub>2</sub> results are displayed in this alternate way for periods of increasing and decreasing frost at each pole. Each curve of GRS data points represents a period of 15° of  $L_s$ . Results from the first Mars year are shown as solid curves, while the partial second

Mars year of data are plotted as dashed curves. Each time period is designated by a unique color that is consistent between the two years of data. For time periods that were shortened because Mars Odyssey entered a safe-mode configuration, the color of the anomalous period is tinted to differ slightly from the full-length period at the same  $L_s$  of the other Mars year. This occurs at  $L_s = 22.5^\circ$  versus  $26.25^\circ$ , and at  $L_s = 97.5^\circ$  versus  $103.125^\circ$ . All time periods are represented by their midpoint  $L_s$  value. This method of plotting is advantageous because it gives a feel for what a cross-section of the seasonal polar cap might look like at any given time. The thicker frost at the pole gradually decreases as one looks at more equatorward latitudes. The rate of  $\text{CO}_2$  condensation and sublimation (and variations thereof) is easily analyzed by observing the frost overburden at equally spaced time intervals.

In Figure 5.22, seasonal frost on the north pole is plotted for those time periods in which the frost is subliming. When Mars Odyssey arrived at Mars and extended its boom, the northern seasonal cap was at a maximum. Starting at  $L_s = 26.25^\circ$ , the condensed frost then began to decrease over time until all of the northern  $\text{CO}_2$  returned to the atmosphere. It remained in the seasonal-frost-free state until about  $L_s = 187.5^\circ$ . At this point, Figure 5.23 starts with the same  $L_s = 187.5^\circ$  line and then shows the subsequent time periods where the  $\text{CO}_2$  begins to condense once again. The  $\text{CO}_2$  increases in columnar thickness consistently into the next Mars year until  $\sim 7.5^\circ$  of  $L_s$  shown by the dashed blue line. (When the gamma ray signal is completely attenuated, no data points are shown in these plots. This occurs at the topmost latitudes during maximum  $\text{CO}_2$  accumulation. Open data points are plotted for those points with unreasonably large or infinite error bars, and therefore, have a high uncertainty.) The dashed  $L_s = 7.5^\circ$  line in Figure 5.23 is also shown in Figure 5.22 because this time period begins the second GRS-observed, north polar sublimation period. Notice in Figure 5.22 that the data at  $L_s = 7.5^\circ$  is nearly linear as a function of latitude. This is characteristic of the manner in which the seasonal frost condenses uniformly at all latitudes. The subsequent time period at  $L_s = 22.5^\circ$  (Yr 2) clearly illustrates that the seasonal cap edge thins and begins sublimation before the more poleward latitudes. This creates a steeper polar cap

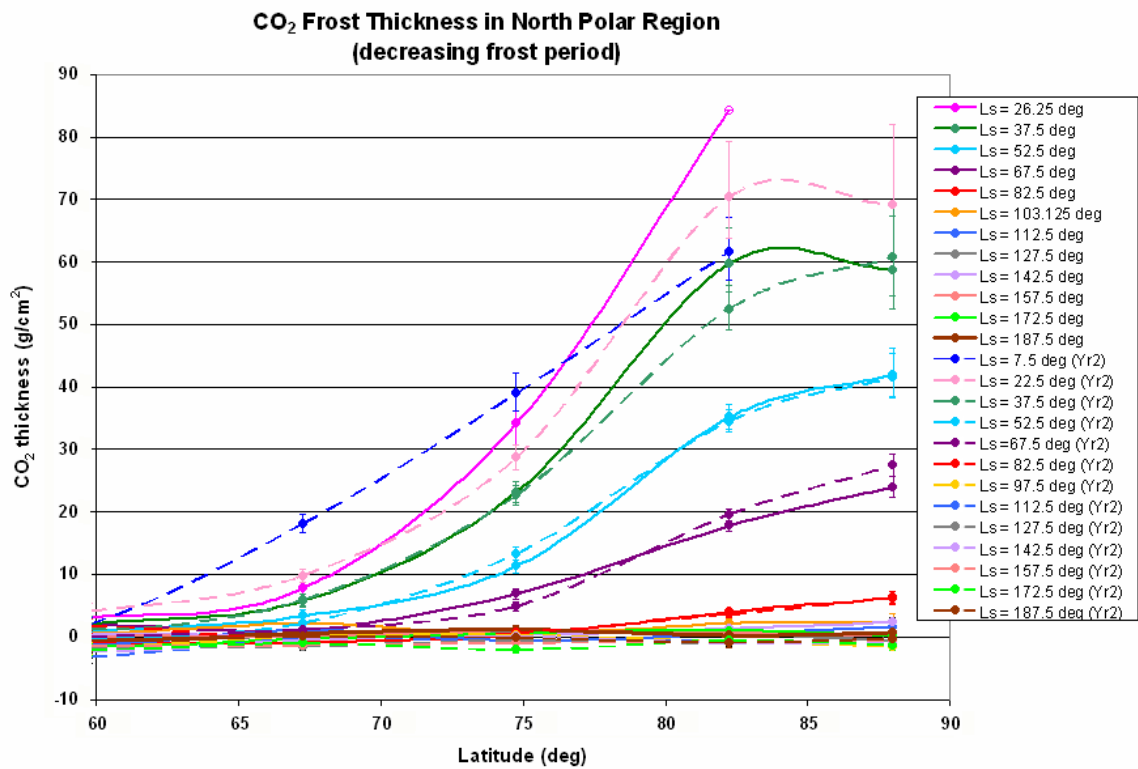


Figure 5.22: CO<sub>2</sub> columnar thickness (g/cm<sup>2</sup>) as a function of Martian latitude. Time increments of approximately 15° of L<sub>s</sub> show the progression of the seasonal frost sublimation period at Mars' north pole. Solid curves represent data from the first Mars year of observation; dashed curves indicate GRS-derived data from the second (partial) Mars year observed. The colors are consistent for like times of each year. Missing or open data points indicate uncertain data derived from a weak or fully attenuated H gamma ray signal due to a thick seasonal CO<sub>2</sub> overburden.

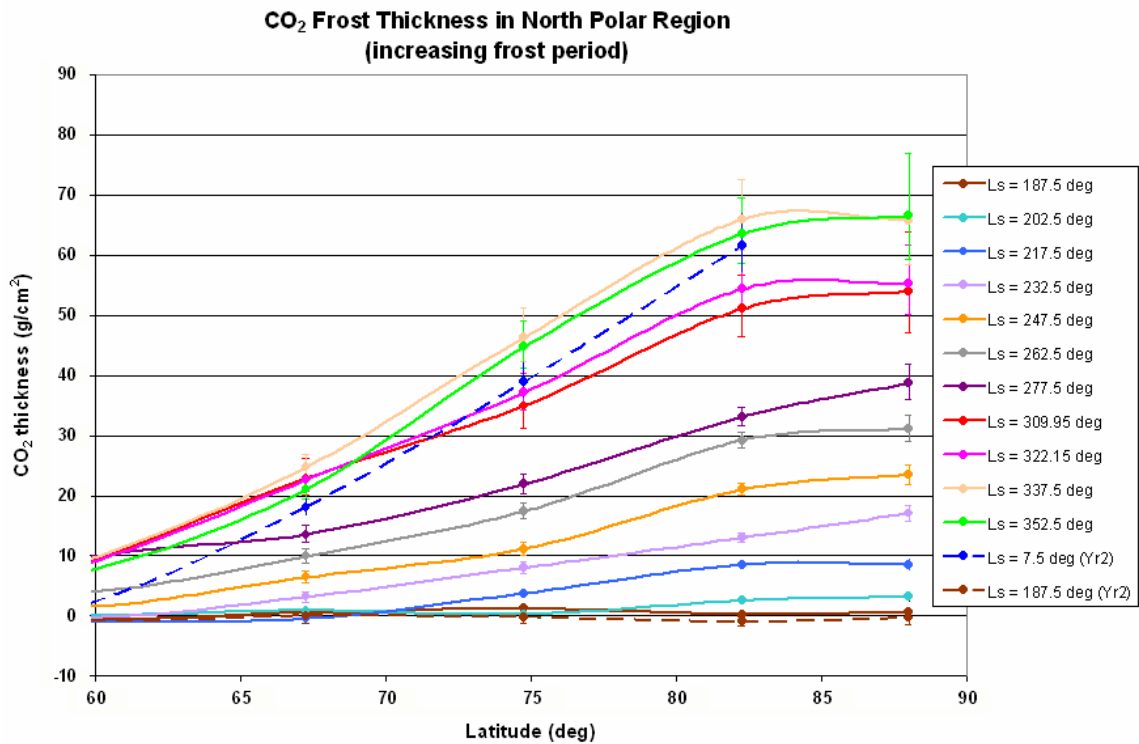


Figure 5.23: CO<sub>2</sub> columnar thickness (g/cm<sup>2</sup>) as a function of Martian latitude. Time increments of approximately 15° of L<sub>s</sub> show the progression of the seasonal frost condensation period at Mars' north pole. Solid curves represent data from the first Mars year of observation; dashed curves indicate GRS-derived data from the second (partial) Mars year observed. The colors are consistent for like times of each year. Missing data points indicate that the H gamma ray signal was fully attenuated by the thick seasonal CO<sub>2</sub> overburden.

cross-section as the cap edge begins to recede while CO<sub>2</sub> continues to accumulate at the pole. These trends were also apparent (and discussed) in Section 5.2.3.

The full north polar CO<sub>2</sub> frost sublimation period was observed for a second time before Mars Odyssey began operating in a safe mode after  $L_s = 187.5^\circ$  of the second Mars year. Interannual variations in columnar thickness and CO<sub>2</sub> sublimation rates are easily studied in these figures. Where there is data, the maximum amount of condensed CO<sub>2</sub> at a given time at the north pole is basically the same between the two years of observations. During periods of thicker frost, the CO<sub>2</sub> depth at lower latitudes varies slightly from year to year. This occurs most significantly at  $82.5^\circ\text{N}$ ; however, the 1-standard-deviation error bars for the disparate points do overlap. In general, it appears that the CO<sub>2</sub> sublimation trends from one Mars year to the next do not vary considerably (at the north pole, at least).

The last period of data observed in the north ( $L_s = 187.5^\circ$ ) occurs at the end of northern summer (or the beginning of northern fall) and is seasonal-frost-free. This period is also plotted as the beginning of the increasing frost period of Mars year two in Figure 5.23.

Figures 5.24 and 5.25 illustrate CO<sub>2</sub> columnar thickness as a function of latitude for Mars' south pole in the same format as was shown for the northern latitudes. Southern summer was just ending when Mars Odyssey arrived at the planet. The first time period observed (shown at  $L_s = 26.25^\circ$  in Figure 5.24) started the season of CO<sub>2</sub> condensation. Seasonal frost continued to condense on the pole fairly constantly over time and over all latitude regions until  $L_s = 172.5^\circ$ . At this point, the CO<sub>2</sub> at the cap edge can be seen to begin its recession. This is the first sign that the sublimation period has begun. (Again, missing data points result when the H gamma ray signal is completely attenuated during times of maximum frost. Open data points and dotted lines represent points with high uncertainty due to unreasonably large, or even infinite, calculated 1-sigma error bars.)

The green curve for  $L_s = 172.5^\circ$  shown in Figure 5.24 is also plotted for continuity as the first time period in Figure 5.25, which displays the decreasing frost period on the south pole. The frost at the topmost latitudes continues to be opaque to gamma

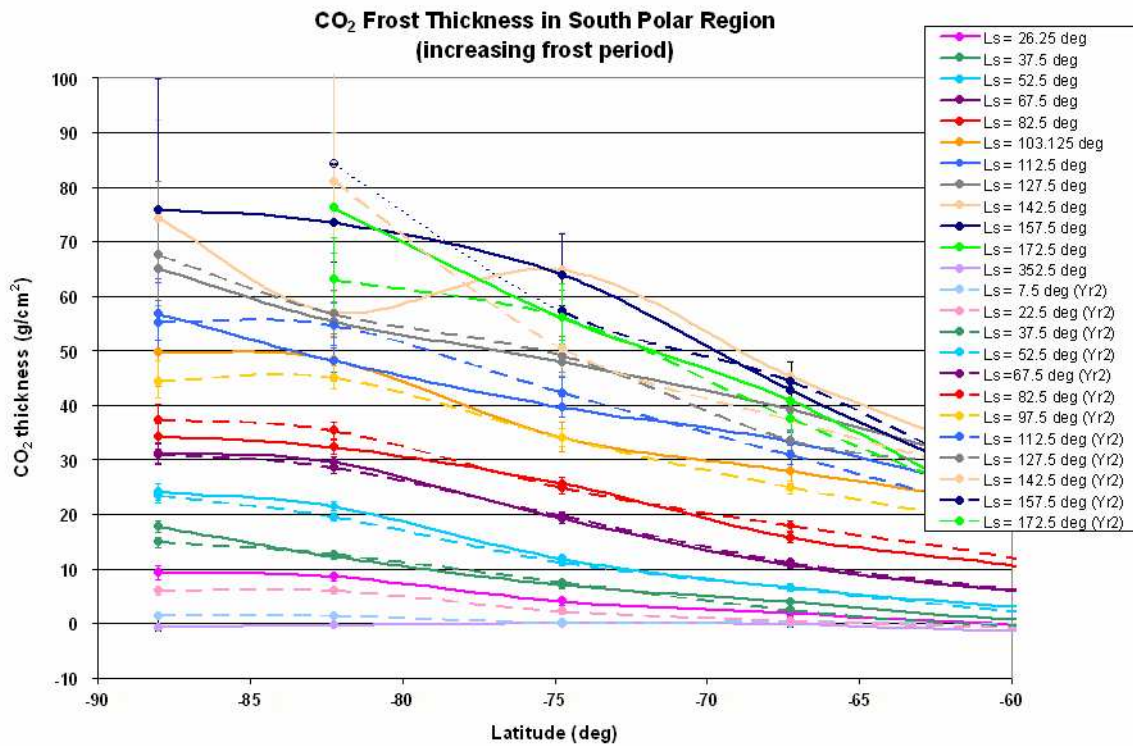


Figure 5.24: CO<sub>2</sub> columnar thickness (g/cm<sup>2</sup>) as a function of Martian latitude. Time increments of approximately 15° of L<sub>s</sub> show the progression of the seasonal frost condensation period at Mars' south pole. Solid curves represent data from the first Mars year of observation; dashed curves indicate GRS data from the second (partial) Mars year observed. The colors are consistent for like times of each year. Missing data points, open data points, and dotted lines indicate uncertain data derived from a weak or fully attenuated H gamma ray signal due to thick CO<sub>2</sub> seasonal frost.

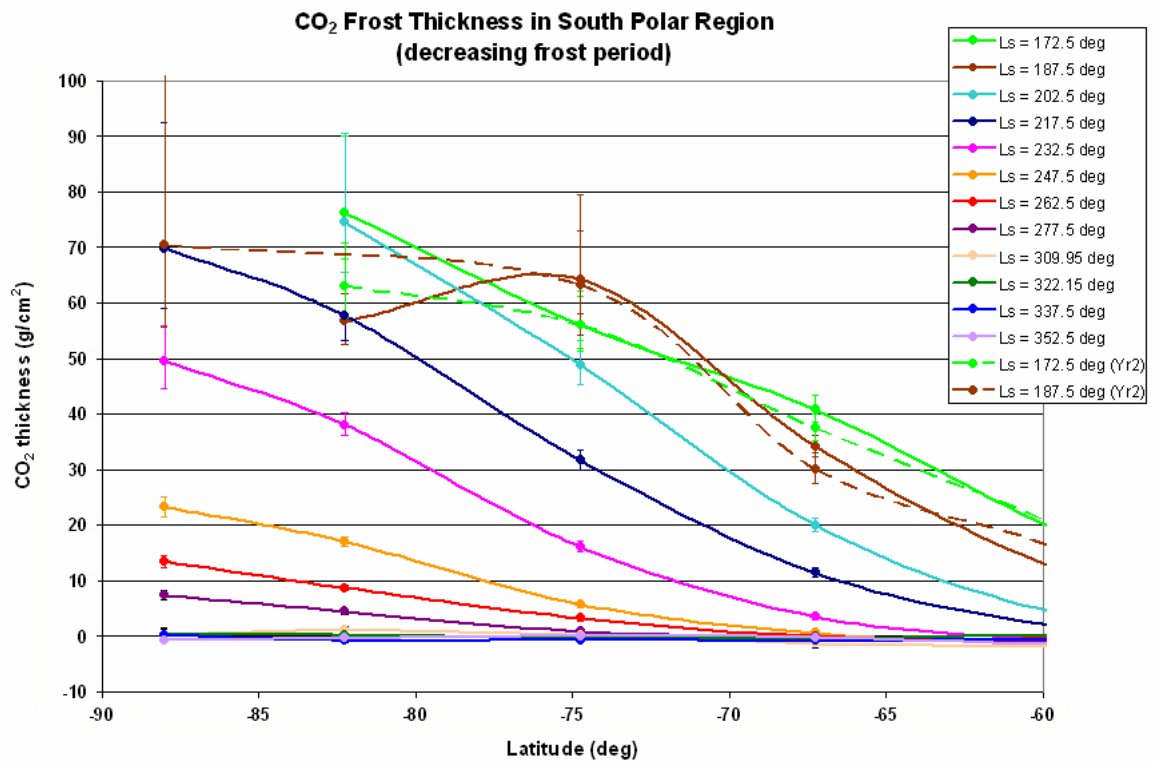


Figure 5.25: CO<sub>2</sub> columnar thickness (g/cm<sup>2</sup>) as a function of Martian latitude. Time increments of approximately 15° of L<sub>s</sub> show the progression of the seasonal frost sublimation period at Mars' south pole. Solid curves represent data from the first Mars year of observation; dashed curves indicate GRS-derived data from the second (partial) Mars year observed. The colors are consistent for like times of each year. Missing data points indicate that the H gamma ray signal was fully attenuated by the thick seasonal CO<sub>2</sub> overburden.

rays as the frost recession begins at the cap edge. The seasonal CO<sub>2</sub> dissipates gradually, as observed in time increments of 15° of L<sub>s</sub> until it reaches a seasonal-frost-free state around L<sub>s</sub> = 300°. The pole remains free from condensed seasonal CO<sub>2</sub> until L<sub>s</sub> ~ 352.5°, at which point the southern fall begins and atmospheric CO<sub>2</sub> begins to accumulate on the polar surface. Looking again at Figure 5.24, this last frost-free data line at L<sub>s</sub> = 352.5° is shown, followed by periods during the second GRS-observed southern condensation season. The CO<sub>2</sub> appears to gain depth at a rate of a little less than 10 g/cm<sup>2</sup> per 15° of L<sub>s</sub>. The variation in the frost accumulation patterns is not large between the two Mars years witnessed. The CO<sub>2</sub> data becomes more sporadic around and after L<sub>s</sub> = 142.5° as the diminished H signal carries greater uncertainty. As in the first Mars year, the seasonal frost cap appears to start subliming at 172.5° of L<sub>s</sub>. The first two time periods for the second year of observed sublimation in the south (L<sub>s</sub> = 172.5° and 187.5°) are shown on the decreasing frost plot in Figure 5.25, after which the Mars Odyssey safe-mode defines the end point of this study.

#### 5.4 CO<sub>2</sub> Mass Calculations, Results, and Comparisons

The columnar thickness of the seasonal carbon dioxide frost at various latitudes and times can also be used to determine the total mass involved in the cycle of CO<sub>2</sub> exchange between the atmosphere and the Martian surface. Ground accumulation in terms of mass (kg) can be specifically quantified by multiplying the column density (g/cm<sup>2</sup>) of the frost by the surface area over which it lies. The totals were computed from frost depth results from hydrogen gamma rays as presented above but was done in 5° latitude by 360° longitude bands for finer resolution. Plots of the CO<sub>2</sub> mass accumulation for both poles separately and for the entire planet (sum of all latitudes containing frost) are presented in Figures 5.26, 5.27, and 5.28.

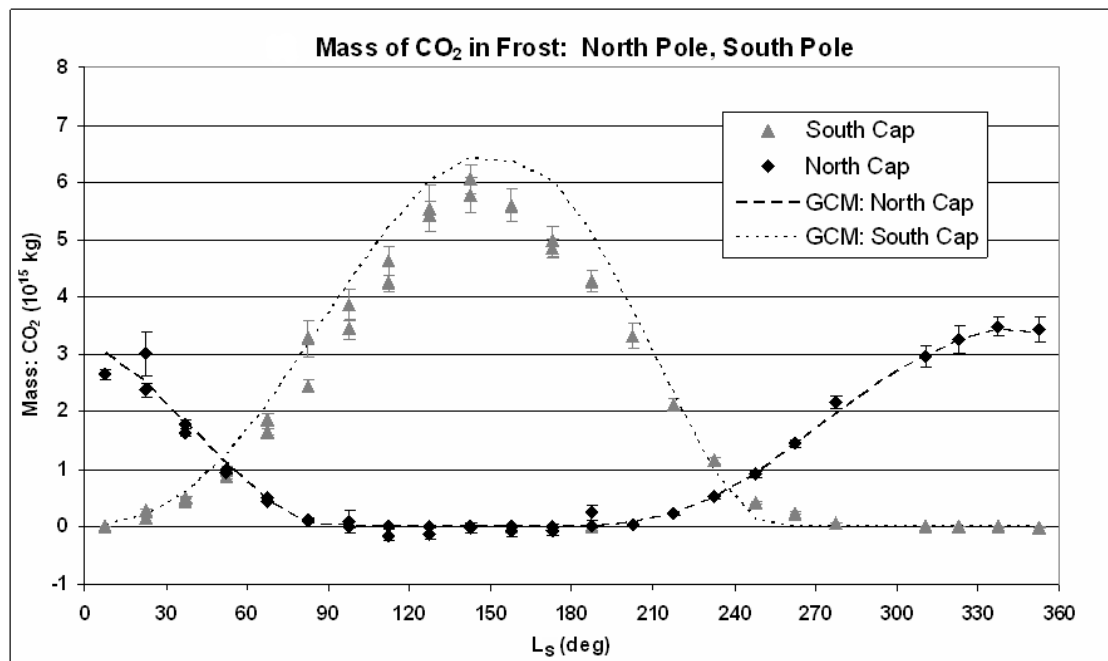


Figure 5.26: Mass of condensed carbon dioxide in units of  $10^{15}$  kg as a function of time (degrees of  $L_s$ ) for  $\sim 1.5$  Martian years. The plot shows the mass of seasonal  $\text{CO}_2$  accumulated on the ground for the north and south poles separately. The model-based predictions from the ARC GCM are shown as dashed curves for comparison.

#### 5.4.1 Mass of Seasonal CO<sub>2</sub> Frost Caps: North and South Poles

Figure 5.26 shows CO<sub>2</sub> mass in units of  $10^{15}$  kg as a function of  $L_s$  for both the north and south poles. For the mass of surface CO<sub>2</sub> determined by summing the condensation in just the northern latitudes, observations from the GRS match remarkably well with the GCM predictions. There is great temporal agreement for the periods of ground mass accumulation and dissipation between the two methods, and the gamma ray results present a maximum mass of  $(3.48 \pm 0.17) \times 10^{15}$  kg versus  $\sim 3.44 \times 10^{15}$  kg for the GCM, both at  $L_s = 337.5^\circ$ . Observations from the HEND instrument provide a maximum value of about  $3.8 \times 10^{15}$  kg that occurs  $10^\circ - 15^\circ$  of  $L_s$  later (Litvak et al., 2006). Recall that from roughly  $L_s = 285^\circ$  to  $300^\circ$ , Mars Odyssey was in a safe-mode configuration and no data were collected.

Results from the summation of the southern CO<sub>2</sub> snow mass are also given in Figure 5.26. Again, the time period of the carbon dioxide condensation/sublimation cycle based on the two methods shown is very similar; however, the GRS reveals a small covering of CO<sub>2</sub> extending  $\sim 15^\circ$  of  $L_s$  after the GCM-determined crocus date (time of frost disappearance). The GCM estimates total southern ground frost as peaking at approximately  $150^\circ$  of  $L_s$  with  $\sim 6.4 \times 10^{15}$  kg of mass, while the GRS observes only about  $(6.1 \pm 0.25) \times 10^{15}$  kg and  $(5.8 \pm 0.30) \times 10^{15}$  kg for the two Martian years at  $L_s = 142.5^\circ$ . Results obtained using neutron inspections give the total closer to  $5.4 \times 10^{15}$  kg around  $L_s = 165^\circ$  from the NS (Prettyman et al., 2005) and, comparable to model predictions,  $\sim 6.4 \times 10^{15}$  kg of mass from the HEND at  $L_s = 155^\circ$  (Litvak et al., 2006). Although it is apparent that the GRS CO<sub>2</sub> frost mass observations yield a slightly lower south polar maximum (even within the 1-sigma error range), in combination, the three instruments and the model provide good constraints on the atmosphere-to-ground CO<sub>2</sub> exchange cycle.

#### 5.4.2 Mass of Total Planet Seasonal CO<sub>2</sub> Frost

The sum of the northern and southern seasonal frost gives the total amount of CO<sub>2</sub> condensed on the surface of Mars as a function of  $L_s$  for  $\sim 1.5$  Martian years as seen

in Figure 5.27. The local maximum around  $L_s = 337.5^\circ$ , which is governed by the north polar winter season, again corresponds well to the GCM predictions. The absolute maximum of this plot occurs during, and is governed by, the large  $\text{CO}_2$  accumulation during the south polar winter. As was seen for the south polar  $\text{CO}_2$  mass data in Figure 5.26, it appears that the GRS observed mass reaches a slightly lower maximum a few degrees of  $L_s$  earlier than that calculated by the GCM. The maximum total ground mass determined using an average of the peak gamma ray results for both Mars years is about  $5.95 \times 10^{15}$  kg, which when compared to the maximum total  $\text{CO}_2$  reservoir of  $\sim 2.7 \times 10^{16}$  kg estimated from the GCM, indicates that on average 22% of the atmosphere took part in the seasonal condensation/sublimation exchange process for these Martian years. This appears to be slightly lower than the previously observed 25% - 30% (cf. James et al. (1992)).

At the two minima of total mass of condensed  $\text{CO}_2$  occurring around  $L_s = 45^\circ - 60^\circ$  and  $L_s = 240^\circ - 255^\circ$ , the uncertainty in Mars Odyssey's background H signal (discussed in Section 3.2.4) is not important because the background signal itself is much smaller in comparison to the larger total observed H flux radiating from Mars. In these cases, the GRS data can be used to calculate the mass of the  $\text{CO}_2$  condensed on the ground with high certainty. The total mass of surface  $\text{CO}_2$  never goes completely to zero. One pole or the other (or both) has seasonal frost at all times of the Martian year.

In terms of the differences between the GRS observations of Mars year one and Mars year two, the greatest interannual variations are seen in Figure 5.27 at about  $L_s = 26^\circ$  and  $L_s = 82.5^\circ$ . The data point in the earlier time period that represents the first Mars year was the first period of observation after the satellite's boom was deployed. This time period was actually only  $\sim 5^\circ$  of  $L_s$  in length, and the value is less certain as can be seen by the increased error bars. As for the later time period, the four sets of points between  $L_s = 60^\circ$  and  $120^\circ$  do show less agreement than would be expected from simple statistics. But, as mentioned when discussing the interannual differences in  $\text{CO}_2$  columnar thickness, the points do not disagree in a uniform direction and therefore do necessarily imply a real difference in  $\text{CO}_2$  mass

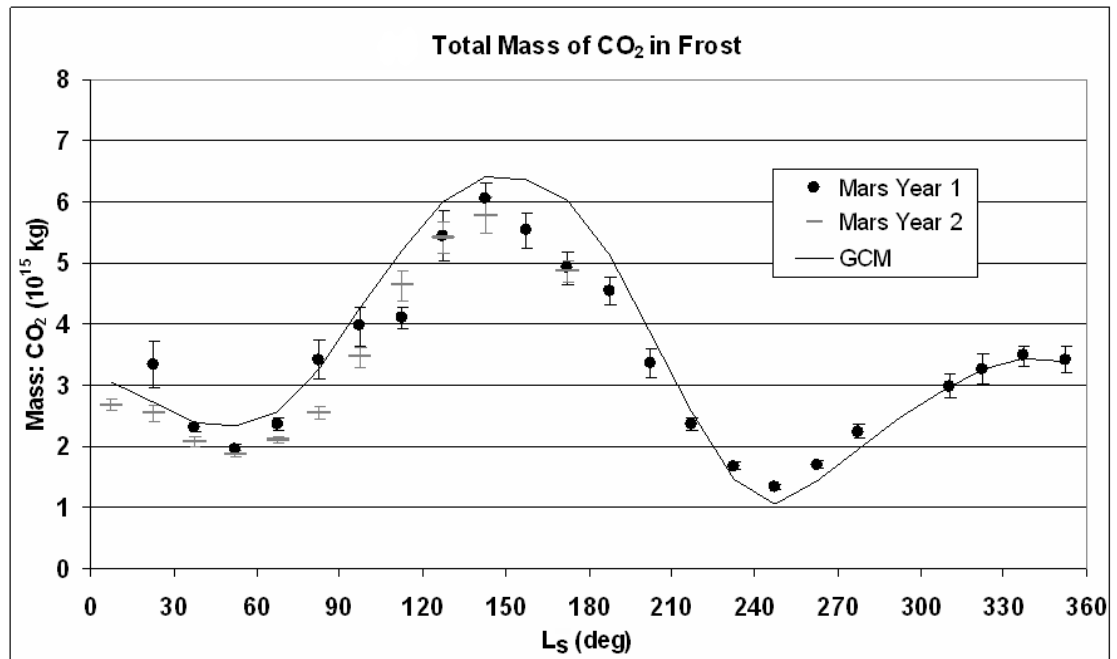


Figure 5.27: Mass of condensed carbon dioxide in units of  $10^{15}$  kg as a function of time (degrees of  $L_s$ ) for  $\sim 1.5$  Martian years. The plot displays the sum of the  $\text{CO}_2$  mass at both poles to depict the total amount of  $\text{CO}_2$  condensed on Mars at any given time. Circular and horizontal-dash data points represent the first and second Mars years of observation by the GRS, respectively. The total condensed  $\text{CO}_2$  mass as predicted by the ARC GCM is shown for comparison by the solid curve. An expanded-scale view of this plot can be seen in Figure 5.28 along with the GCM predictions for atmospheric  $\text{CO}_2$  and the total reservoir of exchangeable  $\text{CO}_2$  on Mars.

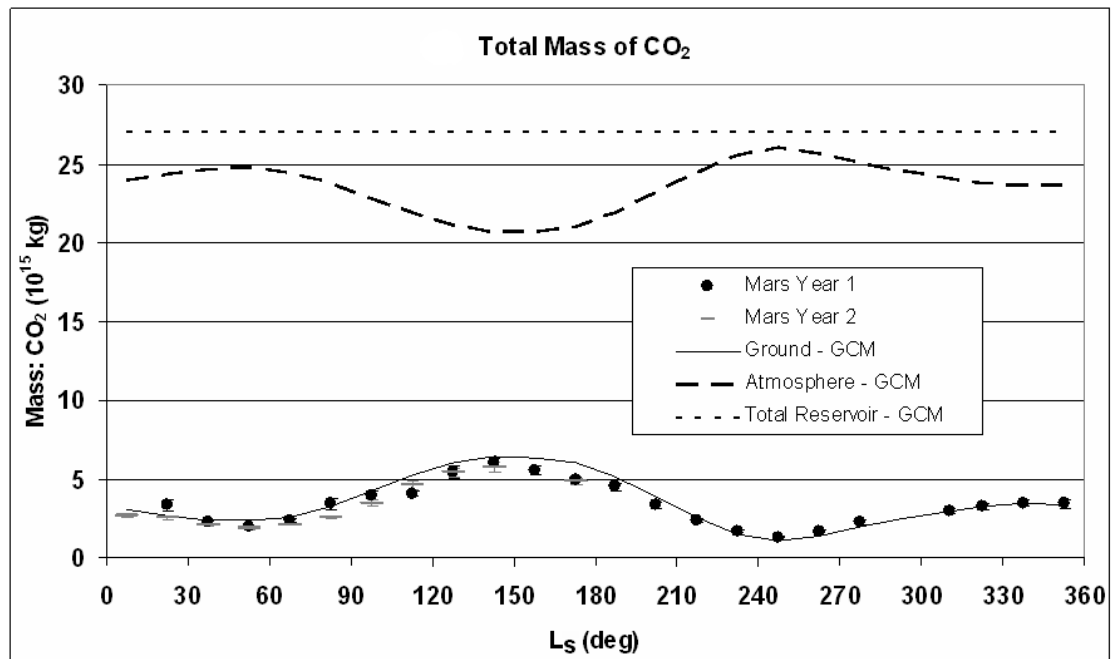


Figure 5.28: An expanded-scale view of Figure 5.27 showing the mass of condensed carbon dioxide in units of  $10^{15}$  kg as a function of time (degrees of  $L_s$ ) for  $\sim 1.5$  Martian years. The sum of the  $\text{CO}_2$  mass at both poles depicts the total amount of  $\text{CO}_2$  condensed on Mars at any given time. Circular and horizontal-dash data points represent the first and second Mars years of observation by the GRS, respectively. The ARC GCM predictions for  $\text{CO}_2$  frost on the ground,  $\text{CO}_2$  in the atmosphere (as determined from Viking Lander atmospheric pressure profiles), and the total reservoir of exchangeable  $\text{CO}_2$  on Mars are also plotted.

from year to year (especially if the error bars are increased to the 2-sigma level). However, note that the data cannot guarantee that there is *not* a real difference, either.

Figure 5.28 shows an expanded-scale view of the total ground mass of CO<sub>2</sub> seen in Figure 5.27. The curves represent predictions from the ARC GCM (based on atmospheric pressure profiles observed by the Viking Landers) for CO<sub>2</sub> mass on the ground, in the atmosphere, and the sum of the two curves for an estimate of the total Martian carbon dioxide reservoir (solid, dashed, and dotted curves, respectively). The data points indicate the ground mass cycle observed by the GRS. The model predicts that maximum surface frost will coincide with the time of minimum atmospheric CO<sub>2</sub>, and the sum of these quantities will be a constant value (indicating no source or sink of carbon dioxide on Mars).

## 5.5 Suggested Future Work

Although the Martian CO<sub>2</sub> cycle is well documented and constrained by the calculations, results, and comparisons presented in this dissertation, there are still many more interesting and informative polar cap studies that could be done with the GRS gamma ray data. The following sections suggest possible (and feasible) future work that would be insightful to the Mars polar science community. *Note that all data and figures included in this Suggested Future Work section are only illustrative examples and are not meant to be taken as precise, defensible results.*

### 5.5.1 CO<sub>2</sub> Longitudinal Variation Studies

A standard method of analyzing spatially varying planetary data is to group the data into latitude bands that extend 360° of longitude around the planet. This allows for easy comparison to current climate model predictions and other spacecraft observations; however, it suppresses the longitudinal degree of freedom. Much information could be gained by studying the GRS data in smaller increments of longitude around Mars. Current areas of interest include the south polar Cryptic Region (an area of

anomalously low albedo and unusual temperature variations), and CO<sub>2</sub> behavior in and influence by Hellas impact basin and numerous other localized areas (mountain ranges, layered terrain, dune fields, etc.) where surface features can affect the CO<sub>2</sub> frost patterns. The asymmetric recession of the southern seasonal cap could also be investigated by such studies. A limiting factor when summing gamma ray data on a finer grid, however, is that zonal data groups must carefully be kept large enough to ensure sufficient statistical certainty.

### 5.5.2 Polar Maps

Another useful technique to investigate gamma ray attenuation and seasonal CO<sub>2</sub> on Mars would be to incorporate IDL mapping software or other visualization tools to display the gamma ray flux and frost variations mapped onto the surface of Mars. Figure 5.29 shows a possible example of such a method where the attenuation of polar H gamma rays can be seen by mapping the ratio of the atmosphere-corrected gamma ray flux at three times of the Martian year to the flux at the seasonal-frost-free time. Created using IDL and 5° latitude by 30° longitude gridded GRS data smoothed with a 10° boxcar filter, periods for a nearly frost-free, an intermediate, and a fully frosty time are displayed.

Similarly, CO<sub>2</sub> frost calculations can be done with the *gridded* GRS data in the same manner as described throughout this document. Polar maps of the CO<sub>2</sub> frost could be produced in increments of 15° of L<sub>s</sub> to study frost longitudinal variations as described in Section 5.5.1. A few examples of mapping the polar CO<sub>2</sub> results onto the surface of Mars can be seen in Figure 5.30. Again, because data from smaller zones of the planet are used in this type of investigation, it is important to be rigorous in determining the statistical significance of the results.

### 5.5.3 Seasonal Polar Cap Edge Studies

The location, longitudinal variation, and temporal behavior of the edge of the seasonal polar frost cap is also an important topic in current Mars research. Many

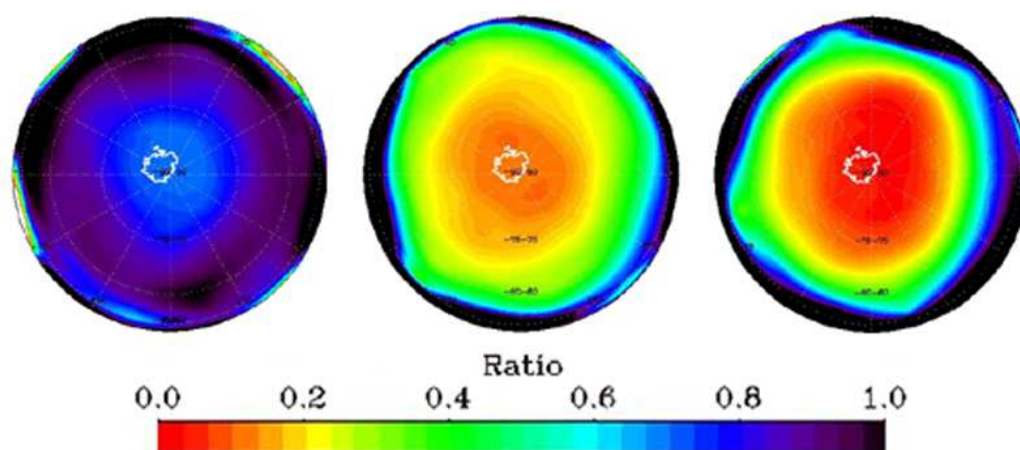


Figure 5.29: Example south polar maps showing the ratio of the atmosphere-corrected gamma ray flux at three times of the Martian year to the flux at the seasonal-frost-free time. The maps represent  $L_s = 22.5^\circ$ ,  $112.5^\circ$ , and  $187.5^\circ$  from left to right corresponding to a nearly frost-free, an intermediate, and a fully frosty time. A ratio value of 0 represents full attenuation of the H gamma rays by the  $\text{CO}_2$  frost, and a ratio value of 1 indicates a frost-free surface. The south polar residual permanent cap is outlined at the center in white. These maps were created using IDL analysis software and  $5^\circ$  latitude by  $30^\circ$  longitude gridded GRS data smoothed with a  $10^\circ$  boxcar filter.

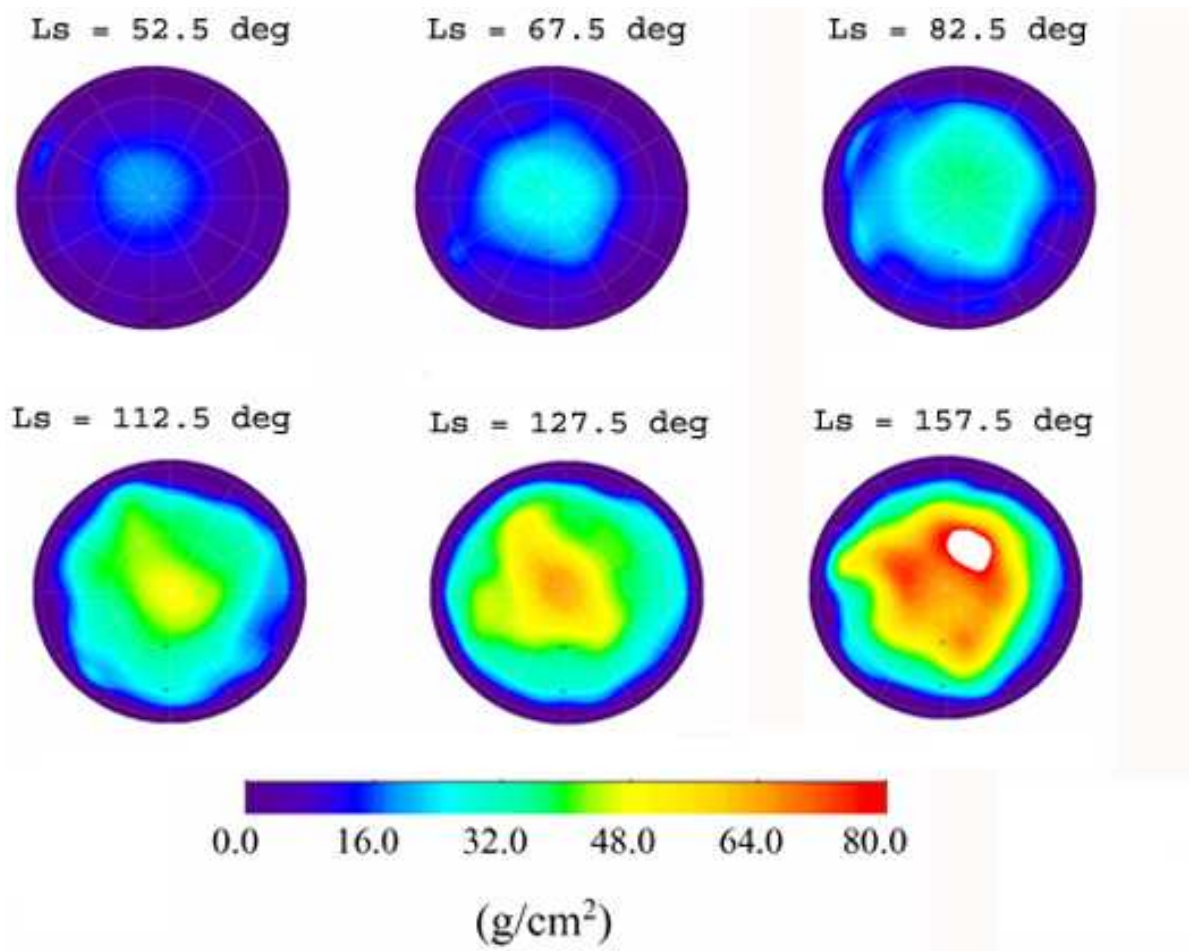


Figure 5.30: Examples of south polar maps of seasonal CO<sub>2</sub> frost columnar thickness in  $\text{g/cm}^2$ . Six times of the year (as represented by the given  $L_s$  values) are displayed to illustrate the growth of the seasonal frost in extent and depth. At  $L_s = 157.5^\circ$ , the white area represents off-scale frost thickness values due to total attenuation of the H gamma ray signal.

independent data sets have been used to plot the latitude of the seasonal cap edge in degrees as a function of time. When represented in such a format, trend lines can be fit to the results to derive equations termed “Regression and Growth Functions”. These functions, which characterize the rate at which the CO<sub>2</sub> condenses and sublimates near the cap edge, can be easily compared and contrasted. The GRS gamma ray data would be useful in this type of study.

Similarly, the polar cap edge can be mapped using visualization software like described in Section 5.5.2. Displaying the data as concentric contours makes it easy to analyze CO<sub>2</sub> longitudinal variations and regression/growth rates at all areas of the cap. Such studies using data from the Thermal Emission Spectrometer (TES) on Mars Global Surveyor (MGS) have been very successful. The TES team has determined in detail the crocus date, or point of total frost sublimation, to map the recession of the cap edge as a function of time ( $L_s$ ). Figure 5.31 shows an example of these results.

By employing IDL analysis software (or a similar program), the GRS data could also be used to display the outline of the polar cap edge over time. I ran a test of this technique, and the outcome seen in Figure 5.32 demonstrates that it would be possible to do a detailed analysis this way. It is necessary to determine (from the GRS data) the latitude and longitude of the boundary of the frost at various times to use as input into the mapping software. Although the figure shown here is only to be used as an illustrative example, if this study were done thoroughly and rigorously, the results would be highly useful to compare to other seasonal CO<sub>2</sub> cap edge observations.

#### 5.5.4 Density Estimates for the Seasonal Polar Frost

Attempts have been made to determine the density of condensed Martian CO<sub>2</sub> in publications such as Aharonson et al. (2004). Theoretically, the columnar thickness of the frost in g/cm<sup>2</sup> reported here from GRS data could be used with measurements of the frost height (in units of cm or m) to derive estimations of the CO<sub>2</sub> density. (Columnar thickness divided by height would give the density.) The re-

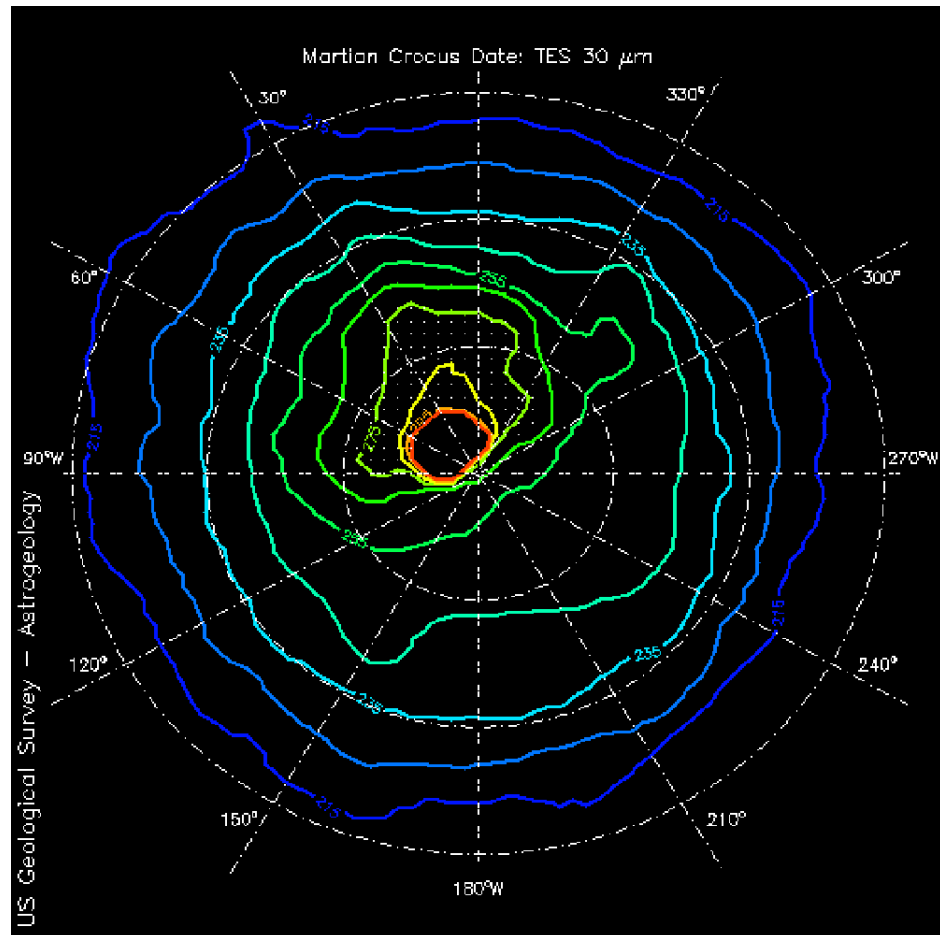


Figure 5.31: South polar seasonal frost cap edge as a function of time (degrees of  $L_s$ ) produced from  $30\ \mu\text{m}$  pre-mapping MGS TES data. The contour lines are spaced at  $10^\circ$  of  $L_s$ , starting with  $215^\circ$  as the dark blue contour. A small region between  $L_s = 275^\circ$  and  $L_s = 295^\circ$  has been shaded to indicate that this region has a large error in the estimate of the cap edge. Figure credit: USGS, MGS/TES.

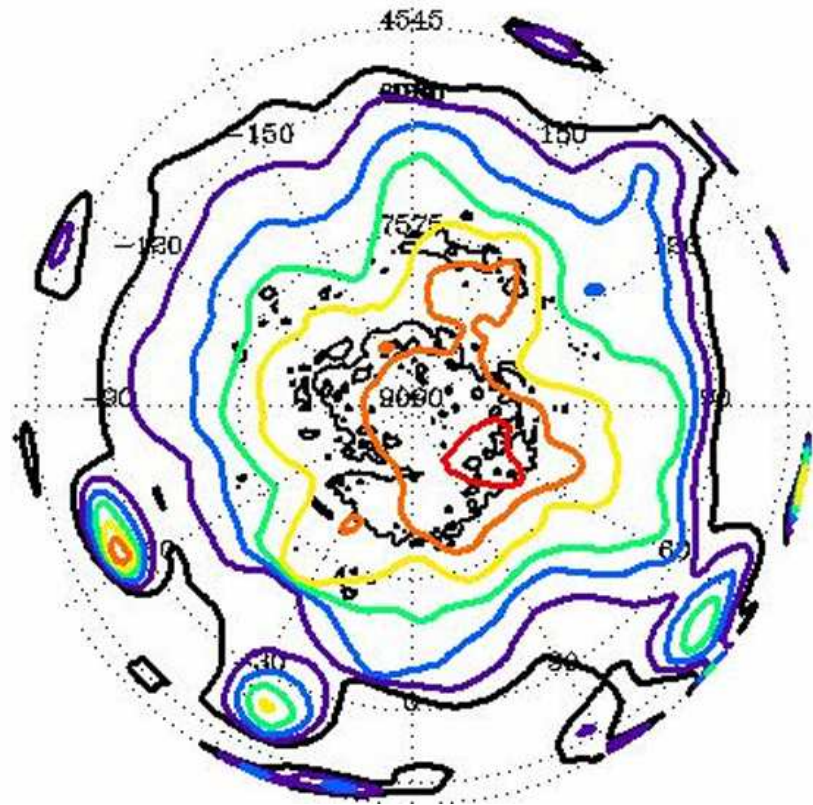


Figure 5.32: Example of a map of the northern seasonal frost cap edge produced using IDL analysis software and GRS data. The contours represent the location of the cap edge at various times of the Martian year. An outline of the permanent northern H<sub>2</sub>O-ice cap is seen at center, and latitude and longitude designations are as marked.

sults, if reliable, would give insight into whether the CO<sub>2</sub> condenses as fine-grained snow, hoarfrost, fluffy deposits, dense slab ice, or as a combination of densities (all of which most likely vary depending on the time of year and level of insolation). The most obvious data set from which to get height data comes from MGS MOLA (the Mars Orbiter Laser Altimeter on Mars Global Surveyor). However, these density calculations have not actively been pursued using GRS data because the uncertainty in the MOLA data becomes large when measuring heights less than a few 10s of centimeters, which is the approximate height scale of a large portion of the GRS CO<sub>2</sub> observations. (The MOLA data set is a great contribution to Mars science when measuring at larger scales and in many other regards.) Current estimations of the frost density range from 0.5 g/cm<sup>3</sup> to greater than 1 g/cm<sup>3</sup>, and perhaps when more fine-scaled height measurements are made by future spacecraft, the GRS data will be applied to obtain even more accurate and precise seasonal CO<sub>2</sub> density values.

## CHAPTER 6

## Conclusion

## 6.1 Project Summary and Research Conclusions

The Gamma Ray Spectrometer is part of an instrument suite onboard the 2001 Mars Odyssey satellite currently in orbit around Mars. Among the many areas of scientific investigation enabled by the vast quantities of data being return from the planet, the study and results of the polar seasonal carbon dioxide cycle are presented here. The significant exchange of CO<sub>2</sub> between the atmosphere and ground is a well documented phenomenon on Mars, and the analysis of gamma ray flux from the surface of the planet allows me to calculate the columnar thickness and total mass accumulation of the polar frost as functions of time and latitude. I compare the results from the GRS to those obtained by previous experimental and theoretical studies.

Using Monte Carlo particle simulations and detailed calculations, relative atmosphere-corrected gamma ray flux profiles are created for various elements. In particular, the investigation here utilizes the attenuation of the hydrogen and potassium gamma ray lines by the varying quantity of CO<sub>2</sub> covering the poles. The analysis is fairly straightforward for naturally radioactive <sup>40</sup>K at 1461 keV because a simple Beer-Lambert Law calculation creates a model-independent means of quantifying the frost accumulation. The flux of the hydrogen line, however, is not constant for all amounts of CO<sub>2</sub> deposition, so regolith and atmosphere models must be incorporated into the derived attenuation calculations. The amount of CO<sub>2</sub> overburden and the distribution of hydrogen with depth in the regolith must be taken into account because neutrons produced in thermalizing processes associated with H and CO<sub>2</sub> are the excitation source for the 2223 keV gamma rays.

For this study, the GRS data were accumulated and summed over 15° of L<sub>s</sub>

in  $5^\circ$  latitude by  $360^\circ$  longitude bands for the  $\text{CO}_2$  mass determinations and in  $7.5^\circ$  latitude by  $360^\circ$  longitude bands (in accordance with the partitions used in the ARC GCM) for investigating  $\text{CO}_2$  columnar thickness. This allowed a comparison of previous model predictions to the GRS observations for all times and locations up to the point of total attenuation of the gamma rays by the  $\text{CO}_2$ . For both hemispheres at any given time, it is clear that the columnar thickness of  $\text{CO}_2$  frost ( $\text{g}/\text{cm}^2$ ) is greater at latitudes closer to the pole. It can also be observed that at the edge of the seasonal frost cap, the surface  $\text{CO}_2$  begins to accumulate later than, and completely sublimates earlier than, at the pole. Corroborating conclusions from the GCM, NS, and HEND data, the evidence from the GRS that the frost peaks later at poleward latitudes implies that snowfall at the pole continues after the boundary of the cap has begun its recession. Both years of H and K gamma ray results for all latitudes of both hemispheres agree well with the GCM predictions for the time periods from the beginning of frost deposition to the crocus date, or complete sublimation of seasonal  $\text{CO}_2$ . These findings are also supported by neutron data analysis.

For all northern latitudes, the maximum zonally averaged  $\text{CO}_2$  columnar thickness as derived from gamma rays is approximately equal to or slightly less than the depth estimated by the GCM. Within the 1-sigma error bars, the agreement for the condensation period is especially good. The time at which maximum frost is reached for the northern latitudes as deduced from the GRS data is found to be the same to a bit earlier when compared to the model predictions. Overall, these results are evidence that the assumed model of 100%  $\text{H}_2\text{O}$ -ice at the north pole covered by various amounts of  $\text{CO}_2$  frost whose columnar thickness changes steadily with time is valid. In the south, the magnitude of the  $\text{CO}_2$  columnar thickness estimated using both H and K gamma ray flux is consistently lower than the results forecasted by the GCM, and the frost growth and dissipation rates appear slower in general. Both years of gamma ray results indicate that the particular time periods for the seasonal cap formation and disappearance agree well. It is possible that an adjustment to the southern regolith model used in the calculations would modify these results. Ideally, we would like to produce H-derived  $\text{CO}_2$  results that correspond well with

the K-based values for points before the weaker 1461 keV K signal is completely attenuated by the thick winter overburden of seasonal frost. Then one can utilize the stronger 2223 keV H signal to extrapolate precise CO<sub>2</sub> measurements to greater frost thicknesses than are possible through the use of <sup>40</sup>K gamma rays alone.

Major differences (or lack thereof) in the CO<sub>2</sub> accumulation and dissipation patterns between the first and second Mars year of observations can be seen most easily in figures plotting CO<sub>2</sub> columnar thickness at various times as a function of latitude. In general and accounting for statistical fluctuations, the GRS frost measurements do not show large interannual variations in the seasonal cap behavior.

The mass of the ground accumulation of CO<sub>2</sub> over time is also determined by multiplying the derived column densities by the area over which the associated frost condenses. Plots of the GRS observations versus the GCM predictions are shown for the north, south, and both poles combined. The figure for total surface CO<sub>2</sub> mass indicates that the GRS measures slightly less ground accumulation until around  $L_s = 230^\circ$ , and the peak of maximum mass occurs a few degrees of  $L_s$  earlier than what the GCM estimates. Nevertheless, the timing of the beginning of frost condensation and its return to the atmosphere when viewing both poles separately shows an excellent agreement to the plotted model predictions. The total northern mass of approximately  $3.5 \times 10^{15}$  kg is very close to the GCM maximum value, and both curves peak at the same time at  $\sim 340^\circ$  of  $L_s$ . In the south, the gamma ray results show a slightly lower mass of CO<sub>2</sub>. In general, however, the GRS mass results presented here are on the order of the GCM predictions and both neutron instruments on the Mars Odyssey satellite. I found that approximately 20% - 25% of the atmospheric CO<sub>2</sub> appears to be involved in the seasonal condensation/sublimation cycle at the poles.

## 6.2 Final Words

The data shown here represent my understanding and evaluation of the seasonal CO<sub>2</sub> frost cycle at the time of publication incorporating gamma ray data from June 2002

to the beginning of April 2005. In combination with neutron studies and the NASA ARC GCM predictions, the GRS has provided the means to quantify the processes at the poles on Mars. The research presented here offers a good glimpse into the inventory and extent of the seasonal polar CO<sub>2</sub> over time and its role in (and effect on) the greater Martian ground-atmosphere CO<sub>2</sub> exchange cycle. Mars Odyssey has now transmitted almost two full Martian years of information, and GRS data will continue to be accumulated and analyzed. Calibrations and corrections during data processing will also progress and be refined as further information becomes available.

## APPENDIX A

## Forward Model Spectrum Calculations

This appendix describes the rationale and approach for the method by which we convert counts in the 2001 Mars Odyssey Gamma Ray Spectrometer (GRS) instrument to elemental concentrations on the surface of Mars. This information is adapted from a GRS team document dated February 28, 2005 (Version 0.5).

We choose to divide the planet into cells that are  $0.5^\circ$  by  $0.5^\circ$  in size. This yields an array of  $720 * 180 = 259,200$  cells. We define the GRS footprint, i.e. the area of the surface from which we will calculate gamma ray contributions to the expected spectrum, as those cells which fall within a circle on the surface of Mars from which 99.9% of the signal would come when Mars is treated as a sphere with no topography and a uniform atmospheric thickness of  $16 \text{ g/cm}^2$ . The footprint size is defined in terms of the angle formed at the planet center between the vector pointing to the spacecraft and the vector pointing to the edge of the footprint. With this definition, the entire limb-to-limb field of view would have a footprint of  $\sim 27^\circ$ . In practice, we adopt a footprint of  $17^\circ$  centered on the sub-spacecraft point. This results in decreasing the calculation time by nearly a factor of 2 from the full field of view footprint while introducing errors in predicted counts of  $>1\%$  only for the highest energy gamma rays and thinnest atmospheres, and introduces no errors  $>2\%$ . We shall also assume that the spacecraft has a constant position and attitude for the duration of the approximately 20 second data collection period and that these will be defined by its position and attitude at the midpoint of the collection period.

We shall have to calculate the contribution to the expected signal from each cell within the footprint. The number of cells varies with latitude, but is on the order of 10,000 ( $\sim 26,000$  cells when near the poles and  $\sim 5,000$  cells when near the equator). For each spectrum we thus will have to process on the order of 10,000 cells, and for

each of these 10,000 cells, we may have to calculate contributions to 100 or so energy peaks. This last group of calculations (of the 100 peaks for each of 10,000 cells) will be done in what is referred to below as the inner loop. This is a loop where we must be very efficient, as we will have to calculate this loop about 1,000,000 times for each spectrum. In addition, we will certainly have to recalculate the model spectrum for every actual spectrum taken during the mission several times as we improve our knowledge of algorithms and composition. Because we will collect a new spectrum every 20 seconds, we will have to be able to do these inner loop calculations in less than 20 microseconds just to keep up. Late in the mission we may need to go back and calculate 48 months or more worth of data. If we want to do the calculations in a month, then we have to do it 48 times quicker, or in about 400 nanoseconds per peak.

We shall therefore pre-compute as many values as possible, hold most of this needed information in arrays in memory, and retrieve only a minimum amount of information from the database for each calculation. These steps will help minimize the number of calculations performed. We shall do the calculation on a spectrum-by-spectrum basis, and the calculations do not depend on what has happened with previous or following spectra. However, individual model spectra will be summed in the same manner as the actual spectra with which they are to be compared.

### **Pre-Calculated Values**

Many of the parameters and values that we will use for the forward calculation of expected spectra can be determined beforehand and it makes sense to pre-calculate these values and store them in arrays or files in a database. This will allow us to simply look them up at the time of use, significantly reducing the amount of time needed to calculate a model spectrum. These values and their storage allocations include the following 6 tables:

1. **Production Constants (K\_TAB):** Using MCNPX or other codes, we calculate the number of gamma ray photons expected to leave the surface-atmosphere interface per incoming cosmic-ray-particle (or other initiating

mechanism, such as time for radiogenic decay) per unit solid angle in the direction of the spacecraft for a given surface composition. We compute these production constants,  $k$ , for each gamma line (peak) of interest and for each reaction which can produce that peak. This production constant,  $k$ , shall be the rate at which photons are produced by each reaction that can make that gamma line. We compute  $k$  for various thicknesses of the atmosphere (to account for atmospheric attenuation of incoming cosmic rays), and for various subsurface emission angles (to account for the effects of path length through the regolith). Thus  $k$  is a five dimensional array. The units of the elements in the array will be photons/(cosmic-ray-particle)/steradian. Note that the area over which the photons are emitted does not enter into the  $k$  values. If one wants fluence of photons/cm<sup>2</sup>, then one can multiply the  $k$  value by the fluence of cosmic ray particles in units of particles/cm<sup>2</sup> and the result will be photons/steradian/cm<sup>2</sup>. This is, in fact, what we shall do. Also note that for gamma ray production by the radioactive elements, K, U, and Th, we shall want the  $k$  values calculated as photons/steradian/cm<sup>2</sup>/sec rather than photons/(cosmic-ray-particle)/steradian. Again, this is just what we do. The five dimensions of the  $k$  values are:

$$k_{C,P,SP,T,\theta}$$

C = composition number

P = Peak number, unique for each energy

SP = Sub-peak number, identifies the reaction contributing to the peak  
(e.g.: the 4438 keV line has contributions from both C and O)

T = atmospheric thickness (vertical column density in g/cm<sup>2</sup>)

$\theta$  = subsurface emission angle (though we will store the data as  $\cos \theta$ ),  
i.e. the angle between the cell normal and the vector to the spacecraft

As each  $k$  is calculated it will be stored in the database in the K\_TAB tables. There will be a separate K\_TAB for each composition, peak and reaction. Each

K\_TAB will contain elements indexed on atmospheric thickness and emission angle and will be stored as Binary Large Objects (BLOBs).

K\_TABs are externally indexed by: `composition_number`, `peak_number`, and `reaction_number`. `Composition_number` is simply the arbitrary index of a composition as it is stored in the composition array, `COMPOSITION_TAB`. `Peak_number` uniquely identifies each energy peak while `Reaction_number` uniquely identifies the type of reaction that produces this peak from this element. These indices are used consistently throughout the various arrays dealing with the production of peaks from the POI (Peaks of Interest) arrays to the FPF array which is the array of results, i.e. the number of expected counts in each peak of a given spectrum for a given surface composition. For purposes of the forward calculations under discussion here, these indices provide access to the location in the `ALL_POI_TAB` where the reaction code is stored. The reaction code gives the particle or mechanism responsible for the reaction(s) to be modelled and thus which fluence (particles/time \* time, or simply time) to use in calculating the expected spectrum.

Each set of C, P, and SP indices points to a 2-dimensional BLOB of k-values. Each k-value BLOB is a two dimensional array of floats, indexed by atmospheric thickness and subsurface emission angle. Currently this array is defined as having k value entries for 22 atmospheric thickness values covering the range 0 - 42 g/cm<sup>2</sup> in 2 g/cm<sup>2</sup> increments, and 21 cosines of subsurface emission angle, in increments of 0.05°, for angles from 0° to 90°, giving a BLOB size of 22 \* 21 \* 4 bytes = 1848 bytes. We then interpolate to the actual atmospheric thicknesses and subsurface emission angles. By the end of the mission we could have 200 peak-reactions and several compositions. Note that the K\_TAB is not the k array that will be entered into memory during a run, but rather the source of a more limited number of k values which will be used at any given time.

The compositions are subject to change with time as we get better data, and we may end up doing the calculation for a variety of compositions. It is expected that we may only need a few different compositions in any given calculation run, but we may end up calculating several different compositions before we are done with the mission.

2. **Planetary Surface Geometry (CELL\_TAB):** To calculate the contribution of various portions of the planet's surface to the signal received by the detector, it is necessary to account for many different aspects of the surface/atmosphere/spacecraft/instrument geometry. To facilitate computations, we precalculate as many of the locations, angles, distances and vectors as possible, particularly those which describe the (invariant) planetary surface. To accomplish this, we start with the surface divided into a series of  $0.5^\circ$  by  $0.5^\circ$  cells. Cells are indexed from north to south starting at the North Pole and from west to east starting at the prime meridian. This single cell index shall begin at 0 for the cell centered at  $89.75^\circ\text{N}$  and  $0.25^\circ\text{E}$  (i.e. the cell whose left edge is on the prime meridian and whose top edge is the North Pole) and run to 719 for the cell centered at  $89.75^\circ\text{N}$  and  $359.75^\circ\text{E}$ . Cell numbering will then continue with cell number 720 being directly south of cell 0 and the numbering again wrapping around to the east and then continue in this manner until all 259,200 cells are numbered. For each cell, we shall calculate (and we only need to calculate these once):

A) Cell area in  $\text{km}^2$  ( $A_i$ ): For a perfectly spherical planet, the area of a cell would be given by (from the area for a polar cap):

$$A_i = \frac{2\pi R_m^2 [\cos(\text{colat1}) - \cos(\text{colat2})]}{N} \quad (\text{A.1})$$

where  $R_m$  is the mean planetary radius in km (3397.0),  $\text{colat1}$  is the colatitude of the northern bounding latitude of the cell,  $\text{colat2}$  is the colatitude of the

southern bounding latitude of the cell,  $N$  is the number of cells in a latitudinal band (720 for  $0.5^\circ$  cells), and  $i$  is the cell index.

However, Mars is not a perfectly spherical planet and we wish to avoid introducing errors that we know will be greater than the 1% level, so we compute cell areas for an oblate spheroid starting with the definition of surface area in spherical coordinates:

$$A_i = \int_{\lambda_1}^{\lambda_2} \int_{\phi_1}^{\phi_2} R_\phi^2 \cos(\phi) d\phi d\lambda \quad (\text{A.2})$$

where, following the IAU convention,  $\phi$  is latitude and  $\lambda$  is (east) longitude, and the figure of an oblate spheroid is given by:

$$R_\phi = a \left( 1 - f \sin^2 \phi - \frac{3}{8} f^2 \sin^2(2\phi) \right) \quad (\text{A.3})$$

with:

$$f = \frac{a - b}{a} \quad (\text{A.4})$$

where  $f$  is the flattening of the sphere,  $a$  is the equatorial radius (3397 km),  $b$  is the polar radius (3375 km), and for Mars,  $f = 0.00647630$ .

B) Average altitude,  $H_i$ , in km (above the reference aeroid, i.e. allowing for the shape of the planet) which will be used to calculate surface pressure and/or atmospheric thickness. These data were generated by Scott Anderson who went back to the original files of all the MOLA laser shots and regenerated the equivalent of  $0.25^\circ$  resolution maps using all the data, not just the preliminary subset of the originals. To determine the altitude of our cells, this data was rebinned to  $0.5^\circ$  resolution.

C) Position vector (to the center of the cell),  $\vec{R}_{CN} = [x_{CN} \ y_{CN} \ z_{CN}]$ , in a Mars-centered Mars-fixed (MCMF) Cartesian coordinate system with its origin at

Mars' center of mass:

$$x_{CN} = R \cos(\phi) \cos(\lambda) \quad (\text{A.5})$$

$$y_{CN} = R \cos(\phi) \sin(\lambda) \quad (\text{A.6})$$

$$z_{CN} = R \sin(\phi) \quad (\text{A.7})$$

where  $R$  is the actual radius of the planet (taken from the MOLA data) averaged over the area of the cell.

D) Vertical (zenith) vector. For a spherical planet, the cell vertical (zenith) is just the normalized planetary radius vector to that point:

$$\hat{n} = \frac{\vec{r}_c}{\|\vec{r}_c\|} \quad (\text{A.8})$$

where  $\vec{r}_c$  is the aerocentric (spherical) radius vector. This is not true for the case of an oblate spheroidal planet, nor is it true in general. For an oblate spheroidal planet, the zenith direction is given by a unit vector  $(\lambda, \phi')$  where  $\lambda$  is the longitude and  $\phi'$  is the areodetic latitude. In other words, when the cell's location is given in areodetic (spheroidal) coordinates, the cell vertical is

$$\hat{n}_c = \begin{bmatrix} n_x \\ n_y \\ n_z \end{bmatrix} = \begin{bmatrix} \cos \phi' \cos \lambda \\ \cos \phi' \sin \lambda \\ \sin \phi' \end{bmatrix} \quad (\text{A.9})$$

Areodetic latitude ( $\phi'$ ) relates to areocentric latitude ( $\phi$ ) by:

$$\phi' = \phi - m \sin(2\phi) - \frac{1}{2} m^2 \sin(2\phi) - \dots \quad (\text{A.10})$$

where  $m$  (in radians) is given by:

$$m = \frac{e^2}{2 - e^2} = f + \frac{1}{2} f^2 - \frac{1}{4} f^4 + \dots \quad (\text{A.11})$$

As noted, for Mars,  $f$  is 0.00647630, so the first two terms are sufficient for our purposes. Thus  $m = 0.006497271$  radians, or  $0.37227^\circ$ . Also, we need to be careful. Although areodetic and areographic longitude are essentially the same, the areodetic longitude is usually measured as positive west, instead of east, in which case the  $n_y$  component of  $\vec{n}_c$  would be  $-\cos \phi' \sin \lambda$ .

E) Normal vector. We have a first set of calculations of the normal vector,  $\vec{N}_c$ , for each cell. These calculations used  $0.5^\circ$  by  $0.5^\circ$  binned data and may be dominated by cross-track errors, since they were based on the old, incomplete,  $16^{th}$  degree MOLA data set. To compute the normal vector of a cell, the positions of the cell center and the eight surrounding cell centers were used to calculate the normal vectors for eight triangular planes around the cell center. These vectors were then summed and normalized to obtain the (average) normal vector for the cell.

Although one can decompose  $\vec{N}_c$  into a 2 parameter (gradient + azimuth) formalism, it is computationally more expedient to retain it as a unit vector,  $[x \ y \ z]$ . The rationale for this is that you eliminate the need for trigonometric operations to decompose  $\vec{N}_c$  into its three components. Additionally, if we later decide to reference a cell to a spheroidal planet or to some other areoid, only recalculation of the normal to the cell's topography will be required.

All these values, once calculated for each cell, are stored in a cell array, CELL\_TAB, in the database. In an ideal world we would create this array/file once and never change it, but to allow for changes or updates while still maintaining the history of CELL\_TAB data that has changed, the structure of CELL\_TAB will be as follows. For each cell there will be a number of iterations or rows in the form of a BLOB. Rows are thus added with each update, but never removed. Each row contains (1) a date/time stamp containing the time of the last update to the cell's entry, (2) an iteration number which is incremented each time the data for a given cell is updated, and (3) the cell

data which consists of: Cell Number, Latitude, Longitude, Area, Altitude, Distance to the center of Mars, Normal Vector (x y z triplet), Vertical Vector (x y z triplet), and Position Vector (x y z triplet). The current size of the CELL\_TAB is approximately 15 Mb, but this may grow in the future.

The Composition\_number, which is the index to the composition of the regolith for each of the cells, is stored in a separate array, CELL\_COMPOSITION\_TAB, which contains just a time stamp and a map of the cell Composition\_numbers, while the array COMPOSITION\_TAB contains a list of Composition\_numbers and text descriptions of them.

3. **GRS Footprint (FOOTPRINT\_TAB):** For any given spectrum, the GRS will see a fairly large area of the surface. We will need to know which cells on the planet's surface are in the GRS field of view and contribute to the signal we would expect to receive. To minimize calculations and database queries, we shall limit the size of the surface area considered to a specific GRS footprint size and pre-calculate the cells which are in this GRS footprint for a given spacecraft location. While the limb-to-limb field of view of the spacecraft in a 400 km orbit is  $26.5^\circ$  of arc, we get  $>99\%$  of the signal from within  $17^\circ$  of the sub-spacecraft point for all gamma rays of interest if we assume that production is evenly distributed with depth. We thus determine which cells fall within this  $17^\circ$  footprint for each spacecraft position, with the assumption that a position over any part of a cell can be treated as though the spacecraft is located over the center of the cell. Since the map of cells in a footprint varies (meaningfully) only with latitude, we calculate one footprint for each of the 360 cell latitude bands. These are indexed such that the cell numbers in a given footprint are simple offsets in longitude from the invariant map. This array of footprints is stored in FOOTPRINT\_TAB and has 360 rows; each row being a reference to a latitude band. Each row has the following structure:

*Latitude\_index*, NUM(6,0), latitude of cell in the center of the footprint

(primary key)

*Start\_lat\_index*, NUM(3,0), index of the northernmost latitude in the footprint

*Number\_of\_lats*, NUM(3,0), number of latitudes in the footprint

Pairs of *Start\_lon\_index*, NUM(3,0), base starting index for cells in this latitude, and *End\_lon\_index*, NUM(3,0), base ending index for cells in this latitude

The contents of each row are a maximum of 77 pairs of numbers. The first pair is a starting (northernmost) latitude index and the number of latitude bands in the footprint. The remaining entries are the starting longitude index and ending longitude index for each of the included latitude bands. Latitude indices run from 0 to 359 from the north to south poles while the longitude indices run from 0 to 719 from the prime meridian east back to the prime meridian. Thus the cell number can be calculated as:

$$Cell\_number = (latitude\_index * 720) + longitude\_index \quad (A.12)$$

Note that we may have a starting longitude of  $350^\circ$ , i.e. index 700, and an ending longitude of  $10^\circ$ , i.e. index 20, when we need to wrap around the planet's prime meridian. The contribution calculation code recognizes this situation and performs the correct wraparound.

The row number in the table is the latitude index of the cell in the center of the circle that makes up the GRS footprint, i.e. the spacecraft's location when the spectrum was taken. The latitudes are all the latitudes that fall in the  $38^\circ$  diameter circle (with a  $0.5^\circ$  spacing, the maximum number is  $38/0.5 = 76$ ). Remembering that we have a start-stop pair for each latitude, as well

as a pair that gives the beginning and number of latitudes, we find the size:  $360 * 77 * 2 = 5,544$  entries = 11,088 bytes (two bytes per entry).

The number of cells in each footprint vary from a minimum when the spacecraft is at the equator to a maximum at the poles. The footprint is  $17^\circ$  in radius. If we are directly over a pole (although we will never be, as the inclination of the orbit is around  $93^\circ$ , i.e.  $3^\circ$  away from the pole) the number of  $0.5^\circ$  cells is  $17.5/0.5 * 360/0.5 = 25,200$ . At the equator, it will be the number of cells in a circle of  $17^\circ$  radius (6,000 approximately).

4. **Atmospheric Conditions (THICKNESS\_TAB):** The atmosphere of Mars attenuates gamma ray photons as they leave the surface and travel to the spacecraft. The degree of attenuation depends on the amount of atmosphere that the gamma rays must traverse, which in turn depends on the season and local temperature. Atmospheric thicknesses and temperatures have been pre-calculated for two times of day (5 a.m. and 5 p.m.) for each cell for each Mars day (Sol) and stored in the array THICKNESS\_TAB. Atmospheric thickness was calculated with the IDL routine `atm_thickness1.pro`, which is based on the MOLA  $0.5^\circ$  by  $0.5^\circ$  elevation map and scale height and pressure variations with latitude and the time of year. Pressure variations and scale height values were obtained from Jim Murphy (AMES) who used the Mars General Circulation Model (GCM). The results of GCM were provided on a grid spacing of  $7.5^\circ$  in latitude and  $9^\circ$  in longitude, excluding polar regions (areas less than  $3.75^\circ$  from the poles). They include evaluations of surface pressure at 40 points (spaced  $9^\circ$  apart in longitude) at each latitude and 16 times per Martian day.

From these data we calculate, for the center of each cell on a new  $0.5^\circ$  by  $0.5^\circ$  grid, the average pressure at 5 a.m. and 5 p.m. (each a 3 hour average). It is assumed that scale height, though it might be different for different latitudes, does not depend on longitude along a constant line of latitude. The 40 points along each latitude corresponded to different elevations and these data were

used to evaluate the scale height at a given latitude. This procedure was repeated for each day of the Martian year. THICKNESS\_TAB has a line for each Sol and each line contains a BLOB of  $259,200 * 2 * 2 * 4 = 4.15$  Mb of data consisting of a temperature and thickness values for each cell.

5. **Atmospheric Attenuation (G\_TAB):** The attenuation of the gamma ray signal as it traverses the atmosphere on its way to the spacecraft is calculated from the atmospheric thickness and the angle between the local vertical and the direction from the cell to the spacecraft, which together give the path length through the atmosphere. For each peak (energy) of interest we define a set of transmission factors:

$$G_{l,P} = e^{-\mu x} \quad (\text{A.13})$$

where  $l$  is the path length index,  $P$  is the peak of interest (energy) index,  $\mu$  is the mass attenuation coefficient, which is a smooth function of energy ( $\text{cm}^2/\text{g}$ ), and  $x$  is the column density of atmosphere along path to spacecraft ( $\text{g}/\text{cm}^2$ ).

The mass attenuation coefficient,  $\mu$ , is calculated using the National Institute of Standards and Technology's XCOM program and its photon cross sections database, on the web at: <http://physics.nist.gov/PhysRefData/Xcom/Text/XCOM.html>. We use a Mars atmosphere composed of (wt%):

CO<sub>2</sub>: 0.965254, N<sub>2</sub>: 0.017407, Ar: 0.014710, CO: 0.001547, O<sub>2</sub>: 0.000957,  
and H<sub>2</sub>O: 0.000124.

To facilitate speed of computation, we do this calculation via a look-up table, G\_TAB. This table will contain 2 BLOBs for each peak in the CONTRIBUTION\_POI\_TAB. These are used to calculate the atmospheric attenuation coefficient for the peak. The structure of G\_TAB is:

*Peak\_number*, NUM(3)

*Gint*, BLOB

*Gfrac*, BLOB

The *Gint* and *Gfrac* BLOBs each contain 100 floats (400 bytes). The *Gint* BLOB contains the integer portion (from 0 to 99 in increments of 1) and *Gfrac* contains the fractional portion (from 0 to 0.99 in increments of 0.01). Thus if  $-\mu x = -xx.yy$  then  $Gint = e^{-xx}$  and  $Gfrac = e^{-yy}$  and

$$G_{l,P} = Gint * Gfrac \quad (A.14)$$

In any given spectrum, path length is a function of the spacecraft position during the collection of that spectrum and the given cell's position. We calculate the path length through the atmosphere using a plane parallel approximation since we have determined that this is sufficiently accurate (<1% error) for our purposes. Otherwise, this will be a pretty static table, only updated when we add a new peak or change our atmospheric attenuation models.

In practice, atmospheric thickness and attenuation calculations are combined in a single computer model and the results stored in G\_TAB files.

6. **Detector Efficiency (E\_TAB):** The efficiency with which the GRS detector head converts incoming gamma rays into counts is not uniform. The efficiency of the detector was mapped out during preflight calibrations and we store efficiencies in the array E\_TAB. This table has a BLOB for each peak in the CONTRIBUTION\_POI\_TAB containing the detector efficiency ( $\varepsilon_{\psi,\xi,P,S}$  in counts/photon) as a function of the nadir angle ( $\psi$ ) and the position angle ( $\xi$ ):

*Peak\_number*, NUM(3)

*$\varepsilon$ \_values*, BLOB

We store the efficiencies for every  $2^\circ$ , so these BLOBs will be  $35 * 181 * 4 = 25,340$  bytes. Note that we limit  $\psi$  to  $0^\circ - 70^\circ$ , and that

we have one extra entry for  $\xi$  to allow us to easily interpolate between  $358^\circ$  and  $360^\circ (= 0^\circ)$ .

### Spectrum Dependent Values

For every 20 second spectrum we initially query the database to determine the spacecraft time, spectrum identifier, live time, cosmic-ray fluence, fast neutron fluence, and thermal neutron fluence. We shall also determine several geometric angles and vectors (Figures A.1 through A.4).

1. **Spacecraft Position Vector ( $\mathbf{R}_{s/c}$ ) (Figure A.1):** From a SPICE call. This is the Mars-centered, Mars-fixed (MCMF) coordinate vector of the spacecraft (S/C).
2. **Instrument Boresight Vector ( $\mathbf{R}_{cx}$ ) (Figure A.1):** From a SPICE call. This is the MCMF coordinates of the boresight/surface intersection.
3. **Gamma Ray Sensor Head (GSH) - North angle ( $\Delta\theta$ ) (Figure A.2):** From a SPICE call. This is the angle between the GSH +Y axis and Mars North projected onto the plane of the footprint.
4. **Vector to Local North ( $\mathbf{R}_{CXN}$ ) (Figure A.3):** The vector from the boresight/surface intersection to the North Pole. This is approximated by the vector from the boresight/surface intersection to the center of the cell immediately surrounding the North Pole that is directly north of the cell in which the boresight/surface intersection falls.
5. **Projection and Rotation of  $\mathbf{R}_{CXN}$  onto the Plane Perpendicular to  $\mathbf{R}_{CX}$  ( $\mathbf{P}_{CXN}$ ) (Figure A.4):**

$$\vec{P}_{CXN} = \vec{R}_{CX} \times \vec{R}_{CXN} \quad (\text{A.15})$$

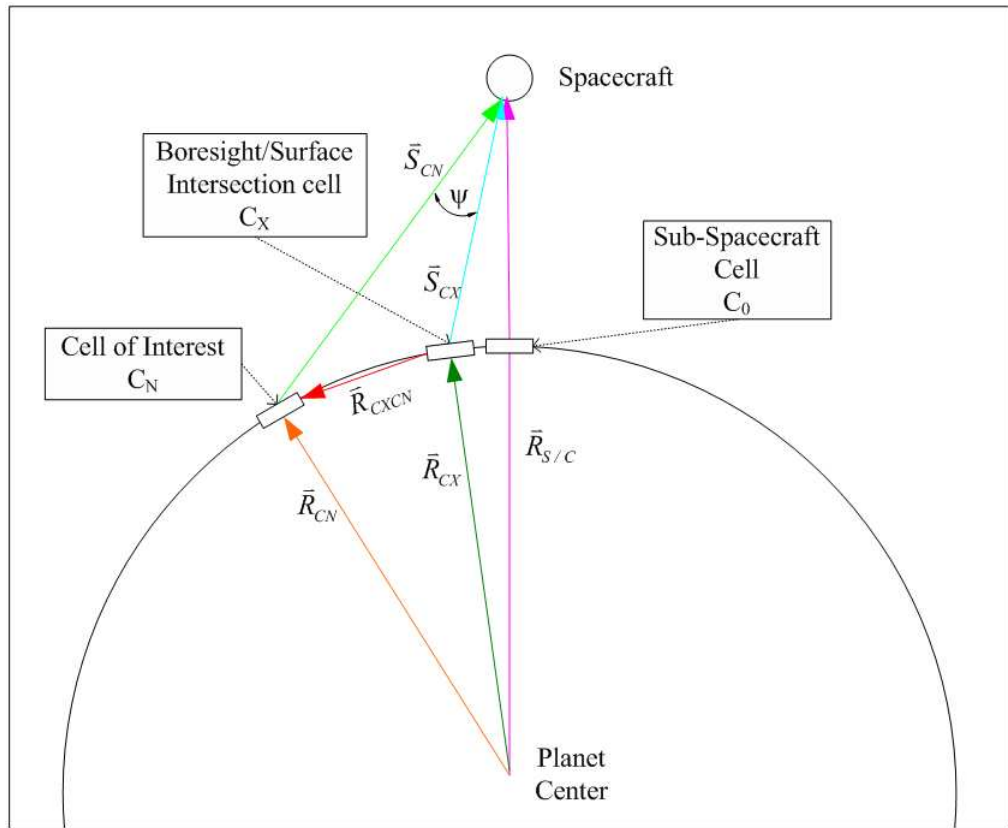


Figure A.1: Diagram 1.

These vectors allow us to walk through each cell in the footprint and calculate its contribution to the signal we expect to receive. We know from  $R_{s/c}$  which cell is in the center of the footprint (which cell is directly below the spacecraft) and, from the precalculated GRS footprints outlined in the *GRS Footprint (FOOTPRINT\_TAB)* section above, which cells we will deal with as contributing to the signal for this spectrum.

### Cell Dependent Values

We now need to determine a number of angles, vectors and distances that depend on both the cell position (recall that cells are indexed by  $i$ ) and the spacecraft position (recall that we are assuming that the spacecraft position is static during a spectrum,  $S$ ). So each value in the following discussion carries the implicit (if not

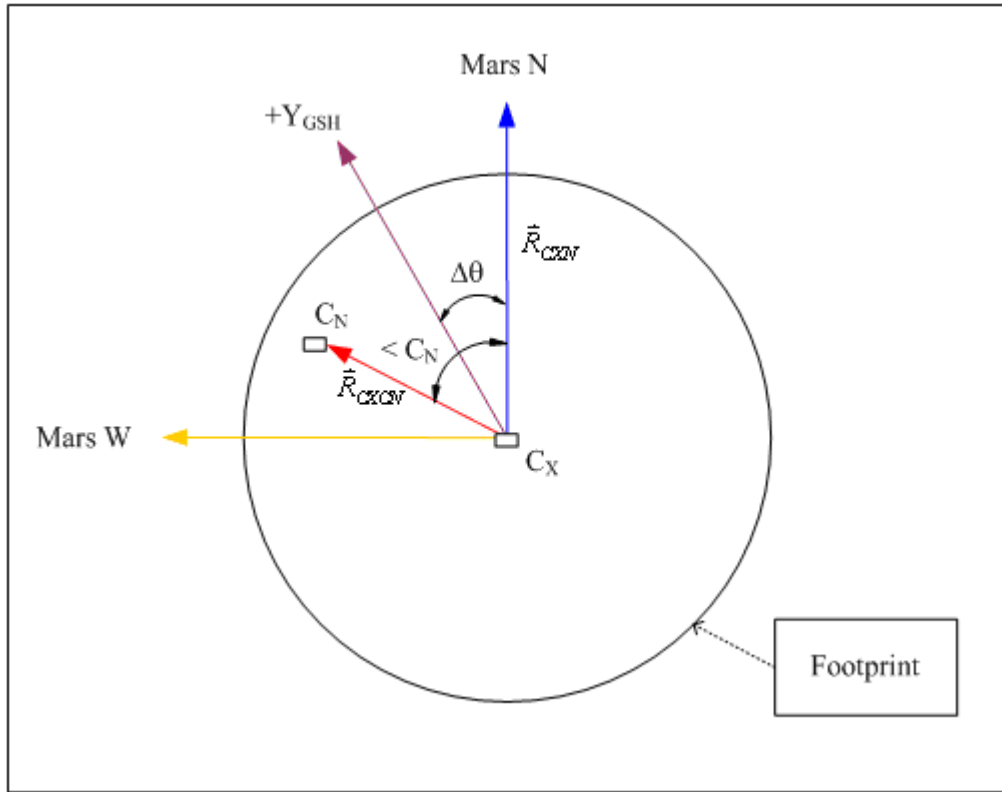


Figure A.2: Diagram 2.

explicit) indices  $i$  and  $S$ . For every cell that contributes to the signal for a given 20 second spectrum we shall determine:

1. **Cell-Spacecraft Vector ( $S_{CN}$ ) (Figures A.1, A.3):** The vector from the cell to the spacecraft.

$$\vec{S}_{CN} = \vec{R}_{S/C} - \vec{R}_{CN} \quad (\text{A.16})$$

where  $R_{CN}$  is the position vector of the cell determined in the *Planetary Surface Geometry (CELL-TAB)*, *Position Vector* section above. Note that the magnitude of  $S_{CN}$  is the distance from the cell to the spacecraft.

2. **Solid Angle of Detector ( $\Omega_{i,S}$ ):** As viewed from the the cell:

$$\Omega_{i,S} = \frac{35.52 \text{ cm}^2}{\|\vec{S}_{CN}\|^2} \quad (\text{A.17})$$

where  $35.52 \text{ cm}^2$  is the cross-sectional area of the detector, the value used in generating the efficiency table. Note that we calculate  $\Omega$  in units of  $\text{cm}^2/\text{km}^2$  for scaling reasons. This is really steradians \*  $10^{10}$ .

3. **Regolith Emission Angle ( $\theta_R$ ):** This is the angle at which the gamma rays travel through the regolith relative to local level and determines their path length within the regolith:

$$\cos \theta_R = \vec{N}_C \cdot \vec{S}_{CN} \quad (\text{A.18})$$

where  $\vec{N}_C$  is the cell's normal vector computed in the *Planetary Surface Geometry (CELL-TAB), Normal Vector* section above.

4. **Atmosphere Emission Angle ( $\theta_A$ ):** This is the angle at which gamma rays leave the surface and travel through the atmosphere:

$$\cos \theta_A = \vec{n}_C \cdot \vec{S}_{CN} \quad (\text{A.19})$$

where  $\vec{n}_C$  is the cell's zenith vector computed in the *Planetary Surface Geometry (CELL-TAB), Vertical (Zenith) Vector* section above.

5. **Atmospheric Path Length:** This is just the atmospheric thickness for this cell for this time (morning or evening) on this day as determined in the *Atmospheric Conditions (THICKNESS-TAB)* section above divided by the cosine of the atmospheric emission angle as determined in the *Atmospheric Emission Angle* section above. We have determined that this plane-atmosphere



$$\vec{S}_{CX} = \vec{R}_{S/C} - \vec{R}_{CX} \quad (\text{A.20})$$

B) Vector from the cell to the spacecraft ( $\vec{S}_{CN}$ ) (Figure A.1):

$$\vec{S}_{CN} = \vec{R}_{S/C} - \vec{R}_{CN} \quad (\text{A.21})$$

C) Angle between the boresight and the spacecraft/cell vector ( $\psi$ ):

$$\psi = \cos^{-1}(\hat{S}_{CX} \cdot \hat{S}_{CN}) \quad (\text{A.22})$$

This is the off-nadir angle from the boresight and one of the two angles we need to find our way into the efficiency map. The other angle we need is the azimuth or clocking angle,  $\xi$ . We continue by finding  $\xi$ :

D) Vector from boresight/surface intersection to the cell center ( $\vec{R}_{CXCN}$ ) (Figure A.4):

$$\vec{R}_{CXCN} = \vec{R}_{CN} - \vec{R}_{CX} \quad (\text{A.23})$$

E) Projection and rotation of  $\vec{R}_{CXCN}$  and  $\vec{R}_{CXN}$  onto the plane perpendicular to  $\vec{R}_{CX}$  ( $\vec{P}_{CXCN}$  and  $\vec{P}_{CXN}$ ) (Figure A.4):

$$\vec{P}_{CXCN} = \vec{R}_{CX} \times \vec{R}_{CXCN} \quad (\text{A.24})$$

$$\vec{P}_{CXN} = \vec{R}_{CX} \times \vec{R}_{CXN} \quad (\text{A.25})$$

F) Angle between vector to cell and vector to north (the clock angle,  $A_C$ ) (labelled  $\angle C_N$  in Figures A.2, A.4):

$$A_C = \cos^{-1}(\hat{P}_{CXN} \cdot \hat{P}_{CXCN}) \quad (\text{A.26})$$

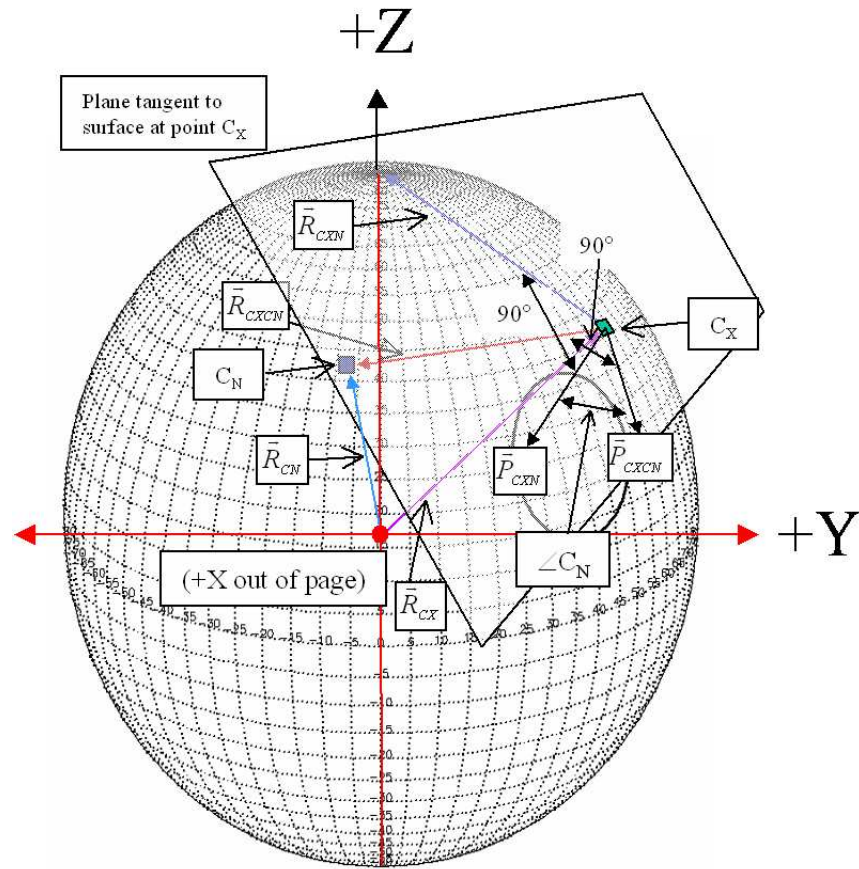


Figure A.4: Diagram 4.

G) And finally, the angle between the vector to the cell and the GSH's prime meridian:

$$\xi = A_C - \Delta\theta \quad (\text{A.27})$$

### Peak Dependent Values

For every peak of interest in a given 20 second spectrum, and for every cell in the footprint that contributes to that spectrum, (One can begin to see why we need to be efficient in our processing, and why at this point everything should just be a

look-up.) we shall determine:

1. **Efficiency of the Detector** ( $\varepsilon_{i,P,S}$ ) for this cell geometry ( $\psi, \xi$ ), for this peak of interest (P), for this spectrum (S), interpolated from the array(s) determined in the *Detector Efficiency (E-TAB)* section above.
2. **Attenuation Coefficient** ( $G_{i,P,S}$ ) for this cell's path length (see the *Atmospheric Path Length* section above) and this peak of interest (P) from the array(s) determined in the *Atmospheric Attenuation (G-TAB)* section above.
3. **Production Constant** ( $k_{i,P,S}$ ) for this cell's composition, slope, and atmospheric thickness, interpolated from the array(s) determined in the *Production Constants (K-TAB)* section above.

### Summation

As we calculate the spectrum, cell, and peak dependent values, we use them to generate the counts expected for that peak in the spectrum. This is the product of the cell's production rate, area and atmospheric attenuation, the detector's solid angle and efficiency, and the fluence. For prompt gamma rays, we shall multiply by the excitation fluence in order to convert to counts, and for radioactivity, we shall multiply by the accumulation time of the spectrum. Note that we have to convert from  $\text{cm}^2$  to  $\text{km}^2$  because the excitation is in units of  $\text{cm}^2$  and the area of the cell is in units of  $\text{km}^2$ . On the other hand, the solid angle of the detector has similar and offsetting units, since the distance from the cell to the spacecraft is measured in km (and this is squared in determining the solid angle) and the area of the cell has units of  $\text{cm}^2$ . This is why we chose to calculate the solid angle of the detector with mixed units. We keep a running summation of the counts. For each peak of interest,  $P$ , for each spectrum,  $S$ , the number of counts expected is:

$$(Counts)_{P,S} = \sum_i [k_{i,P,S} * G_{i,P,S} * A_i * \Omega_{i,S} * \varepsilon_{i,P,S}] * (particle\_fluence)_S \quad (\text{A.28})$$

For naturally radioactive elements, the formula is similar except that we multiply by accumulation time rather than by the fluence of excitation particles. For radioactive elements that are made from solar particle events (SPE), the situation is a lot more complicated, as the count rate depends not on what the flux is at the time of the measurement, but the flux history over a time scale that is comparable to several half lives of the nuclide emitting the gamma ray. We shall not calculate these peaks for now.

**Spectral summation and analysis:** The expected counts in any given ( $\sim 20$  sec) spectrum will be very small, less than a single count in most cases. In order to get reasonable statistics, we add up many spectra over a particular region of the planet. To calculate the expected counts for each peak in the summed spectrum for that region, we simply add up the counts expected from each individual spectrum.

$$(Counts)_{P,R} = \sum_S (Counts)_{P,S} \quad (\text{A.29})$$

where  $R$  is the designation of the region of interest over which the spectra are summed.

## Glossary

*Cell:* a  $0.5^\circ \times 0.5^\circ$  area on the surface of the planet. The edges of the cells will be on half-integral degree boundaries, and the midpoints will be a quarter-degree offset from those even half-degree boundaries.

*Pixel:* a data set from a single data interval in the instrument, typically 20 seconds long. It will be stored and indexed by the time at the midpoint of the accumulation and the latitude and longitude at the time of the midpoint of the accumulation.

*Footprint:* The spot on the Mars surface from which some fraction of the signal occurs. It is a function of energy, being smaller for lower energies. For a gamma

line of 3 MeV, 50% of the signal comes from a circle of diameter about 600 km. Some signal comes all the way from limb to limb. For calculation purposes, we will assume we are talking about limb to limb.

*Concentration:* the fraction, by mass, of an element in the region under study, usually given in %, ppm (parts per million), or mass fraction.

*Composition:* This is the characterization of the region under study that is the collection of all of the concentrations of all elements present. (We don't determine all of the elements in the periodic table, but we do enough to account for over 99% of the mass.)

## REFERENCES

- Aharonson, O., M. T. Zuber, D. E. Smith, G. A. Neumann, W. C. Feldman, and T. H. Prettyman (2004). Depth, Distribution, and Density of CO<sub>2</sub> Deposition on Mars. *Journal of Geophysical Research (Planets)*, **109**, pp. 5004–+. doi: 10.1029/2003JE002223.
- Arvidson, R. E., E. A. Guinness, H. J. Moore, J. Tillman, and S. D. Wall (1983). Three Mars years - Viking Lander 1 imaging observations. *Science*, **222**, pp. 463–468.
- Arvidson, R. E. and S. Slavney (2005). PDS Geosciences Node: Viking Orbiter MAWD. <http://pds-geosciences.wustl.edu/missions/viking/mawd.html>. Retrieved 27 October 2005.
- Barker, E. S., R. A. Schorn, A. Woszczyk, R. G. Tull, and S. J. Little (1970). Mars: Detection of atmospheric water vapor during the southern hemisphere spring and summer season. *Science*, **170**, pp. 1308–1310.
- Baum, W. A., R. L. Millis, S. E. Jones, and L. J. Martin (1970). The International Planetary Patrol Program. *Icarus*, **12**, pp. 435–+.
- Bell, J. F., W. M. Calvin, M. E. Ockert-Bell, D. Crisp, J. B. Pollack, and J. Spencer (1996). Detection and monitoring of H<sub>2</sub>O and CO<sub>2</sub> ice clouds on Mars. *Journal of Geophysical Research*, **101**, pp. 9227–9238. doi:10.1029/96JE00689.
- Bell, J. F., T. B. McCord, and P. G. Lucey (1989). High-Resolution Imagery Probes Mars during the 1988 Opposition. *Earth and Space*, **1**, pp. 2–3.
- Berger, M. J., J. H. Hubbell, S. M. Seltzer, J. Chang, J. S. Coursey, R. Sukumar, and D. S. Zucker (1998). XCOM: Photon Cross Sections Database, NIST Standard Reference Database 8 (XGAM). <http://physics.nist.gov/PhysRefData/Xcom/Text/XCOM.html>.
- Bonev, B. P., J. E. Bjorkman, G. B. Hansen, P. B. James, and M. J. Wolff (2002a). Effects of surface dust on the sublimation of CO<sub>2</sub> on Mars. Radiative equilibrium atmospheric modeling. *Bulletin of the American Astronomical Society*, **34**, pp. 866–+.
- Bonev, B. P., P. B. James, J. E. Bjorkman, and M. J. Wolff (2002b). Regression of the Mountains of Mitchel polar ice after the onset of a global dust storm on Mars. *Geophysical Research Letters*, **29**, pp. 13–1.

- Boynton, W. V., W. Feldman, T. Prettyman, and D. Hamara (2002a). Subsurface Ice Content in the Polar Region of Mars: Comparison Between North and South. *AGU Fall Meeting Abstracts*, pp. B2+.
- Boynton, W. V., W. C. Feldman, I. G. Mitrofanov, L. G. Evans, R. C. Reedy, S. W. Squyres, R. Starr, J. I. Trombka, C. d'Uston, J. R. Arnold, P. A. J. Englert, A. E. Metzger, H. Wänke, J. Brückner, D. M. Drake, C. Shinohara, C. Fellows, D. K. Hamara, K. Harshman, K. Kerry, C. Turner, M. Ward, H. Barthe, K. R. Fuller, S. A. Storms, G. W. Thornton, J. L. Longmire, M. L. Litvak, and A. K. Ton'chev (2004a). The Mars Odyssey Gamma-Ray Spectrometer Instrument Suite. *Space Science Reviews*, **110**, pp. 37–83.
- Boynton, W. V., W. C. Feldman, S. W. Squyres, T. H. Prettyman, J. Brückner, L. G. Evans, R. C. Reedy, R. Starr, J. R. Arnold, D. M. Drake, P. A. J. Englert, A. E. Metzger, I. Mitrofanov, J. I. Trombka, C. d'Uston, H. Wänke, O. Gasnault, D. K. Hamara, D. M. Janes, R. L. Marcialis, S. Maurice, I. Mikheeva, G. J. Taylor, R. Tokar, and C. Shinohara (2002b). Distribution of Hydrogen in the Near Surface of Mars: Evidence for Subsurface Ice Deposits. *Science*, **297**, pp. 81–85. doi:10.1126/science.1073722.
- Boynton, W. V., R. Haberle, N. J. Kelly, and A. Sprague (2006a). Use of Mars Odyssey GRS Results to Constrain the Exchangeable Mass of Martian CO<sub>2</sub>. In *Mars Atmosphere Modelling and Observations, 2nd Workshop*. Granada, Spain.
- Boynton, W. V., K. Kim, D. Janes, K. Kerry, R. Williams, R. Reedy, and D. Drake (2004b). Spatial and Depth Distribution of Sub-surface Ice in the Polar Regions of Mars. In *35th COSPAR Scientific Assembly*, pp. 4074–+.
- Boynton, W. V., K. J. Kim, D. Drake, R. C. Reedy, D. Janes, K. Kerry, R. Williams, K. Crombie, and The GRS Science Team (2005). Determination of Both Depth and Ice Content of Sub-Surface Ice in the Polar Regions. In *36th Annual Lunar and Planetary Science Conference*, pp. 2154–+.
- Boynton, W. V., G. J. Taylor, L. G. Evans, R. C. Reedy, D. M. Janes, K. Kerry, D. M. Drake, K. J. Kim, R. M. S. Williams, K. Crombie, J. M. Dohm, V. Baker, A. E. Metzger, S. Karunatillake, J. Keller, J. R. Arnold, J. Brückner, P. A. J. Englert, O. Gasnault, A. L. Sprague, S. W. Squyres, J. I. Trombka, C. d'Uston, and H. Wänke (2006b). Concentration of H, Si, Cl, K, Fe, and Th in the low and mid latitude regions of Mars. *Journal of Geophysical Research*. Submitted.
- Boynton, W. V., J. I. Trombka, W. C. Feldman, J. R. Arnold, P. A. J. Englert, A. E. Metzger, R. C. Reedy, S. W. Squyres, H. Wänke, S. H. Bailey, J. Brückner, J. L. Callas, D. M. Drake, P. Duke, L. G. Evans, E. L. Haines, F. C. McCloskey, H. Mills, C. Shinohara, and R. Starr (1992). Science Applications of the Mars

- Observer Gamma Ray Spectrometer. *Journal of Geophysical Research*, **97**, pp. 7681–7698.
- Briggs, G., K. Klaasen, T. Thorpe, J. Wellman, and W. Baum (1977). Martian dynamical phenomena during June–November 1976: Viking orbiter imaging results. *Journal of Geophysical Research*, **82**, pp. 4121–4149.
- Briggs, G. A. (1974). The nature of the residual Martian polar caps. *Icarus*, **23**, pp. 167–191.
- Briggs, G. A. and C. B. Leovy (1974). Mariner Observations of the Mars North Polar Hood. *Bulletin of the American Meteorological Society*, **55**, pp. 278–278.
- Brückner, J., U. Fabian, A. Patnaik, H. Wänke, P. Cloth, G. Dagge, V. Druke, D. Filges, P. A. J. Englert, D. M. Drake, R. C. Reedy, and B. Parlier (1992). Simulation Experiments for Planetary Gamma-Ray Spectroscopy by Means of Thick Target High-Energy Proton Irradiations. In *Lunar and Planetary Institute Conference Abstracts*, pp. 169–+.
- Brückner, J., M. Körfer, H. Wänke, A. N. F. Schröder, D. Filges, P. Dragovitsch, P. A. J. Englert, R. Starr, and J. I. Trombka (1991). Proton-induced radiation damage in germanium detectors. *IEEE Transactions on Nuclear Science*, **38**, pp. 209–217.
- Brückner, J., H. Wänke, and R. C. Reedy (1987). Neutron-induced gamma ray spectroscopy: Simulations for chemical mapping of planetary surfaces. *Journal of Geophysical Research*, **92**, pp. 603–+.
- Bryne, S. and A. P. Ingersoll (2003). A Sublimation Model for Martian South Polar Ice Features. *Science*, **299**, pp. 1051–1053.
- Capen, C. F. and V. W. Capen (1970). Martian north polar cap, 1962–68. *Icarus*, **13**, pp. 100–108.
- Carr, M. H. (1998). *Mars: Surface and Interior*, pp. 291–308. Encyclopedia of the Solar System.
- Clark, R. N., R. B. Singer, G. A. Swayze, and A. Tokunaga (1989). Discovery of globally distributed scapolite on Mars. In *Fourth International Conference on Mars*, pp. 82–83.
- Colaprete, A. and O. B. Toon (2002). Carbon dioxide snow storms during the polar night on Mars. *Journal of Geophysical Research (Planets)*, **107**, pp. 5–1. doi:10.1029/2001JE001758.

- Colburn, D. S., J. B. Pollack, and R. M. Haberle (1989). Diurnal variations in optical depth at Mars. *Icarus*, **79**, pp. 159–189. doi:10.1016/0019-1035(89)90114-0.
- Connerney, J. E. P., M. H. Acuna, P. J. Wasilewski, N. F. Ness, H. Reme, C. Mazelle, D. Vignes, R. P. Lin, D. L. Mitchell, and P. A. Cloutier (1999). Magnetic Lineations in the Ancient Crust of Mars. *Science*, **284**, pp. 794–+.
- Cross, C. A. (1971). The heat balance of the martian polar caps. *Icarus*, **15**, pp. 110–114.
- Davies, D. W. (1979). Effects of dust on the heating of Mars' surface and atmosphere. *Journal of Geophysical Research*, **84**, pp. 8289–8293.
- Davies, D. W., C. B. Farmer, and D. D. Laporte (1977). Behavior of volatiles in Mars' polar areas - A model incorporating new experimental data. *Journal of Geophysical Research*, **82**, pp. 3815–3822.
- de Vaucouleurs, G. (1989). The best telescopic pictures of Mars. *Sky and Telescope*, **77**, pp. 15–17.
- Dobbins, T. A., D. C. Parker, and C. F. Capen (1988). *Introduction to observing and photographing the solar system*. Richmond, Va., U.S.A. : Willmann-Bell.
- Dollfus, A. (1957). Étude des planètes par la polarisation de leur lumière. *Ann. Astrophys. Suppl.*, **4**, pp. 3–114. English trans.: NASA-TT-F-188.
- Dollfus, A. (1965). Étude de la planète Mars de 1954 à 1958. *Annales d'Astrophysique*, **28**, pp. 722–747.
- Dollfus, A. (1973). New optical measurements of planetary diameters. IV. Size of the north polar cap of Mars. *Icarus*, **18**, pp. 142–155.
- Eluszkiewicz, J. (1993). On the microphysical state of the Martian seasonal caps. *Icarus*, **103**, pp. 43–48. doi:10.1006/icar.1993.1056.
- Eluszkiewicz, J. and T. N. Titus (2002). Application of a Sintering Model to the Analysis of TES Spectra of the Seasonal Caps. *Bulletin of the American Astronomical Society*, **34**, pp. 866–+.
- Evans, L. G., R. C. Reedy, and R. D. Starr (2006). Analysis of Gamma Ray Spectra Measured by Mars Odyssey. *Journal of Geophysical Research*. Submitted.
- Evans, L. G., R. C. Reedy, and J. I. Trombka (1993). *Introduction to planetary remote sensing gamma ray spectroscopy*, chapter in Remote Geochemical Analyses: Elemental and Mineralogical Composition, pp. 167–198. Cambridge Univ. Press, New York.

- Fedorova, A. A., A. V. Rodin, and I. V. Baklanova (2004). Seasonal cycle of water vapor in the atmosphere of Mars as revealed from the MAWD/Viking 1 and 2 experiment. *Solar System Research*, **38**, pp. 421–433. doi:10.1007/s11208-005-0009-2.
- Feldman, W. C., W. V. Boynton, T. H. Prettyman, S. W. Squyres, and R. L. Tokar (2002a). Time Variation of the North Polar Seasonal Frost Cap of Mars. *AGU Fall Meeting Abstracts*, pp. B3+.
- Feldman, W. C., W. V. Boynton, R. L. Tokar, T. H. Prettyman, O. Gasnault, S. W. Squyres, R. C. Elphic, D. J. Lawrence, S. L. Lawson, S. Maurice, G. W. McKinney, K. R. Moore, and R. C. Reedy (2002b). Global Distribution of Neutrons from Mars: Results from Mars Odyssey. *Science*, **297**, pp. 75–78. doi:10.1126/science.1073541.
- Feldman, W. C. and D. M. Drake (1986). A Doppler filter technique to measure the hydrogen content of planetary surfaces. *Nuclear Instruments and Methods in Physics Research A*, **245**, pp. 182–190.
- Feldman, W. C., T. H. Prettyman, W. V. Boynton, J. R. Murphy, S. Squyres, S. Karunatillake, S. Maurice, R. L. Tokar, G. W. McKinney, D. K. Hamara, N. Kelly, and K. Kerry (2003). CO<sub>2</sub> frost cap thickness on Mars during northern winter and spring. *Journal of Geophysical Research (Planets)*, **108**, pp. 7–1.
- Firestone, R. B. (1996). *Table of Isotopes, 8th Ed.* John Wiley & Sons, New York.
- Fischbacher, G. E., L. J. Martin, and W. A. Baum (1969). Mars Polar Cap Boundaries. *Final Rept. under JPL Contract 951547 (Flagstaff: Planetary Research Center, Lowell Obs.)*, **4**, pp. 3–114.
- Fishbaugh, K. E. and J. W. Head (2001). Comparison of the North and South Polar Caps of Mars: New Observations from MOLA Data and Discussion of Some Outstanding Questions. *Icarus*, **154**, pp. 145–161. doi:10.1006/icar.2001.6666.
- Fjeldbo, G., W. C. Fjeldbo, and V. R. Eshleman (1966). Models for the Atmosphere of Mars Based on the Mariner 4 Occultation Experiment. *Journal of Geophysical Research*, **71**, pp. 2307–+.
- Gierasch, P. J. and R. M. Goody (1968). A study of the thermal and dynamical structure of the martian lower atmosphere. *Planetary and Space Science*, **16**, pp. 615–+.
- Gierasch, P. J. and R. M. Goody (1973). A Model of a Martian Great Dust Storm. *Journal of Atmospheric Sciences*, **30**, pp. 169–179.
- Goodall, K. (1997). Mars Pathfinder. <http://marsprogram.jpl.nasa.gov/MPF/>. Retrieved 14 July 2005.

- Goodall, K. and The MGS Team (2005). Mars Global Surveyor Homepage. <http://mars.jpl.nasa.gov/mgs/>. Retrieved 03 August 2005.
- Haberle, R. M., M. M. Joshi, J. R. Murphy, J. R. Barnes, J. T. Schofield, G. Wilson, M. Lopez-Valverde, J. L. Hollingsworth, A. F. C. Bridger, and J. Schaeffer (1999). General circulation model simulations of the Mars Pathfinder atmospheric structure investigation/meteorology data. *Journal of Geophysical Research*, **104**, pp. 8957–8974.
- Haberle, R. M., C. B. Leovy, and J. B. Pollack (1982). Some effects of global dust storms on the atmospheric circulation of Mars. *Icarus*, **50**, pp. 322–367. doi:10.1016/0019-1035(82)90129-4.
- Haberle, R. M., J. B. Pollack, J. R. Barnes, R. W. Zurek, C. B. Leovy, J. R. Murphy, H. Lee, and J. Schaeffer (1993). Mars atmospheric dynamics as simulated by the NASA AMES General Circulation Model. I - The zonal-mean circulation. *Journal of Geophysical Research*, **98**, pp. 3093–3123.
- Hamara, D. (2003). GRS Igor Procedures, V2.05. *University of Arizona, Lunar and Planetary Laboratory Internal Report*.
- Hamilton, V. E. and S. W. Ruff (2005). Mars Global Surveyor Thermal Emission Spectrometer Homepage. <http://tes.asu.edu/>. Retrieved 27 October 2005.
- Hansen, G. B. (1997). The infrared absorption spectrum of carbon dioxide ice from 1.8 to 333  $\mu\text{m}$ . *Journal of Geophysical Research*, **102**, pp. 21569–21588. doi:10.1029/97JE01875.
- Hansen, G. B. (1999). Control of the radiative behavior of the Martian polar caps by surface CO<sub>2</sub> ice: Evidence from Mars Global Surveyor measurements. *Journal of Geophysical Research*, **104**, pp. 16471–16486. doi:10.1029/1998JE000626.
- Hess, S. L., R. M. Henry, and J. E. Tillman (1979). The seasonal variation of atmospheric pressure on Mars as affected by the south polar cap. *Journal of Geophysical Research*, **84**, pp. 2923–2927.
- Howard, A. D., J. A. Cutts, and K. R. Blasius (1982). Stratigraphic relationships within Martian polar cap deposits. *Icarus*, **50**, pp. 161–215. doi:10.1016/0019-1035(82)90123-3.
- Ingersoll, A. P. (1974). Mars: The case against permanent CO<sub>2</sub> frost caps. *Journal of Geophysical Research*, **79**, pp. 3403–3410.
- Ivanov, A. B. and D. O. Muhleman (2001). Cloud Reflection Observations: Results from the Mars Orbiter Laser Altimeter. *Icarus*, **154**, pp. 190–206. doi:10.1006/icar.2001.6686.

- Iwasaki, K., Y. Saito, and T. Akabane (1979). Behavior of the Martian North Polar Cap, 1975-1978. *Journal of Geophysical Research*, **84**, pp. 8311–8316.
- Iwasaki, K., Y. Saito, and T. Akabane (1982). Martian North Polar Cap 1979-1980. *Journal of Geophysical Research*, **87**, pp. 10265–10269.
- Iwasaki, K., Y. Saito, and T. Akabane (1984). Martian north polar cap and haze 1981-1982. *Publ. Astron. Soc. Japan*, **36**, pp. 347–356.
- Iwasaki, K., Y. Saito, and T. Akabane (1986). Martian south polar cap 1973. *Publ. Astron. Soc. Japan*, **38**, pp. 267–275.
- Iwasaki, K., Y. Saito, Y. Nakai, T. Akabane, and E. Panjaitan (1988). Martian south polar cap 1986. *Vistas in Astronomy*, **31**, pp. 141–146.
- Iwasaki, K., Y. Saito, Y. Nakai, T. Akabane, and E. Panjaitan (1989). Behavior of the Martian south polar cap 1986. *Publ. Astron. Soc. Japan*, **41**, pp. 1083–1094.
- Iwasaki, K., Y. Saito, Y. Nakai, T. Akabane, and E. Panjaitan (1990). Martian south polar cap 1988. *Journal of Geophysical Research*, **95**, pp. 14751–14754.
- Jakosky, B. M. (1985). The seasonal cycle of water on Mars. *Space Science Reviews*, **41**, pp. 131–200.
- Jakosky, B. M. and C. B. Farmer (1982). The seasonal and global behavior of water vapor in the Mars atmosphere - Complete global results of the Viking atmospheric water detector experiment. *Journal of Geophysical Research*, **87**, pp. 2999–3019.
- Jakosky, B. M. and R. M. Haberle (1990). Year-to-year instability of the Mars south polar cap. *Journal of Geophysical Research*, **95**, pp. 1359–1365.
- Jakosky, B. M. and R. M. Haberle (1992). *The seasonal behavior of water on Mars*, pp. 969–1016. Mars.
- James, P. B. and B. A. Cantor (2001). Martian North Polar Cap Recession: 2000 Mars Orbiter Camera Observations. *Icarus*, **154**, pp. 131–144. doi:10.1006/icar.2001.6653.
- James, P. B., B. A. Cantor, and S. Davis (2001). Mars Orbiter Camera observations of the Martian south polar cap in 1999-2000. *Journal of Geophysical Research*, **106**, pp. 23635–23652. doi:10.1029/2000JE001313.
- James, P. B., G. B. Hansen, and T. N. Titus (2005). The carbon dioxide cycle. *Advances in Space Research*, **35**, pp. 14–20. doi:10.1016/j.asr.2003.04.056.

- James, P. B., J. L. Hollingsworth, M. J. Wolff, and S. W. Lee (1999). North Polar Dust Storms in Early Spring on Mars. *Icarus*, **138**, pp. 64–73. doi:10.1006/icar.1998.6060.
- James, P. B., H. H. Kieffer, and D. A. Paige (1992). *The seasonal cycle of carbon dioxide on Mars*, pp. 934–968. Mars.
- James, P. B. and K. Lumme (1982). Martian south polar cap boundary: 1971 and 1973 data. *Icarus*, **50**, pp. 368–380.
- James, P. B., L. J. Martin, J. R. Henson, and P. V. Birch (1990). Seasonal recession of Mars' south polar cap in 1986. *Journal of Geophysical Research*, **95**, pp. 1337–1341.
- James, P. B., M. Pierce, and L. J. Martin (1987). Martian north polar cap and circumpolar clouds: 1975 - 1980 telescopic observations. *Icarus*, **71**, pp. 306–312.
- Janes, D. (2002). Production and Attenuation of Radiogenic Gamma Rays in the Martian Regolith. *University of Arizona, Lunar and Planetary Laboratory Internal Document*.
- Kahn, R. A., T. Z. Martin, R. W. Zurek, and S. W. Lee (1992). *The Martian dust cycle*, pp. 1017–1053. Mars.
- Karol, P. and D. Catling (2003). Mars Chronology: Renaissance to the Space Age. [http://www1.nasa.gov/lb/audience/forstudents/9-12/features/F\\_Mars\\_Chronology.html](http://www1.nasa.gov/lb/audience/forstudents/9-12/features/F_Mars_Chronology.html). Retrieved 22 April 2005.
- Kasting, J. F. (1991). CO<sub>2</sub> condensation and the climate of early Mars. *Icarus*, **94**, pp. 1–13. doi:10.1016/0019-1035(91)90137-I.
- Kieffer, H. H. (1970a). Interpretation of the martian polar cap spectra. *Journal of Geophysical Research*, **75**, pp. 510–514.
- Kieffer, H. H. (1970b). Spectral reflectance of CO<sub>2</sub>-H<sub>2</sub>O frosts. *Journal of Geophysical Research*, **75**, pp. 501–509.
- Kieffer, H. H. (1979). Mars south polar spring and summer temperatures: A residual CO<sub>2</sub> frost. *Journal of Geophysical Research*, **84**, pp. 8263–8288.
- Kieffer, H. H. (1990). H<sub>2</sub>O grain size and the amount of dust in Mars' residual north polar cap. *Journal of Geophysical Research*, **95**, pp. 1481–1493.
- Kieffer, H. H., B. M. Jakosky, and C. W. Snyder (1992). *The Planet Mars: From Antiquity to the Present*, pp. 1–33. Mars.

- Kieffer, H. H., T. Z. Martin, A. R. Peterfreund, B. M. Jakosky, E. D. Miner, and F. D. Palluconi (1977). Thermal and albedo mapping of Mars during the Viking primary mission. *Journal of Geophysical Research*, **82**, pp. 4249–4291.
- Kieffer, H. H., T. N. Titus, K. F. Mullins, and P. R. Christensen (2000). Mars south polar spring and summer behavior observed by TES: Seasonal cap evolution controlled by frost grain size. *Journal of Geophysical Research*, **105**, pp. 9653–9700. doi:10.1029/1999JE001136.
- Kim, K. J., D. M. Drake, R. C. Reedy, R. M. S. Williams, and W. V. Boynton (2006). Theoretical fluxes of gamma rays from the martian surface. *Journal of Geophysical Research*. Submitted.
- Krane, K. S. (1988). *Introductory Nuclear Physics*. John Wiley & Sons, Inc.
- Kuiper, G. P. (1952). *The atmospheres of the earth and planets*. Chicago, University of Chicago Press [1952] Rev. ed.
- Laul, J. C., M. R. Smith, H. Wanke, E. Jagoutz, G. Dreibus, H. Palme, B. Spettel, A. Burgehele, M. E. Lipschutz, and R. M. Verkouteren (1986). Chemical systematics of the Shergotty meteorite and the composition of its parent body (Mars). *Geochimica et Cosmochimica Acta*, **50**, pp. 909–926. doi:10.1016/0016-7037(86)90373-X.
- Leighton, R. R. and B. C. Murray (1966). Behavior of carbon dioxide and other volatiles on Mars. *Science*, **153**, pp. 136–144.
- Leovy, C. and Y. Mintz (1969). Numerical Simulation of the Atmospheric Circulation and Climate of Mars. *Journal of Atmospheric Sciences*, **26**, pp. 1167–1190.
- Leovy, C. E., R. W. Zurek, and J. B. Pollack (1973). Mechanisms for Mars Dust Storms. *Journal of Atmospheric Sciences*, **30**, pp. 749–762.
- Lide, D. R. (1991). *CRC Handbook of chemistry and physics : a ready-reference book of chemical and physical data, special student edition*. 72nd ed., Boca Raton: CRC Press, Inc.
- Litvak, M. L., I. G. Mitrofanov, A. S. Kozyrev, A. B. Sanin, V. I. Tretyakov, W. V. Boynton, N. J. Kelly, D. Hamara, C. Shinohara, and R. S. Saunders (2006). Comparison Between Polar Regions of Mars from HEND/Odyssey Data. *Icarus*, **180**, pp. 23–37. doi:10.1016/j.icarus.2005.08.009.
- Martin, L. J., P. B. James, A. Dollfus, K. Iwasaki, and J. D. Beish (1992). *Telescopic Observations: Visual, Photographic, Polarimetric*, pp. 34–70. Mars.

- Martin, L. J. and W. M. McKinney (1974). North polar hood of Mars in 1969 (May 18-July 25). I - Blue light. *Icarus*, **23**, pp. 380–387. doi:10.1016/0019-1035(74)90056-6.
- Masarik, J. and R. C. Reedy (1996). Gamma ray production and transport in Mars. *Journal of Geophysical Research*, **101**, pp. 18891–18912.
- Mellon, M. T., W. C. Feldman, and T. H. Prettyman (2004). The presence and stability of ground ice in the southern hemisphere of Mars. *Icarus*, **169**, pp. 324–340. doi:10.1016/j.icarus.2003.10.022.
- Metzger, A. E. and J. R. Arnold (1970). Gamma-ray spectroscopic measurements of Mars. *Appl. Opt.*, **9**, pp. 1289–1303.
- Meyers, C. H. and M. S. Van Dusen (1933). *Journal of Research National Bureau of Standards*, **84**, pp. 2843–2852.
- Mitrofanov, I., D. Anfimov, A. Kozyrev, M. Litvak, A. Sanin, V. Tret'yakov, A. Krylov, V. Shvetsov, W. V. Boynton, C. Shinohara, D. Hamara, and R. S. Saunders (2002a). Maps of Subsurface Hydrogen from the High Energy Neutron Detector, Mars Odyssey. *Science*, **297**, pp. 78–81. doi:10.1126/science.1073616.
- Mitrofanov, I., A. Kozyrev, M. Litvak, A. Sanin, W. V. Boynton, C. Shinohara, D. Hamara, and S. Saunders (2002b). Mapping of High Energy Neutrons from Mars: Results from Odyssey. *AGU Fall Meeting Abstracts*, pp. B4+.
- Mitrofanov, I. G., M. T. Zuber, M. L. Litvak, W. V. Boynton, D. E. Smith, D. Drake, D. Hamara, A. S. Kozyrev, A. B. Sanin, C. Shinohara, R. S. Saunders, and V. Tret'yakov (2003). CO<sub>2</sub> Snow Depth and Subsurface Water-Ice Abundance in the Northern Hemisphere of Mars. *Science*, **300**, pp. 2081–2084.
- Miyamoto, S. (1963). Meteorological observations of Mars during the 1962-1963 opposition. *Contributions from the Kwasan and Hida Observatories University of Kyoto*, **124**, pp. 1–80.
- Murphy, J. R., J. B. Pollack, R. M. Haberle, C. B. Leovy, O. B. Toon, and J. Schaeffer (1995). Three-dimensional numerical simulation of Martian global dust storms. *Journal of Geophysical Research*, **100**, pp. 26357–26376. doi:10.1029/95JE02984.
- O'Meara, S. J. (1988). Behold, Mars. *Sky and Telescope*, **76**, pp. 614–+.
- Osberg, W. E. and D. F. Hornig (1952). The vibrational spectra of molecules and complex ions in crystals. *Journal of Chemical Physics*, **20**, pp. 1345–1347.
- Owen, T. (1992). *The composition and early history of the atmosphere of Mars*, pp. 818–834. Mars.

- Paige, D. A. and A. P. Ingersoll (1985). Annual heat balance of Martian polar caps - Viking observations. *Science*, **228**, pp. 1160–1168.
- Parker, D. C., C. F. Capen, and J. D. Beish (1983). Exploring the Martian arctic. *Sky and Telescope*, **65**, pp. 218–220.
- Phillips, G. W. and K. W. Marlow (1976). Automatic analysis of gamma-ray spectra from germanium detectors. *Nucl. Instrum. and Methods*, **137**, pp. 525–536.
- Plaxco, J. (1999a). Mars Timeline of Discovery: 1570 B.C. thru 1799. <http://www.astrodigital.org/mars/timeline1.html>. Retrieved 19 April 2005.
- Plaxco, J. (1999b). Mars Timeline of Discovery: 1800 thru 1962. <http://www.astrodigital.org/mars/timeline2.html>. Retrieved 20 April 2005.
- Pollack, J. B., R. M. Haberle, J. Schaeffer, and H. Lee (1990). Simulations of the general circulation of the Martian atmosphere. I - Polar processes. *Journal of Geophysical Research*, **95**, pp. 1447–1473.
- Portyankina, G., W. J. Markiewicz, and K. J. Kossacki (2005). Seasonal evolution of the Martian cryptic region: influence of the atmospheric opacity. *AAS/Division for Planetary Sciences Meeting Abstracts*, **37**.
- Prettyman, T. H., R. C. Elphic, W. C. Feldman, J. R. Murphy, S. M. Nelli, T. N. Titus, and R. L. Tokar (2005). Spatial Deconvolution of Mars Odyssey Neutron Spectroscopy Data: Analysis of Mars Southern Seasonal Cap. In Mackwell, S. and E. Stansbery (eds.) *36th Annual Lunar and Planetary Science Conference*, pp. 1384–+.
- Prettyman, T. H., W. C. Feldman, D. J. Lawrence, G. W. McKinney, A. B. Binder, R. C. Elphic, O. M. Gasnault, S. Maurice, and K. R. Moore (2002). Library Least Squares Analysis of Lunar Prospector Gamma Ray Spectra. In *Lunar and Planetary Institute Conference Abstracts*, pp. 2012–+.
- Prettyman, T. H., W. C. Feldman, M. T. Mellon, G. W. McKinney, W. V. Boynton, S. Karunatillake, D. J. Lawrence, S. Maurice, A. E. Metzger, J. R. Murphy, S. W. Squyres, R. D. Starr, and R. L. Tokar (2004). Composition and structure of the Martian surface at high southern latitudes from neutron spectroscopy. *Journal of Geophysical Research (Planets)*, pp. 5001–+.
- Rayl, A. J. S. (2003). Researchers Find Mars' South Pole Cap is Mostly Water Ice. *The Planetary Society, Article Archives*: <http://www.planetary.org>.
- Reedy, R. C. (1978). Planetary gamma-ray spectroscopy. In *Lunar and Planetary Science Conference*, pp. 2961–2984.

- Reedy, R. C., J. R. Arnold, and J. I. Trombka (1973). Expected gamma ray emission spectra from the lunar surface as a function of chemical composition. *Journal of Geophysical Research*, **78**, pp. 5847–5866.
- Saunders, R. S., R. E. Arvidson, G. D. Badhwar, W. V. Boynton, P. R. Christensen, F. A. Cucinotta, W. C. Feldman, R. G. Gibbs, C. Kloss, M. R. Landano, R. A. Mase, G. W. McSmith, M. A. Meyer, I. G. Mitrofanov, G. D. Pace, J. J. Plaut, W. P. Sidney, D. A. Spencer, T. W. Thompson, and C. J. Zeitlin (2004). 2001 Mars Odyssey Mission Summary. *Space Science Reviews*, **110**, pp. 1–36.
- Singer, R. B., E. S. Bus, K. W. Wells, and J. S. Miller (1989). Spectral imaging of Mars during the 1988 apparition. In *Fourth International Conference on Mars*, p. 185.
- Slipher, E. C. (1962). The photographic story of Mars. In *Mars*, p. 20. Cambridge, Mass., Sky Pub. Corp.
- Smith, D. E. and M. T. Zuber (1998). The relationship between MOLA northern hemisphere topography and the 6.1-mbar atmospheric pressure surface of Mars. *Geophysical Research Letters*, **25**, pp. 4397–4400. doi:10.1029/1998GL900085.
- Smith, D. E., M. T. Zuber, H. V. Frey, J. B. Garvin, J. W. Head, D. O. Muhleman, G. H. Pettengill, R. J. Phillips, S. C. Solomon, H. J. Zwally, W. B. Banerdt, T. C. Duxbury, M. P. Golombek, F. G. Lemoine, G. A. Neumann, D. D. Rowlands, O. Aharonson, P. G. Ford, A. B. Ivanov, C. L. Johnson, P. J. McGovern, J. B. Abshire, R. S. Afzal, and X. Sun (2001a). Mars Orbiter Laser Altimeter: Experiment summary after the first year of global mapping of Mars. *Journal of Geophysical Research*, **106**, pp. 23689–23722. doi:10.1029/2000JE001364.
- Smith, D. E., M. T. Zuber, and G. A. Neumann (2001b). Seasonal Variations of Snow Depth on Mars. *Science*, **294**, pp. 2141–2146. doi:10.1126/science.1066556.
- Smith, M. D. (2002). The annual cycle of water vapor on Mars as observed by the Thermal Emission Spectrometer. *Journal of Geophysical Research (Planets)*, **107**, pp. 25–1. doi:10.1029/2001JE001522.
- Smith, M. D. (2004). Interannual variability in TES atmospheric observations of Mars during 1999–2003. *Icarus*, **167**, pp. 148–165. doi:10.1016/S0019-1035(03)00287-2.
- Snyder, C. W. (1979). The planet Mars as seen at the end of the Viking mission. *Journal of Geophysical Research*, **84**, pp. 8487–8519.
- Special Issue: The Year in Science (2003). The 100 Top Science Stories of 2002. *Discover*, **24**(1).

- Sprague, A. L., W. V. Boynton, K. Kerry, D. Janes, N. J. Kelly, M. Crombie, S. Nelli, J. R. Murphy, R. C. Reedy, and A. Metzger (2006). Mars' atmospheric argon: tracer for understanding martian atmospheric circulation and dynamics. *Journal of Geophysical Research*. Accepted for publication.
- Sprague, A. L., W. V. Boynton, K. E. Kerry, D. M. Janes, D. M. Hunten, K. J. Kim, R. C. Reedy, and A. E. Metzger (2004). Mars' South Polar Ar Enhancement: A Tracer for South Polar Seasonal Meridional Mixing. *Science*, **306**, pp. 1364–1367. doi:10.1126/science.1098496.
- Telecommunications Definitions (1994). Department of Defense Dictionary of Military and Associated Terms. *DOD Joint Staff Publication No. 1-02*.
- Thakur, A. N. (1997). Analysis Of Gamma-Ray Continuum Spectra to Determine the Chemical Composition. *J. Radioanal. Nucl. Chem.*, **215**, pp. 161–167.
- Thomas, P., J. Veverka, and R. Campos-Marquetti (1979). Frost streaks in the south polar cap of Mars. *Journal of Geophysical Research*, **84**, pp. 4621–4633.
- Tillman, J. E. (1988). Mars global atmospheric oscillations: Annually synchronized, transient normal-mode oscillations and the triggering of global dust storms. *Journal of Geophysical Research*, **93**, pp. 9433–9451.
- Tillman, J. E., N. C. Johnson, P. Guttorp, and D. B. Percival (1993). The Martian annual atmospheric pressure cycle - Years without great dust storms. *Journal of Geophysical Research*, **98**, pp. 10963–+.
- Titus, T. N. (2005). Mars Polar Cap Edges Tracked over 3 Full Mars Years. In *36th Annual Lunar and Planetary Science Conference*, pp. 1993–+.
- Titus, T. N., H. H. Kieffer, and P. R. Christensen (2003a). Exposed Water Ice Discovered near the South Pole of Mars. *Science*, **299**, pp. 1048–1051. doi: 10.1126/science.1080497.
- Titus, T. N., H. H. Kieffer, K. F. Mullins, and P. R. Christensen (2001). TES premapping data: Slab ice and snow flurries in the Martian north polar night. *Journal of Geophysical Research*, **106**, pp. 23181–23196. doi:10.1029/2000JE001284.
- Titus, T. N., H. H. Kieffer, J. J. Plaut, P. R. Christensen, A. B. Ivanov, and Themis Science Team (2003b). South Polar Cryptic Region Revisited: THEMIS Observations. In *Third International Conference on Mars Polar Science and Exploration*, pp. 8081–+.

- Toon, O. B., J. B. Pollack, W. Ward, J. A. Burns, and K. Bilski (1980). The astronomical theory of climatic change on Mars. *Icarus*, **44**, pp. 552–607. doi: 10.1016/0019-1035(80)90130-X.
- Vasavada, A., K. Zito, A. Stohl, and I. McEwan (1998). Exploring-Mars.com. <http://www.exploringmars.com/science/ataglance.html>. Retrieved 18 April 2005.
- Veverka, J. and J. Goguen (1973). The Nonuniform Recession of the South Polar Cap of Mars. *Journal of the Royal Astronomical Society of Canada*, **67**, pp. 273–+.
- Viotti, M., K. Goodall, J. Beck, S. Hulme, R. Baalke, C. Waste, R. Passaniti, Z. Gorjian, J. Callas, C. Johnson, S. Lievense, L. Doran, and C. Sharkey (2005a). NASA/JPL 2001 Mars Odyssey. <http://mars.jpl.nasa.gov/odyssey/>. Retrieved 15 Dec 2005.
- Viotti, M., K. Goodall, J. Beck, S. Hulme, R. Baalke, C. Waste, R. Passaniti, C. Johnson, S. Lievense, L. Doran, and C. Sharkey (2005b). NASA's Mars Exploration Program. <http://mars.jpl.nasa.gov/missions/>. Retrieved 13 July 2005.
- Wänke, H., J. Brückner, G. Dreibus, R. Rieder, and I. Ryabchikov (2001). Chemical Composition of Rocks and Soils at the Pathfinder Site. *Space Science Reviews*, **96**, pp. 317–330.
- Wang, H. and A. P. Ingersoll (2002). Martian clouds observed by Mars Global Surveyor Mars Orbiter Camera. *Journal of Geophysical Research (Planets)*, pp. 8–1.
- Ward, W. R. (1979). Present obliquity oscillations of Mars - Fourth-order accuracy in orbital E and I. *Journal of Geophysical Research*, **84**, pp. 237–241.
- Washburn, E. W. (1948). *International Critical Tables of Numerical Data, Physics, Chemistry, and Technology, Volume 3*. New York: McGraw Hill.
- Waters, L. S. (1999). MCNPX User's Guide. *Los Alamos National Laboratory, document LA-UR-99-6058*.
- Wilson, R. J. and M. D. Smith (2005). The Effects of Atmospheric Opacity on the Seasonal Variation of Martian Surface Temperature. In *36th Annual Lunar and Planetary Science Conference*, pp. 1947–+.
- Zuber, M. T., D. E. Smith, S. C. Solomon, J. B. Abshire, R. S. Afzal, O. Aharonson, K. Fishbaugh, P. G. Ford, H. V. Frey, J. B. Garvin, J. W. Head, A. B. Ivanov,

C. L. Johnson, D. O. Muhleman, G. A. Neumann, G. H. Pettengill, R. J. Phillips, X. Sun, H. J. Zwally, W. B. Banerdt, and T. C. Duxbury (1998). Observations of the North Polar Region of Mars from the Mars Orbiter Laser Altimeter. *Science*, **282**, pp. 2053–+.

Zurek, R. W. (1992). *Comparative aspects of the climate of Mars - an introduction to the current atmosphere*, pp. 799–817. Mars.